Thin film rimming flow subject to droplet impact at the surface

Joanne Williams, BA (Hons), MSc.

Thesis submitted to The University of Nottingham
for the degree of Doctor of Philosophy

Dec 2008

To Ernie Miller, who would have been proud.

Abstract

A BEARING CHAMBER MAY BE MODELLED as a horizontal cylinder, stationary or rotating about its axis, with a film of fluid coating the inside of the cylinder wall. The impact of droplets from a two-phase flow in the core of the chamber drives the motion of the oil film. In this thesis we develop a model for the film based on conservation of mass and momentum across the interface between the film and the core, droplet-laden flow. We derive a fourth-order partial differential equation for the film thickness which can be applied to a range of droplet parameters. Solution of this equation is primarily numerical, but approximating it by a cubic also provides useful analytical results.

The equation for film thickness contains terms omitted by previous models of the bearing chamber. In particular, we show that terms due to the azimuthal component of droplet motion have a significant effect on film profiles, as they tend to destabilise shock solutions. A dominance of surface tension over the azimuthal droplet momentum is critical for stable steady shock solutions to exist.

We consider the effect of the droplet impact being non-uniform about the cylinder, and the positioning of a sink to remove the mass added to the film by the droplets. We will also examine the underlying flow in the film, with particular note of recirculation regions and the residence time of the fluid in the chamber. These factors may be key to the effectiveness of the fluid as a coolant. We also show that Marangoni stresses on the film surface, one of the effects of heating the cylinder, can be modelled using the same film equation and also has a destabilizing effect.

Acknowledgements

I gratefully acknowledge the support and hard work of my supervisors, David Riley, Henry Power and Stephen Hibberd, at the University of Nottingham and the many other staff and students who have contributed to my time there.

I would like also to thank the many teachers of mathematics and fluid dynamics who have inspired me to study this subject, including the late Howell Peregrine who taught me at Bristol.

I am grateful for the financial support of Rolls Royce and EPSRC, through the University Technology Centre for Gas Turbine Transmission Systems project JF32. And especially to the organisers of the CISM course on thin films, at which I met my husband. To him, thank-you for keeping me sane and for your love and patience.

Contents

1 Introduction **1**

1.1 The aeroengine bearing chamber 1

1.2 Models of droplet impact 3

1.2.1 Interaction of droplets and the film 3

1.2.2 Distribution of droplets in the chamber 4

1.3 A brief introduction to rimming and coating flow 6

1.3.1 Experiment 6

1.3.2 Theory 6

1.4 The governing equation for the film thickness 7

1.5 The value of the two-dimensional model 8

1.6 Leading order solution 10

1.7 Surface tension 11

1.8 Gravity 13

1.9 Key developments in droplet terms 14

1.10 Sinks and sources 15

1.11 Thermal effects 16

1.12 Timescales 17

1.13 Stability 17

1.14 Recirculation within the film 20

2 Derivation of an evolution equation for a thin film driven by surface mass and momentum transfer **21**

2.1 Model formulation 22

2.2 The Navier-Stokes equations 22
2.3 Boundary conditions at the film interface 23
2.3.1 Conservation relations across a general interface 24
a) Conservation of a general quantity over a discontinuity 24
b) Conservation of mass over a discontinuity 25
c) Conservation of momentum over a discontinuity 26
2.3.2 Interface conditions for rimming flow driven by droplet impact . 27
a) Kinematic Condition 28
b) Dynamic Conditions 28
2.4 Boundary conditions at the cylinder wall 30
2.5 Non-dimensionalisation of governing equations and boundary conditions 30
2.5.1 Conversion to annular coordinate system 30
2.5.2 Non-dimensional and scaled formulation for thin film flows . . . 32
2.5.3 Scalings for the interface conditions 33
2.5.4 Isolation of droplet properties in interface boundary conditions . 35
2.6 Thin-film approximation 36
2.6.1 Governing equations 36
2.6.2 Boundary Conditions 37
2.7 Film-height equation to $O(1)$ 38
2.8 Distinguished limits - the effect of droplet impact 39
2.8.1 Very low droplet volume fraction 40
2.8.2 Low droplet volume fraction 42
2.8.3 Moderate droplet volume fraction 43
2.9 Area of the film 43
2.10 Key features of the film evolution equation 44

3 Film profile for significant uniform droplet momentum but negligible mass transfer at the surface. 46

3.1 Steady solution when shear balances gravity with negligible surface tension and azimuthal droplet momentum, $\zeta, \alpha_u = 0$ 47

3.1.1 Shock solutions 49
3.1.2 Explicit expression for area 51
3.2 Smoothing of shocks by surface tension and droplets 51
3.2.1 Surface tension dominant 52
3.2.2 Droplet momentum dominant 55
a) Linearization method 55
b) Direct method 56
3.2.3 Summary of matching outcomes 57
3.3 Numerical solutions using a steady-state solver 58
3.3.1 Steady-state solver 58
3.3.2 Testing of solver 59
a) Mesh refinement 59
b) Initial shock position 60
3.3.3 Results from steady-state solver 62
a) Effect of surface tension ζ 62
b) Effect of azimuthal droplet momentum α_u 62
c) Comparison across α_u, ζ 63
3.4 Numerical solutions from a transient solver 65
3.4.1 Method using transient solver 65
3.4.2 Results from transient solver 67
a) Parameter map of steady solutions 67
b) Effect of surface tension ζ 68
c) Effect of azimuthal droplet momentum. 69
d) Effect of cross-sectional area A 69
3.5 Stability of solutions 70
3.5.1 Evolution of a perturbation to a steady-state solution 71
3.5.2 Linear stability using eigenvalue analysis 73
3.5.3 Stability of the leading order equation, $\zeta, \alpha_u = 0$, $q < 1/6$ 74
3.5.4 Kinematic Wave Speed, $\zeta, \alpha_u = 0$ 74

3.5.5 Numerical methods for assessing stability, $\zeta, \alpha_u > 0$ 76
a) Finite Difference Method 77
b) Spectral method 79
3.5.6 Numerical results of stability assessment 80
a) Specific case: a film profile expected to be stable 83
b) Specific case: a film profile expected to be unstable . . 84
c) Stability of low-area profiles 84
3.5.7 A comparison of finite difference and spectral methods 85
3.6 Summary of this chapter 88

4 Formulation of film profile and underlying flows, with significant variable droplet mass and momentum transfer at the surface 89

4.1 Updates to derivation and solution method of film profile equation . . . 89
4.1.1 Boundary conditions to allow flow out of a sink ($v_{cyl} \neq 0$), wall rotation ($u_{cyl} \neq 0$), and variable droplet input. 89
4.1.2 Numerical solution methods 91
4.1.3 Numerical implementation of sinks 92
4.1.4 Parameter continuation 93
4.2 Modelling variable droplet input 94
4.2.1 Input function to model a single injector 94
4.2.2 Input function to model distributed injector points 96
4.3 Underlying flow 98
4.3.1 Derivation of streamfunction 98
4.3.2 Method of plotting streamlines 100
4.3.3 Streamlines used to calculate residence times 101
4.3.4 Recirculation, stagnation and hotspots 102
4.3.5 Polar plots 102
4.4 Summary of this chapter 103

5 Film profiles for significant variable mass and momentum transfer at the surface 104

5.1 Results with uniform droplet mass input 104
5.1.1 Non-physical cases 105
5.1.2 Varying c_6, when $c_5 = 0$ 105
5.1.3 Varying c_6, when $c_5 = -1$ 108
5.1.4 Varying c_5 when $c_6 = 0$ 109
5.1.5 Residence times 110
5.2 The leading order when the azimuthal droplet mass term dominates . . 111
5.2.1 Solutions of the cubic with the linear (c_5) term. 111
5.2.2 Possible stable shock solutions of the cubic 119
5.2.3 Maximum supportable film area 123
5.3 Further results for uniform droplet input 126
5.3.1 The effect of cross-sectional area A 126
5.3.2 The effect of increasing droplet mass contribution 127
5.4 The effect of sink position 131
5.5 An example with dimensional parameters 134
5.6 Results with variable droplet input 138
5.6.1 Single injector point for droplets 139
5.6.2 Intermediate Single Injector cases 141
5.6.3 Distributed sources 142
5.7 Summary of this chapter 142

6 Films with the additional features of rotation and thermal effects 145

6.1 Rotating wall and droplet mass contribution 145
6.1.1 Surface profiles for uniform injection of mass as verification of code 146
6.1.2 Underlying flow for uniform injection of mass 147
6.1.3 A rotating cylinder with non-uniform injection of mass 149
6.2 The distinction between the wall rotation (u_{cyl}) and azimuthal mass (c_5) terms 151
6.3 Rotation with opposing surface shear. 153
6.3.1 Re-examination of Villegas-Díaz' results 154

6.3.2 Effect of azimuthal droplet momentum c_3 on shear and rotation cases . . . 155
6.4 Derivation of heating effects . . . 159
6.4.1 Heat equation . . . 159
6.4.2 Thermal Boundary Conditions . . . 160
6.4.3 Temperature of the film to leading order . . . 160
6.4.4 Surface Tension . . . 161
6.5 Summary of this chapter . . . 163

7 Conclusions **164**

A Nomenclature **168**

B Useful Identities **171**
B.1 Grad and Div in cylindrical coordinates. . . . 171
B.2 Stress Tensor . . . 171

C Film-height equation to $O(\epsilon)$ **172**
C.1 Film height equation for generic droplet conditions . . . 172
C.2 Distinguished limits - Droplet cases . . . 174
C.2.1 Very low droplet volume fraction, steep angle $k = 3$, $\beta = -1$ . . . 174
C.2.2 Very low droplet volume fraction, shallow angle $k = 3$, $\beta = 1$ . . . 174
C.2.3 Low droplet volume fraction $k = 2$, $\beta = 0$ . . . 174
C.2.4 Moderate droplet volume fraction $k = 1$, $\beta = 1$ . . . 174

D Extension of analysis to negative u_E **175**
D.1 Smoothing of shocks by surface tension and droplets . . . 175
D.1.1 Surface tension dominant . . . 175
D.1.2 Droplet momentum dominant . . . 176

E Derivation of linear stability analysis **177**

References **179**

Chapter 1

Introduction

1.1 The aeroengine bearing chamber

This thesis concerns the modelling of oil films driven by the impact of droplets, such as may be found in aero-engine bearing chambers. A typical chamber considered is that of the Rolls-Royce Trent series, a schematic of which is shown in figure 1.1. This particular chamber has co-rotating shafts, although in other engines there are contra-rotating shafts. The region of interest is enclosed by two concentric cylinders rotating about their axis. The walls of the chamber comprise parts moving at three speeds: the HP shaft at up to 10000rpm; the IP shaft at up to 7000rpm; and stationary sections [32].

Cross section	Inner shaft	Outer cylinder
A	7000rpm	7000 rpm
B	7000rpm	stationary
C	7000rpm	10000 rpm

The fluid in the chamber is a mixture of air and oil, rotating with the central IP shaft. Oil enters the chamber from the oil injector, and forms a mist in the air, impacting on the outer wall as small droplets. It acts as a lubricant for the bearings, and also as a coolant of the hot metal surfaces. It is important that a constant flow of oil is maintained around the wall, since stagnant or dry patches may overheat, and in extreme cases lead to coking on the bearing walls. Oil leaves the chamber through one or more sumps (not illustrated). It is the behaviour of the oil film that forms on the inside of the outer shaft, henceforth referred to as the *cylinder wall*, that primarily concerns us in this thesis. The chamber has been modelled before, notably by Farrall [15, 17, 18] using a three-part composite numerical model, comprising the core air flow in the chamber, the oil droplet motion in the core, and the oil film motion. However the motion of the oil

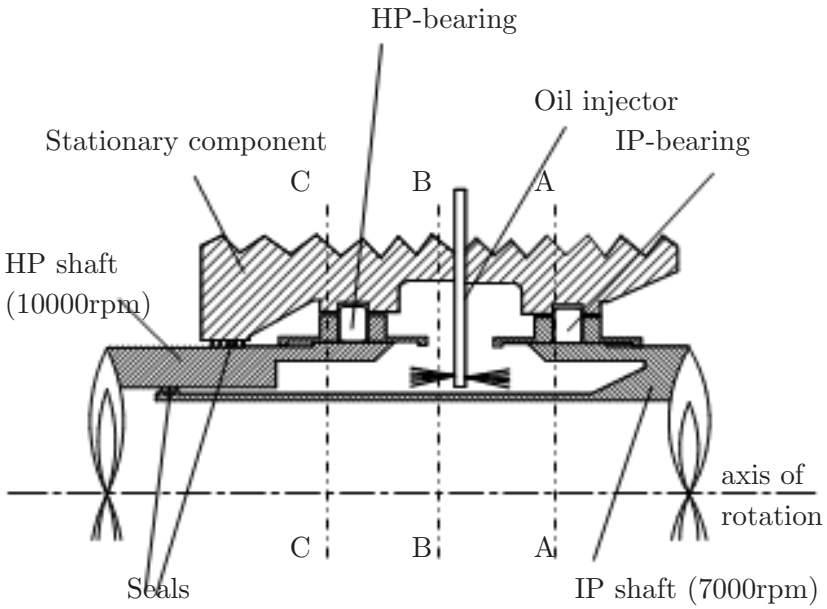

Figure 1.1: Schematic of part of the Trent 800 aeroengine bearing chamber. The chamber (central white area) is approximately rotationally symmetric about the horizontal axis. (After Maqableh *et al.* [32])

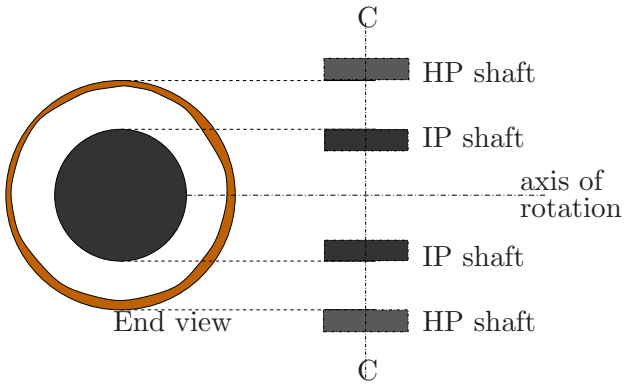

Figure 1.2: The region of interest is an annulus between the rotating shafts, where a film of oil forms on the outer cylinder.

film in response to droplet impacts is insufficiently understood, and further analysis is needed.

The aims of the thesis are to develop a suitable consistent model of droplet impact on rimming flow, and hence derive and analyse an expression for film thickness. In particular, we need to establish whether there are any terms in this equation omitted by previous work in the field, and how such terms may affect solutions at leading order. We will also establish a link between terms in this equation arising from droplet impact and influences such as temperature and the cylinder wall rotation.

Although three-dimensional behaviour is seen in the chamber, we want to reduce complexity and focus on the effect of droplets driving the rimming film, thus we will focus on the three distinct axial cross-sections of the cylinder illustrated in figures 1.1 and

1.2. In these sections, a two-dimensional approximation to the flow will be studied. The core flow is rotating, and the outer cylinder may either be rotating or stationary. In practice, there may be irregularities in the wall which can also cause disruption to the flow, but in this thesis we will focus on the droplet effects, and assume the cylinder wall is smooth, with no obstructions.

Thus the problem posed is to investigate the flow of a thin film of oil on the inside of a smooth rigid cylinder, which may be rotating or stationary, under the influences of gravity and a core rotating flow consisting of a mixture of air and oil droplets. Furthermore, the cylinder may be heated relative to the incoming oil. The oil may leave the chamber through a sink on the cylinder wall.

1.2 Models of droplet impact

The oil in the core air flow of the chamber is sprayed from one or more injectors, and its motion modified by the rotating air flow. Droplets impact on and drive the film on the wall of the bearing chamber. Previous work on bearing chambers, in particular by Farrall [15], provides information on droplet behaviour and helps inform our choice of parameter regimes.

1.2.1 Interaction of droplets and the film

In reality the droplets interact with the film in a complex manner, rebounding, splashing and breaking up as well as being absorbed [15, 17, 18]. As a starting point however it is reasonable to smooth the droplet flow spatially and consider a continuous distribution rather than discrete droplets.

This approach was adopted in two limiting models of droplet impact at the surface of rimming film flow. Noakes [34–36], ignoring momentum, added mass at the surface and removed it at a sink, in an investigation of draining and filling flows. In contrast, Villegas-Díaz [51–53] modelled the two-phase core flow as a fluid of low density which imparted a shear to the surface of the film and neglected droplet mass.

An ad hoc modelling approach would be to simply combine these independent mass and momentum contributions. Instead, in Chapter 2 our model will ensure continuity of mass and momentum across the interface between the film and the core flow. We will derive the governing equation for the film thickness h and find that both the previous models omit critical terms. In particular, the previously neglected azimuthal component of droplets impacting on the surface where surface gradients are non-zero, can be significant

and can destabilise the film.

1.2.2 Distribution of droplets in the chamber

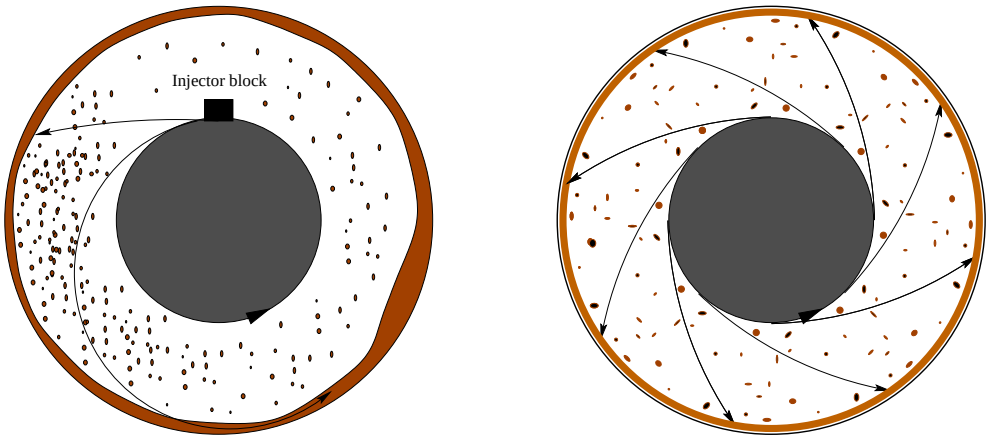

Figure 1.3: Illustration of how the conditions in the core flow outside the film may vary azimuthally

In this thesis we will initially assume that droplets impact uniformly about the cylinder. In Chapter 4 we will consider spatial distributions of droplet impact. There are two particular configurations of interest, as illustrated in figure 1.3. In an aeroengine bearing chamber, although oil may be scattered from many surfaces, it originates from a single fixed injector block, and one group of numerical models by Farrall [15], Noakes [34] and Wang *et al.* [54–56] reflects this. The second group of models is based on an experimental chamber at the University of Karlsruhe, which has the oil injected in the bearing casing, so it enters the chamber by being shed from the central shaft. These models track droplets from 10 or 18 points evenly distributed around the shaft, as an approximation to a completely even distribution [15, 16].

Much of the work on flow in bearing chambers has been based on tracking the path of individual or groups of droplets. Wang *et al.* [54–56] tracked droplets from an injector block in an axially varying three-dimensional model of the chamber with a co- or contra-rotating central shaft. They used commercial CFD software to model the underlying airflow with a progressive level of coupling with the droplet motion in the later studies, which also show that a simplified model of the chamber is acceptable for the CFD. Mass deposition figures were given in the azimuthal (θ) and axial (z) directions. The coupling has little effect on the deposition pattern of large droplets, but some effect on the deposition of smaller droplets, and results show a strong dependence on the position and nature of the injector block. Some airflow velocities are given in [54, 56] but with no indication of droplet velocities upon impact with the film. Plots of droplet trajectories

in the annulus suggest that the angle of input may vary around the chamber with a steep angle for droplets that impact close to the injector at the top, shallow for those that travel to the bottom, and very shallow for those that travel right round [55]. Graphs of droplet speeds (not velocities) versus residence time, for different droplet sizes and injector locations have also been reported [55].

Farrall [16–18] built a numerical model of the full bearing chamber, coupling a numerical model of the film with data about the core air-flow from the commercial code CFX, and droplet tracking through the core from a finite number of sources. The film model does not include surface tension or a complete description of droplet momentum and mass transfer. Droplet impact is modelled using the dominant azimuthal shear force and a secondary axial shear force, arising from secondary flow in chamber (due to droplet collisions etc). Mass, azimuthal and axial momentum, at z, r and θ, and azimuthal and axial shear at θ and z, are required as inputs to the film module [16]. It may therefore be possible to extract these from the full system code if it were rerun, but they are not output in the reports available. The only available data are tutorials with the documentation, with some typical examples.

Farrall's computation of the composite numerical model for the two-phase flow in the bearing chamber predicted the profile of droplet impact on the outer wall of the cylinder resulting from droplet motion. He found that droplets above a critical diameter impact on the outer cylinder before completing an entire circuit of the annulus, this droplet diameter being reduced by an increase in inner shaft speed or injection velocity of the droplets [15]. The larger droplets impact close to the top of the cylinder, the smaller droplets, having lower radial momentum, travel further round the cylinder before impacting. Noakes [34], requiring only a mass influx for her film model which assumed momentum to be negligible, used a variable mass flux based on Farrall's result with a single injector location at the top of the cylinder and a Rossin-Rammler distribution of droplet diameters. Noakes anticipated the rimming flow to cause a spread in the deposition, although this is not quantified, and approximated the mass distribution with a half-normal in $-2.14 \leq \theta \leq 0.86$ and zero elsewhere, a distribution that is qualitatively similar to Farrall's results.

A different approach was taken by Maqableh *et al.* [32], who used the commercial software code CFX with a mixture model to study the bearing chamber. Speeds (but not velocity components) are reported for air, oil, and droplet phases with respect to the radius of the chamber annulus, but no azimuthal variations are reported.

1.3 A brief introduction to rimming and coating flow

The methods employed in this thesis to model the thin film owe much to previous work, for rimming and coating flows occur in a wide range of industrial processes and have elaborate yet mathematically tractable behaviour. It is well known that fluid inside a horizontally rotating cylinder may form a variety of profiles, according to factors such as the rotation rate, fill percentage, viscosity and surface tension. We use the term rimming flow to describe a film covering the inside of a horizontal rotating cylinder, and coating flow to refer to a film on the outside of the cylinder. The term coating flow is sometimes used for both [25], and the two problems are closely related.

1.3.1 Experiment

Moffatt [33] presented some pioneering qualitative experiments on coating flows in 1977. There has since been a great deal of work on coating and rimming flows, both analytical and experimental [14]. There are many different states that the film can take. Instabilities in three dimensions, time periodic and chaotic motions were documented in the unpublished manuscript by Benjamin, Pritchard and Taverner [9]. Then experimental work by Thoroddsen and Mahadevan [45, 46] revealed that in various parameter regimes flow inside a cylinder could give rise to configurations including: sloshing; rimming flow; a stable axial front; weak undulations on the front; shark's-teeth patterns along the cylinder's axis; travelling waves; stationary pendants randomly spaced along the cylinder's axis; fluid curtains dividing the cylinder into cells (hygrocysts); counter-flowing jets; air entrainment; incomplete pullover into centrifugal mode; turbulence inside the fluid sheet; or random motions inside the bottom pool. Both these papers include excellent photographs of the shark's-teeth patterns, which were also observed and termed a 'scallop pattern' by Johnson [26]. A review of the experimental work is given by Evans, Schwartz and Roy [14].

1.3.2 Theory

Ruschak and Scriven [41] studied steady rimming flow using a rigid-body approximation, but as Moffatt noted, in parameter ranges for which there is significant shear across the film, this is not valid. Moffatt, studying coating flow, found that in two dimensions at leading order, if surface tension is neglected, the film profile can be described by solutions of a cubic equation. There is a critical mass of fluid, below which the film forms a smooth profile. Similarly, a lubrication approximation, with the dominant balance between gravity and viscous forces was adopted by Johnson [25] to study steady, two-

dimensional rimming flows. He derived to $O(\epsilon)$, where ϵ is the ratio of the film thickness to cylinder radius, the evolution equation for rimming flow, but assumed negligible inertia in the flow, and neglected surface tension and any effects of the gas above the free surface. His simple approach of classifying flows using the bounded properties of $\cos\theta$ was subsequently used by Villegas-Díaz [51]. Johnson demonstrated that these limits led to various cases of continuous or partial films. He showed that as the flux q increases, the variation in the film thickness increases, owing to the increasing influence of the gravity force, and that continuous films may sustain shocks, i.e. sudden variations in thickness. Such films may include a recirculation zone. In the absence of surface tension, these solutions would have discontinuous thickness, and thus Johnson retained $O(\epsilon)$ pressure and gravitational terms for smoothing.

A crucial difference between coating and rimming flow is that finite thickness films involving shocks cannot occur in coating flows, though they occur in rimming flows. In coating flows load shedding occurs when the weight of fluid is increased beyond critical, whereas in rimming flow the extra fluid can form a shock. This was shown by Duffy and Wilson [12] who considered the coating flow, particularly curtain flows, that ensue when fluid is supplied continuously as a curtain from above the cylinder, so that it flows around the cylinder and eventually falls off near the bottom. (Such a flow could be seen as a film with infinite thickness at the top and bottom of the cylinder.) As far as lubrication theory is concerned rimming flow and coating flow are the same, but when secondary effects such as surface tension are included then they differ.

In rimming flow the primary force balance is between gravity and the viscous effects of the wall rotation, but as we will see, surface shear can also drive the film to form similar profiles. Correspondingly, these flows are related to thin film flow down a slope with an overlying air flow, or the problem of a fluid film carried upwards on a moving wall whose slope changes abruptly [58].

1.4 The governing equation for the film thickness

In Chapters 2 and 4 of this thesis we will derive the following general equation for the film thickness h, with respect to time t and angle θ, measured anticlockwise from the

bottom of the cylinder:

$$\frac{\partial h}{\partial t} + \frac{\partial}{\partial \theta}\left(\overbrace{c_1\left(\frac{\partial h}{\partial \theta} + \frac{\partial^3 h}{\partial \theta^3}\right)\frac{h^3}{3}}^{\textit{Surface Tension}} + \overbrace{c_2 \sin\theta \frac{h^3}{3}}^{\textit{Gravity}} + \overbrace{\left(c_3(\theta)\frac{\partial h}{\partial \theta} + c_4(\theta)\right)\frac{h^2}{2}}^{\textit{Droplet Momentum}} \right) + \underbrace{\left(c_5(\theta)\frac{\partial h}{\partial \theta} + c_6(\theta)\right)}_{\textit{Droplet Mass}} + \underbrace{\frac{\partial}{\partial \theta}\left(u_{cyl} h\right)}_{\textit{Wall Rotation}} - \underbrace{v_{cyl}}_{\textit{Sink}} = 0. \quad (1.1)$$

The coefficients c_i will be explained in due course. For now, note that c_3 and c_4 represent azimuthal and radial components of the droplet momentum, and c_5, c_6 the azimuthal and radial components of droplet mass. u_{cyl} and v_{cyl} arise from boundary conditions on the cylinder wall, and could be integrated into the coefficients c_i, but are left separate for convenience. Similar film equations are familiar from other work and Table 1.1 shows which terms are common to (1.1).

In the next few sections of this introduction we will overview the formulation of (1.1) term by term.

1.5 The value of the two-dimensional model

Throughout this thesis, we will concentrate on two-dimensional flows, neglecting axial variation and instabilities. Although experiments show that three-dimensional behaviours occur in rimming flow, a good understanding of two-dimensional behaviour is a prerequisite for an investigation of the third, axial dimension. When Hosoi and Mahadevan [22] numerically reproduced the shark's teeth and some other three-dimensional features of previous experiments [45, 46], they found that axial instability arises from a localised ridge which forms near the bottom of the cylinder. This is a similar situation to the flow of fluid down an inclined plane — a ridge at the leading edge triggers a transverse fingering instability, where the dominant destabilizing mechanism is due to gravitational and viscous forces. When perturbed axially, this ridge may lose stability, mainly due to the fact that thicker regions travel faster than thinner regions. This development occurs when second-order inertial terms are included, consistent with the findings of Benjamin *et al.* [9] that in the absence of inertia, the leading order system is always linearly stable to axial variations. Following the nonlinear evolution of the axial instability, Hosoi and Mahadevan [22] showed that this results in the stationary shark-teeth pattern observed in experiments. Thus if in two dimensions we find such a ridge, it may develop into a more complex three-dimensional instability.

$$\frac{\partial h}{\partial t}+\frac{\partial}{\partial\theta}\left(c_1\left(\frac{\partial h}{\partial\theta}+\frac{\partial^3 h}{\partial\theta^3}\right)\frac{h^3}{3}+c_2\sin\theta\frac{h^3}{3}+\left(c_3(\theta)\frac{\partial h}{\partial\theta}+c_4(\theta)\right)\frac{h^2}{2}\right)+\left(c_5(\theta)\frac{\partial h}{\partial\theta}+c_6(\theta)\right)+\frac{\partial}{\partial\theta}\left(u_{cyl}h\right)-v_{cyl}=0.$$

	Surface tension	*Gravity*	*Azimuthal momentum and/or Marangoni*	*Shear and/or 2nd order Gravity*	*Azimuthal droplet mass and/or wall rotation*	*Radial droplet mass and/or wall flux*	
	c_1	c_2	c_3	c_4	c_5/u_{cyl}	c_6/v_{cyl}	Other terms
Leading order cubic	x	✓	x	✓	✓	x	
Momentum only (Chap. 3)	ζ	-1	α_u	1	0	0	
Full mass and momentum (Chap. 5)	$\mathrm{Re_f We_f}$	$-\mathrm{Re_f/Fr}$	$\mathrm{Re_f}au_E^2$	$\mathrm{Re_f}au_E(-v_E)$	$-au_E$	$-a(-v_E)$	
Noakes [34], rotation (Chap. 6)	ϵ	-1	0	0	1	λI	
Villegas-Díaz[51], rotation, shear (Chap. 6)	B^{-1}	$-\Gamma$	0	γ	1	0	
Marangoni terms (Chap. 6)	0	-1	Ma Bi	0	1	0	
Moffatt [33]	x	✓	x	✓	✓	x	
Wilson *et al.* [59] Smoothing by S.T.	partial	✓	x	✓	x	x	
Wilson *et al.* [59] Smoothing by gravity		✓	x	✓	x	x	2nd order gravity
Wilson *et al.* [59] Rotating		✓	x	✓	✓	x	
Benjamin *et al.* [9] eqn. 30	✓	✓	x	✓ gravity	✓	x	2nd order gravity
Acrivos *et al.* [2, 47]	✓	✓	x	x	✓	x	2nd order gravity
Hinch *et al.* [20, 21]	✓	✓	x	x	✓	x	

Table 1.1: Coefficients of (1.1) and similar equations in other literature

This development also occurs in coating flow, where a two-dimensional axial ridge may break up into drops near the underside of the cylinder, rings, or fingering. This was shown experimentally and numerically by Evans, Schwartz and Roy [13, 14], whose model, in a similar manner to the work of Acrivos [2, 47], included terms that may be asymptotically of higher order, but are claimed to be significant.

Hosoi and Mahadevan [22] use α, a ratio of viscous to gravitational forces, as an expansion parameter, rather than the aspect ratio ϵ, and find the flux to first order in α. They prefer it to the usual aspect ratio used in lubrication theory, to avoid the potential problem with larger filling fractions of large changes in aspect ratio in some region due to volume conservation in the confined geometry of a cylinder.

1.6 Leading order solution

In the case when surface tension is small, the droplet momentum approximated by a surface shear, and there is negligible droplet mass, (1.1) can be simplified to

$$\frac{\partial h}{\partial t} + \frac{\partial q}{\partial \theta} = 0, \tag{1.2}$$

where

$$q = \frac{h^3}{3}\sin\theta + c_4\frac{h^2}{2} + u_{cyl}h. \tag{1.3}$$

For steady-state conditions the flux q is constant and the cubic polynomial (1.3) can be solved analytically, and has attracted much attention. The case $c_4 = 0$ is Moffatt's classic problem [33], while the shear-driven flow with $c_4 = 1$ was tackled by Wilson *et al.* [59] and Villegas-Díaz [51].

The cubic can have up to three positive real solutions. Villegas-Díaz drew up a chart in c_4-q space[1], with $u_{cyl} = 1$, to show the various possible solutions, and in Chapter 5 we show the equivalent in u_{cyl}-q space with $c_4 = 1$.

For the Moffatt problem of $c_4 = 0$, $u_{cyl} = 1$, there is a critical flux value of $q_c = 2/3$, above which there are no completely wetting solutions for h. Below this value, there is a completely wetting solution, and a partial solution between $0 < \theta < \pi$, and the two solutions meet at a corner at $q = 2/3$. The completely wetting solution in this case is termed the critical solution, and the total mass of fluid in the film, $A = 4.442$ [12], is the maximum that can be supported without a shock up to the partial solution — and hence the maximum supportable mass for coating flow. (Moffatt [33] gave the maximum value $A = 4.428$, but Duffy and Wilson [12] noted minor errors in his calculation of the

[1] $c_4 = \gamma$ in Villegas-Díaz' notation

maximum weight and h at the critical point.) For rimming flow with a shock, there is a second maximum mass of about $A = 6.88$, before such steady-state solutions are not possible and pooling will occur.

Tirumkudulu and Acrivos [47] noted that recirculation can occur within the film (ie a region of reverse flow) when $4.983 < A < 6.954$, although the latter value slightly exceeds the maximum area possible according to Duffy and Wilson.

The four possible configurations that can occur for rimming flow, with a maximum of one shock between solutions, were also derived using a different method by Johnson [25]. He did not tackle stability in this paper, and indeed two of them, involving a jump in the upper quadrant of the cylinder $\pi/2 < \theta < \pi$ are not physically realisable.

In this thesis, we will initially consider the shear-only case where $c_4 = 1$ and $u_{cyl} = 0$, in order to focus on the importance of the term with coefficient c_3. Reintroducing the rotation is a secondary objective, although important, and in Chapter 4 and 5 we will see that the rotation term has much in common with one component of the droplet mass.

For the shear-only case the solutions take a similar form to the rotation-only case, but this time the critical flux is $q = 1/6$. The mass of fluid in the film under shock solutions can be given in a closed form [59] but the closed form when rotation is also included is too unwieldy to be of use. The maximum mass without including a shock is $A = 3.951$. With a shock, for shear-driven film the mass can increase indefinitely, although the thin-film approximation ceases to be valid. In practice the maximum mass is limited by stability.

The underlying flow in the shear problem has qualitative differences from the Moffatt problem, for which recirculating flow occurs only when the shock position is $0 < \theta < \pi/6$ and the recirculation zone lies near the free surface. With shear and no rotation, recirculating flow near the cylinder wall occurs for all shock positions [59].

When both shear and rotation are included, then the range of solutions increases, and multiple shocks become possible. The case when rotation opposes shear is particularly interesting [51].

1.7 Surface tension

Even if the coefficient of surface tension is small, because it is associated with the fourth derivative of h, it has significant effect around shocks and short-wave perturbations. It is therefore important to include this term, with the coefficient c_1 in (1.1). We will see

this confirmed in Chapter 3.

Benjamin, Pritchard and Tavener [9] formulated a treatment of steady and unsteady flows and the smoothing of shock solutions by surface tension and has prompted similar work by others. Ashmore, Hosoi and Stone [3] characterised surface tension effects, identifying three regimes dependent on λ, a measure of gravitational to viscous effects[2]. When $0 < \lambda \leq 2$ viscous effects dominate and surface tension has little effect, as the profiles are already smooth. When $\lambda > 5$, pooling of the fluid at the bottom of the cylinder occurs, and the inclusion of surface tension is particularly important. When $2 < \lambda < 5$, the region of particular physical interest in the current study, viscous and gravity terms are of the same order. Surface tension has a significant qualitative effect, as its introduction smooths solutions that would otherwise be discontinuous. (A minor error in the higher orders of surface curvature κ was corrected by Villegas-Díaz [51].)

Wilson and Williams [58] also argued that shock solutions from the Moffatt cubic equation cannot physically exist without some smoothing mechanism, but that surface tension makes them possible. Explicit criteria for determining whether or not shock solutions occur were given in the work of O'Brien and Gath [39], who determined the shock location in terms of the average film thickness. Contrary to Wilson and Williams they claimed that a straight-forward lubrication theory can model the shock location and height, without taking account of surface tension (they consider no external shear effects). But numerical study by Wilson, Hunt and Duffy [60] revealed that behaviours of the critical solution in the thin film limit $\epsilon \to 0$ near $\theta = \pi/2$ are not captured by the outer asymptotic solution in integer powers of ϵ. Even in the absence of surface tension, the corner predicted by Moffatt's leading-order solution never occurs. For physical parameter values, the higher-order terms obtained by Wilson *et al.* [60] dominate the formally lower-order terms that can be obtained without detailed knowledge of the solution in the inner region, so these higher-order terms must be included in order to obtain an accurate correction to Moffatt's leading-order value of the critical weight, although the difference from Moffatt's value is small in absolute terms. This is why shock solutions require smoothing by surface tension or higher-order gravitational terms.

The stabilising influence of surface tension on rimming flow was also investigated by Benilov and co-workers [6–8]. Benilov, O'Brien and Sazonov [8] described both harmonic, neutrally stable solutions and non-harmonic, developing singularities in real time, so-called explosive instabilities. Their work involves detailed asymptotics, but is limited to zero surface tension. These authors went on to show that this is not relevant to physical

[2] They define $\lambda = A^2\rho g R/\mu\Omega$ where A is filling fraction, ρ density, g gravity, R radius, μ viscosity, and Ω rotation.

rimming flows in [7], where they show that surface tension eliminates these exploding solutions and has in general a stabilising effect. However in a certain parameter range some eigenmodes become unstable.

Benilov [5] continued work on whether surface tension has a stabilising effect, considering multidimensional and 'exploding'disturbances. In the case of short wavelength disturbances, surface tension is a stabilizing effect. In the case of long-scale disturbances, with axial wavelength greater than the radius of the cylinder, Acrivos and Jin [2] showed that surface tension destabilizes some of the eigenmodes, but Benilov argued that the corresponding growth rate of these is much smaller than that of the inertial instability.

However as Acrivos observes [2], this method is controversial since such high-frequency modes are incompatible with the thin film approximation, given that derivatives with respect to θ are no longer $O(1)$. So high-frequency modes will have to satisfy a more complicated equation than that derived from the thin-film approximation.

One exception to the general conclusion that surface tension acts as a stabilizing influence is the case of axial disturbances to rimming flow. Acrivos and Jin [2] explain this as surface tension always tending to minimize the area of the airliquid interface of the thin film, thereby destabilizing the thin film to axial disturbances but stabilizing it in the two-dimensional case.

1.8 Gravity

The c_2 term in (1.1) occurs in all models of rimming flow except in the case of high speed rotation where the flow is closer to rigid body motion. At high rotation rates the effects of gravity may be neglected. This is the regime considered by the numerical study of Orr and Scriven [40] and later by Noakes *et al.* [35].

Gravitational smoothing was studied by Wilson, Duffy and Black [59] and shown to produce similar effects to smoothing by surface tension. However higher-order gravity effects can smooth the shock present in the leading-order solution for rimming flow but not for coating flow, whereas surface tension effects can do so in both situations.

Benjamin *et al.* [9] included smoothing by gravity, leading to extra terms at second order with derivatives of h, but also a term $-\alpha h^2/2$, equivalent to the coefficient c_4. They sought solutions around $c_4 = -0.07$, but with a flux $q = 0.66$, and found only a narrow parameter range gave any solutions, struggling for convergence with their numerical solver. From Villegas-Díaz's chart of q-c_4 space, (figure 32 of [51]) and definition of the critical flux curve, the critical flux for $c_4 = -0.07$ is $q = 0.6329$. At the higher flux for

which Benjamin *et al.* were seeking solutions, no leading order complete film solutions exist, hence perhaps identifying the cause of the difficulties they experienced.

Working in the regime of high effective capillary numbers, i.e. surface tension low and gravity high, Tirumkudulu and Acrivos also required gravitational smoothing to sustain shocks and presented a modified lubrication analysis [47]. They proposed a model evolution equation similar to that obtained by Benjamin *et al.* [9] by an $O(\epsilon)$ asymptotic analysis. Although the model equation cannot be derived from a formal perturbation expansion, and they neglect surface tension at leading order, they showed that it captures behaviour seen numerically and experimentally. One of the benefits of the model equation is that it includes the effect of gravity in producing a puddle of liquid at the base of the cylinder when the rotation is small or absent, and so extends the classical theory to a wider range of filling fractions.

Villegas-Díaz [51] looked at gravitational and surface tension smoothing with surface shear ($c_4 \neq 0$), and found that it is the surface tension term that generally determines the inner behaviour. In this thesis only the leading-order gravitation term will be included and gravitational smoothing will not be considered; surface tension smoothing is included.

1.9 Key developments in droplet terms

The key contribution of this thesis is a more thorough development and analysis of the interaction between the core droplet-laden flow and the rimming film than has previously been undertaken.

Rimming flow with an imposed surface shear may be used as a simple model of this system, as in recent work by Villegas-Díaz, Power and Riley [51–53]. Noakes [34] on the other hand did include mass injection on her numerical model of the cylinder, but did not account for droplets transferring momentum to the film.

Shear and rotation together produce interesting dynamics, the equation being qualitatively unlike the case of rotation or shear alone. This was demonstrated by Villegas-Díaz *et al.* [51, 52], who made use of the method suggested by Johnson [25], employing the properties of $\cos\theta$. If shear is in the same direction as rotation there is nothing new. The most interesting case is that when shear opposes rotation, a greater variety of shock positions may occur.

Continuing the analysis begun in [52], Villegas-Díaz *et al.* [53] used a parameter γ, a measure of rotation to surface shear, to classify the branches of the solution to the

lubrication theory. γ may be negative, representing cases where rotation opposes shear. There is a rich diversity of shock solutions between various branches, that are smoothed by surface tension. There may be double-shock solutions and multiple shocks. Villegas-Díaz *et al.* used numerical techniques to find these smoothed solutions, and related them to the branches of the lubrication theory solution.

We will show in Chapter 2, that droplets also contribute the terms in (1.1) with coefficients c_3 and c_5. There are various distinguished limits described in Chapter 2, for which these terms have varying importance. As as seen in (2.65–2.70), the Villegas-Díaz limit can be reproduced for very small droplet volume fractions, $\alpha = O(\epsilon^3)$. But for $\alpha = O(\epsilon^2)$ or larger, then if the c_3 term is negligible, then there *must* be a c_6 contribution for this limit to be consistent. In other words, if the film is driven by shear with larger droplet volume fractions, and the angle of droplet impact is such that there is no azimuthal momentum contribution ($c_3 = 0$) then there must be a significant radial mass contribution. If the radial mass contribution is so small that c_6 can be neglected, as in the study of Villegas-Díaz, and the flow is driven by shear, then there must be a significant contribution from c_3. We will establish in Chapter 3 that the c_3 term has a significant effect on the solutions that can be found.

1.10 Sinks and sources

The droplets impart mass to the film, corresponding to terms c_5 and c_6 in (1.1). The effect of mass addition on rimming film has previously been modelled by Noakes, who studied draining and filling flows [34]. In her model, mass is added to the rimming flow film, but with negligible momentum, and assuming it does not come from a shallow angle, that is she used only c_6 to model the droplets. There was no shear contribution, and she accounted for fluid inflow/outflow through incorporating flux functions into the formulation of mass balance.

Since if mass added to the film with no outflow the thickness will grow indefinitely, Noakes included a sink on the cylinder wall, which we will use in Chapters 4–6. In our model it will be incorporated as the wall boundary condition v_{cyl}, a narrow region usually at the bottom of the cylinder, through which fluid flows at a fixed rate. In Noakes' model the outflow and inflow are summed, to give a net fluid injection or extraction dependent on θ.

If mass is injected uniformly from a steep angle, without extraction, then the film profile progresses through the various steady states, with thickening at $\theta = \pi/2$, then a shock forming at $0 < \theta < \pi/2$, which progresses down the lower quadrant of the cylinder to

$\theta = 0$, and then a pool forms. But although qualitatively similar, these filling profiles are not identical to the steady-state solutions of equivalent mass, since inflow leads to more fluid on the rising side than is the case for the steady state.

In the bearing chamber, oil may be injected from a single point and thus not impact uniformly on the surface of the film. This issue will be discussed in detail in Chapter 4. Uniform injection over a small section at at the top of the cylinder causes a front to occur where the fluid is added [34]. Noakes also looked at a non-uniform injection profile based on the results of Farrall [15]. This profile was discontinuous, with most of the mass being injected at $\theta = -\pi + 1$, slightly past the top of the cylinder. Although the injection is discontinuous, the film has no shock at the injector, but a sudden change in gradient. This profile will be discussed in Chapter 6.

When fluid is extracted at a rate to match the injection, then a steady-state can be found. There is a discontinuity at the region of fluid extraction, the height of which is proportional to the rate of inflow. The location of the outflow at the base of the cylinder ($\theta = 0$) prevents fluid moving to the rising side, so the usual shock profile is disrupted or prevented from forming. Furthermore, as the inflow/outflow rate is increased, more fluid can be held in a film without formation of a front than when there is no extra mass [34].

We will reproduce Noakes' results as a verification of our method and code, but also in order to examine the flow within the film. Streamlines will enable us to trace the path of fluid from the injection at the surface to the outflow, and thus see how many times the fresh oil circulates around the cylinder before leaving at the sink. We will also examine the impact of the extra terms c_3, c_4 and c_5 which do not occur in Noakes' model.

1.11 Thermal effects

One of the purposes of oil injection in the aero-engine bearing chamber is to cool the cylinder walls. A full analysis of heating effects on the film is beyond the scope of this thesis, but in Chapter 6 we will consider one specific aspect. The surface tension of the film is affected by temperature and non-uniform surface temperature creates Marangoni stresses on the surface. This phenomenon has been investigated in the context of film flow down a heated plane, where it has been shown that profile gradient terms of the form $(h^2 h_x)_x$ arise [27, 44, 50]. This can create undercompressive shocks and travelling waves (Bertozzi, Münch and Shearer [10, 11]). Incidentally the simplified geometry of a plane is often used as a local approximation to flow around a large cylinder, however there are important distinctions. For flow in or around a cylinder the effect of gravity

is variable, its local direction depending on the position around the cylinder, and the solution must also be periodic.

In Chapter 6 we will derive a governing equation for thin film rimming flow with a uniformly heated cylinder wall, and show that a term of the form $\frac{\partial}{\partial\theta}\left(h^2\frac{\partial h}{\partial\theta}\right)$ appears in (1.1), which has a destabilising effect on the film. Since this is equivalent to the term with coefficient c_3, derived from the azimuthal component of droplet momentum, results obtained from droplet impact can be applied to the heating case.

1.12 Timescales

The dominant motion in the film is the flow around the cylinder, whether this is driven by the shear effect of the incoming droplets or rotation of the cylinder wall, so this is the primary timescale used in this thesis. However this is not the only possible approach.

The fastest time-scale is the rotation of the cylinder, followed by the timescale corresponding to the action of the surface tension, drift and decay of free surface perturbations. Hinch, Kelmanson and Metcalfe [20, 21] highlighted these multiple time-scales and presented a rescaling that yields explicit formulae for decay and drift rates.

Noakes, King and Riley [34–36] also extended the model of Moffatt [33] through a systematic multiple-scales analysis to include centrifugal and surface-tension effects, with the determination of the governing equation for the film profile on the long timescale. This approach was first attempted by Hynes [24] for coating flows. (Noakes demonstrated that some terms were wrongly discarded due to an inconsistency in scalings in the work of Hynes, and included a correction, although this showed that the conclusions of Hynes remain valid. She also showed that the corresponding equation for rimming flows simply differs in the sign of the centrifugal term.) The resulting equation was seen to combine the features of the usual small reduced Reynolds number model with more complicated terms resulting from the inclusion of inertial effects.

1.13 Stability

Throughout this thesis the primary concern is with steady-state solutions. The ideal situation for the bearing chamber is that the film achieves a steady flow which continually replenishes the oil in all areas. Some transients are acceptable, but it important that the film does not flow in a steady state in which some oil is never replaced, or one in which any part is left dry. In an environment continually subject to variations, the only physically meaningful steady states are those which are stable to small perturbations.

Thus some analysis of stability is necessary.

In Chapter 3 we will consider the stability of the solutions we find therein in some detail. However since our main solution method will be a transient numerical solver, almost all of the steady-state solutions given in this thesis will be stable.

For coating (not rimming) flow, Moffatt [33] found using a kinematic wave theory that sudden increases in film thickness with rotation direction will tend to grow and thus be unstable. This is physically intuitive, as according to the possible solutions of the cubic (1.3) such increases can only occur in $0 < \theta < \pi/2$ so will be hanging from the underside of the rotating cylinder.

The base solutions to the Moffatt equation for rimming flow, (1.3) with $c_4 = 0$ and with no shocks, were shown to be neutrally stable to two-dimensional disturbances, by O'Brien [37]; by Acrivos and Jin [2], who made use of the model equation of Tirumkudulu and Acrivos [47] to address the stability of rimming flow; and also by Benjamin *et al.* [9], who used a functional based on the energy of the flow. However Villegas-Diaz, Power and Riley [52], prompted by a suggestion of Benjamin *et al.*, employed a technique using a functional equal to the kinematic wave speed of a small disturbance to the film. They showed that when $q = q_c$, disturbances could be 'trapped' by a point of zero kinematic wave speed. An initial disturbance having positive amplitude continuously grows at the focussing point; one with a negative amplitude will eventually rupture the fluid film. So such a solution will be *unstable*, although applying the Benjamin stability criterion based on energy one would find it to be neutrally stable. This difference may arise since the energy functional integrates the data, so may smooth over the singularity at the critical point seen by the kinematic wave method. We will make use of kinematic wave theory in Chapters 3 and 5 to indicate which shock solutions may be stable. Solutions with $q < q_c$, with no shocks, are stable [52].

Shock solutions with a shock in the lower quadrant ($0 < \theta < \pi/2$) are stable to small two-dimensional disturbances, as was shown using kinematic wave theory by O'Brien [37], Acrivos and Jin [2], Benjamin *et al.* [9] and Villegas-Díaz *et al.* However, if the shock is in the upper quadrant ($\pi/2 < \theta < \pi$), then the solution is unstable [9, 37, 52]. Furthermore, the solution with one shock in each quadrant is also unstable [9, 52]. Most of these papers ignored the possibility of multiple shocks in the same quadrant.

Surface tension has a stabilising effect on two-dimensional disturbances, and in the second part of his paper [38], O'Brien extended lubrication theory to $O(\epsilon)$, including terms in pressure and surface tension and showed that surface tension places a restriction on the critical wave number when instability occurs [38]. Without surface tension, O'Brien's higher order lubrication approximation gives rise to unstable solutions. He

attributed instability to variations in pressure across the film thickness at higher order, since small local increases in film thickness give rise to a pressure gradient, which forces more liquid towards the disturbance so it grows. The situation is however complicated by convection effects.

O'Brien speculated that the instabilities on lower-quadrant shocks observed experimentally by others arise due to higher order effects in two dimensions, as well as three-dimensional effects.

This two-dimensional stability analysis cannot be expected to predict hygrocysts, (ring instabilities) since they require three-dimensional axial variation. The shock solutions are asymptotically stable to axial perturbations, even for zero surface tension, according to Acrivos and Jin, but homogeneous profiles are asymptotically unstable to axial disturbances, and inclusion of weak surface-tension effects then confirms that the homogeneous solutions are susceptible to an instability of long wavelength in the axial direction. The axial wavelength λ of the instability satisfies the power law $\lambda \sim \sigma^{1/3}$ where σ is surface tension[22].

So far this stability analysis on shock solutions is for rimming flow with no surface shear, but the same techniques can be applied to the case of $c_4 \neq 0$ [51, 52]. With $u_{cyl} = 0$ and the flow driven purely by shear, the result is qualitatively unchanged from the pure rotation case, with the $q < q_c$ profile and the profile with a shock in the fourth quadrant being linearly stable and all other profiles unstable. This is also the case when the rotation and shear are both positive.

But more interesting dynamics occur when the rotation and shear are opposing. There are two cases, one where the shear dominates and the flux q has the same sign as c_4, and one where the rotation dominates and the flux q has the same sign as u_{cyl}. The latter case especially has rich dynamics, and shocks can occur in many places between the three solutions of (1.3). As a general rule, a stable profile cannot exist if the kinematic wave direction along any part of it causes disturbances to be focussed at a critical point where multiple solutions meet [52].

In an independent, unpublished work provided by Wilson *et al.* [59], stability results for stationary cylinders found by Villegas-Díaz *et al.* [52] were confirmed using the techniques suggested by O'Brien, which Wilson suggested are simpler. However they also showed that these techniques must be used with care as O'Brien's analysis [38] is incomplete.

We will show, in Chapter 3 when the azimuthal droplet momentum term c_3 is included in (1.1), that the surface tension is critical for the stability of shock solutions. If the

surface tension term is small compared to c_3, then shock solutions are unstable.

In aero-engines, the axial length can be much less than the radius and so three-dimensional stability cannot be inferred from the previous studies since the class of allowable disturbances is quite different [52].

1.14 Recirculation within the film

When the mass exceeds the critical in rimming flow, and shocks occur, recirculation occurs near the surface of the film, as shown for example by Tirumkudulu and Acrivos [47] or Thoroddsen and Mahadevan [46]. But when the flow is driven by shear, the recirculation is located near to the wall, eg Wilson *et al.* [59]. This was shown analytically to occur for smoothing of shocks by either gravity or surface tension for the shear-driven case. In practical terms considering the cooling role of the oil, recirculation near the wall is more likely to cause problems.

We will show in Chapter 5 that although the c_5 terms arising from the azimuthal droplet mass is analogous to cylinder rotation u_{cyl} in the film-profile equation (1.1), because one term arises from the cylinder wall boundary condition and one from the interface, the underlying flows are different in nature.

Chapter 2

Derivation of an evolution equation for a thin film driven by surface mass and momentum transfer

In the first part of this chapter we will outline the model of a two-dimensional liquid film flowing around the inside of a smooth rigid circular cylinder, driven by droplets of the same liquid impacting on the free surface. The cylinder is taken to be stationary; rotation will be introduced in Chapters 4–6. The bulk flow of the film is taken as Newtonian, satisfying the Navier-Stokes equations, and laminar flow. We will model the interface in §2.3, where we will consider conservation of a general quantity across this interface, and use this to derive boundary conditions based on conservation of mass and momentum.

Since we are studying the thickness of the film a natural coordinate system is annular, with the azimuthal coordinate around the perimeter of the cylinder and a positive film thickness. However the initial derivation of an exact film model is clearer in cylindrical coordinates, so we will begin here and move to an annular system in §2.5.

In the second part of this chapter we will estimate appropriate physical parameters to determine scalings and obtain a simplified film model. In particular, we use the information that the film has small aspect ratio (of film thickness to azimuthal length scale) to greatly simplify the governing equations and boundary conditions. We then consider various parameter ranges for the droplets, and in each case derive a single governing equation for the film profile. There are two key cases: in the first the droplets impart momentum to the film, but the mass contribution is negligible; in the second there is both mass and momentum transfer .

2.1 Model formulation

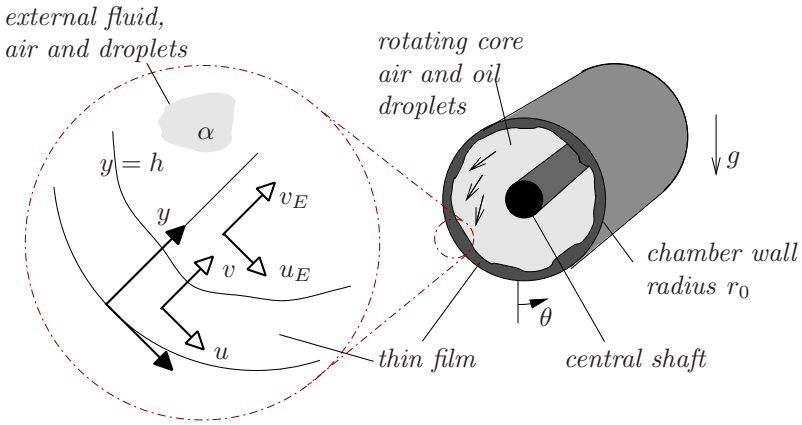

Figure 2.1: Non-dimensional geometry system for bearing chamber flow.

We model the aero-engine bearing chamber as a cylinder of radius r_0 with a thin film of liquid on its inner surface. It is assumed that there are no axial variations in the flow, reducing the problem to two dimensions. Liquid droplets are modelled upon impact with the film as a contribution to the surface forces and mass flux across the surface. The droplets are initially assumed to be of the same constant density ρ and viscosity μ as the liquid film, with a droplet volume fraction α. The velocity of the droplets is modelled as constant in time, and such that the angle between local droplet velocity and the cylinder wall is constant. We define two-dimensional cylindrical polar coordinates $\hat{r}, \theta$, with origin at the centre of the horizontal cylinder and θ measured anti-clockwise from the downward vertical.

2.2 The Navier-Stokes equations

The radial and azimuthal velocity of the fluid in the film, $\hat{u}_r, \hat{u}_\theta$ and pressure $\hat{p}$ satisfy the Navier-Stokes and continuity equations. Introducing $\hat{t}$ time and g acceleration due to gravity, these are [1]:

$$\frac{\partial \hat{u}_\theta}{\partial \hat{t}} + \frac{\hat{u}_\theta}{\hat{r}}\frac{\partial \hat{u}_\theta}{\partial \theta} + \hat{u}_r\frac{\partial \hat{u}_\theta}{\partial \hat{r}} + \frac{\hat{u}_\theta \hat{u}_r}{\hat{r}} = -\frac{1}{\rho\hat{r}}\frac{\partial \hat{p}}{\partial \theta} + \frac{\mu}{\rho}\left(\frac{1}{\hat{r}^2}\frac{\partial^2 \hat{u}_\theta}{\partial \theta^2} + \frac{2}{\hat{r}^2}\frac{\partial \hat{u}_r}{\partial \theta} + \frac{\partial^2 \hat{u}_\theta}{\partial \hat{r}^2} + \frac{1}{\hat{r}}\frac{\partial \hat{u}_\theta}{\partial \hat{r}} - \frac{\hat{u}_\theta}{\hat{r}^2}\right) - g\sin\theta, \tag{2.1}$$

$$\frac{\partial \hat{u}_r}{\partial \hat{t}} + \frac{\hat{u}_\theta}{\hat{r}}\frac{\partial \hat{u}_r}{\partial \theta} + \hat{u}_r\frac{\partial \hat{u}_r}{\partial \hat{r}} - \frac{\hat{u}_\theta^2}{\hat{r}} = -\frac{1}{\rho}\frac{\partial \hat{p}}{\partial \hat{r}} + \frac{\mu}{\rho}\left(\frac{1}{\hat{r}^2}\frac{\partial^2 \hat{u}_r}{\partial \theta^2} - \frac{2}{\hat{r}^2}\frac{\partial \hat{u}_\theta}{\partial \theta} + \frac{\partial^2 \hat{u}_r}{\partial \hat{r}^2} + \frac{1}{\hat{r}}\frac{\partial \hat{u}_r}{\partial \hat{r}} - \frac{\hat{u}_r}{\hat{r}^2}\right) + g\cos\theta, \tag{2.2}$$

and

$$\frac{1}{\hat{r}}\frac{\partial \hat{u}_\theta}{\partial \theta} + \frac{1}{\hat{r}}\frac{\partial}{\partial \hat{r}}\left(\hat{r}\hat{u}_r\right) = 0. \tag{2.3}$$

2.3 Boundary conditions at the film interface

There is a well-established method for deriving a free-surface boundary condition for a viscous liquid under a layer of pure gas [1, 4]. However to include the impact of droplets into the liquid from an external fluid consisting of a gas/liquid mixture a modified treatment is required, for the film does not have a 'surface' according to the conventional definition.

We will use the subscript $_E$ to refer to the two-phase gas-droplet mix *external* to the film and $_I$ for *internal*, the fluid in the film. Later, where there is no ambiguity, the internal subscript will be dropped. We will use the jump notation $[.]$, so for example $[\rho] = \rho_E - \rho_I$.

The external fluid (in the core of the cylinder) is a two-phase flow, of air with density ρ_g, and a volume fraction α of liquid droplets with density ρ_I. The average density of the mixture is therefore $\bar{\rho_E} = \alpha\rho_I + (1-\alpha)\rho_g$. We assume that $\rho_g \ll \alpha\rho_I$, so the external fluid is modelled as continuous and of constant density $\rho_E = \alpha\rho_I$. Note that this assumption may not apply to all physical parameter ranges, in particular if $\alpha < 10^{-4}$.

The boundary between these internal and external fluids is in reality a complex region, where droplets splash and rebound [15]. Here it is modelled as a single interface through which droplet exchange occurs, below which the fluid density is ρ_I, and above which it is ρ_E. In this study, we are not concerned with the detail of the two-phase core flow, so the behaviour far from the cylinder wall is not included in the model. We model droplets as having velocity $\mathbf{u_E}$, constant in time and at a constant angle relative to the

cylinder wall. Within the film the fluid has velocity $\mathbf{u_I}$, to be determined. We label the interface position as $\xi = 0$ velocity $\mathbf{U}$, with components U_j.

According to this model, mass and momentum may leave the film as well as enter, and this may happen in extreme cases of droplet parameters. Physically, we have not included a mechanism for fluid to leave the film, so this is a limitation of the model. However, in the majority of the droplet parameter range studied herein, fluid will only enter the film, and in all other cases where fluid leaves the film correspond to unphysical droplet parameters. More detail will be given in Chapters 4 and 5.

2.3.1 Conservation relations across a general interface

To identify general relationships valid at an interface, we initially use a general orthogonal coordinate system (x_1, x_2, x_3), and tensor notation. In §2.3.2 we will apply these general results to a cylindrical coordinate system, for the case of rimming flow.

a) Conservation of a general quantity over a discontinuity

We consider conservation of a general quantity P, such as mass or momentum, with a flux Q and source terms R (for example body forces in the conservation of momentum), across an interface between the two regions. Across the interface there may be discontinuity in velocity and density.

Consider a conservation relation in an arbitrary volume $V(t)$:

$$\int_{V(t)} \frac{\partial P}{\partial t} + \frac{\partial Q_j}{\partial x_j} + R \, \mathrm{d}V = 0.$$

Then if $\mathbf{u}$ is the velocity of the fluid, by the Reynolds' Transport Theorem

$$\frac{\mathrm{d}}{\mathrm{d}t} \int_{V(t)} P \, \mathrm{d}V - \int_{V(t)} \frac{\partial \left(P u_j\right)}{\partial x_j} \, \mathrm{d}V + \int_{V(t)} \frac{\partial Q_j}{\partial x_j} \, \mathrm{d}V + \int_{V(t)} R \, \mathrm{d}V = 0,$$

and by Gauss' (the Divergence) Theorem

$$\frac{\mathrm{d}}{\mathrm{d}t} \int_{V(t)} P \, \mathrm{d}V - \int_{\partial V(t)} (P u_j) n_j \, \mathrm{d}S + \int_{\partial V(t)} Q_j n_j \, \mathrm{d}S + \int_{V(t)} R \, \mathrm{d}V = 0.$$

In the above n_j is a component of the normal outwards from the volume. Now we apply this to a 'pillbox' volume as illustrated in figure 2.2, which has finite length along the interface, but with thickness δ across the interface, which approaches zero. The volume integrals satisfy

$$\lim_{\delta \to 0} \left(\frac{\mathrm{d}}{\mathrm{d}t} \int_{V(t)} P \, \mathrm{d}V, \quad \int_{V(t)} R \, \mathrm{d}V \right) = 0.$$

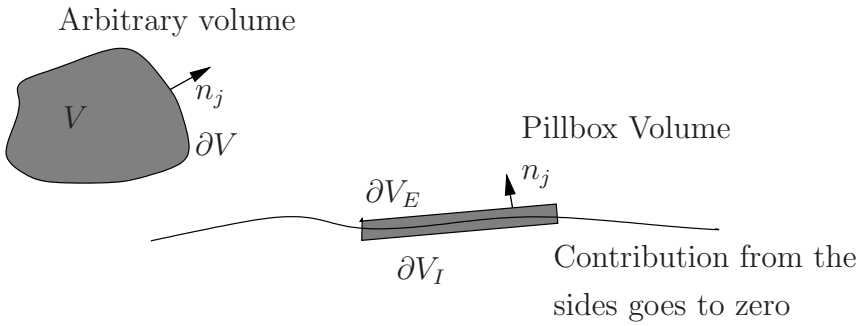

Figure 2.2: Illustration of arbitrary and pillbox volumes

The velocity of the fluid tends to **U**, the velocity of the interface, hence the surface integrals lead to

$$\lim_{\delta \to 0} \left(\int_{\partial V(t)} ((PU_j)n_j - Q_j n_j) \ \mathrm{d}S \right) = 0.$$

Also, as the pillbox shrinks towards zero thickness, the contribution from the sides tends to zero, so the surface integral is just the sum of the ∂V_E and ∂V_I surfaces. The normal to the pillbox on ∂V_E is opposite to the normal on ∂V_I. So defining the normal with component n_j to be outwards-facing on the ∂V_E surface,

$$\int_{\partial V(t)_E} ((PU_j)n_j - Q_j n_j) \ \mathrm{d}S - \int_{\partial V(t)_I} ((PU_j)n_j - Q_j n_j) \ \mathrm{d}S = 0. \tag{2.4}$$

This result is valid for any choice of pillbox volume element enclosing the interface and the length of interface enclosed is not specified. So

$$((PU_j)n_j - Q_j n_j)|_E - ((PU_j)n_j - Q_j n_j)|_I = 0,$$

or in the jump notation

$$[PU_j n_j - Q_j n_j] = 0.$$

The velocity of the interface, **U**, is common to the two surfaces so

$$[P]U_j n_j - [Q_j n_j] = 0. \tag{2.5}$$

b) Conservation of mass over a discontinuity

The general result can be applied to obtain a mass conservation relation across the interface. Conservation of mass gives, for an arbitrary volume of fluid of density ρ and velocity **u**:

$$\int_{V(t)} \left(\frac{\partial \rho}{\partial t} + \frac{\partial (\rho u_i)}{\partial x_j} \right) \ \mathrm{d}V = 0. \tag{2.6}$$

Taking

$$P = \rho, \quad Q_j = \rho u_j, \quad R = 0$$

in the conservation of a general quantity over a discontinuity, (2.5) implies

$$[\rho]U_j n_j = [\rho u_j n_j],$$

or

$$(\rho_E - \rho_I)U_j n_j = \rho_E u_{Ej} n_j - \rho_I u_{Ij} n_j.$$

Since $\rho_E = \alpha\rho_I$ then

$$(\alpha - 1)U_j n_j = \alpha u_{Ej} n_j - u_{Ij} n_j \tag{2.7}$$

In the special case when the external fluid contains no droplets, $\alpha \to 0$, then $\rho_E \to 0$ and we have $\mathbf{U} \cdot \mathbf{n} = \mathbf{u_I} \cdot \mathbf{n}$, the familiar boundary condition used when the external fluid is pure gas. In the case $\alpha = 1$, $\rho_I = \rho_E$, fluid of the same density is in both regions and $\mathbf{u_E} \cdot \mathbf{n} = \mathbf{u_I} \cdot \mathbf{n}$, the normal components of velocity are equal, since the interface is effectively a line within a single fluid. Since we are considering low droplet density, in what follows we assume $\alpha \neq 1$, to allow division by $1 - \alpha$.

c) Conservation of momentum over a discontinuity

The general result can also be applied to ensure a balance of momentum transfer across the interface. The conservation of momentum gives for an arbitrary element of fluid,

$$\int_{V(t)} \left(\rho \frac{\mathrm{D}u_i}{\mathrm{D}t} - \frac{\partial T_{ij}}{\partial x_j} - \rho g_i \right) \mathrm{d}V = 0, \tag{2.8}$$

where $T_{ij} = -p\delta_{ij} + 2\mu e_{ij}$ is the Newtonian stress tensor [4].

However when the element contains an interface between two different fluids, we need to include the surface tension forces. This can be introduced by using a Dirac δ function, such that surface forces in a volume enclosing a portion of the interface are localised along the interface. The surface tension acting on the portion of the interface $S(t)$ contained within a pillbox volume $V(t)$ can be written as

$$\int_{S(t)} s_i \, \mathrm{d}S = \int_{V(t)} s_i \delta_s \, \mathrm{d}V,$$

where s_i is ith component of the surface tension force acting on $S(t)$ and δ_s is the delta function on the interface. Adding the surface tension into (2.8), expanding the convective derivative, and simplifying using (2.6) leads to

$$\int_{V(t)} \left(\frac{\partial}{\partial t}(\rho u_i) + \frac{\partial}{\partial x_j}(u_i \rho u_j - T_{ij}) - \rho g_i + s_i \delta_s \right) \mathrm{d}V = 0.$$

Applying the method for conservation of a general quantity, with

$$P_i = \rho u_i, \quad Q_{ij} = u_i \rho u_j - T_{ij}, \quad R_i = -\rho g_i$$

as in deriving (2.4), gives

$$\left(\int_{\partial V(t)_E} - \int_{\partial V(t)_I}\right)\left((\rho u_i U_j)n_j - (u_i \rho u_j - T_{ij})\, n_j\right)\mathrm{d}S - \int_{V(t)} s_i \delta_s \, \mathrm{d}V = 0.$$

Again this applies to any pillbox volume across the interface, and noting the definition of δ_s, then

$$[(\rho u_i U_j)n_j - (u_i \rho u_j - T_{ij})\, n_j] = s_i.$$

The surface tension force is assumed to act normal to the interface is proportional to the curvature κ, so $s_i = -\sigma\kappa n_i$ where σ is the effective surface tension coefficient between the liquid and the mixture. Hence

$$[(\rho u_i U_j)n_j - (u_i \rho u_j - T_{ij})] = -\sigma\kappa n_i.$$

Using the mass interface condition (2.7) to further simplify this leads to the condition for momentum conservation across the interface

$$-\sigma\kappa n_i = \frac{\alpha\rho_I}{1-\alpha}[u_i][u_j]n_j - [T_{ij}n_j]. \tag{2.9}$$

In the right-hand-side of the force balance (2.9) the first term arises from conservation of momentum, and the second from pressure and viscous forces. Note that when $\alpha = 0$ this reduces to a standard free-surface condition, and in the limit $\alpha \to 1$, $\mathbf{u_I}\cdot\mathbf{n} = \mathbf{u_E}\cdot\mathbf{n}$, i.e. the normal components of velocity are equal across the interface. The effect of surface tension is reduced as α increases.

2.3.2 Interface conditions for rimming flow driven by droplet impact

In this section we apply the boundary conditions derived in §2.3.1 for droplet impact onto a general interface, to the case of flow on the inside of a circular cylinder. The cylinder wall is at $\hat{r} = \hat{r}_0$, and the film surface is at $\hat{r} = \hat{h}_r(\theta, \hat{t})$ where $\hat{h}_r < \hat{r}_0$.

The film surface can be conveniently expressed as $\xi = -\hat{r} + \hat{h}_r(\theta, \hat{t}) = 0$. Correspondingly, the unit normal pointing towards the centre of the cylinder is given by $\mathbf{n} = \frac{\nabla\xi}{|\nabla\xi|}$, with components (see Appendix B.1)

$$n_r = -\left(1 + \left(\frac{1}{\hat{r}}\frac{\partial\hat{h}_r}{\partial\theta}\right)^2\right)^{-1/2}, \quad n_\theta = \frac{1}{\hat{r}}\frac{\partial\hat{h}_r}{\partial\theta}\left(1 + \left(\frac{1}{\hat{r}}\frac{\partial\hat{h}_r}{\partial\theta}\right)^2\right)^{-1/2}.$$

The surface curvature is given by $\kappa = \nabla\cdot\mathbf{n}|_{\hat{r}=\hat{h}_r}$, i.e.

$$\kappa = \nabla\cdot\mathbf{n} = -\frac{1}{\hat{h}_r}\left(1 + \left(\frac{1}{\hat{h}_r}\frac{\partial\hat{h}_r}{\partial\theta}\right)^2\right)^{-3/2}\left(1 + \frac{2}{\hat{h}_r^2}\left(\frac{\partial\hat{h}_r}{\partial\theta}\right)^2 - \frac{1}{\hat{h}_r}\frac{\partial^2\hat{h}_r}{\partial\theta^2}\right).$$

We will use the notation

$$N \equiv \left(1 + \left(\frac{1}{\hat{r}}\frac{\partial \hat{h}_r}{\partial \theta}\right)^2\right)^{-1/2}.$$

a) Kinematic Condition

Since the velocity of the interface is U_j, the convective derivative of the interface position $\xi = 0$ is

$$\frac{\partial \xi}{\partial t} + U_j \frac{\partial \xi}{\partial x_j} = 0,$$

and gives the kinematic interface condition,

$$\frac{\partial h_r}{\partial \hat{t}} N + U_j n_j = 0.$$

Substituting in the interface mass condition (2.7) gives the mass/kinematic condition

$$(1-\alpha)\frac{\partial \hat{h}_r}{\partial \hat{t}} + \left(\hat{u}_{I\theta}\frac{1}{\hat{r}}\frac{\partial \hat{h}_r}{\partial \theta} - \hat{u}_{Ir}\right) = \alpha\left(\hat{u}_{E\theta}\frac{1}{\hat{r}}\frac{\partial \hat{h}_r}{\partial \theta} - \hat{u}_{Er}\right), \quad \text{on} \quad \hat{r} = \hat{h}_r. \tag{2.10}$$

Again the limits $\alpha \to 0$ and $\alpha \to 1$ yield the standard interface conditions.

b) Dynamic Conditions

From (2.9) the normal and tangential components of the stress boundary conditions on the interface are

$$-\sigma\kappa = \frac{\alpha\rho_I}{1-\alpha}[\hat{u}_i][\hat{u}_j]n_j n_i - [T_{ij}n_j]n_i, \tag{2.11}$$

$$0 = \frac{\alpha\rho_I}{1-\alpha}[\hat{u}_i][\hat{u}_j]n_j t_i - [T_{ij}n_j]t_i. \tag{2.12}$$

In polar coordinates and using the summation convention the components of $T_{ij}n_j$ become (see Appendix B.2)

$$\begin{aligned}
T_{\theta\theta}n_\theta &= -pn_\theta + 2\mu\left(\frac{1}{\hat{r}}\frac{\partial \hat{u}_\theta}{\partial \theta} + \frac{\hat{u}_r}{\hat{r}}\right)\left(\frac{1}{\hat{r}}\frac{\partial \hat{h}_r}{\partial \theta}\right)N,\\
T_{\theta r}n_r &= -\mu\left(\hat{r}\frac{\partial}{\partial \hat{r}}\left(\frac{\hat{u}_\theta}{\hat{r}}\right) + \frac{1}{\hat{r}}\frac{\partial \hat{u}_r}{\partial \theta}\right)N,\\
T_{r\theta}n_\theta &= \mu\left(\hat{r}\frac{\partial}{\partial \hat{r}}\left(\frac{\hat{u}_\theta}{\hat{r}}\right) + \frac{1}{\hat{r}}\frac{\partial \hat{u}_r}{\partial \theta}\right)\left(\frac{1}{\hat{r}}\frac{\partial \hat{h}_r}{\partial \theta}\right)N,\\
T_{rr}n_r &= -pn_r - 2\mu\frac{\partial \hat{u}_r}{\partial \hat{r}}N.
\end{aligned}$$

So

$$T_{\theta j}n_j n_\theta = -pn_\theta n_\theta + \mu\left(2\left(\frac{1}{\hat{r}}\frac{\partial \hat{u}_\theta}{\partial \theta} + \frac{\hat{u}_r}{\hat{r}}\right)\left(\frac{1}{\hat{r}}\frac{\partial \hat{h}_r}{\partial \theta}\right) - \left(\hat{r}\frac{\partial}{\partial \hat{r}}\left(\frac{\hat{u}_\theta}{\hat{r}}\right) + \frac{1}{\hat{r}}\frac{\partial \hat{u}_r}{\partial \theta}\right)\right)\left(\frac{1}{\hat{r}}\frac{\partial \hat{h}_r}{\partial \theta}\right)N^2,$$

and

$$T_{rj}n_jn_r = -pn_rn_r - \mu\left(\left(\hat{r}\frac{\partial}{\partial\hat{r}}\left(\frac{\hat{u}_\theta}{\hat{r}}\right) + \frac{1}{\hat{r}}\frac{\partial\hat{u}_r}{\partial\theta}\right)\left(\frac{1}{\hat{r}}\frac{\partial\hat{h}_r}{\partial\theta}\right) - 2\frac{\partial\hat{u}_r}{\partial\hat{r}}\right)N^2.$$

Hence

$$T_{ij}n_jn_i = -p+2\mu\left(\left(\frac{1}{\hat{r}}\frac{\partial\hat{h}_r}{\partial\theta}\right)^2\left(\frac{1}{\hat{r}}\frac{\partial\hat{u}_\theta}{\partial\theta} + \frac{\hat{u}_r}{\hat{r}}\right) - \left(\frac{1}{\hat{r}}\frac{\partial\hat{h}_r}{\partial\theta}\right)\left(\frac{\partial\hat{u}_\theta}{\partial\hat{r}} - \frac{\hat{u}_\theta}{\hat{r}} + \frac{1}{\hat{r}}\frac{\partial\hat{u}_r}{\partial\theta}\right) + \frac{\partial\hat{u}_r}{\partial\hat{r}}\right)N^2.$$

Similarly, the tangent vector in the same sense as θ has components

$$t_\theta = -n_r = N, \qquad t_r = n_\theta = \frac{1}{\hat{r}}\frac{\partial\hat{h}_r}{\partial\theta}N,$$

giving

$$\begin{aligned}T_{ij}n_jt_i = \mu\Bigg(&\left(\frac{1}{\hat{r}}\frac{\partial\hat{h}_r}{\partial\theta}\right)^2\left(\frac{\partial\hat{u}_\theta}{\partial\hat{r}} - \frac{\hat{u}_\theta}{\hat{r}} + \frac{1}{\hat{r}}\frac{\partial\hat{u}_r}{\partial\theta}\right)\\ &+2\left(\frac{1}{\hat{r}}\frac{\partial\hat{h}_r}{\partial\theta}\right)\left(\frac{1}{\hat{r}}\frac{\partial\hat{u}_\theta}{\partial\theta} + \frac{\hat{u}_r}{\hat{r}} - \frac{\partial\hat{u}_r}{\partial\hat{r}}\right) - \left(\frac{\partial\hat{u}_\theta}{\partial\hat{r}} - \frac{\hat{u}_\theta}{\hat{r}} + \frac{1}{\hat{r}}\frac{\partial\hat{u}_r}{\partial\theta}\right)\Bigg)N^2.\end{aligned}$$

Viscosity in the external two-phase flow is strongly dependent on the droplet fraction, in a non-linear fashion. There have been several approximations proposed, as summarised by Kleinstreuer [29]. If $\alpha \to 1$, the viscosity approaches that of the liquid, but with a substantial air fraction the gas phase lubricates the flow. For the purposes of this thesis, since the droplet fraction is low the external flow is taken as inviscid. So the normal and tangential boundary conditions (2.11, 2.12) on the interface, in cylindrical polar coordinates, are respectively

$$\begin{aligned}-\sigma\kappa =&\frac{\alpha\rho}{1-\alpha}\left(\hat{u}_{E\theta}\frac{1}{\hat{h}_r}\frac{\partial\hat{h}_r}{\partial\theta} - \hat{u}_{Er} - \hat{u}_{I\theta}\frac{1}{\hat{h}_r}\frac{\partial\hat{h}_r}{\partial\theta} + \hat{u}_{Ir}\right)^2 N^2 + p_E - p_I\\ &+2\mu\Bigg(\left(\frac{1}{\hat{h}_r}\frac{\partial\hat{h}_r}{\partial\theta}\right)^2\left(\frac{1}{\hat{h}_r}\frac{\partial\hat{u}_{I\theta}}{\partial\theta} + \frac{\hat{u}_{Ir}}{\hat{h}_r}\right)\\ &-\left(\frac{1}{\hat{h}_r}\frac{\partial\hat{h}_r}{\partial\theta}\right)\left(\frac{\partial\hat{u}_{I\theta}}{\partial\hat{r}} - \frac{\hat{u}_{I\theta}}{\hat{h}_r} + \frac{1}{\hat{h}_r}\frac{\partial\hat{u}_{Ir}}{\partial\theta}\right) + \frac{\partial\hat{u}_{Ir}}{\partial\hat{r}}\Bigg)N^2,\end{aligned} \tag{2.13}$$

and

$$\begin{aligned}0 =&\frac{\alpha\rho}{1-\alpha}\left(\hat{u}_{E\theta} + \hat{u}_{Er}\frac{1}{\hat{h}_r}\frac{\partial\hat{h}_r}{\partial\theta} - \hat{u}_{I\theta} - \hat{u}_{Ir}\frac{1}{\hat{h}_r}\frac{\partial\hat{h}_r}{\partial\theta}\right)\left(\hat{u}_{E\theta}\frac{1}{\hat{h}_r}\frac{\partial\hat{h}_r}{\partial\theta} - \hat{u}_{Er} - \hat{u}_{I\theta}\frac{1}{\hat{h}_r}\frac{\partial\hat{h}_r}{\partial\theta} + \hat{u}_{Ir}\right)\\ &+\mu\Bigg(\left(\frac{1}{\hat{h}_r}\frac{\partial\hat{h}_r}{\partial\theta}\right)^2\left(\frac{\partial\hat{u}_{I\theta}}{\partial\hat{r}} - \frac{\hat{u}_{I\theta}}{\hat{h}_r} + \frac{1}{\hat{h}_r}\frac{\partial\hat{u}_{Ir}}{\partial\theta}\right)\\ &+2\left(\frac{1}{\hat{h}_r}\frac{\partial\hat{h}_r}{\partial\theta}\right)\left(\frac{1}{\hat{h}_r}\frac{\partial\hat{u}_{I\theta}}{\partial\theta} + \frac{\hat{u}_{Ir}}{\hat{h}_r} - \frac{\partial\hat{u}_{Ir}}{\partial\hat{r}}\right) - \left(\frac{\partial\hat{u}_{I\theta}}{\partial\hat{r}} - \frac{\hat{u}_{I\theta}}{\hat{h}_r} + \frac{1}{\hat{h}_r}\frac{\partial\hat{u}_{Ir}}{\partial\theta}\right)\Bigg)N^2.\end{aligned} \tag{2.14}$$

2.4 Boundary conditions at the cylinder wall

It is assumed in this chapter that the cylinder is everywhere impermeable and stationary. Hence there is no flow through the cylinder wall,

$$\hat{u}_r = 0 \quad \text{on} \quad \hat{r} = r_0, \tag{2.15}$$

and there is no slip on the cylinder wall,

$$\hat{u}_\theta = 0 \quad \text{on} \quad \hat{r} = r_0. \tag{2.16}$$

2.5 Non-dimensionalisation of governing equations and boundary conditions

In order to take advantage of the thin aspect ratio of the film, the above formulation is re-expressed in suitable non-dimensional form based on parameters typical to a bearing chamber.

2.5.1 Conversion to annular coordinate system

For rimming flow it is convenient to work in an annular coordinate system, so that the film surface is at a small positive height $\hat{y} = \hat{h}$. The annular coordinate variables are the tangential coordinate θ and annular coordinate $\hat{y} = r_0 - \hat{r}$. The film surface height is $\hat{h} = r_0 - \hat{h_r}$; tangential velocity $\hat{u} = \hat{u}_\theta$ and annular velocity $\hat{v} = -\hat{u}_r$, as illustrated in figure 2.3.

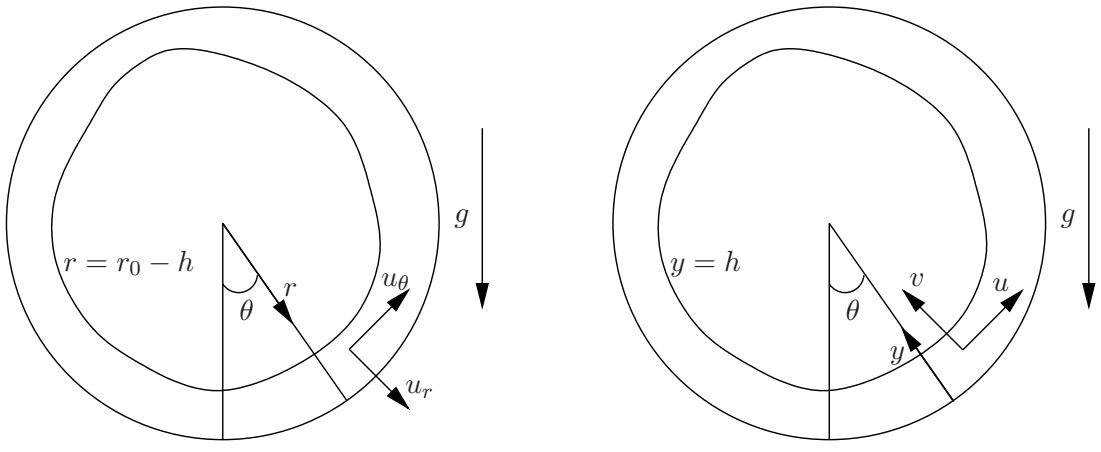

(i) Cylindrical (ii) Annular

Figure 2.3: Comparison of film variables in cylindrical and annular coordinates.

Transforming the Navier-Stokes and continuity equations (2.1-2.3) gives:

$$\frac{\partial \hat{u}}{\partial \hat{t}} + \frac{\hat{u}}{r_0 - \hat{y}}\frac{\partial \hat{u}}{\partial \theta} + \hat{v}\frac{\partial \hat{u}}{\partial \hat{y}} - \frac{\hat{u}\hat{v}}{r_0 - \hat{y}} = -\frac{1}{\rho(r_0 - \hat{y})}\frac{\partial \hat{p}}{\partial \theta} + \frac{\mu}{\rho}\left(\frac{1}{(r_0 - \hat{y})^2}\frac{\partial^2 \hat{u}}{\partial \theta^2} - \frac{2}{(r_0 - \hat{y})^2}\frac{\partial \hat{v}}{\partial \theta} + \frac{\partial^2 \hat{u}}{\partial \hat{y}^2} - \frac{1}{r_0 - \hat{y}}\frac{\partial \hat{u}}{\partial \hat{y}} - \frac{\hat{u}}{(r_0 - \hat{y})^2}\right) - g\sin\theta, \tag{2.17}$$

$$\frac{\partial \hat{v}}{\partial \hat{t}} + \frac{\hat{u}}{r_0 - \hat{y}}\frac{\partial \hat{v}}{\partial \theta} + \hat{v}\frac{\partial \hat{v}}{\partial \hat{y}} + \frac{\hat{u}^2}{r_0 - \hat{y}} = -\frac{1}{\rho}\frac{\partial \hat{p}}{\partial \hat{y}} + \frac{\mu}{\rho}\left(\frac{1}{(r_0 - \hat{y})^2}\frac{\partial^2 \hat{v}}{\partial \theta^2} + \frac{2}{(r_0 - \hat{y})^2}\frac{\partial \hat{u}}{\partial \theta} + \frac{\partial^2 \hat{v}}{\partial \hat{y}^2} - \frac{1}{r_0 - \hat{y}}\frac{\partial \hat{v}}{\partial \hat{y}} - \frac{\hat{v}}{(r_0 - \hat{y})^2}\right) - g\cos\theta, \tag{2.18}$$

and

$$\frac{1}{r_0 - \hat{y}}\frac{\partial \hat{u}}{\partial \theta} + \frac{1}{r_0 - \hat{y}}\frac{\partial}{\partial \hat{y}}\left((r_0 - \hat{y})\hat{v}\right) = 0. \tag{2.19}$$

Similarly, $\hat{u_E} = \hat{u}_{E\theta}$ and $\hat{v_E} = -\hat{u}_{Er}$. The internal subscript $_I$ is now dropped, and the interface boundary conditions (2.13-2.10) on $\hat{y} = \hat{h}$ are

$$\begin{aligned}
-\sigma\kappa =& \frac{\alpha\rho}{1-\alpha}\left(-\hat{u}_E\frac{1}{r_0 - \hat{y}}\frac{\partial \hat{h}}{\partial \theta} + \hat{v}_E + \hat{u}\frac{1}{r_0 - \hat{y}}\frac{\partial \hat{h}}{\partial \theta} - \hat{v}\right)^2 N^2 + \hat{p}_E - \hat{p} \\
&+ 2\mu\left(\left(\frac{1}{r_0 - \hat{y}}\frac{\partial \hat{h}}{\partial \theta}\right)^2\left(\frac{1}{r_0 - \hat{y}}\frac{\partial \hat{u}}{\partial \theta} - \frac{\hat{v}}{r_0 - \hat{y}}\right)\right. \\
&\left. - \left(\frac{1}{r_0 - \hat{y}}\frac{\partial \hat{h}}{\partial \theta}\right)\left(\frac{\partial \hat{u}}{\partial \hat{y}} + \frac{\hat{u}}{r_0 - \hat{y}} + \frac{1}{r_0 - \hat{y}}\frac{\partial \hat{v}}{\partial \theta}\right) + \frac{\partial \hat{v}}{\partial \hat{y}}\right) N^2,
\end{aligned} \tag{2.20}$$

$$\begin{aligned}
0 =& \frac{\alpha\rho}{1-\alpha}\left(\hat{u}_E + \hat{v}_E\frac{1}{r_0 - \hat{y}}\frac{\partial \hat{h}}{\partial \theta} - \hat{u} - \hat{v}\frac{1}{r_0 - \hat{y}}\frac{\partial \hat{h}}{\partial \theta}\right)\left(-\hat{u}_E\frac{1}{r_0 - \hat{y}}\frac{\partial \hat{h}}{\partial \theta} + \hat{v}_E + \hat{u}\frac{1}{r_0 - \hat{y}}\frac{\partial h}{\partial \theta} - \hat{v}\right) \\
&+ \mu\left(-\left(\frac{1}{r_0 - \hat{y}}\frac{\partial \hat{h}}{\partial \theta}\right)^2\left(\frac{\partial \hat{u}}{\partial \hat{y}} + \frac{\hat{u}}{r_0 - \hat{y}} + \frac{1}{r_0 - \hat{y}}\frac{\partial \hat{v}}{\partial \theta}\right)\right. \\
&+2\left(\frac{1}{r_0 - \hat{y}}\frac{\partial \hat{h}}{\partial \theta}\right)\left(-\frac{1}{r_0 - \hat{y}}\frac{\partial \hat{u}}{\partial \theta} + \frac{\hat{v}}{r_0 - \hat{y}} + \frac{\partial \hat{v}}{\partial \hat{y}}\right) \\
&\left. + \left(\frac{\partial \hat{u}}{\partial \hat{y}} + \frac{\hat{u}}{r_0 - \hat{y}} + \frac{1}{r_0 - \hat{y}}\frac{\partial \hat{v}}{\partial \theta}\right)\right) N^2,
\end{aligned} \tag{2.21}$$

and

$$(1-\alpha)\frac{\partial \hat{h}}{\partial \hat{t}} + \left(\hat{u}\frac{1}{r_0 - \hat{y}}\frac{\partial \hat{h}}{\partial \theta} - \hat{v}\right) = \alpha\left(\hat{u}_E\frac{1}{r_0 - \hat{y}}\frac{\partial \hat{h}}{\partial \theta} - \hat{v}_E\right). \tag{2.22}$$

In the above,

$$N = \left(1 + \left(\frac{1}{r_0 - \hat{y}}\frac{\partial \hat{h}}{\partial \theta}\right)^2\right)^{-1/2},$$

and the curvature

$$\kappa = -\frac{1}{r_0 - \hat{h}} \left(1 + \left(\frac{1}{r_0 - \hat{h}} \frac{\partial \hat{h}}{\partial \theta} \right)^2 \right)^{-3/2} \left(1 + \frac{2}{(r_0 - \hat{h})^2} \left(\frac{\partial \hat{h}}{\partial \theta} \right)^2 + \frac{1}{r_0 - \hat{h}} \frac{\partial^2 \hat{h}}{\partial \theta^2} \right).$$

The wall boundary conditions (2.15, 2.16) on $\hat{y} = 0$ are

$$\hat{v} = 0, \tag{2.23}$$

$$\hat{u} = 0. \tag{2.24}$$

2.5.2 Non-dimensional and scaled formulation for thin film flows

Physical estimates for typical bearing chamber conditions are given in Table 2.1, informed by published bearing chamber studies. These provide a guideline to which limits may be appropriate in an industrial application, although should only be taken to be order of magnitude estimates.

Property		Order of Magnitude	Source
Gravity	g	$10^1 \mathrm{m\,s^{-2}}$	
Density of oil	ρ	$10^3 \mathrm{kg\,m^{-3}}$	p126, Farrall [15]
Viscosity of oil	μ	$10^{-2} \mathrm{kg\,m^{-1}s^{-1}}$	Farrall [15]
Cylinder radius	r_0	$10^{-1} \mathrm{m}$	Farrall [15]
Film thickness	h_0	$10^{-3} \mathrm{m}$	Farrall [15]
Film rotation velocity	U	$10^{-1}$to$1 \mathrm{m\,s^{-1}}$	Maqableh [31]
Surface tension of oil	σ	$10^{-2} \mathrm{kg\,s^{-2}}$	Batchelor [4], Washburn [57]
Inner shaft totation		7000rpm	Farrall [15]
Core air velocity	U_E	$10^2 \mathrm{m\,s^{-1}}$	of same order as shaft rotation

Table 2.1: Estimates of physical parameters relevant to a typical bearing chamber flow.

Table 2.2 shows definitions of relevant dimensionless groups together with estimates of their size relative to the film aspect ratio, denoted by

$$\epsilon = \frac{h_0}{r_0}.$$

We use the lower bound of the range of U given by Maqableh. On the basis of this information the non-dimensional and scaled variables y, u and p are introduced, such that

$$\hat{y} = h_0 y, \quad \hat{u} = U u, \quad \hat{p} = \frac{\rho U^2}{\epsilon} p.$$

Aspect ratio	ϵ	$\frac{h_0}{r_0}$	10^{-2}	$O(\epsilon)$
Reynolds Number	$\mathrm{Re_f}$	$\frac{\rho U h_0}{\mu}$	10	$O(1)$
Inverse Weber Number	$\mathrm{We_f}$	$\frac{\sigma h_0^2}{U^2 \rho r_0^3}$	10^{-6}	$O(\epsilon^3)$
Froude Number	Fr	$\frac{U^2}{g h_0}$	1	$O(1)$

Table 2.2: Estimates of size of non-dimensional groups

In the following analysis, the film is taken to be thin relative to the radius of the cylinder, i.e. the aspect ratio is small, $0 < \epsilon \ll 1$. For consistency in the continuity equation, this leads to the scaling for non-dimensional v

$$\hat{v} = \epsilon U v.$$

Furthermore it is assumed that $\mathrm{Re_f} = O(1)$, and $\mathrm{Fr}^{-1} = O(1)$ as $\epsilon \to 0$. The timescale for movement of the film is that of a particle of fluid moving around the cylinder, and hence a non-dimensional time is given by $\hat{t} = \frac{r_0}{U} t$.

The governing equations (2.17-2.19) in scaled dimensionless variables become

$$\epsilon \frac{\partial u}{\partial t}(1-\epsilon y)^2 + \epsilon(1-\epsilon y)u\frac{\partial u}{\partial \theta} + \epsilon v(1-\epsilon y)^2\frac{\partial u}{\partial y} - \epsilon^2(1-\epsilon y)uv = -(1-\epsilon y)\frac{\partial p}{\partial \theta} + \frac{1}{\mathrm{Re_f}}\left(\epsilon^2\frac{\partial^2 u}{\partial \theta^2} - 2\epsilon^3\frac{\partial v}{\partial \theta} + (1-\epsilon y)^2\frac{\partial^2 u}{\partial y^2} - \epsilon(1-\epsilon y)\frac{\partial u}{\partial y} - \epsilon^2 u\right) - (1-\epsilon y)^2\frac{1}{\mathrm{Fr}}\sin\theta \tag{2.25}$$

$$\epsilon^3(1-\epsilon y)^2\frac{\partial v}{\partial t} + \epsilon^3(1-\epsilon y)u\frac{\partial v}{\partial \theta} + \epsilon^3(1-\epsilon y)^2 v\frac{\partial v}{\partial y} + \epsilon^2(1-\epsilon y)u^2 = -(1-\epsilon y)^2\frac{\partial p}{\partial y} + \frac{\epsilon^2}{\mathrm{Re_f}}\left(\epsilon^2\frac{\partial^2 v}{\partial \theta^2} + 2\epsilon\frac{\partial u}{\partial \theta} + (1-\epsilon y)^2\frac{\partial^2 v}{\partial y^2} - \epsilon(1-\epsilon y)\frac{\partial v}{\partial y} - \epsilon^2 v\right) - \frac{\epsilon}{\mathrm{Fr}}\cos\theta(1-\epsilon y)^2, \tag{2.26}$$

and

$$\frac{\partial u}{\partial \theta} - \epsilon v + \frac{\partial v}{\partial y} - \epsilon y\frac{\partial v}{\partial y} = 0. \tag{2.27}$$

2.5.3 Scalings for the interface conditions

Along with the governing equations, scaled and non-dimensional formulations of the boundary conditions are required. The wall boundary conditions on $y = h$, (2.23,2.24) become simply:

$$v = 0, \tag{2.28}$$

$$u = 0. \tag{2.29}$$

For the interface conditions, the droplet density is scaled

$$\alpha = \epsilon^k a,$$

where $a = O(1)$ as $\epsilon \to 0$, and the velocity components are scaled such that

$$\hat{u}_E = U_E u_E, \quad \hat{v}_E = V_E v_E.$$

In the following, droplet scalings k, U_E and V_E are left as general as possible, but we do make the assumption that the primary mechanism for driving the surface is through droplet impact. This implies that the azimuthal droplet momentum balances viscous shear at the surface. Taking azimuthal momentum $\sim \hat{v}_E(\alpha\hat{\rho}\hat{u}_E)$, shear $\sim \mu d\hat{u}/d\hat{y}$, and $\mathrm{Re_f} \sim 1$, the balance requires that

$$\frac{\epsilon^k U_E V_E}{U^2} = 1. \tag{2.30}$$

A reduced inverse Weber number is given by $\mathrm{We_f} = \frac{\sigma h_0^2}{U^2 \rho r_0^3}$, and is also left unfixed as yet. For later convenience, and without loss of generality, the external pressure is given by $\hat{p}_E = \frac{\rho U}{\epsilon}\left(p_E - \frac{\mathrm{We_f}}{\epsilon}\right)$.

Non-dimensional boundary conditions derived from (2.20-2.22) are as follows:

Normal stress on $y = h$:

$$\begin{aligned}
&\frac{\mathrm{We_f}}{\epsilon^2}\frac{1}{1-\epsilon h}\left(1+\left(\frac{\epsilon}{1-\epsilon h}\frac{\partial h}{\partial\theta}\right)^2\right)^{-3/2}\left(1+\frac{2\epsilon^2}{(1-\epsilon h)^2}\left(\frac{\partial h}{\partial\theta}\right)^2+\frac{\epsilon}{(1-\epsilon h)}\frac{\partial^2 h}{\partial\theta^2}\right)\\
&\quad=\frac{\epsilon^k a}{1-\epsilon^k a}\left(-\frac{\epsilon}{1-\epsilon h}\frac{U_E}{U}u_E\frac{\partial h}{\partial\theta}+\frac{V_E}{U}v_E+\frac{\epsilon}{1-\epsilon h}u\frac{\partial h}{\partial\theta}-\epsilon v\right)^2 N^2+\frac{1}{\epsilon}\left(p_E-\frac{\mathrm{We_f}}{\epsilon}\right)-\frac{1}{\epsilon}p\\
&+\frac{2\epsilon}{\mathrm{Re_f}}\left(\left(\frac{\epsilon}{1-\epsilon h}\frac{\partial h}{\partial\theta}\right)^2\left(\frac{1}{1-\epsilon h}\frac{\partial u}{\partial\theta}-\frac{\epsilon v}{1-\epsilon h}\right)\right.\\
&\quad\left.-\left(\frac{\epsilon}{1-\epsilon h}\frac{\partial h}{\partial\theta}\right)\left(\frac{1}{\epsilon}\frac{\partial u}{\partial y}+\frac{u}{1-\epsilon h}+\frac{\epsilon}{1-\epsilon h}\frac{\partial v}{\partial\theta}\right)+\frac{\partial v}{\partial y}\right)N^2.
\end{aligned} \tag{2.31}$$

Tangential stress on $y = h$:

$$\begin{aligned}
0=&\frac{\epsilon^k a}{1-\epsilon^k a}\left(\frac{U_E}{U}u_E+\frac{\epsilon}{1-\epsilon h}\frac{V_E}{U}v_E\frac{\partial h}{\partial\theta}-u-\frac{\epsilon^2}{1-\epsilon h}v\frac{\partial h}{\partial\theta}\right)\\
&\times\left(-\frac{U_E}{U}u_E\frac{\epsilon}{1-\epsilon h}\frac{\partial h}{\partial\theta}+\frac{V_E}{U}v_E+u\frac{\epsilon}{1-\epsilon h}\frac{\partial h}{\partial\theta}-\epsilon v)\right)\\
&+\frac{1}{\mathrm{Re_f}}\left(-\left(\frac{\epsilon}{1-\epsilon h}\frac{\partial h}{\partial\theta}\right)^2\left(\frac{\partial u}{\partial y}+\frac{\epsilon u}{1-\epsilon h}+\frac{\epsilon^2}{1-\epsilon h}\frac{\partial v}{\partial\theta}\right)\right.\\
&+2\left(\frac{\epsilon}{1-\epsilon h}\frac{\partial h}{\partial\theta}\right)\left(-\frac{\epsilon}{1-\epsilon h}\frac{\partial u}{\partial\theta}+\frac{\epsilon^2 v}{1-\epsilon h}+\epsilon\frac{\partial v}{\partial y}\right)\\
&\left.+\left(\frac{\partial u}{\partial y}+\frac{\epsilon u}{1-\epsilon h}+\frac{\epsilon^2}{1-\epsilon h}\frac{\partial v}{\partial\theta}\right)\right)N^2.
\end{aligned} \tag{2.32}$$

The mass/kinematic condition on $y = h$:

$$\left(1 - \epsilon^k a\right) \frac{\partial h}{\partial t} + \left(u \frac{1}{1 - \epsilon h} \frac{\partial h}{\partial \theta} - v\right) = \epsilon^k a \left(\frac{U_E}{U} u_E \frac{1}{1 - \epsilon h} \frac{\partial h}{\partial \theta} - \frac{V_E}{\epsilon U} v_E\right), \tag{2.33}$$

where

$$N = \left(1 + \left(\frac{\epsilon}{1 - \epsilon h} \frac{\partial h}{\partial \theta}\right)^2\right)^{-1/2}.$$

2.5.4 Isolation of droplet properties in interface boundary conditions

We are going to consider several problems with various droplet conditions. For convenience, we rewrite the boundary conditions (2.31-2.33) so that terms dependent on the droplet parameters k, U_E, V_E and $\mathrm{We_f}$ are in a single parameter for each equation, N_l, T and M respectively. For consistency, we assume that N_l, T and M are $O(1)$ as $\epsilon \to 0$. This will impose restrictions on the combinations of k, U_E and V_E. The conditions to be satisfied on $y = h$ become:

$$\begin{aligned}(1 - \epsilon h)^3 (p - p_E) - \frac{2\epsilon^2}{\mathrm{Re_f}} \Bigg(& \epsilon^2 \left(\frac{\partial h}{\partial \theta}\right)^2 \left(\frac{\partial u}{\partial \theta} - \epsilon v\right) \\ & - (1 - \epsilon h) \left(\frac{\partial h}{\partial \theta}\right) \left((1 - \epsilon h) \frac{\partial u}{\partial y} + \epsilon u + \epsilon^2 \frac{\partial v}{\partial \theta}\right) + (1 - \epsilon h)^3 \frac{\partial v}{\partial y} \Bigg) N^2 \\ & = N_l(\theta, t), \end{aligned} \tag{2.34}$$

$$\begin{aligned} \Bigg(& -\epsilon^2 \left(\frac{\partial h}{\partial \theta}\right)^2 \left((1 - \epsilon h) \frac{\partial u}{\partial y} + \epsilon u + \epsilon^2 \frac{\partial v}{\partial \theta}\right) \\ & + 2\epsilon^2 (1 - \epsilon h) \left(\frac{\partial h}{\partial \theta}\right) \left(-\frac{\partial u}{\partial \theta} + \epsilon v + (1 - \epsilon h) \frac{\partial v}{\partial y}\right) \\ & + \left((1 - \epsilon h)^3 \frac{\partial u}{\partial y} + \epsilon u (1 - \epsilon h)^2 + \epsilon^2 (1 - \epsilon h)^2 \frac{\partial v}{\partial \theta}\right) \Bigg) N^2 = T(\theta, t), \end{aligned} \tag{2.35}$$

and

$$(1 - \epsilon h) \frac{\partial h}{\partial t} + \left(u \frac{\partial h}{\partial \theta} - (1 - \epsilon h) v\right) = M(\theta, t), \tag{2.36}$$

where

$$N_l = -\frac{\mathrm{We_f}}{\epsilon}\left(1+\left(\frac{\epsilon}{1-\epsilon h}\frac{\partial h}{\partial\theta}\right)^2\right)^{-3/2}\left((1-\epsilon h)^2+2\epsilon^2\left(\frac{\partial h}{\partial\theta}\right)^2+\epsilon(1-\epsilon h)\frac{\partial^2 h}{\partial\theta^2}\right) + (1-\epsilon h)^3\frac{\mathrm{We_f}}{\epsilon} + \epsilon\frac{\epsilon^k a}{1-\epsilon^k a}(1-\epsilon h)\left(-\epsilon\frac{U_E}{U}u_E\frac{\partial h}{\partial\theta}+(1-\epsilon h)\frac{V_E}{U}v_E+\epsilon u\frac{\partial h}{\partial\theta}-\epsilon(1-\epsilon h)v\right)^2 N^2 \tag{2.37}$$

$$T = -\mathrm{Re_f}\frac{\epsilon^k a}{1-\epsilon^k a}(1-\epsilon h)\left((1-\epsilon h)\frac{U_E}{U}u_E+\epsilon\frac{V_E}{U}v_E\frac{\partial h}{\partial\theta}-(1-\epsilon h)u-\epsilon^2 v\frac{\partial h}{\partial\theta}\right) \times\left(-\frac{U_E}{U}u_E\epsilon\frac{\partial h}{\partial\theta}+(1-\epsilon h)\frac{V_E}{U}v_E+u\epsilon\frac{\partial h}{\partial\theta}-\epsilon(1-\epsilon h)v\right), \tag{2.38}$$

and

$$M = \epsilon^k a(1-\epsilon h)\frac{\partial h}{\partial t}+\epsilon^k a\left(\frac{U_E}{U}u_E\frac{\partial h}{\partial\theta}-\frac{V_E}{U}(1-\epsilon h)\frac{v_E}{\epsilon}\right). \tag{2.39}$$

2.6 Thin-film approximation

A full analytical solution for the film height $h(\theta,t)$, fluid velocities $u(y,\theta,t)$, $v(y,\theta,t)$ and pressure $p(y,\theta,t)$, is considered intractable. We seek an asymptotic approximation based on the film aspect-ratio parameter $\epsilon \ll 1$, and assume

$$u = u_0 + \epsilon u_1 + O(\epsilon^2), \tag{2.40}$$

$$v = v_0 + \epsilon v_1 + O(\epsilon^2), \tag{2.41}$$

$$p = p_0 + \epsilon p_1 + O(\epsilon^2), \tag{2.42}$$

$$h = h_0 + \epsilon h_1 + O(\epsilon^2). \tag{2.43}$$

In outline, we seek a solution for u, using equations (2.25, 2.26), the interface boundary conditions (2.34, 2.35) and the wall boundary conditions (2.28, 2.29). Then by substituting into the continuity equation (2.27) and using the kinematic condition (2.36) we will get an evolution equation for the film height h.

2.6.1 Governing equations

Substituting the expansion (2.40-2.42) into (2.25-2.27) leads to a regular expansion of terms involving powers of ϵ. Equating terms gives:

Leading order, $O(1)$

$$\frac{1}{\mathrm{Re_f}}\left(\frac{\partial^2 u_0}{\partial y^2}\right) - \frac{\partial p_0}{\partial \theta} = \frac{1}{\mathrm{Fr}}\sin\theta, \tag{2.44}$$

$$\frac{\partial p_0}{\partial y} = 0, \tag{2.45}$$

$$\frac{\partial u_0}{\partial \theta} + \frac{\partial v_0}{\partial y} = 0. \tag{2.46}$$

First order, $O(\epsilon)$

$$\frac{1}{\mathrm{Re_f}}\frac{\partial^2 u_1}{\partial y^2} - \frac{\partial p_1}{\partial \theta} = \frac{\partial u_0}{\partial t} + u_0\frac{\partial u_0}{\partial \theta} + v_0\frac{\partial u_0}{\partial y} - y\frac{\partial p_0}{\partial \theta} + \frac{1}{\mathrm{Re_f}}\left(2y\frac{\partial^2 u_0}{\partial y^2} + \frac{\partial u_0}{\partial y}\right) - 2y\frac{1}{\mathrm{Fr}}\sin\theta, \tag{2.47}$$

$$\frac{\partial p_1}{\partial y} = 2y\frac{\partial p_0}{\partial y} - \frac{1}{\mathrm{Fr}}\cos\theta, \tag{2.48}$$

$$\frac{\partial u_1}{\partial \theta} + \frac{\partial v_1}{\partial y} = v_0 + y\frac{\partial v_0}{\partial y}. \tag{2.49}$$

Observe here that the pressure is constant in y at leading order (2.45) and hydrostatic pressure only appears at $O(\epsilon)$ (2.48). This is consistent with the model of Villegas-Díaz[51], who then retained the $O(\epsilon)$ term in order to examine the secondary effects of gravity, in particular in smoothing shock solutions. However he found it not to be as significant as surface tension, and it is not retained in this thesis as we will focus instead on the droplet effects.

2.6.2 Boundary Conditions

The boundary conditions are given on $y = h_0 + \epsilon h_1 + O(\epsilon^2)$. To apply them on $y = h_0$ we apply Taylor expansions,[1] for example

$$\begin{aligned} u(\theta, y)|_{y=h} &= u(\theta, y)|_{y=h_0} + \epsilon h_1 \left.\frac{\partial u}{\partial y}(\theta, y)\right|_{y=h_0} + O(\epsilon^2), \\ &= u_0(\theta, h_0) + \epsilon u_1(\theta, h_0) + \epsilon h_1 \frac{\partial u_0}{\partial y}(\theta, h_0) + O(\epsilon^2), \end{aligned}$$

and equate like terms in ϵ.

A regular expansion of droplet property terms is denoted by

$$\begin{aligned} N_l(\theta, t) &= N_{l0} + \epsilon N_{l1} + O(\epsilon^2), \\ T(\theta, t) &= T_0 + \epsilon T_1 + O(\epsilon^2), \\ M(\theta, t) &= M_0 + \epsilon M_1 + O(\epsilon^2), \end{aligned}$$

[1] This method captures $O(\epsilon)$ cross-terms that would be omitted by application of the boundary conditions to $y = h$ and only afterwards taking like terms in ϵ.

where N_{l0} *etc.* are dependent on droplet scalings yet to be selected.

Substituting the expansions (2.40-2.42) into the boundary conditions (2.34-2.36) leads to the following.

Leading order, $O(1)$ On $y = h_0$

$$p_0 - p_E = N_{l0}, \tag{2.50}$$

$$\frac{\partial u_0}{\partial y} = T_0, \tag{2.51}$$

$$\frac{\partial h_0}{\partial t} + \left(u_0 \frac{\partial h_0}{\partial \theta} - v_0 \right) = M_0. \tag{2.52}$$

On $y = 0$

$$u_0 = 0, \tag{2.53}$$

$$v_0 = 0. \tag{2.54}$$

First order, $O(\epsilon)$ On $y = h_0$

$$p_1 + h_1 \frac{\partial p_0}{\partial y} - 3h_0 N_{l0} = N_{l1}, \tag{2.55}$$

$$\frac{\partial u_1}{\partial y} + h_1 \frac{\partial^2 u_0}{\partial y^2} - 3h_0 T_0 + u_0 = T_1, \tag{2.56}$$

$$\frac{\partial h_1}{\partial t} + u_0 \frac{\partial h_1}{\partial \theta} - h_1 \frac{\partial v_0}{\partial y} + h_1 T_0 \frac{\partial h_0}{\partial \theta} + u_1 \frac{\partial h_0}{\partial \theta} - v_1 - h_0 \frac{\partial h_0}{\partial t} + h_0 v_0 = M_1. \tag{2.57}$$

On $y = 0$:

$$u_1 = 0, \tag{2.58}$$

$$v_1 = 0, \tag{2.59}$$

The expressions on the right-hand side of (2.50–2.52) will be given for specific droplet cases in §2.8, and those in the $O(\epsilon)$ conditions (2.55–2.57) will be given in Appendix C.

2.7 Film-height equation to $O(1)$

To leading order, an equation for the film thickness can be derived from the leading-order governing equations (2.44-2.46) with boundary conditions (2.50-2.52). Integrating (2.45) with the normal boundary condition (2.50) on $y = h$ gives

$$p_0 = p_E + N_{l0}(\theta, t). \tag{2.60}$$

Differentiating with respect to θ and substituting into the first governing equation (2.44),

$$\frac{\partial^2 u_0}{\partial y^2} = \mathrm{Re_f}\left(\frac{\partial N_{l0}}{\partial \theta} + \frac{1}{\mathrm{Fr}}\sin\theta\right).$$

It is convenient to write

$$F_0(\theta, t) = \mathrm{Re_f}\left(\frac{\partial N_{l0}}{\partial \theta} + \frac{1}{\mathrm{Fr}}\sin\theta\right). \tag{2.61}$$

Then integrating twice, applying the tangential boundary condition on $y = h_0$ (2.51) and the no-slip boundary condition on $y = 0$ (2.53), gives

$$u_0 = F_0\left(\frac{y^2}{2} - h_0 y\right) + T_0 y. \tag{2.62}$$

Differentiating (2.62) with respect to θ, substituting into the continuity equation (2.46), integrating and using the no-flow boundary condition on $y = 0$ (2.54) gives

$$v_0 = -\left(\frac{\partial F_0}{\partial \theta}\frac{y^3}{6} + \frac{\partial}{\partial \theta}\left(-F_0 h_0 + T_0\right)\frac{y^2}{2}\right). \tag{2.63}$$

Evaluating u_0 and v_0 at $y = h_0$, the kinematic condition (2.52) gives:

$$\frac{\partial h_0}{\partial t} - \frac{\partial}{\partial \theta}\left(F_0\frac{h_0^3}{3}\right) + \frac{\partial}{\partial \theta}\left(T_0\frac{h_0^2}{2}\right) = M_0.$$

Hence the evolution equation for the film to $O(1)$ is

$$\frac{\partial h_0}{\partial t} - \frac{\partial}{\partial \theta}\left(\mathrm{Re_f}\left(\frac{\partial N_{l0}}{\partial \theta} + \frac{1}{\mathrm{Fr}}\sin\theta\right)\frac{h_0^3}{3}\right) + \frac{\partial}{\partial \theta}\left(T_0\frac{h^2}{2}\right) - M_0 = 0, \tag{2.64}$$

where N_{l0}, T_0 and M_0, the leading order terms of (2.37-2.39) are dependent on droplet parameters, examples of which are given in the following section. The film height is also derived to $O(\epsilon)$ and displayed in Appendix C.

2.8 Distinguished limits - the effect of droplet impact

Within this study, the film is driven by droplet impact, which is characterised by the droplet mass and momentum. In the following we consider several distinct possible cases, consistent with a thin film approximation and hence find appropriate expressions for N_{l0}, T_0 and M_0 to substitute into (2.64).

Droplets approach the film with dimensional velocity $(\hat{u}_E, \hat{v}_E)$, at some prescribed angle ϕ from the azimuthal direction, so $\tan\phi = \hat{v}_E/\hat{u}_E$. The scalings for the droplet velocity components are taken as U_E and $V_E = \epsilon^\beta U_E$, giving droplet velocity $(U_E u_E, \epsilon^\beta U_E v_E)$, where u_E, v_E are non-dimensional velocities, and $\tan\phi = \epsilon^\beta v_E/u_E$. Physically, as illustrated in figure 2.4, $\beta = 1$ corresponds to $\tan\phi = O(\epsilon)$, droplet impact at a very shallow

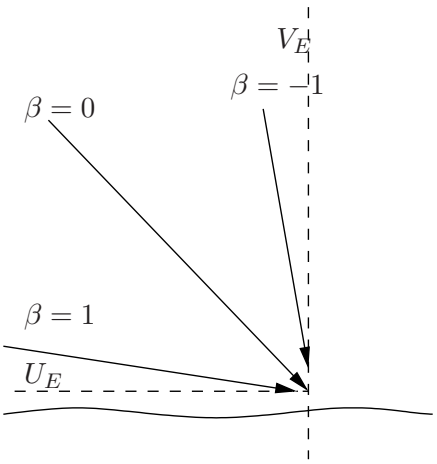

Figure 2.4: Droplet impact angle is characterised by β

angle, and $\beta = -1$ corresponds to $\tan\phi = O(\epsilon^{-1})$, droplet impact at a very steep angle. $\beta > 1$ is unphysical, since it could represent droplets from within the film.

Droplet density is given by $\alpha = \epsilon^k a$. By the restriction (2.30),

$$U_E/U = \epsilon^{-(k+\beta)/2} \quad \text{and} \quad V_E/U = \epsilon^{-(k-\beta)/2}.$$

In this section we will consider in turn the three cases of droplet volume fraction[2], $k = 3, 2, 1$. Given k, and substituting into (2.37-2.39), we will find the range of β is consistent with $N_l, T, M = O(1)$. Then for consistent parameter ranges we will state the $O(1)$ terms of the droplet parameter terms (2.37-2.39), and then the leading-order film evolution equation (2.64). For completeness, $O(\epsilon)$ terms are given in Appendix C.

In all cases, $\mathrm{We_f}$ is assumed to be $O(1)$.

2.8.1 Very low droplet volume fraction

If $k = 3$, the droplet volume fraction is given by

$$\alpha = \epsilon^3 a,$$

and the velocity scalings are $U_E/U = \epsilon^{-(3+\beta)/2}$ and $V_E/U = \epsilon^{-(3-\beta)/2}$. Consistent scaling such that $M = O(1)$ requires $\beta \geq -1$.

[2]Note that droplet fraction increases with decreasing k, and $k = 0$ is not a valid limit under assumptions already made. If $k = 0$, then $\alpha = a$, $U_E/U = \epsilon^{-\beta/2}$ and $V_E/U = \epsilon^{\beta/2}$. Then $\beta \geq 2$ is required for $M = O(1)$, but $\beta > 1$ is unphysical. Too great a fraction of droplets breaches either the shear assumption or the assumption that the timescale can be based on azimuthal film flow.

With these scalings, (2.37-2.39) become

$$
\begin{aligned}
N_l = &-\frac{\mathrm{We_f}}{\epsilon}\left(1+\left(\frac{\epsilon}{1-\epsilon h}\frac{\partial h}{\partial\theta}\right)^2\right)^{-3/2}\left((1-\epsilon h)^2+2\epsilon^2\left(\frac{\partial h}{\partial\theta}\right)^2+\epsilon(1-\epsilon h)\frac{\partial^2 h}{\partial\theta^2}\right)\\
&+(1-\epsilon h)^3\frac{\mathrm{We_f}}{\epsilon}\\
&+a\frac{1}{1-\epsilon^3 a}(1-\epsilon h)\left(-\epsilon^{(3-\beta)/2}u_E\frac{\partial h}{\partial\theta}+(1-\epsilon h)\epsilon^{(1+\beta)/2}v_E+\epsilon^3 u\frac{\partial h}{\partial\theta}-\epsilon^3(1-\epsilon h)v\right)^2 N^2,\\
T = &-\mathrm{Re_f}a\frac{1}{1-\epsilon^3 a}(1-\epsilon h)\left((1-\epsilon h)\epsilon^{(1-\beta)/2}u_E+\epsilon^{(3+\beta)/2}v_E\frac{\partial h}{\partial\theta}-(1-\epsilon h)\epsilon^2 u-\epsilon^4 v\frac{\partial h}{\partial\theta}\right)\\
&\times\left(-\epsilon^{(1-\beta)/2}u_E\frac{\partial h}{\partial\theta}+(1-\epsilon h)\epsilon^{(-1+\beta)/2}v_E+u\epsilon^2\frac{\partial h}{\partial\theta}-\epsilon^2(1-\epsilon h)v)\right),\\
M = &\,\epsilon^3 a(1-\epsilon h)\frac{\partial h}{\partial t}+\epsilon a\left(\epsilon^{(1-\beta)/2}u_E\frac{\partial h}{\partial\theta}-\epsilon^{(-1+\beta)/2}(1-\epsilon h)v_E\right).
\end{aligned}
$$

The dominant terms are

$$
\begin{aligned}
N_{l0} &= -\mathrm{We_f}\left(h_0+\frac{\partial^2 h_0}{\partial\theta^2}\right)+a\epsilon^{1+\beta}v_E^2,\\
T_0 &= -\mathrm{Re_f}a\left(-\epsilon^{1-\beta}u_E u_E\frac{\partial h_0}{\partial\theta}+u_E v_E+\epsilon^{1+\beta}v_E\frac{\partial h_0}{\partial\theta}v_E\right),\\
M_0 &= a\left(-\epsilon^{(1+\beta)/2}v_E\right).
\end{aligned}
$$

Substituting into (2.64) gives

$$
\begin{aligned}
\frac{\partial h_0}{\partial t}+\mathrm{Re_f}\frac{\partial}{\partial\theta}\Bigg(&\mathrm{We_f}\left(\frac{\partial h_0}{\partial\theta}+\frac{\partial^3 h_0}{\partial\theta^3}\right)\frac{h_0^3}{3}-\frac{\sin\theta}{\mathrm{Fr}}\frac{h_0^3}{3}\\
&+a\left(\epsilon^{1-\beta}u_E u_E\frac{\partial h_0}{\partial\theta}-u_E v_E-\epsilon^{1+\beta}v_E\frac{\partial h_0}{\partial\theta}v_E\right)\frac{h_0^2}{2}\Bigg)+a\left(\epsilon^{(1+\beta)/2}v_E\right)=0.
\end{aligned}
$$

Thus $\beta=-1$, a steep angle of droplet approach, leads to a film profile equation:

$$
\frac{\partial h_0}{\partial t}+\mathrm{Re_f}\frac{\partial}{\partial\theta}\left(\mathrm{We_f}\left(\frac{\partial h_0}{\partial\theta}+\frac{\partial^3 h_0}{\partial\theta^3}\right)\frac{h_0^3}{3}-\frac{\sin\theta}{\mathrm{Fr}}\frac{h_0^3}{3}-a\left(u_E+v_E\frac{\partial h_0}{\partial\theta}\right)v_E\frac{h_0^2}{2}\right)-a\left(-v_E\right)=0. \tag{2.65}
$$

Thus $\beta=0$, a moderate angle of droplet approach, leads to a film profile equation:

$$
\frac{\partial h_0}{\partial t}+\mathrm{Re_f}\frac{\partial}{\partial\theta}\left(\mathrm{We_f}\left(\frac{\partial h_0}{\partial\theta}+\frac{\partial^3 h_0}{\partial\theta^3}\right)\frac{h_0^3}{3}-\frac{\sin\theta}{\mathrm{Fr}}\frac{h_0^3}{3}+au_E(-v_E)\frac{h_0^2}{2}\right)=0. \tag{2.66}
$$

$\beta=1$, a shallow angle of droplet approach, leads a film profile equation:

$$
\frac{\partial h_0}{\partial t}+\mathrm{Re_f}\frac{\partial}{\partial\theta}\left(\mathrm{We_f}\left(\frac{\partial h_0}{\partial\theta}+\frac{\partial^3 h_0}{\partial\theta^3}\right)\frac{h_0^3}{3}-\frac{\sin\theta}{\mathrm{Fr}}\frac{h_0^3}{3}+au_E\left(u_E\frac{\partial h_0}{\partial\theta}-v_E\right)\frac{h_0^2}{2}\right)=0. \tag{2.67}
$$

The latter case corresponds to a film profile driven by only droplet momentum at leading order. Effects of droplet mass are only at higher order. We will be focussing further on this important limit in Chapter 3.

2.8.2 Low droplet volume fraction

If $k = 2$, the droplet volume fraction is given by

$$\alpha = \epsilon^2 a,$$

and the velocity scalings are $U_E/U = \epsilon^{-1-\beta/2}$ and $V_E/U = \epsilon^{-1+\beta/2}$. Consistent scaling such that $M = O(1)$ requires $\beta \geq 0$.

With these scalings, (2.37-2.39) become

$$\begin{aligned}
N_l =& -\frac{\mathrm{We_f}}{\epsilon}\left(1+\left(\frac{\epsilon}{1-\epsilon h}\frac{\partial h}{\partial\theta}\right)^2\right)^{-3/2}\left((1-\epsilon h)^2+2\epsilon^2\left(\frac{\partial h}{\partial\theta}\right)^2+\epsilon(1-\epsilon h)\frac{\partial^2 h}{\partial\theta^2}\right)\\
&+(1-\epsilon h)^3\frac{\mathrm{We_f}}{\epsilon}\\
&+\epsilon\frac{\epsilon^2 a}{1-\epsilon^2 a}(1-\epsilon h)\left(-\epsilon^{-\beta/2}u_E\frac{\partial h}{\partial\theta}+(1-\epsilon h)\epsilon^{-1+\beta/2}v_E+\epsilon u\frac{\partial h}{\partial\theta}-\epsilon(1-\epsilon h)v\right)^2 N^2,\\
T =& -\mathrm{Re_f}\frac{\epsilon^2 a}{1-\epsilon^2 a}(1-\epsilon h)\left((1-\epsilon h)\epsilon^{-1-\beta/2}u_E+\epsilon^{\beta/2}v_E\frac{\partial h}{\partial\theta}-(1-\epsilon h)u-\epsilon^2 v\frac{\partial h}{\partial\theta}\right)\\
&\times\left(-\epsilon^{-1-\beta/2}u_E\epsilon\frac{\partial h}{\partial\theta}+(1-\epsilon h)\epsilon^{-1+\beta/2}v_E+u\epsilon\frac{\partial h}{\partial\theta}-\epsilon(1-\epsilon h)v\right),\\
M =& \epsilon^2 a(1-\epsilon h)\frac{\partial h}{\partial t}+\epsilon^2 a\left(\epsilon^{-1-\beta/2}u_E\frac{\partial h}{\partial\theta}-\epsilon^{-1+\beta/2}(1-\epsilon h)\frac{v_E}{\epsilon}\right).
\end{aligned}$$

The dominant terms are

$$\begin{aligned}
N_{l0} &= -\mathrm{We_f}\left(h_0+\frac{\partial^2 h_0}{\partial\theta^2}\right),\\
T_0 &= -\mathrm{Re_f}a\left(-\epsilon^{1-\beta}u_E u_E\frac{\partial h_0}{\partial\theta}+u_E v_E\right),\\
M_0 &= a\left(-\epsilon^{\beta/2}v_E\right).
\end{aligned}$$

Substituting into (2.64) gives:

$$\begin{aligned}
\frac{\partial h_0}{\partial t}+\mathrm{Re_f}\frac{\partial}{\partial\theta}\left(\mathrm{We_f}\left(\frac{\partial h_0}{\partial\theta}+\frac{\partial^3 h_0}{\partial\theta^3}\right)\frac{h_0^3}{3}-\frac{\sin\theta}{\mathrm{Fr}}\frac{h_0^3}{3}+au_E\left(\epsilon^{1-\beta}u_E\frac{\partial h_0}{\partial\theta}-v_E\right)\frac{h_0^2}{2}\right)\\
-a\epsilon^{\beta/2}(-v_E)=0.
\end{aligned}$$

Thus $\beta = 0$, a moderate angle of droplet approach, leads to a film profile equation

$$\begin{aligned}
\frac{\partial h_0}{\partial t}+\mathrm{Re_f}\frac{\partial}{\partial\theta}\left(\mathrm{We_f}\left(\frac{\partial h_0}{\partial\theta}+\frac{\partial^3 h_0}{\partial\theta^3}\right)\frac{h_0^3}{3}-\frac{\sin\theta}{\mathrm{Fr}}\frac{h_0^3}{3}+au_E\left(-v_E\right)\frac{h_0^2}{2}\right)\\
-a(-v_E)=0. \quad (2.68)
\end{aligned}$$

$\beta = 1$, a shallow angle of droplet approach, leads to a film profile equation

$$\frac{\partial h_0}{\partial t}+\mathrm{Re_f}\frac{\partial}{\partial\theta}\left(\mathrm{We_f}\left(\frac{\partial h_0}{\partial\theta}+\frac{\partial^3 h_0}{\partial\theta^3}\right)\frac{h_0^3}{3}-\frac{\sin\theta}{\mathrm{Fr}}\frac{h_0^3}{3}+au_E\left(u_E\frac{\partial h_0}{\partial\theta}-v_E\right)\frac{h_0^2}{2}\right)=0. \quad (2.69)$$

This is identical to (2.67), which arises in the case $k = 3$, $\beta = 1$.

2.8.3 Moderate droplet volume fraction

If $k = 1$, the droplet volume fraction is given by

$$\alpha = \epsilon a,$$

and the velocity scalings are $U_E/U = \epsilon^{-1/2-\beta/2}$ and $V_E/U = \epsilon^{-1/2+\beta/2}$. Consistent scaling such that $M = O(1)$ requires $\beta \geq 1$. So $\beta = 1$, a shallow angle of droplet approach.

Substituting $U_E/U = \epsilon^{-1}$, and $V_E/U = 1$ into (2.37-2.39),

$$\begin{aligned} N_{l0} &= -\mathrm{We_f}\left(h_0 + \frac{\partial^2 h_0}{\partial\theta^2}\right), \\ T_0 &= -\mathrm{Re_f} a u_E \left(-u_E \frac{\partial h_0}{\partial\theta} + v_E\right), \\ M_0 &= a\left(u_E \frac{\partial h_0}{\partial\theta} - v_E\right). \end{aligned}$$

Then substituting into (2.64) the film profile evolution equation is given by

$$\frac{\partial h_0}{\partial t} + \mathrm{Re_f}\frac{\partial}{\partial\theta}\left(\mathrm{We_f}\left(\frac{\partial h_0}{\partial\theta} + \frac{\partial^3 h_0}{\partial\theta^3}\right)\frac{h_0^3}{3} - \frac{\sin\theta}{\mathrm{Fr}}\frac{h_0^3}{3} + a u_E\left(u_E\frac{\partial h_0}{\partial\theta} - v_E\right)\frac{h_0^2}{2}\right) - a\left(u_E\frac{\partial h_0}{\partial\theta} - v_E\right) = 0. \quad (2.70)$$

This case corresponds to a film profile driven by both droplet momentum and mass addition. We will be focussing further on this important limit in Chapter 4.

2.9 Area of the film

An important parameter is the total mass of the fluid in the film, or equivalently the filling fraction of the cylinder, or cross-sectional area per unit length.

The dimensional area is a function of $\hat{h}$, and is given by

$$\hat{A} = \int_{-\pi}^{\pi}\int_{\hat{h}_r}^{r_0} \hat{r}\,\mathrm{d}\hat{r}\mathrm{d}\theta.$$

Substituting in the non-dimensional variables leads to

$$\hat{A} = h_0 r_0 \int_{-\pi}^{\pi} h + \frac{\epsilon h^2}{2}\,\mathrm{d}\theta.$$

So to leading order a non-dimensional film area measure is given by

$$A = \int_{-\pi}^{\pi} h\,\mathrm{d}\theta.$$

2.10 Key features of the film evolution equation

In summary, each of the five cases derived in this chapter and given in (2.65-2.70) can be written as

$$\frac{\partial h}{\partial t}+\frac{\partial}{\partial \theta}\left(c_1\left(\frac{\partial h}{\partial \theta}+\frac{\partial^3 h}{\partial \theta^3}\right)\frac{h^3}{3}+c_2\sin\theta\frac{h^3}{3}+\left(c_3\frac{\partial h}{\partial \theta}+c_4\right)\frac{h^2}{2}\right)+\left(c_5\frac{\partial h}{\partial \theta}+c_6\right)=0, \tag{2.71}$$

with constant coefficients given by table 2.3:

Eqn. no.	k	β	c_1	c_2	c_3	c_4	c_5	c_6
(2.65)	3	-1	$\mathrm{Re_f We_f}$	$-\mathrm{Re_f}/\mathrm{Fr}$	$-\mathrm{Re_f}av_E^2$	$-\mathrm{Re_f}au_Ev_E$	0	av_E
(2.66)	3	0	$\mathrm{Re_f We_f}$	$-\mathrm{Re_f}/\mathrm{Fr}$	0	$-\mathrm{Re_f}au_Ev_E$	0	0
(2.67)	3	1	$\mathrm{Re_f We_f}$	$-\mathrm{Re_f}/\mathrm{Fr}$	$\mathrm{Re_f}au_E^2$	$-\mathrm{Re_f}au_Ev_E$	0	0
(2.68)	2	0	$\mathrm{Re_f We_f}$	$-\mathrm{Re_f}/\mathrm{Fr}$	0	$-\mathrm{Re_f}au_Ev_E$	0	av_E
(2.69)	2	1	$\mathrm{Re_f We_f}$	$-\mathrm{Re_f}/\mathrm{Fr}$	$\mathrm{Re_f}au_E^2$	$-\mathrm{Re_f}au_Ev_E$	0	0
(2.70)	1	1	$\mathrm{Re_f We_f}$	$-\mathrm{Re_f}/\mathrm{Fr}$	$\mathrm{Re_f}au_E^2$	$-\mathrm{Re_f}au_Ev_E$	$-au_E$	av_E

Table 2.3: Coefficients of (2.71) for various droplet limits

It is instructive to identify the physical basis for the terms in (2.65-2.70) for later reference and analysis. All cases have common terms c_1 and c_2, involving surface tension and gravity. The first-order derivative in the surface tension term is due to the curvature of the cylinder, and would not arise in a case of flow down a plane. The c_1 coefficients may physically be smaller than $O(1)$ — see Table 2.2 — but being a function of $\mathrm{We_f}$ is independent of other coefficients and we retain it in order to study its effect, since it acts on the highest derivative of h. The same is not done for second order gravitational effects — see §1.8. The coefficient $c_4 = -\mathrm{Re_f}au_Ev_E$ occurs in every droplet scaling case; this is analogous to an imposed shear on the surface, such as was studied by Villegas-Díaz et al. [53].

However as the droplet fraction increases, the effect of mass addition to the film increases, and the impact angle of droplets which may drive a shear flow decreases. The term with coefficient c_3 is equivalent to the azimuthal component of droplet momentum. It is also analogous to a temperature-dependent term which arises in the problem of flow down a heated plane or rimming flow with a heated cylinder wall [50], and we will consider it in this context in Chapter 6. The terms c_5 and c_6 arise from the contribution of droplet mass. The first derivative is again equivalent to the azimuthal component of droplet mass, and the constant term to the radial component.

In Chapter 3 we will focus on the case with negligible droplet mass, as arises from (2.67). Then in Chapter 4 we will return to the case of significant mass impact, and also introduce rotation of the cylinder.

Chapter 3

Film profile for significant uniform droplet momentum but negligible mass transfer at the surface.

In this chapter we will consider the leading-order film evolution for the situation where the impact velocity of droplets into a film is sufficiently high for the droplet momentum to drive the film, but the effect of additional mass to the film is negligibly small. In the notation of Chapter 2, this is the limit $k = 3$, $\beta = 1$, i.e. $\alpha = \epsilon^3 a$, $U_E/U = O(\epsilon^{-2})$ and $V_E/U = O(\epsilon^{-1})$. The governing equation for the film height is given by (2.67) and is equivalent to (2.71) with $c_5, c_6 = 0$.

By taking both surface tension and the azimuthal droplet momentum to have negligible effects, exact solutions to the steady-state film-height equation can be obtained analytically. An indication of the solutions that may exist with small, but non-negligible, surface tension and azimuthal droplet momentum is then given by a perturbation analysis. We will then employ numerical methods to find specific solutions and further analyse the effects of these parameters. We will also consider the stability of the steady-state solutions that we find.

In order to focus on the key terms of surface tension and the azimuthal droplet momentum, we choose a characteristic film thickness h_0 and film velocity U

$$h_0 = \left(\frac{U\mu}{\rho g}\right)^{1/2}, \quad U = \left(\frac{\mu g}{a^2|u_E|^2|v_E|^2\rho}\right)^{1/3},$$

so that

$$\frac{\mathrm{Re_f}}{\mathrm{Fr}} = \frac{\rho g h_0^2}{\mu U} \equiv 1$$

and

$$\mathrm{Re_f} a u_E|v_E| = \left(\frac{\rho U^3}{g\mu}\right)^{1/2} a u_E|v_E| = \frac{u_E}{|u_E|} = \mathrm{sign}(u_E).$$

Then (2.67) becomes

$$\frac{\partial h}{\partial t}+\frac{\partial}{\partial\theta}\left(\mathrm{Re_f We_f}\left(\frac{\partial h}{\partial\theta}+\frac{\partial^3 h}{\partial\theta^3}\right)\frac{h^3}{3}-\sin\theta\frac{h^3}{3}+\left(\frac{|u_E|}{|v_E|}\frac{\partial h}{\partial\theta}+\mathrm{sign}(u_E)\right)\frac{h^2}{2}\right)=0. \quad (3.1)$$

v_E is always negative, for the droplets to move radially outwards towards the film, but u_E could be positive or negative. In what follows we will assume u_E to be positive and some of the corresponding results for $u_E<0$ are in Appendix D.

For brevity of notation, we define

$$\zeta=\mathrm{Re_f We_f},\quad \alpha_u=\frac{u_E}{|v_E|},$$

to obtain[1]

$$\frac{\partial h}{\partial t}+\frac{\partial q}{\partial\theta}=0,\qquad q=\zeta\frac{h^3}{3}\left(\frac{\partial h}{\partial\theta}+\frac{\partial^3 h}{\partial\theta^3}\right)-\sin\theta\frac{h^3}{3}+\left(\alpha_u\frac{\partial h}{\partial\theta}+1\right)\frac{h^2}{2}. \quad (3.2)$$

This is (2.71) with $c_1=\zeta$, $c_2=-1$, $c_3=\alpha_u$, $c_4=1$, $c_5=0$ and $c_6=0$.

3.1 Steady solution when shear balances gravity with negligible surface tension and azimuthal droplet momentum, $\zeta,\alpha_u=0$

In the first instance, steady-state solutions are sought that are maintained by a balance of surface shear and gravity, so $\zeta,\alpha_u=0$. An explicit solution can be found. The solutions for small non-zero ζ,α_u are expected to be close to this, except where derivatives of h are large, causing the terms involving ζ,α_u to have a significant effect.

Taking $\zeta,\alpha_u=0$, we have

$$q=-\sin\theta\frac{h^3}{3}+\frac{h^2}{2}. \quad (3.3)$$

Equation (3.3) is a cubic polynomial with real coefficients, so has 3 roots, either 3 real or 1 real and 2 complex depending on the value of q. This is similar to the well-known Moffatt solution where gravity balances rotation of the cylinder [33], where there is a critical value of $q=2/3$. In this case, there is a critical value of $q=1/6$, and the possible

[1] An equivalent equation focussing on surface tension and azimuthal droplet momentum may also be obtained directly from (2.67) using the change of variables $h_*=\frac{1}{au_E\mathrm{Fr}(-v_E)}h$, $t_*=\frac{\mathrm{Re_f}}{\mathrm{Fr}}\left(au_E\mathrm{Fr}(-v_E)\right)^2 t$, $q_*=\frac{\mathrm{Fr}}{\mathrm{Re_f}}\left(\frac{1}{au_E\mathrm{Fr}(-v_E)}\right)^3 q$ etc.

roots in $-\pi \leq \theta \leq \pi$ are categorised as follows:

$$
\begin{aligned}
q < 1/6 &\begin{cases} 1 \text{ positive real root for all } \theta; \end{cases} \\
q = 1/6 &\begin{cases} 1 \text{ positive real root for } \theta \in [-\pi, 0], \\ 2 \text{ positive real roots for } \theta \in (0, \pi); \end{cases} \\
q > 1/6 &\begin{cases} 1 \text{ positive real root for } \theta \in [-\pi, 0], \\ 2 \text{ positive real roots for } \theta \in (0, \theta_c] \cup [\pi - \theta_c, \pi), \\ 0 \text{ positive real roots for } \theta \in (\theta_c, \pi - \theta_c); \end{cases}
\end{aligned}
$$

where θ_c is a critical value dependent on q.

Thus for $\theta < 0$, the descending side of the cylinder, there can only be one solution. On the ascending side, $\theta > 0$, there is only a bounded completely-wetting solution for $q \leq 1/6$. The positive real roots of (3.3) corresponding to selective values of q are illustrated by figure 3.1.

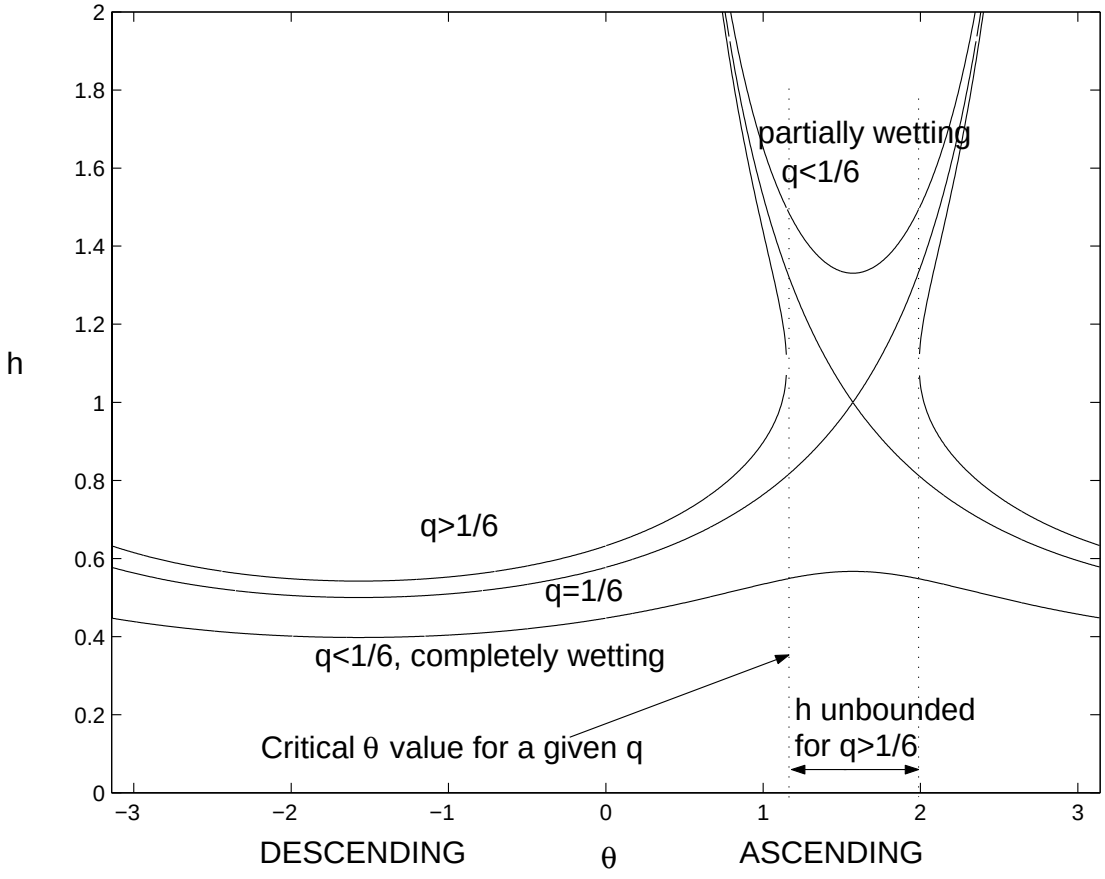

Figure 3.1: Positive solutions to $q = -\frac{h^3}{3}\sin\theta + \frac{h^2}{2}$

Wilson *et al.* [59] provide explicit expressions for $h(\theta)$ when $0 < q \leq 1/6$. The

completely-wetting solution has a height profile

$$h_f(\theta) = \begin{cases} \frac{1}{2\sin\theta} + \frac{1}{\sin\theta}\cos\left(\frac{\pi}{3} + \frac{1}{3}\cos^{-1}\left(-1 + 12q\sin^2\theta\right)\right) & \text{for } 0 < \theta < \pi, \\ \sqrt{2q} & \text{for } \theta = 0, \pi, \\ \frac{1}{2\sin\theta} - \frac{1}{\sin\theta}\cos\left(\frac{\pi}{3} - \frac{1}{3}\cos^{-1}\left(1 - 12q\sin^2\theta\right)\right) & \text{for } -\pi < \theta < 0. \end{cases} \tag{3.4}$$

The upper, partially-wetting solution, has a height profile

$$h_c(\theta) = \begin{cases} \frac{1}{2\sin\theta} + \frac{1}{\sin\theta}\cos\left(\frac{\pi}{3} - \frac{1}{3}\cos^{-1}\left(-1 + 12q\sin^2\theta\right)\right) & \text{for } 0 < \theta < \pi, \\ \text{not defined} & \text{for } -\pi \leq \theta \leq 0, \end{cases} \tag{3.5}$$

and is unbounded,

$$h_c \sim \begin{cases} \frac{3}{2\theta} & \text{as } \theta \to 0_+ \text{ (bottom of cylinder)} \\ \frac{3}{2(\pi-\theta)} & \text{as } \theta \to \pi_- \text{ (top of cylinder).} \end{cases}$$

As $q \to 0$, the full solution h_f thins to zero. The upper solution grows to a limit of $h_c = \frac{3}{2\sin\theta}$, and $h_c(\pi/2) = 1.5$.

In the case $q = 1/6$, (3.4, 3.5) reduce to

$$h_f(\theta) = \frac{1}{2}\sec\left(\frac{\pi}{3} - \left|\frac{\theta}{3} - \frac{\pi}{6}\right|\right) \leq 1, \tag{3.6}$$

$$h_c(\theta) = \frac{1}{2}\sec\left(\frac{\pi}{3} + \left|\frac{\theta}{3} - \frac{\pi}{6}\right|\right) \geq 1, \tag{3.7}$$

and at $\theta = \pi/2$ the two solutions meet, $h_f = h_c = 1$.

In the case $q > 1/6$ then both solutions break down physically, since there exist values of θ for which $\cos^{-1}\left(-1 + 12q\sin^2\theta\right)$ is not real, and there is no completely wetting solution.

3.1.1 Shock solutions

Physically, within the model of an oil film cooling a bearing chamber, we seek bounded, completely-wetting, steady-state film profiles. However the partially-wetting upper solution in figure 3.1 may occur as part of a 'shock' solution. A shock solution comprises a sudden jump in height joining two otherwise disconnected smooth solutions. There are infinitely many steady-state, completely wetting film profiles, featuring multiple shocks. Whether such profiles are physically realisable will depend on their stability and the total flux.

Consider first the steady solutions of

$$\frac{\partial h}{\partial t} - \frac{\partial}{\partial \theta}\left(\frac{h^3}{3}\sin(\theta) + \frac{h^2}{2}\right) = 0.$$

As we have seen above, for $q \leq 1/6$ we have two positive real solutions, one which is completely wetting and a second which only exists within $0 < \theta < \pi$, and which is unbounded for $\theta \to 0_+$, $\theta \to \pi_-$. For $q = 1/6$ the two parts meet, but for $q < 1/6$ they are separate.

For $q < 1/6$ there can only be an even number of shocks, as for every shock up to the upper solution, there must be one back down to the lower.

For $q = 1/6$ there may be an odd number of shocks, with the first solution being rejoined at the crossing point of $\theta = \pi/2$. A single shock at $\theta = \theta_K$ facing backwards and forwards is illustrated in figures 3.2 (i) and (ii) respectively, and the latter is plotted on a polar axis in figure 3.3 as a reminder of what that physically means.

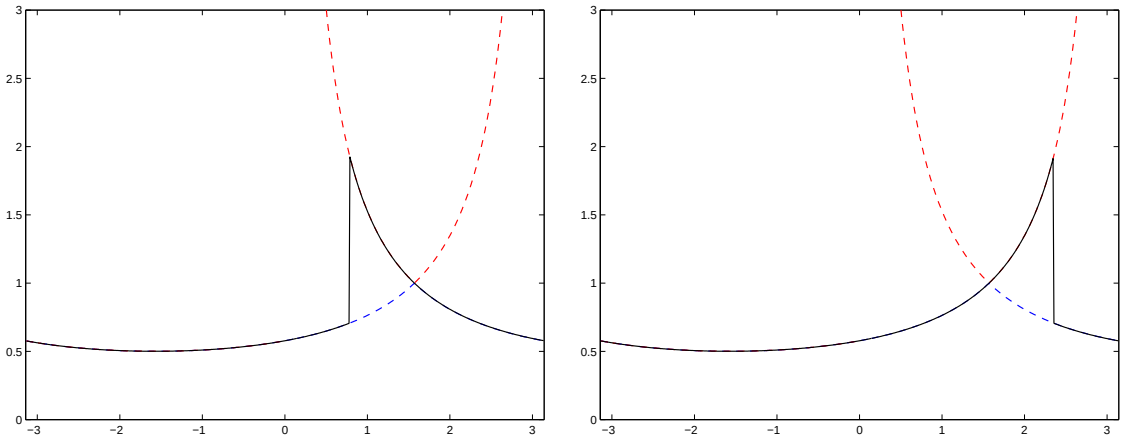

(i) (ii)

Figure 3.2: (i) A backwards facing (rising) shock at $\theta_K = \pi/4$ (ii) A forwards facing (falling) shock at $\theta_K = 3\pi/4$

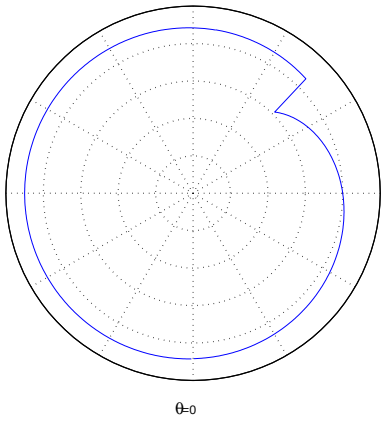

Figure 3.3: A forwards facing shock at $\theta_K = 3\pi/4$

3.1.2 Explicit expression for area

Wilson *et al.* [59] derived an explicit expression for area in the case of $q = 1/6$ and a shock at $\theta = \theta_K$, equivalent to

$$A = \frac{3}{2}\ln\left(\frac{2\cos\left(\theta_K/3 - \pi/6\right) + \sqrt{3}}{2\cos\left(\theta_K/3 - \pi/6\right) - \sqrt{3}}\right). \tag{3.8}$$

The area when there is no shock but just the completely wetting profile is critical and is given by

$$A_{crit} = 3\ln\left(2 + \sqrt{3}\right) \approx 3.951. \tag{3.9}$$

When the shock position tends to $\theta = 0$, the area is unbounded, with $A \to \infty$ according to

$$A = \frac{3}{2}\ln\left(\frac{6\sqrt{3}}{\theta_K}\right) + \frac{\theta_K}{\sqrt{3}} + O(\theta_K^2). \tag{3.10}$$

Thus in the absence of surface tension, the shock solution to the flow driven by surface shear and gravity can support an arbitrarily large area A of fluid, up to the limit of validity of the thin-film approximation. This is in contrast to the solution given by Moffatt [33] for flow driven by cylinder rotation and gravity, which has a maximum supportable area A=6.88.

3.2 Smoothing of shocks by surface tension and droplets

In a physical system, non-zero surface tension and azimuthal component of droplet momentum, associated with parameters ζ and α_u, have a smoothing effect on the profile. Typical values of ζ, α_u are small, but in (3.2) they multiply derivatives $\frac{\partial h}{\partial \theta}$ and $\frac{\partial^3 h}{\partial \theta^3}$. These are very large in the region of a shock, so ζ and α_u terms can become locally significant and determine whether shock-like solutions may exist physically.

To analyse which shock solutions are still feasible, we expand in the region around the shock position at $\theta = \theta_K$, using, say, $\theta = \theta_K + \delta\phi$. The outer solution is given by the cubic (3.3), which in $0 < \theta < \pi$ has positive real roots which we label $h = h_j$, where $j = 1, 2$ on the upper and lower branches respectively, and a negative root h_3.

As illustrated in figure 3.4, we take a local profile $H(\phi) = h(\theta)$ as $\phi \to 0$ to be an inner solution and examine whether is is possible to match it to the outer solution branches h_j as $\phi \to \pm\infty$. We will find that it is not always possible to match the inner and outer solutions, and this restricts the possible shock solutions. Substituting into (3.2) implies

$$q = \zeta\frac{H^3}{3}\left(\frac{1}{\delta^3}\frac{\mathrm{d}^3 H}{\mathrm{d}\phi^3} + \frac{1}{\delta}\frac{\mathrm{d}H}{\mathrm{d}\phi}\right) - \frac{H^3}{3}\sin(\theta_K + \delta\phi) + \frac{H^2}{2}\left(1 + \frac{\alpha_u}{\delta}\frac{\mathrm{d}H}{\mathrm{d}\phi}\right). \tag{3.11}$$

In the limit $\delta \to 0$ we analyse if matching is possible, depending on the balance of parameters α_u and ζ. Inspection of the first and last terms of (3.11) suggests investigating the balance $\alpha_u^3 \sim \zeta$.

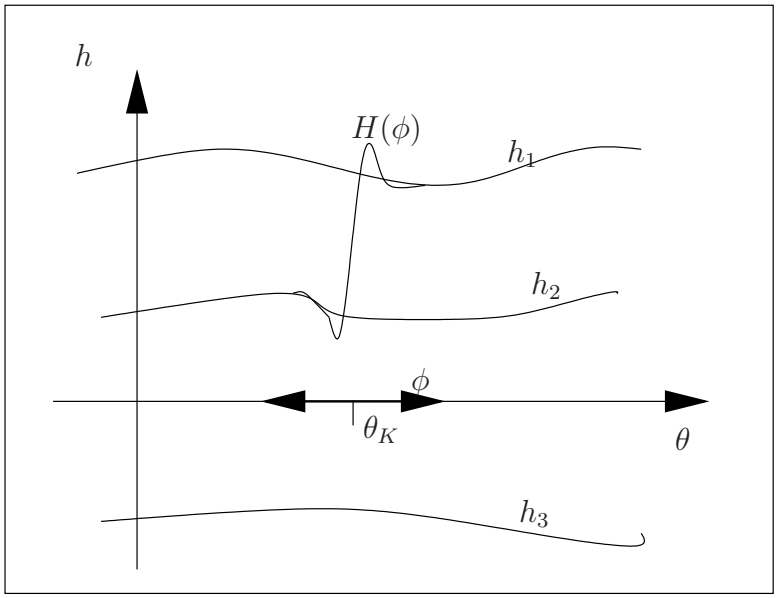

Figure 3.4: Illustration of matching a smoothed shock inner solution H to outer solutions h_1 and h_2. The third solution h_3 is non-physical. In this sketch a rising shock is matched, so $H \to h_2$ as $\phi \to -\infty$ and $H \to h_1$ as $\phi \to \infty$.

3.2.1 Surface tension dominant

Suppose surface tension dominates or balances the azimuthal droplet momentum term. With the change of variables $\phi = \frac{\zeta^{1/3}}{\delta}\phi'$, (3.11) becomes

$$q = \frac{H^3}{3}\left(\frac{\mathrm{d}^3 H}{\mathrm{d}\phi'^3}\right) - \frac{H^3}{3}\sin(\theta_K) + \frac{H^2}{2}\left(1 + \frac{\alpha_u}{\zeta^{1/3}}\frac{\mathrm{d}H}{\mathrm{d}\phi'}\right) + O(\delta, \zeta). \tag{3.12}$$

For surface tension dominant or balancing the azimuthal droplet momentum, $\frac{\alpha_u}{\zeta^{1/3}} = O(1)$ and thus to leading order:

$$q = \frac{H^3}{3}\left(\frac{\mathrm{d}^3 H}{\mathrm{d}\phi'^3}\right) - \frac{H^3}{3}\sin(\theta_K) + \frac{H^2}{2}\left(1 + \frac{\alpha_u}{\zeta^{1/3}}\frac{\mathrm{d}H}{\mathrm{d}\phi'}\right). \tag{3.13}$$

Rearranging (3.13):

$$\frac{\mathrm{d}^3 H}{\mathrm{d}\phi'^3} = \frac{3}{H^3}\left(q + \frac{H^3}{3}\sin(\theta_K) - \frac{H^2}{2}\left(1 + \frac{\alpha_u}{\zeta^{1/3}}\frac{\mathrm{d}H}{\mathrm{d}\phi'}\right)\right). \tag{3.14}$$

To make further progress, we linearize H around each h_j in turn at the shock position θ_K, so for small f_j,

$$H(\phi') = h_j + f_j(\phi'). \tag{3.15}$$

Then we will examine f_j as $\phi' \to \pm\infty$. We will find that the requirement that f_j is bounded, as $\phi' \to \infty$ or $\phi' \to -\infty$, imposes bounds on h_j which dictate whether the shock can be rising or falling.

Substituting (3.15) into (3.14), then, ignoring terms of $O(f_j^2)$,

$$\frac{\mathrm{d}^3 f_j}{\mathrm{d}\phi'^3} = \frac{3}{h_j^3}\left(1 - \frac{3f_j}{h_j}\right)\left(q + \frac{1}{3}\left(h_j^3 + 3h_j^2 f\right)\sin\theta_K - \frac{1}{2}\left(h_j^2 + 2h_j f\right)\left(1 + \frac{\alpha_u}{\zeta^{1/3}}\frac{\mathrm{d}f_j}{\mathrm{d}\phi'}\right)\right).$$

Since h_j satisfies (3.3), simplification leads to

$$\frac{\mathrm{d}^3 f_j}{\mathrm{d}\phi'^3} + a_j\frac{\mathrm{d}f_j}{\mathrm{d}\phi'} + b_j f_j = 0, \tag{3.16}$$

$$\text{where} \quad a_j = \frac{3\alpha_u}{2\zeta^{1/3}}\frac{1}{h_j}, \quad b_j = \frac{3}{2h_j^2}\left(-h_j\sin\theta_K + 1\right).$$

In (3.16), since by (3.6, 3.7) $0 < h_2 < 1 < h_1$, $0 < \theta_K < \pi$, and
$\mathrm{sign}(b_j) = \mathrm{sign}(-h_j\sin\theta_K + 1)$, then

$$a_1 > 0, \quad a_2 > 0, \quad b_1 < 0, \quad \text{and} \quad b_2 > 0.$$

Seeking solutions to (3.16) of the form $f_j = Ce^{\lambda_j\phi'}$, leads to the cubic indicial equation for λ_j:

$$\lambda_j^3 + a_j\lambda_j + b_j = 0. \tag{3.17}$$

Since $a_j > 0$, (3.17) has one real and two complex conjugate roots, given by x_j, $-\frac{x_j}{2} + iy_j$, and $-\frac{x_j}{2} - iy_j$ for some real x_j, y_j.

So

$$f_j = C_1 e^{x_j\phi'} + C_2 e^{(-x_j/2 + iy_j)\phi'} + C_3 e^{(-x_j/2 - iy_j)\phi'}. \tag{3.18}$$

Since x_j is a root of (3.17), $x_j = -\frac{b_j}{x_j^2 + a_j}$. $a_j > 0$, so $\mathrm{sign}(x_j) = -\mathrm{sign}(b_j)$. For the lower branch: $x_2 < 0$; for the upper branch: $x_1 > 0$.

Now, in order for f_j to be bounded as $\phi' \to \pm\infty$, we must either have that $C_1 = 0$, $C_2, C_3 \neq 0$, permitting an oscillating matching or that $C_1 \neq 0$, $C_2, C_3 = 0$, permitting a monotonic matching. There is more flexibility in this problem than is usual in similar work, because the sign of b_j depends on the solution branch rather than being constant. Let us consider the cases in turn.

As $\phi' \to \infty$, for a monotonic matching, f_j can only be bounded if $C_1 \neq 0$, $C_2, C_3 = 0$, and $x_j < 0$, which is only satisfied by x_2. The inner solution $H(\phi)$ can only be matched at $\phi' \to \infty$ by the lower branch.

As $\phi' \to \infty$, for an oscillating matching, f_j can only be bounded if $C_1 = 0$, $C_2, C_3 \neq 0$, and $x_j > 0$, which is only satisfied by x_1. The inner solution $H(\phi)$ can only be matched at $\phi' \to \infty$ by the upper branch.

As $\phi' \to -\infty$, for a monotonic matching, f_j can only be bounded if $C_1 \neq 0$, $C_2, C_3 = 0$, and $x_j > 0$, which is only satisfied by x_1. The inner solution $H(\phi)$ can only be matched at $\phi' \to -\infty$ by the upper branch.

As $\phi' \to -\infty$, for an oscillating matching, f_j can only be bounded if $C_1 = 0$, $C_2, C_3 \neq 0$, and $x_j < 0$, which is only satisfied by x_2. The inner solution $H(\phi)$ can only be matched at $\phi' \to -\infty$ by the lower branch.

A different branch must be matched at either side of the shock in order for it to *be* a shock, so we must either have two oscillating or two monotonic matchings. This permits either a rising shock, from h_2 to h_1, with oscillating matchings, or a falling shock, from h_1 to h_2, with monotonic matchings.

For surface tension dominant or balancing droplet momentum, $a_j = O(1)$, and the possibility of matching is independent of the size of a_j or b_j, within this limit. (But observe that if $a_j \gg 1$, then $x_j \ll 1$, and solutions oscillates rapidly but are slowly modulated. Equation (3.17) reduces to a linear equation, similar to that for droplet momentum dominant in the next section.)

For $q = 1/6$, it is also possible to move between the two branches at the cross-over point $\theta = \pi/2$. The requirement that the solution is also periodic leads to the possible shock combinations sketched in figure 3.5.

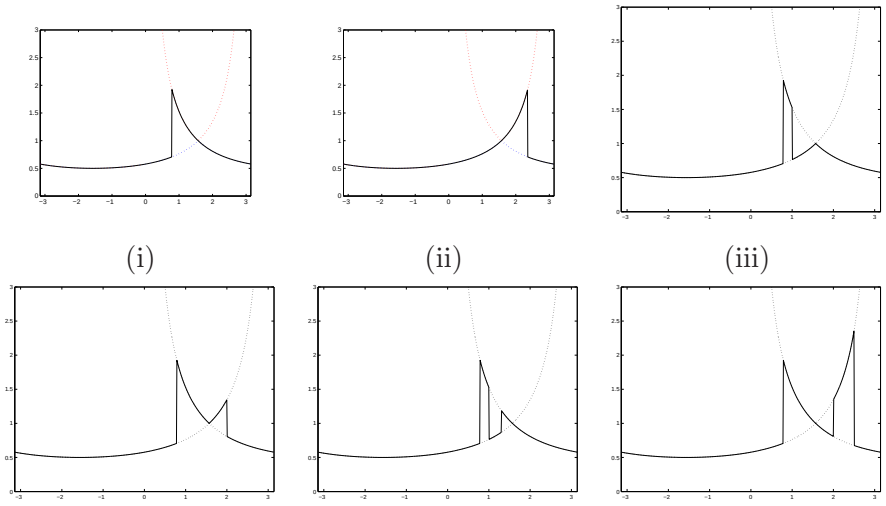

Figure 3.5: Various shock combinations possible with surface tension smoothing. Kinematic wave theory will show (ii), (iii) and (iv) to be unstable, and (i) is the only shock seen in numerical solutions. Rising shocks are matched using an oscillating matching, falling shocks a monotonic matching.

So with surface tension dominant or balancing the azimuthal droplet momentum, it is only possible with only oscillating matching to match the inner solution to the outer

cubic for a shock rising from the lower branch to the upper branch. To return to the lower branch needs the cross-over point that occurs only for $q = 1/6$; only a single shock is possible and the shock must occur in $0 < \theta_K < \pi/2$, the lower ascending quadrant. With monotonic matching, more combinations are possible, and may include double shocks. [2] We emphasise that the existence of a matching is not shown by this argument, only a limitation on such an inner solution.

3.2.2 Droplet momentum dominant

Now suppose the azimuthal droplet momentum dominates the surface tension term. This time use the change of variables

$$\phi = \frac{\alpha_u}{\delta}\phi',$$

then (3.11) becomes

$$q = \frac{H^3}{3}\left(\frac{\zeta}{\alpha_u^3}\frac{\mathrm{d}^3 H}{\mathrm{d}\phi'^3} + \frac{\zeta}{\alpha_u}\frac{\mathrm{d}H}{\mathrm{d}\phi'}\right) - \frac{H^3}{3}\sin(\theta_K) + \frac{H^2}{2}\left(1 + \frac{\mathrm{d}H}{\mathrm{d}\phi'}\right) + O(\alpha_u). \tag{3.19}$$

For azimuthal droplet momentum dominant, $\frac{\zeta}{\alpha_u^3} \ll 1$, and to leading order this becomes

$$q = -\frac{H^3}{3}\sin\theta_K + \frac{H^2}{2}\left(1 + \frac{\mathrm{d}H}{\mathrm{d}\phi'}\right). \tag{3.20}$$

a) Linearization method

Rearranging (3.20),

$$\frac{\mathrm{d}H}{\mathrm{d}\phi'} = \frac{2\left(q + \frac{H^3}{3}\sin(\theta_K) - \frac{H^2}{2}\right)}{H^2}. \tag{3.21}$$

We linearize H around each h_j in turn at the shock position θ_K, so for small f_j,

$$H(\phi') = h_j + f_j(\phi'). \tag{3.22}$$

Then

$$\frac{\mathrm{d}f_j}{\mathrm{d}\phi'} = 2\left(\frac{1}{h_j^2} - \frac{2f_j}{h_j^3}\right)\left(q + \left(\frac{h_j^3}{3} + h_j^2 f_j\right)\sin(\theta_K) - \left(\frac{h_j^2}{2} + h_j f_j\right)\right) + O(f_j^2). \tag{3.23}$$

Since h_j satisfies (3.3), simplification leads to

$$\frac{\mathrm{d}f_j}{\mathrm{d}\phi'} = \frac{2}{h_j}\left(h_j\sin(\theta_K) - 1\right) f_j, \tag{3.24}$$

[2] It has been argued in a similar case [53] that monotonic matchings are less likely than oscillating, there being insufficient freedom in the coefficients to effect the matching.

at leading order in f_j, which has solutions of the form

$$f_j = Ce^{\lambda_j \phi'}, \quad \lambda_j = \frac{2}{h_j}\left(h_j \sin(\theta_K) - 1\right). \tag{3.25}$$

A monotonic matching may be possible (f_j is bounded) if $\lambda_j\, \phi' < 0$. We have $\lambda_1 > 0$ and $\lambda_2 < 0$, so:

as $\phi \to -\infty$, matching is only possible on h_1, the upper branch;

as $\phi \to \infty$**,** matching is only possible on h_2, the lower branch.

It is only possible to match a falling shock, with a monotonic matching from h_1 to h_2, such as illustrated in figure 3.5(ii).

b) Direct method

Alternatively, (3.20) can be examined directly, without using linearisation. Rearranging (3.20),

$$\frac{\mathrm{d}\phi'}{\mathrm{d}H} = \frac{H^2}{2\left(q + \frac{H^3}{3}\sin(\theta_K) - \frac{H^2}{2}\right)}. \tag{3.26}$$

The roots h_j of (3.3) satisfy

$$\frac{-\sin\theta_K}{3}(H-h_1)(H-h_2)(H-h_3) = -\frac{H^3}{3}\sin\theta_K + H^2 - q,$$

rearranging this and using (3.26) leads to

$$\frac{2}{3}\sin\theta_K \frac{\mathrm{d}\phi'}{\mathrm{d}H} = \frac{H^2}{(H-h_1)(H-h_2)(H-h_3)}.$$

Integrating this (using partial fractions) gives

$$\phi' \sin\theta_K = \frac{3h_1^2}{2(h_1-h_2)(h_1-h_3)}\ln|H-h_1| - \frac{3h_2^2}{2(h_1-h_2)(h_2-h_3)}\ln|H-h_2| + \frac{3h_3^2}{2(h_2-h_3)(h_1-h_3)}\ln|H-h_3| + const. \tag{3.27}$$

Consider first matching H to h_1. As $H \to h_1$, $\ln|H-h_1| \to -\infty$ and dominates (3.27), so

$$\phi' \sin\theta_K \sim \frac{3h_1^2}{2(h_1-h_2)(h_1-h_3)}\ln|H-h_1|. \tag{3.28}$$

Recall that only in $0 < \theta < \pi$ are there multiple solutions, so $\sin\theta_K > 0$, and by definition $h_1 > h_2 > h_3$. So

$$\phi' \to -\infty$$

and the inner solution H can only be matched to h_1 for $\theta < \theta_K$, i.e. on the left-hand side.

Now consider matching H to h_2. As $H \to h_2$, $\ln|H - h_2| \to -\infty$ so from (3.27)

$$\phi' \sin\theta_K \sim -\frac{3h_2^2}{2(h_1 - h_2)(h_2 - h_3)} \ln|H - h_2| \,. \tag{3.29}$$

So

$$\phi' \to \infty$$

and the inner solution H can only be matched to h_2 for $\theta > \theta_K$, i.e. on the right-hand side.

In conclusion, for solutions varying over the length-scale α_u, it is only possible to match a falling shock, from h_1 to h_2.

So with azimuthal droplet momentum dominating the surface tension, it is only possible to match the inner solution to the outer cubic for a shock falling from the upper branch to the lower branch. For $q < 1/6$, the smoothing of the droplet momentum is not sufficient to give a steady shock solution, as we cannot transfer from the lower branch to the higher. For $q = 1/6$, we can get a single shock solution, by transferring from the lower branch to the higher at the cross-over point $\theta = \pi/2$, then via a shock back down to the lower branch, as is illustrated in figure 3.2(ii). These shocks can only occur for $\pi/2 < \theta < \pi$, i.e. in the upper ascending quadrant. Once again, we emphasise that the existence of a matching is not shown by this argument, only a limitation on such an inner solution.

3.2.3 Summary of matching outcomes

The results in this section can be summarised as follows. When the cross-sectional area of the film is less than A_{crit}, steady-state solutions without shocks may exist for any range of ζ, α_u. When the cross-sectional area of the film exceeds A_{crit}, then for parameter values

- $\alpha_u = 0$, $\zeta = 0$: Steady-state solutions with shocks anywhere in $0 < \theta < \pi$ can exist.
- $\frac{\alpha_u^3}{\zeta} = O(1)$: Surface tensions dominates or balances droplet momentum. Steady-state solutions with smoothed shocks can exist, rising shocks having an oscillating matching and falling shocks having a monotonic matching. Various possibilities are illustrated in figure 3.5, but we will see later that only the single rising shocks in the lower quadrant $0 < \theta < \pi/2$ are likely to be stable.
- $\frac{\zeta}{\alpha_u^3} \ll 1$: Droplet momentum dominates surface tension. Steady-state solutions with smoothed shocks in upper quadrant $\pi/2 < \theta < \pi$ can exist. We will see later that such solutions are likely to be unstable, so are not physically sustainable.

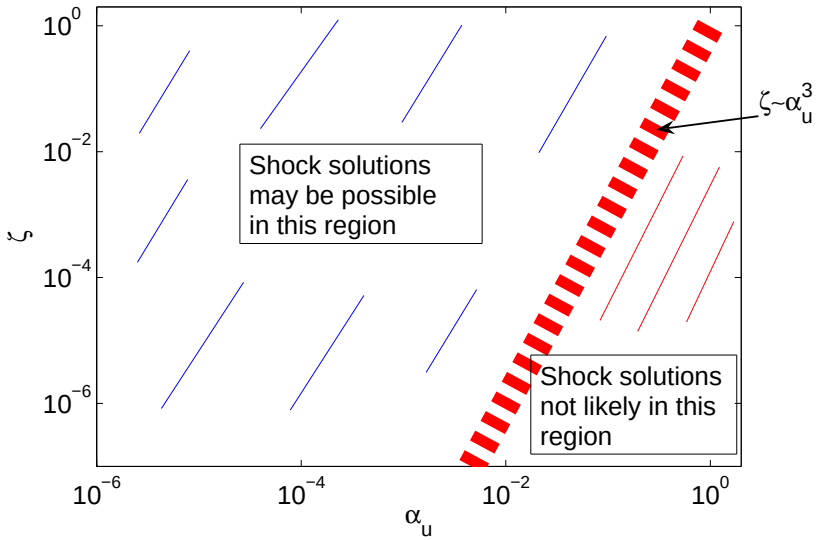

Figure 3.6: ζ, α_u parameter space where steady solutions are indicated by asymptotic matching when $A > A_{crit} = 3.951$.

The regions of parameters where shock solutions are likely to be possible are illustrated in figure 3.6.

3.3 Numerical solutions using a steady-state solver

An exact solution exists for (3.2) in the case of $\zeta, \alpha_u = 0$, and the matching argument of §3.2 gives an indication of which smoothed shock solutions may exist for $A > A_{crit}$ when $\zeta, \alpha_u > 0$. But for full solutions of (3.2) we turn to a numerical method. We use two approaches, first a steady-state solver and then a transient method; the method and results of each are described below.

3.3.1 Steady-state solver

One numerical approach is to use a steady-state solver, based on the Matlab ODE solver `bvp4c`. The solver finds solutions to (3.2), when $\frac{\partial h}{\partial t} = 0$, using the specified parameters ζ, α_u, close to some initial guess. However this approach does not conserve A, the cross-sectional area of the film, and we will see that this limits its usefulness.

Equation (3.2) is rearranged in terms of the highest derivative,

$$\frac{\partial^3 h}{\partial \theta^3} = \frac{3}{\zeta h^3}\left(q + \frac{h^3}{3}\sin(\theta) - \left(1 + \alpha_u \frac{\partial h}{\partial \theta}\right)\frac{h^2}{2}\right) - \frac{\partial h}{\partial \theta}.$$

Writing $H_1 = h(\theta)$, the 3rd order ODE is then expressed in terms of an equivalent

system of 3 first-order equations,

$$\begin{aligned} H_1' =& H_2, \\ H_2' =& H_3, \\ H_3' =& H_1''' = \frac{3}{\zeta H_1^3}\left(q + \frac{H_1^3}{3}\sin(\theta) - (1+\alpha_u H_2)\frac{H_1^2}{2}\right) - H_2. \end{aligned}$$

The solution must satisfy the periodic boundary conditions,

$$H_i(-\pi) = H_i(\pi), \quad i = 1 \ldots 3.$$

This system is then passed to the Matlab boundary-value problem solver `bvp4c`. This is a finite-difference code that implements the 3-stage Lobatto IIIa formula [42]. The collocation technique uses a mesh of points to divide the interval of integration into sub-intervals. We provide the points of the first mesh as well as an initial guess for the solution at these mesh points. The solver determines a continuous function that is a cubic polynomial on each subinterval, and a fourth order approximation to the exact solution. The solver then estimates the error of the numerical solution on each subinterval. If the solution does not satisfy the tolerance criteria, the solver adapts the mesh and repeats the process. Mesh points are added where residuals are high and removed where they are low in order to optimise the efficiency of the calculation. Afterwards, the Matlab tool `deval` can be used to find the solution values at some fixed points rather than the mesh generated. This makes use of the polynomial information, so is more accurate than linear interpolation.

The choice of initial guess determines which solution the solver will pick up. H_1, the initial guess for the solver is provided by the solution to (3.3), and H_2, H_3 are set to the derivatives of H_1, found by applying central difference formulae. A shock solution can also be specified as an initial guess.

3.3.2 Testing of solver

a) Mesh refinement

Testing was carried out to see how fine the initial mesh needed to be. Because `bvp4c` carries out adaptive mesh refinement, it is not necessary to provide a particularly fine initial mesh. As figure 3.7 shows, the mesh spacing just needs to be sufficiently small that the initial solution contains the shock. However it was found that the mesh should be chosen to have an odd number of points, to avoid points where a singularity is possible, such as $\theta = 0$. S=155 is sufficient and used subsequently.

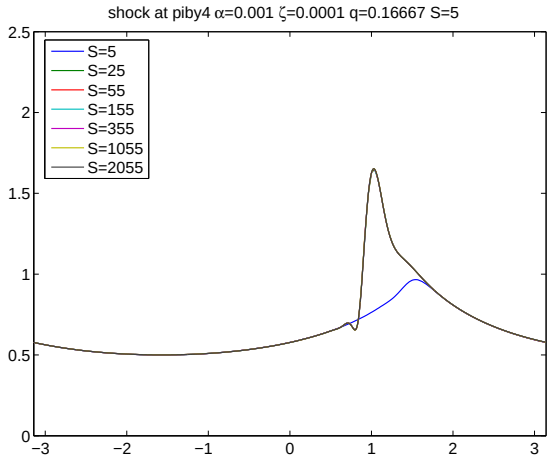

Figure 3.7: Film profile resulting from initial mesh spacing from S=5 to S=2055. All results apart from $S = 5$ are indistinguishable.

b) Initial shock position

Another test was to vary the position of the shock in the initial solution. Figure 3.8(i) shows the range of initial shock positions used, and figures 3.8(ii) and (iii) show the steady solutions found using those initial positions. In figure 3.8(ii), $\alpha_u = 10^{-3}$ and $\zeta = 10^{-4}$. This is within the range predicted by the matching argument to allow shocks in $0 < \theta < \pi/2$ only. This may explain why the results $\theta_K = 1.8, 1.9, 2.0$ have a shock in $0 < \theta < \pi/2$ rather than than $\pi/2 < \theta < \pi$. However there is surprisingly little correspondence between the initial shock position and the output. A is not conserved during the calculation, and the solution converges on one of five possible outputs, with results 0.7–0.9 1.0–1.1, 1.2–1.3, 1.4–1.7 and 1.8–2.0 being indistinguishable. It is not clear why the intermediate solutions are not found. Figure 3.8(iii) shows similar results for $\alpha_u = 10^{-5}$ and $\zeta = 10^{-4}$. These parameters are again within the range predicted by the matching argument to allow shocks in $0 < \theta < \pi/2$ only. In this case, some of the simulations failed to run, as indicated by (J) or (D) on the key.[3] Again, the result for $\theta_K = 2.0$ shows a shock in $0 < \theta < \pi/2$ rather than near the initial shock position.

[3] `bvp4c` failure exit codes, (J) singular Jacobian, (D) divergent solution.

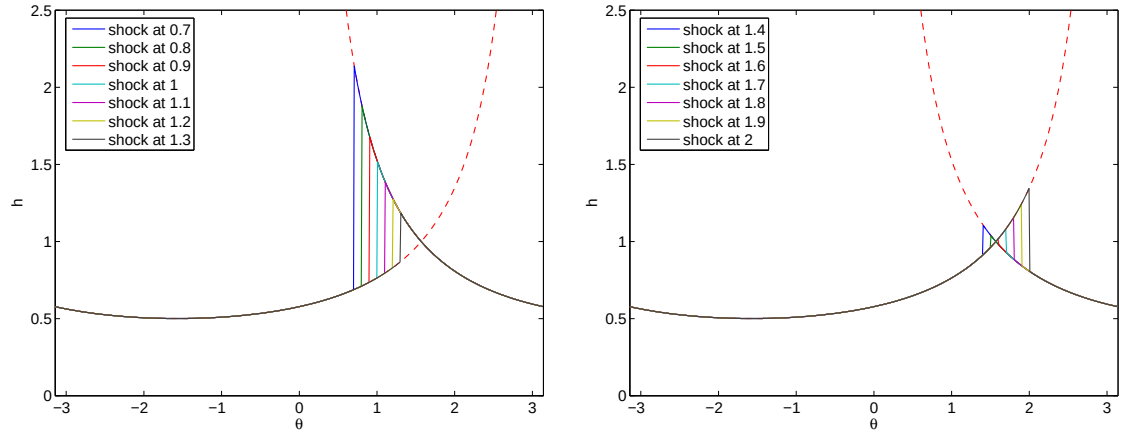

(i) Shock positions of initial solution

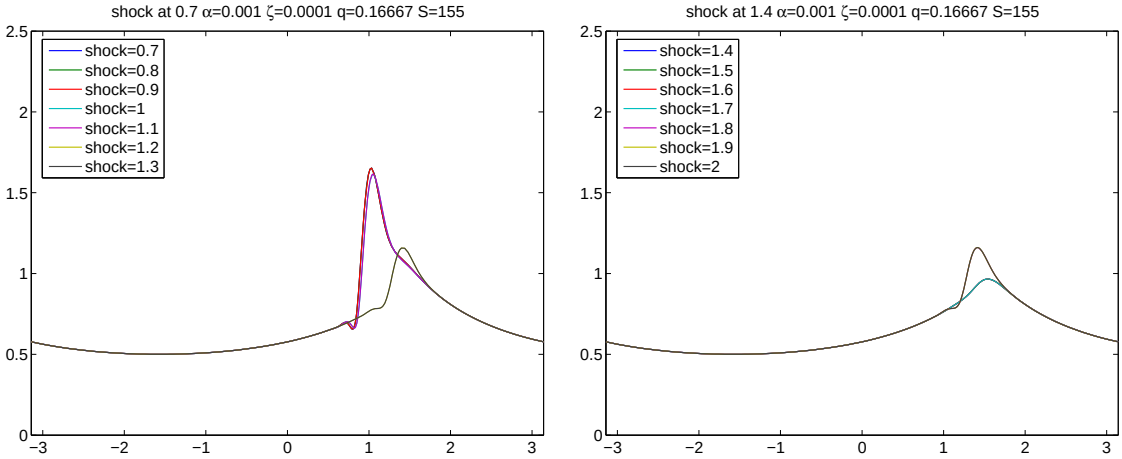

(ii) Resulting film profiles for $\alpha_u = 10^{-3}$, $\zeta = 10^{-4}$

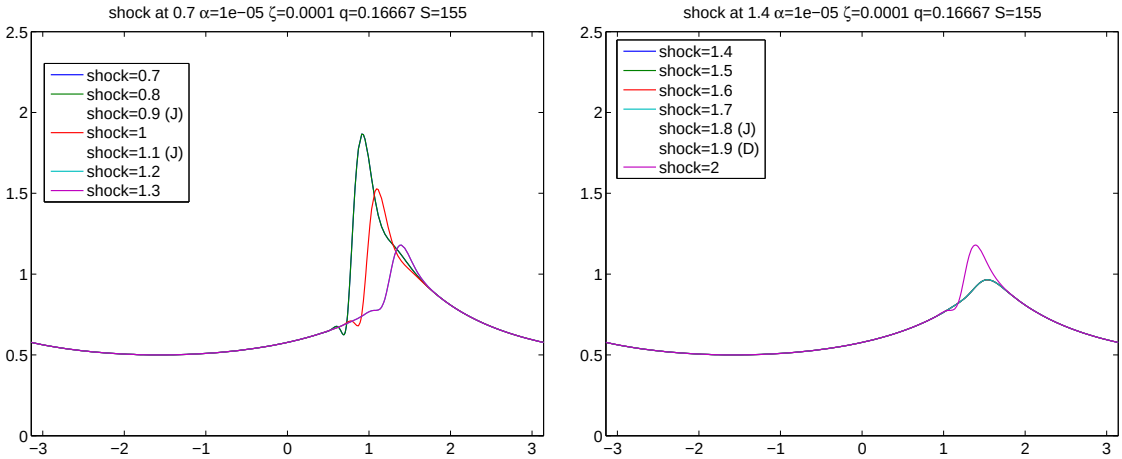

(iii) Resulting film profiles for $\alpha_u = 10^{-5}$, $\zeta = 10^{-4}$

Figure 3.8: Film profiles resulting from the steady-state solver, effect of initial shock position θ_K. First column, $\theta_K = 0.7, \ldots, 1.3$, second column $\theta_K = 1.4, \ldots, 2.0$

3.3.3 Results from steady-state solver

a) Effect of surface tension ζ

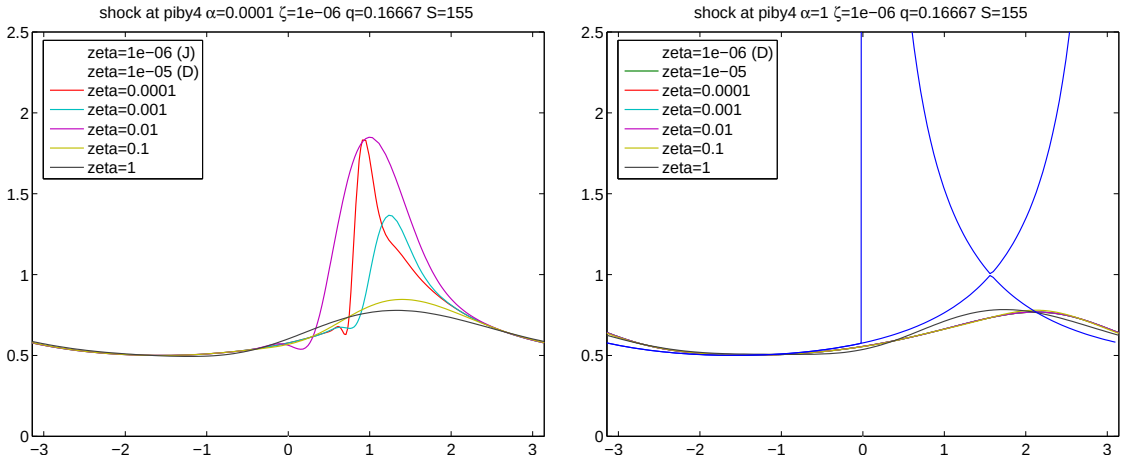

(i) (ii)

Figure 3.9: Effect of varying ζ using steady-state solver. (i) $\alpha_u = 10^{-4}$, (ii) $\alpha_u = 1$. Initial shock was at $\theta_K = \pi/4$, with $A = 4.382$, but A is not conserved.

Figure 3.9 shows the effect of varying the surface tension parameter ζ, with (i) $\alpha_u = 10^{-4}$ and (ii) $\alpha_u = 1$. In each case the initial guess was the solution to the cubic with shock at $\theta_K = \pi/4$, as illustrated in figure 3.2(i).

In case (i), with $\alpha_u = 10^{-4}$, it can be seen that increasing ζ tends to damp down the shock. For $\zeta = 10^{-4}$ the solver selects a film profile with a steep shock, and less steep profiles for increasing ζ. A, the area of the film is not conserved, and for larger ζ the solver selects film profiles with lower area.

In case (ii), with $\alpha_u = 1$ the solver selects solutions with $A < A_{crit}$ for all values of ζ used. This is consistent with the findings of the matching argument, which predicts that there are no solutions near the initial guess of a shock at $\theta_K = \pi/4$ for $\zeta < \alpha_u^3 = 1$.

In (i), when $\zeta \leq 10^{-5}$, and in (ii) when $\zeta = 10^{-6}$, the code does not successfully converge.

b) Effect of azimuthal droplet momentum α_u

Figure 3.10 shows the effect of varying the azimuthal droplet momentum, α_u. The initial shock position is at $\theta_K = \pi/4$ and $\zeta = 10^{-4}$. Varying α_u has a less significant effect than varying ζ, with the solver selecting almost identical film profiles. A solution with slightly smaller area was found for $\alpha_u = 10^{-3}$ than for $\alpha_u \leq 10^{-4}$. The code was found not to converge for $\alpha_u = 0.01$ or $\alpha_u = 0.05$, perhaps consistent with the matching analysis,

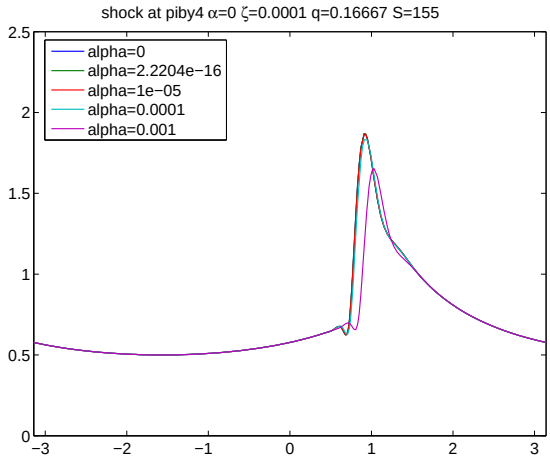

Figure 3.10: Effect of varying α_u. $\alpha_u = 0.01, 0.05$ failed. The initial shock is at $\pi/4 \approx 0.79$.

which indicates that a rising shock cannot be matched for $\alpha_u > \zeta^{1/3} = 0.046$.

c) Comparison across α_u, ζ

The steady-state solver was then applied for a range of α_u and ζ values, for various initial shock positions θ_K. Figure 3.11 summarises these results in a parameter map, where $\circ$ indicates that the solver converged on a solution where there was some correspondence to the initial shock, in the manner of figure 3.10, and $\times$ indicates that the solver failed to converge. Where the solver fails, it may be because the solution diverges or because the Jacobian becomes singular. It failed for the full range of α_u when $\zeta = 10^{-9}, 10^{-12}$. $\zeta = 0$ was also tried and it failed in all cases for $\alpha_u < 0.1$ and succeeded for $\alpha_u = 0.1, 1$. The successful solutions for $\zeta = 0$ looked similar to those for $\zeta = 10^{-6}$. Points marked $\diamond$ on the map indicate that the solver converges on a solution with $A < A_{crit}$, similar to those in figure 3.9(ii). All of the solutions that converged in the range $\zeta > \alpha_u^3$ were of this form.

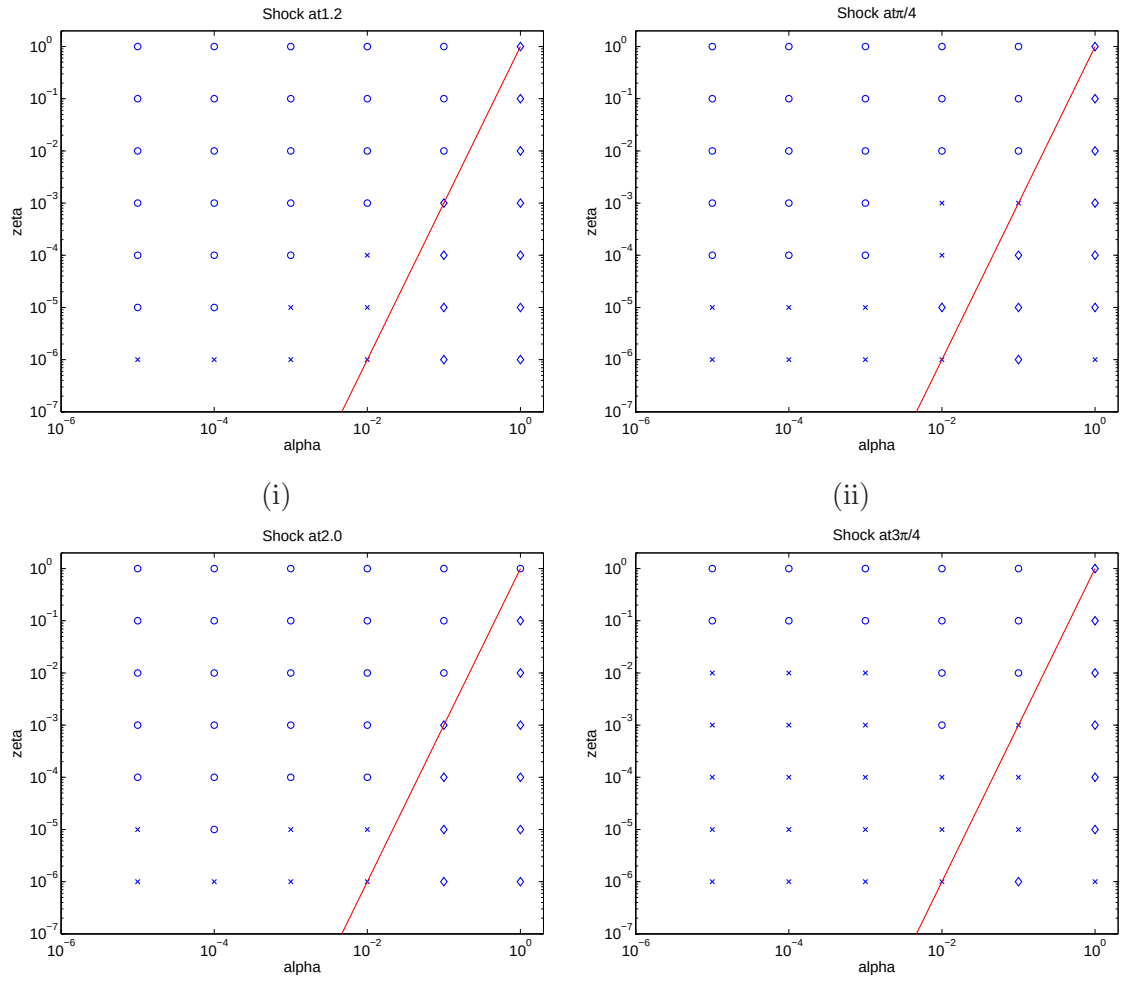

Figure 3.11: Parameter map of α_u and ζ values for which the steady-state solver returns a solution. Initial shock at (i)1.2, (ii) $\pi/4$, (iii) 2.0, (iv) $3\pi/4$. $\circ$ solution with shock in $0 < \theta_K < \pi/2$, $\diamond$ low-area solution, $A < A_{crit}$, $\times$ no solution. — line is $\zeta = \alpha_u^3$.

3.4 Numerical solutions from a transient solver

A disadvantage of the steady-state solver is that it does not conserve A, which is a measure of the mass in the system, and thus any one of a family of solutions may be found, depending on the initial guess. This gives insight into possible solutions but it is difficult to draw meaningful conclusions about the results for *fixed* areas. We also found that the solver often failed to converge in cases where ζ was small.

A more versatile approach was to develop a full transient solver, and seek steady solutions by looking for convergence through time. We again used the powerful solver `bvp4c`, as part of a timestepping simulation.

3.4.1 Method using transient solver

Equation (3.2) is discretised in time using a fully-implicit backward-time difference scheme as

$$\frac{h(\theta,t+\delta t)-h(\theta,t)}{\delta t}+\frac{\partial q}{\partial\theta}(\theta,t+\delta t)=0. \tag{3.30}$$

Writing $h_j(\theta)=h(\theta,t)$, $h_{j+1}(\theta)=h(\theta,t+\delta t)$, $q_j(\theta)=q(\theta,t)$ etc, then

$$\frac{h_{j+1}-h_j}{\delta t}+\frac{\mathrm{d}q_{j+1}}{\mathrm{d}\theta}=0. \tag{3.31}$$

Substituting from (3.2)

$$\frac{\mathrm{d}q_{j+1}}{\mathrm{d}\theta}=\frac{\mathrm{d}}{\mathrm{d}\theta}\left(\zeta\frac{h_{j+1}^3}{3}\left(\frac{\mathrm{d}^3h_{j+1}}{\mathrm{d}\theta^3}+\frac{\mathrm{d}h_{j+1}}{\mathrm{d}\theta}\right)-\frac{h_{j+1}^3}{3}\sin\theta+\left(1+\alpha_u\frac{\mathrm{d}h_{j+1}}{\mathrm{d}\theta}\right)\frac{h_{j+1}^2}{2}\right). \tag{3.32}$$

Rearranging (3.31) and (3.32) to express in terms of the highest derivative:

$$\begin{aligned}\frac{\mathrm{d}^4h_{j+1}}{\mathrm{d}\theta^4}=-\frac{\mathrm{d}^2h_{j+1}}{\mathrm{d}\theta^2}+\frac{3}{\zeta h_{j+1}^3}\Bigg(&-\zeta h_{j+1}^2\frac{\mathrm{d}h_{j+1}}{\mathrm{d}\theta}\left(\frac{\mathrm{d}^3h_{j+1}}{\mathrm{d}\theta^3}+\frac{\mathrm{d}h_{j+1}}{\mathrm{d}\theta}\right)+h_{j+1}^2\frac{\mathrm{d}h_{j+1}}{\mathrm{d}\theta}\sin\theta\\&+\frac{h_{j+1}^3}{3}\cos\theta-\left(\alpha_u\frac{\mathrm{d}^2h_{j+1}}{\mathrm{d}\theta^2}\right)\frac{h_{j+1}^2}{2}\\&-\left(1+\alpha_u\frac{\mathrm{d}h_{j+1}}{\mathrm{d}\theta}\right)h_{j+1}\frac{\mathrm{d}h_{j+1}}{\mathrm{d}\theta}-\frac{h_{j+1}-h_j}{\delta t}\Bigg).\end{aligned} \tag{3.33}$$

Writing $H_1(\theta)=h_{j+1}$, $H_n=H'_{n-1}$, the 4th order ODE (3.33) can be expressed in terms

of an equivalent set of four first-order equations:

$$\begin{aligned}
H_1' &= H_2, \\
H_2' &= H_1'' = H_3, \\
H_3' &= H_1^{(3)} = H_4, \\
H_4' &= H_1^{(4)} = -H_3 + \frac{3}{\zeta H_1^3}\Bigg(- \zeta H_1^2 H_2 \left(H_4 + H_2\right) + H_1^2 H_2 \sin\theta \\
&\qquad + \frac{H_1^3}{3}\cos\theta - \left(\alpha_u H_3\right)\frac{H_1^2}{2} \\
&\qquad - \left(1 + \alpha_u H_2\right) H_1 H_2 - \frac{H_1 - h_j}{\delta t}\Bigg).
\end{aligned} \tag{3.34}$$

In the calculation of the $(j+1)th$ timestep, h_j is provided by the jth timestep (or the initial condition, for the first timestep).

The solution must satisfy the periodic boundary conditions, that h_{j+1} and its derivatives are continuous on the ends of the domain, i.e.

$$H_i(-\pi) = H_i(\pi), \quad i = 1 \ldots 4. \tag{3.35}$$

This system is then passed to the Matlab boundary-value problem solver `bvp4c`. At each timestep, the first mesh and an approximation for the solution at these mesh points is based on the result at the previous timestep. The solver determines a continuous function as an approximation to the exact solution. If this function does not satisfy the tolerance criteria, the solver adapts the mesh and repeats the process. Once the tolerance criteria are satisfied, the solver moves on to the next timestep.

In principle, the initial film profile may be arbitrarily specified. A uniform height is the easiest way to impose a specific value of A; a cubic solution with a shock imposed near the expected location is sometimes used. Continuation from a smooth solution found for another parameter set reduces the time to compute the steady-state solution from that starting from a uniform or shock solution; in some cases it may allow us to find solutions which would be numerically unstable from a different starting point. We check that A is conserved through time using the trapezoidal rule, which is accurate up to $O(\delta\theta^3)$.

A timestep of $\delta t = 0.1$ was found to provide sufficient accuracy in most cases. The simulation is terminated and a steady solution assumed to be reached when the maximum change in h between one timestep and the next is less than 0.001.

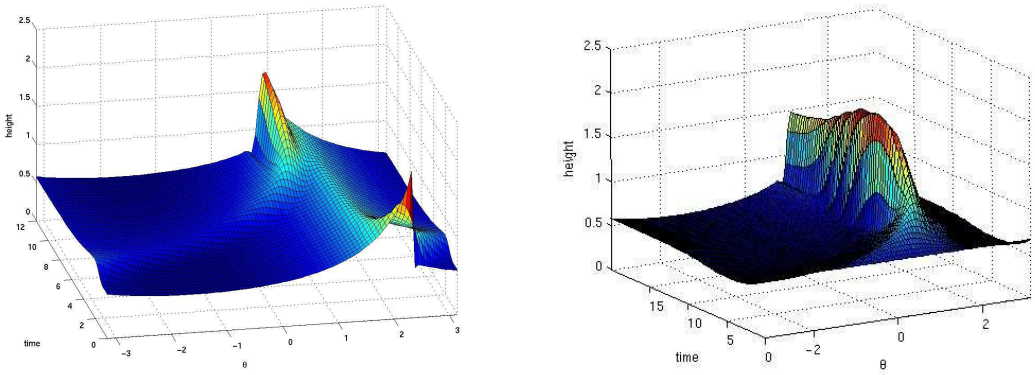

(i) (ii)

Figure 3.12: Evolution of the film. $\zeta = 10^{-3}$, $\alpha_u = 10^{-3}$, $A = 4.382$. Initial condition (i) shock at $3\pi/4$ (ii) uniform.

3.4.2 Results from transient solver

Figure 3.12 shows two typical examples of the evolution of the film through time. In (i) an initial condition is imposed with a shock in the upper quadrant, at $\theta_K = 3\pi/4$. This solution is not stable, and the excess fluid moves around the cylinder and builds a peak at about $\pi/4$. The solution is approaching a stable steady state with a shock in the lower quadrant. In (ii) the initial film profile is uniform, also with $A = 4.382$. A peak rapidly develops, with the same shock at $\pi/4$. In both cases, once this solution with a shock in $0 < \theta < \pi/2$ is reached it is stable and remains if the timestepper is continued.

a) Parameter map of steady solutions

The transient code is useful in finding steady solutions, and because it preserves A, we can find a set of steady solutions for different ζ, α_u, but fixed cross-sectional area. Steady solutions have been found at the positions indicated in Figure 3.13 for $A = 4.382$, the area are equivalent to a solution for $\zeta, \alpha_u = 0$ with shock at $\pi/4$. Almost identical plots were obtained for $A = 4.044$ and $A = 3.951$, equivalent to a shock at $\pi/4$, and the critical area with no shock respectively. The agreement with the indication of the asymptotic matching is excellent, although solutions close to the $\zeta = \alpha_u^3$ cut-off are difficult to find and require continuation from nearby solutions. For $\zeta < \alpha_u^3$ the matching does predict shocks in the upper quadrant but as we will see later, kinematic wave theory suggests these will be unstable, so it is unsurprising that our numerical code does not find them.

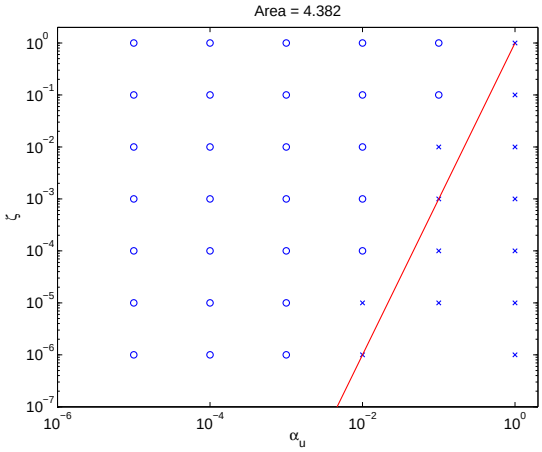

Figure 3.13: ζ, α_u parameter space where steady solutions have been found using the transient solver, with $A = 4.382$. Points marked $\circ$ converged steady solutions, $\times$ failed to find steady solution. Solid line — is $\zeta = \alpha_u^3$, the cut-off predicted by asymptotic matching.

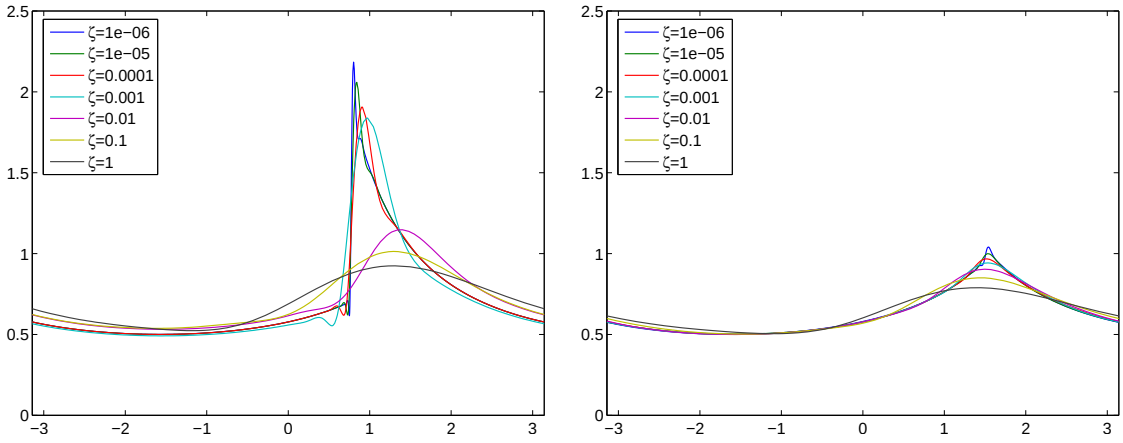

(i) (ii)

Figure 3.14: Effect of increasing surface tension. Other parameters are $\alpha_u = 10^{-3}$ and (i) $A = 4.382$, (ii) $A = 3.951$

b) Effect of surface tension ζ

Figure 3.14 shows the effect of varying the surface tension, for two different values of A, equivalent to a vertical cut through the map of figure 3.13. The strong smoothing effect of surface tension can be seen in both examples. In figure 3.14(i) $A = 4.382$, an area equivalent to that of the cubic solution with shock at $\pi/4$. When surface tension is small, $\zeta = 10^{-6}$, the resulting profile is close to that of the cubic shock solution. Note the small capillary wave at the foot of the shock. As ζ increases, the shock is levelled, with the excess mass being spread around the cylinder, mostly in $0 < \theta < \pi$, until for $\zeta = 1$ only a smooth thickening in the ascending quadrant occurs.

In figure 3.14(ii), $A = 3.951$, equivalent to the cubic solution with no shock. Again, $\zeta = 10^{-6}$ is very close to the $\zeta = 0$ solution, although there is a slight capillary wave and smoothing of the corner is still discernable. With larger ζ, mass is redistributed upstream, in $0 < \theta < \pi/2$.

c) Effect of azimuthal droplet momentum.

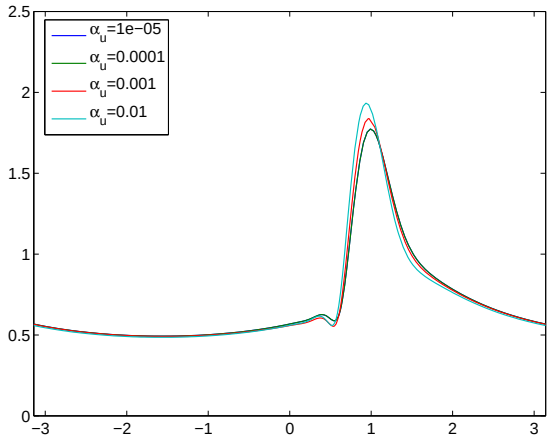

Figure 3.15: Effect of increasing α_u. Other parameters are $\zeta = 10^{-3}$, $A = 4.382$.

Figure 3.15 shows the effect of varying azimuthal droplet momentum α_u. This is equivalent to a horizontal cut through the map of figure 3.13. Increasing α_u has little quantitative effect on the film profile, only a slight steepening of the shock, until we reach the cut-off of $\alpha_u^3 = \zeta$ predicted by the matching argument. At this point the destabilising effect of α_u is too large, and no steady solutions are sustained.

d) Effect of cross-sectional area A

Figure 3.16 shows the effect of increasing the cross-sectional area A. A steady-state film can be found with $A = 1.0$, for which the profile is almost uniform. For increased area, the profile develops a bulge around $\theta = \pi/2$, until it achieves the critical film profile at around $A = 3.951$. Any further increase in area is incorporated with an ascending shock in $0 < \theta < \pi/2$, as illustrated here with $A = 5.0$. The shock has a slight capillary wave at its base.

Figure 3.17 shows the effect of increasing A, the cross-sectional area of the film, beyond the critical value $A = 3.951$. In figure 3.17(i), $\zeta = 10^{-6}$ and $\alpha_u = 10^{-5}$, both effects are very small. The resulting film profiles are close to the shock solutions of (3.3), apart from a slight overshoot at the top of the peak and capillary wave at the foot. In

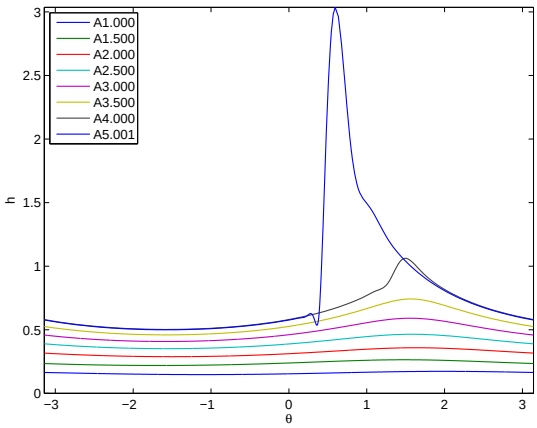

Figure 3.16: Film profile h for various A. Other parameters are $\zeta = 10^{-4}$, $\alpha_u = 10^{-3}$.

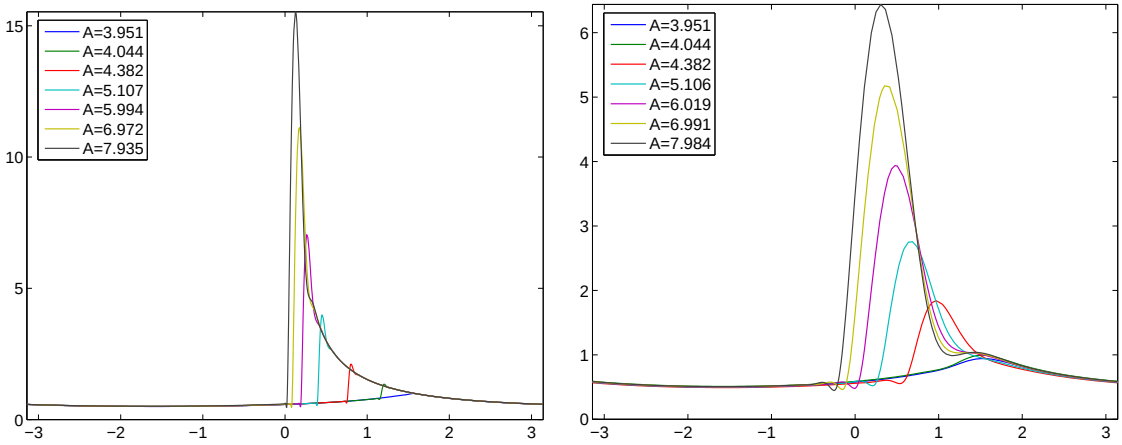

(i) (ii)

Figure 3.17: Effect of increasing A. Other parameters are (i) $\zeta = 10^{-6}$, $\alpha_u = 10^{-5}$, (ii) $\zeta = 10^{-3}$, $\alpha_u = 10^{-3}$.

figure 3.17(ii), $\zeta = 10^{-3}$ and $\alpha_u = 10^{-3}$, still within the limit $\alpha_u^3 < \zeta$. With these values the shocks are smoothed considerably.

3.5 Stability of solutions

In §3.3 and §3.4 we have found various steady solutions to (3.2), the height of a film driven by droplet momentum. In §3.3 they have been found using a steady state solver; in §3.4 using the transient solver. It is expected that those found by the transient code solver are stable, as the method involves waiting for a transient solution to become steady. But in order to confirm this, an analysis of stability was undertaken, and this returned some curious results. In this section we will firstly use the transient solver to follow the evolution of perturbations to some of the steady solutions found. We will

then use analytical methods to look at stability in the case $\zeta, \alpha_u = 0$, then turn to a numerical approach for the general case.

3.5.1 Evolution of a perturbation to a steady-state solution

If a steady solution is linearly stable, then a small perturbation applied to it (without adding any mass) will decay to zero as the transient solution evolves, i.e. the solution will return to its original form. If the solution is unstable, then the perturbation will grow. Restricting the perturbation to not add or subtract any mass from the system will permit decay back to the initial solution.

For example, consider adding a perturbation of the form of a single sine wave centred on p, with width w and amplitude a, so

$$pert = \begin{cases} a \sin\left(2\pi \frac{\theta - p}{w}\right), & p - \frac{w}{2} < \theta < p + \frac{w}{2} \\ 0, & \text{otherwise,} \end{cases}$$

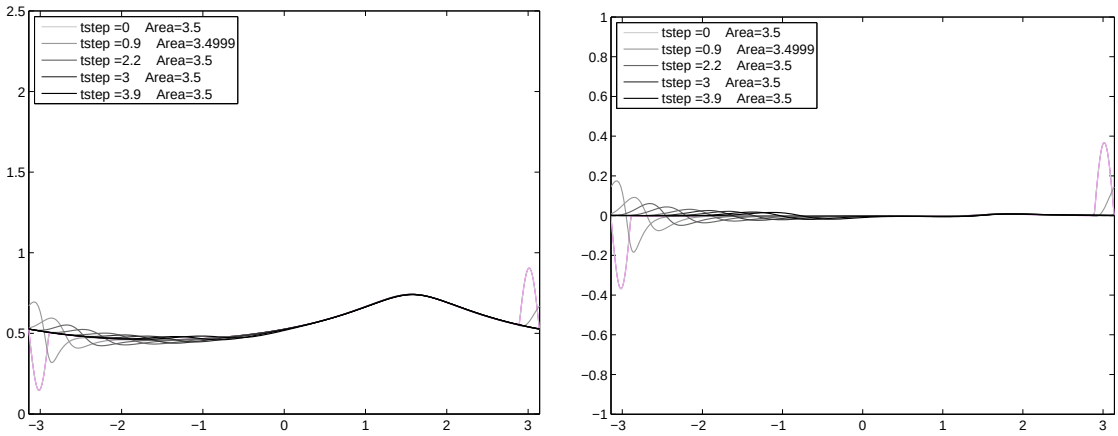

(i) (ii)

Figure 3.18: Evolution of a stable film profile with a zero-mass perturbation. (i) Film profile, (ii) perturbation. Parameters $\zeta = 10^{-4}$, $\alpha_u = 10^{-3}$, $A = 3.5$.

Figure 3.18 shows the evolution of such a perturbation applied to the stable steady solution h_s found when $\zeta = 10^{-4}$, $\alpha_u = 10^{-3}$ and $A = 3.5$. The perturbation is centred at $p = \pi$; $w = 0.5$ and $a = 0.8 \min(h_s)$. Figure 3.18(i) shows the film profile, including the perturbation, whilst (ii) shows just the perturbation, by plotting the difference between the current and final timesteps. The perturbation adds no mass, and decays to leave the original solution. For clarity, only the first few timesteps are illustrated here.

Figure 3.19 illustrates an example where a small perturbation does not decay, but causes further oscillations in the steady solution which then cause the transient solver to break

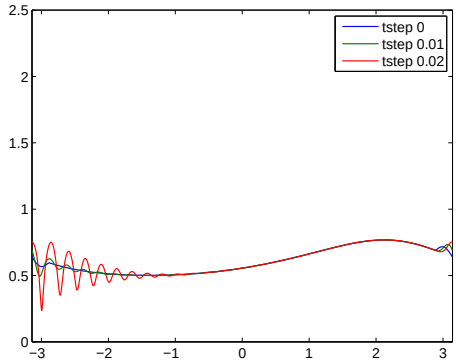

Figure 3.19: Evolution of an unstable film profile with a small perturbation. Parameters $\zeta = 10^{-5}$, $\alpha_u = 1$, $A = 3.951$. Perturbation has $p = \pi$, $w = 0.5$, $a = 0.8\min(h_s)$.

down. In this case the base solution, with parameters $\zeta = 10^{-5}$, $\alpha_u = 1$, is unstable. The initial film profile was found using the steady-state solver, but could not be found with the transient solver. This is in the parameter range $\zeta < \alpha_u^3$, and is an example where only solutions with $A < A_{crit}$ were found.

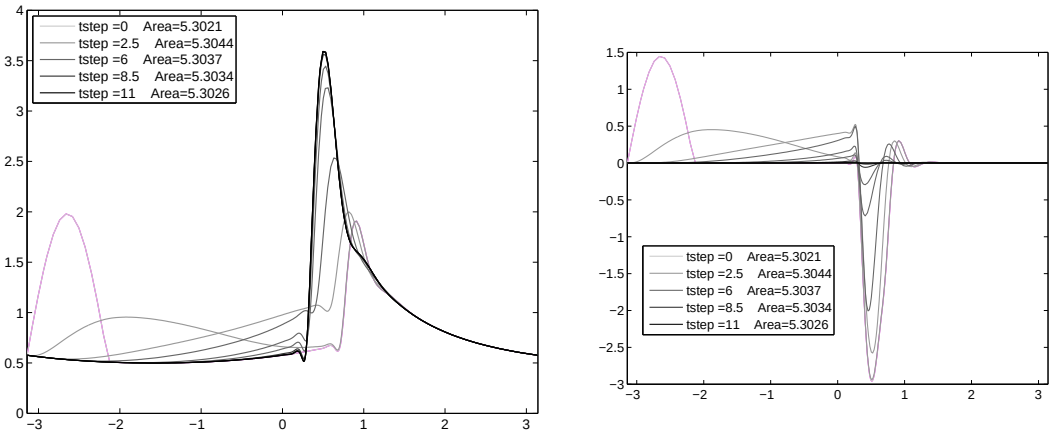

Figure 3.20: Evolution of a perturbation to a steady-state solution ($A = 4.382$) which adds mass, moving it to a new steady state ($A = 5.302$). Parameters $\zeta = 10^{-4}$, $\alpha_u = 10^{-3}$. (i) Film profile, (ii) perturbation.

If the perturbation to the film adds or subtracts mass, then it cannot decay to leave the original solution, but the film profile may evolve to a solution nearby the original. For example, figure 3.20 shows the effect of adding a substantial mass to a steady-state solution, using a perturbation of the form

$$pert = \begin{cases} a\sin\left(2\pi\frac{\theta+\pi}{w}\right), & -\pi < \theta < -\pi + \frac{w}{2} \\ 0, & \text{otherwise.} \end{cases}$$

The original profile has $A = 4.382$, and therefore a shock near $\theta = \pi/4$. The additional

mass is in the form of half a sine wave with $a = 1.45$, $w = 2$ and $p = -\pi$. As the profile evolves with time, the extra mass spreads through $\theta = 0$ — falling down the left hand side of the cylinder — and then joins the existing shock. The shock grows in size, the front moving down the cylinder towards $\theta = 0$. The back of the shock, the smooth profile through $\theta = \pi/2$, is unaffected as a new shock front develops.

3.5.2 Linear stability using eigenvalue analysis

Studying the evolution of a single perturbation is a useful demonstration of stability, but to prove that a steady solution h_s of (3.2) is linearly stable we must show that *all* small perturbations decay. We will use a linear analysis to investigate the growth of a general small perturbation $h = h_s(\theta) + \xi(\theta, t)$. Neglecting non-linear terms in ξ, (3.2) leads[4] to

$$\begin{aligned}\frac{\partial \xi}{\partial t} + \frac{\partial}{\partial \theta}\Bigg[&\left(\zeta h_s^2\left(\frac{\mathrm{d}^3 h_s}{\mathrm{d}\theta^3} + \frac{\mathrm{d}h_s}{\mathrm{d}\theta}\right) - h_s^2 \sin\theta + \left(\mathrm{sign}(\alpha_u) + |\alpha_u|\frac{\mathrm{d}h_s}{\mathrm{d}\theta}\right) h_s\right)\xi \\ &+ \left(|\alpha_u|\frac{h_s^2}{2} + \zeta\frac{h_s^3}{3}\right)\frac{\mathrm{d}\xi}{\mathrm{d}\theta} + \left(\zeta\frac{h_s^3}{3}\right)\frac{\mathrm{d}^3\xi}{\mathrm{d}\theta^3}\Bigg] = 0.\end{aligned} \tag{3.36}$$

We will consider perturbations of the form $\xi = \eta(\theta)e^{\sigma t}$, where η is 2π-periodic and σ complex, leading to a 4th order ODE in η:

$$\begin{aligned}-\sigma\eta = &\left(\zeta 2h_s\frac{\partial h_s}{\partial\theta}\left(\frac{\partial^3 h_s}{\partial\theta^3} + \frac{\partial h_s}{\partial\theta}\right) + \zeta h_s^2\left(\frac{\partial^4 h_s}{\partial\theta^4} + \frac{\partial^2 h_s}{\partial\theta^2}\right) - 2h_s\frac{\partial h_s}{\partial\theta}\sin\theta - h_s^2\cos\theta\right. \\ &\left. + \left(1 + \alpha_u\frac{\partial h_s}{\partial\theta}\right)\frac{\partial h_s}{\partial\theta} + \left(\alpha_u\frac{\partial^2 h_s}{\partial\theta^2}\right)h_s\right)\eta \\ &+ \left(\zeta h_s^2\left(\frac{\partial^3 h_s}{\partial\theta^3} + 2\frac{\partial h_s}{\partial\theta}\right) - h_s^2\sin\theta + \left(1 + 2\alpha_u\frac{\partial h_s}{\partial\theta}\right)h_s\right)\frac{\mathrm{d}\eta}{\mathrm{d}\theta} \\ &+ \left(\alpha_u\frac{h_s^2}{2} + \zeta\frac{h_s^3}{3}\right)\frac{\mathrm{d}^2\eta}{\mathrm{d}\theta^2} + \zeta h_s^2\frac{\partial h_s}{\partial\theta}\frac{\mathrm{d}^3\eta}{\mathrm{d}\theta^3} + \zeta\frac{h_s^3}{3}\frac{\mathrm{d}^4\eta}{\mathrm{d}\theta^4}.\end{aligned} \tag{3.37}$$

Examining the possible forms of σ in (3.37) reveals the nature of the time-dependent behaviour, thus whether the perturbation grows, decays, is unchanging or oscillates in the long term.

[4] See Appendix E for details

3.5.3 Stability of the leading order equation, $\zeta, \alpha_u = 0$, $q < 1/6$

A simplified analysis is available when $\zeta, \alpha_u = 0$, and $q < 1/6$. Equation (3.37) reduces to

$$\sigma\eta + \frac{\mathrm{d}}{\mathrm{d}\theta}\left(-h_s^2\eta\sin\theta + h_s\eta\right) = 0,$$

which can be rearranged to give

$$-\frac{\frac{\mathrm{d}\eta}{\mathrm{d}\theta}}{\eta} = \frac{\frac{\mathrm{d}}{\mathrm{d}\theta}\left(-h_s^2\sin\theta + h_s\right) + \sigma}{\left(-h_s^2\sin\theta + h_s\right)}.$$

Integrating:

$$-\ln\eta = \ln\left(-h_s^2\sin\theta + h_s\right) + \sigma\int^{\theta}\frac{\mathrm{d}\theta}{\left(-h_s^2\sin\theta + h_s\right)} + const,$$

i.e.

$$\eta(\theta) = \frac{const}{\left(-h_s^2\sin\theta + h_s\right)}e^{-\sigma\int^{\theta}\frac{\mathrm{d}\theta}{\left(-h_s^2\sin\theta + h_s\right)}}. \tag{3.38}$$

We avoid $q = 1/6$, because at the corner at $\theta = \pi$, $h_s = 1$ and (3.38) is undefined.

For the lower physical branch of the solution when $q < 1/6$, $h_s < 1$ and so $\left(-h_s^2\sin\theta + h_s\right) > 0$. Since h_s and $\sin\theta$ are periodic, $\int^{\theta}\frac{\mathrm{d}\theta}{\left(-h_s^2\sin\theta + h_s\right)}$ is a positive, increasing function of θ. In order that η be periodic, $\Re(\sigma) = 0$ and σ is purely imaginary. So the lower branch of h_s is neutrally stable, the perturbation is periodic with time and does not grow or decay.

For the upper branch of the solution when $q < 1/6$, $\left(-h_s^2\sin\theta + h_s\right) < 0$. So $\int^{\theta}\frac{\mathrm{d}\theta}{\left(-h_s^2\sin\theta + h_s\right)}$ is a negative function of θ. Again, in order that η be periodic, $\Re(\sigma) = 0$ and σ is purely imaginary. So the upper branch of h_s is neutrally stable, any perturbation is periodic with time and does not grow or decay.

3.5.4 Kinematic Wave Speed, $\zeta, \alpha_u = 0$

Another useful approach when $\zeta, \alpha_u = 0$ is to apply kinematic wave theory, which extends to $q = 1/6$ and the cases with shock solutions. Equation (3.36) is a convection-diffusion equation of the form

$$\frac{\partial\xi}{\partial t} + \underbrace{\frac{\partial}{\partial\theta}\left(w\xi\right)}_{\text{convection}} = \underbrace{\frac{\partial}{\partial\theta}\left(D\frac{\partial\xi}{\partial\theta}\right)}_{\text{diffusion}} - \underbrace{\frac{\partial}{\partial\theta}\left(\zeta\frac{h_s^3}{3}\frac{\partial^3\xi}{\partial\theta^3}\right)}_{\text{higher order diffusion}}, \tag{3.39}$$

where

$$w = \zeta h_s^2\left(\frac{\mathrm{d}^3 h_s}{\mathrm{d}\theta^3} + \frac{\mathrm{d}h_s}{\mathrm{d}\theta}\right) - h_s^2\sin\theta + \left(1 + \alpha_u\frac{\mathrm{d}h_s}{\mathrm{d}\theta}\right)h_s$$

and

$$D = -\left(\alpha_u\frac{h_s^2}{2} + \zeta\frac{h_s^3}{3}\right) < 0,$$

D is a negative diffusion, and always has a destabilising effect, but the higher order diffusivity term $\zeta\frac{h_s^3}{3}$ can have a stabilising effect. Without the higher order diffusivity, (3.39) is an ill-posed problem, and is unstable for all possible wavenumbers, but with it (3.39) is an almost ill-posed problem, which can be stable for some wavelengths and unstable for some others, as discussed by Hsieh and Ho [23]. Since the flux

$$q_s = \zeta\frac{h_s^3}{3}\left(\frac{\mathrm{d}^3 h_s}{\mathrm{d}\theta^3} + \frac{\mathrm{d}h_s}{\mathrm{d}\theta}\right) - \frac{h_s^3}{3}\sin\theta + \left(1 + \alpha_u\frac{\mathrm{d}h_s}{\mathrm{d}\theta}\right)h_s = const,$$

we also have that

$$w = \frac{\partial}{\partial h_s}\left(q_s\left(h_s, \frac{\mathrm{d}h_s}{\mathrm{d}\theta}, \frac{\mathrm{d}^3 h_s}{\mathrm{d}\theta^3}\right)\right).$$

When $\zeta, \alpha_u \ll 1$, (3.39) reduces to

$$\frac{\partial\xi}{\partial t} + \frac{\partial}{\partial\theta}(w\xi) = 0 \tag{3.40}$$

with the velocity of kinematic waves given by

$$w = -h_s^2\sin\theta + h_s = \frac{3q_s}{h_s} - \frac{h_s}{2}.$$

The general solution of (3.40) is given by kinematic wave theory [52] as

$$\xi(\theta, t) = \frac{1}{w(\theta)}\Lambda\left(t - \int_0^\theta \frac{\mathrm{d}s}{w(s)}\right),$$

along the characteristic curve $\chi = t - \int_0^\theta \frac{\mathrm{d}s}{w(s)}$ and corresponds to an initial perturbation of the form

$$\xi(\theta, 0) = \frac{1}{w(\theta)}\Lambda\left(-\int_0^\theta \frac{\mathrm{d}s}{w(s)}\right).$$

If there is a point where $w(\theta) = 0$, then waves are unable to travel through it and the amplitude of the kinematic wave goes to infinity, so it acts as a focus for any disturbances. Disturbances that travel towards such a point will build up and thus the solution is unstable.

Stable solutions must avoid such points. Solutions may be stable if disturbances move away from shocks, so long as they don't get to singular points (for example if they get absorbed by another shock).If a small disturbance is travelling towards a shock at θ_K, i.e.

$$\begin{aligned} & w(\theta) > 0, \quad (\theta < \theta_K), \\ \text{or} \quad & w(\theta) < 0, \quad (\theta > \theta_K), \end{aligned}$$

then the shock will absorb the disturbance.

For $\zeta, \alpha_u \ll 1$, $w < 0$ for the upper solution branch and $w > 0$ for the lower, so waves travel towards an ascending shock and away from a descending one, as sketched in

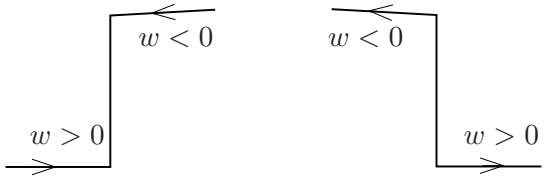

Figure 3.21: When $\zeta, \alpha_u = 0$, disturbances travel towards an ascending shock and away from a descending one.

figure 3.21. For the critical solution $q = 1/6$, the kinematic wave velocity $w = 0$ at $\theta = \pi/2$, so waves are focussed at the critical point. This makes solutions with a single shock on the lower quadrant ($0 < \theta < \pi/2$) stable, and solutions with a shock on the upper quadrant ($\pi/2 < \theta < \pi$) unstable, as illustrated in figure 3.22. Certain multiple shock solutions may also be stable, but were not seen numerically, perhaps because the single shock solutions with equivalent area were more favourable.

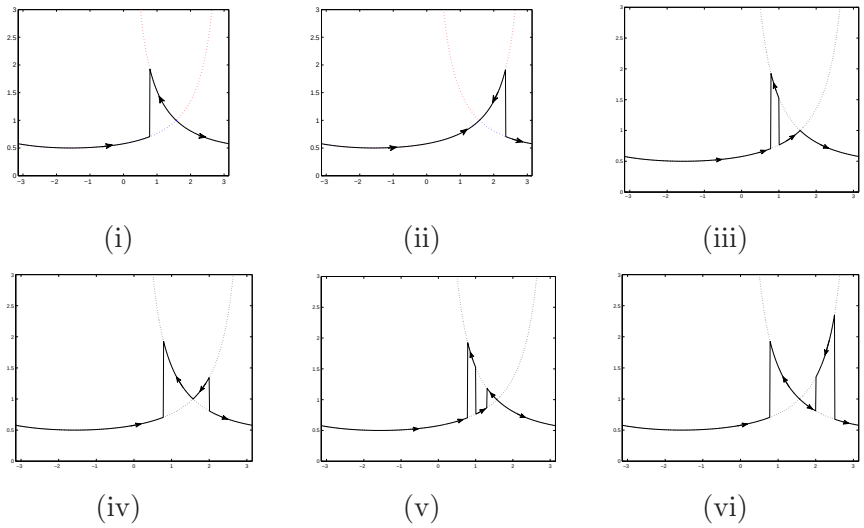

Figure 3.22: Various shock combinations. (i) stable; (ii),(iii),(iv) unstable; (v), (vi) stable according to K.W.T, but not seen in numerical solutions.

3.5.5 Numerical methods for assessing stability, $\zeta, \alpha_u > 0$

For $\alpha_u, \zeta > 0$, kinematic wave theory is not applicable, as q includes additional derivative terms, and we can find no analytical solution of (3.37), the 4th order ode in η. It would be possible to solve this numerically using the Matlab function `bvp4c` with the eigenvalue option, but this only solves for one eigenvalue at a time. So we seek to discretise η to a vector $\vec{\eta}$ and write (3.37) as a matrix equation

$$\sigma\vec{\eta} = B\vec{\eta},$$

and then find the eigenvalues σ and eigenvectors of B. Two approaches are used to find B, as described below.

a) Finite Difference Method

For the finite difference method, the equation is discretised using a central difference. The region is uniformly divided into $\theta_i = -\pi, -\pi + \delta_s, -\pi + 2\delta_s \ldots, -\pi + S\delta_s$, where $S = 2\pi/\delta_s - 1$, so that θ_i is periodic, and the ith element of $\vec{\eta}$ is $\eta_i = \eta(\theta_i)$ etc.

The steady solutions h_s have been found on non-uniform meshes. So we use `deval`, the interpolation facility of the Matlab `bvp` suite, to evaluate the piecewise polynomial which approximates the solution at the regular mesh points θ_i. It also evaluates the derivatives $\frac{\partial h_s}{\partial \theta}$ etc.

The second-order central differences are given by

$$\begin{aligned}
\frac{\partial \eta_i}{\partial \theta} &= \frac{\eta_{i+1} - \eta_{i-1}}{2\delta_s} + O(\delta_s^2), \\
\frac{\partial^2 \eta_i}{\partial \theta^2} &= \frac{\eta_{i+1} - 2\eta_i + \eta_{i-1}}{\delta_s^2} + O(\delta_s^2), \\
\frac{\partial^3 \eta_i}{\partial \theta^3} &= \frac{\eta_{i+2} - 2\eta_{i+1} + 2\eta_{i-1} - \eta_{i-2}}{2\delta_s^3} + O(\delta_s^2), \\
\frac{\partial^4 \eta_i}{\partial \theta^4} &= \frac{\eta_{i+2} - 4\eta_{i+1} + 6\eta_i - 4\eta_{i-1} + \eta_{i-2}}{\delta_s^4} + O(\delta_s^2).
\end{aligned} \tag{3.41}$$

A fourth-order scheme also used is given by

$$\begin{aligned}
\frac{\partial \eta_i}{\partial \theta} &= \frac{\eta_{i-2} - 8\eta_{i-1} + 8\eta_{i+1} - \eta_{i+2}}{12\delta}, \\
\frac{\partial^2 \eta_i}{\partial \theta^2} &= \frac{-\eta_{i-2} + 16\eta_{i-1} - 30\eta_i + 16\eta_{i+1} - \eta_{i+2}}{12\delta^2}, \\
\frac{\partial^3 \eta_i}{\partial \theta^3} &= \frac{\eta_{i-3} - 8\eta_{i-2} + 13\eta_{i-1} - 13\eta_{i+1} + 8\eta_{i+2} - \eta_{i+3}}{8\delta^3}, \\
\frac{\partial^4 \eta_i}{\partial \theta^4} &= \frac{-\eta_{i-3} + 12\eta_{i-2} - 39\eta_{i-1} + 56\eta_i - 39\eta_{i+1} + 12\eta_{i+2} - \eta_{i+3}}{6\delta^4}.
\end{aligned}$$

Substituting the second order scheme (3.41) into (3.37),

$$\begin{aligned}
\sigma\eta_i = f_0\eta_i + f_1\frac{\eta_{i+1} - \eta_{i-1}}{2\delta_s} + f_2\frac{\eta_{i+1} - 2\eta_i + \eta_{i-1}}{\delta_s^2} \\
+ f_3\frac{\eta_{i+2} - 2\eta_{i+1} + 2\eta_{i-1} - \eta_{i-2}}{2\delta_s^3} + f_4\frac{\eta_{i+2} - 4\eta_{i+1} + 6\eta_i - 4\eta_{i-1} + \eta_{i-2}}{\delta_s^4},
\end{aligned} \tag{3.42}$$

where

$$\begin{aligned}
f_0 = -\Bigg(\zeta 2h_s\frac{\partial h_s}{\partial \theta}\left(\frac{\partial^3 h_s}{\partial \theta^3} + \frac{\partial h_s}{\partial \theta}\right) + h_s^2\left(\frac{\partial^4 h_s}{\partial \theta^4} + \frac{\partial^2 h_s}{\partial \theta^2}\right) - 2h_s\frac{\partial h_s}{\partial \theta}\sin\theta - h_s^2\cos\theta \\
+\frac{\partial h_s}{\partial \theta}\left(1 + \alpha_u\frac{\partial h_s}{\partial \theta}\right) + h_s\left(\alpha_u\frac{\partial^2 h_s}{\partial \theta^2}\right)\Bigg),
\end{aligned}$$

$$f_1 = -\left(\zeta h_s^2\left(\frac{\partial^3 h_s}{\partial\theta^3} + 2\frac{\partial h_s}{\partial\theta}\right) - h_s^2\sin\theta + h_s\left(1 + 2\alpha_u\frac{\partial h_s}{\partial\theta}\right)\right),$$

$$f_2 = -\left(\alpha_u\frac{h_s^2}{2} + \zeta\frac{h_s^3}{3}\right),$$

$$f_3 = -\zeta h_s^2\frac{\partial h_s}{\partial\theta},$$

$$f_4 = -\zeta\frac{h_s^3}{3}.$$

Equation (3.42) can be written

$$\sigma\eta_i = a_{2,i}\,\eta_{i+2} + a_{1,i}\,\eta_{i+1} + a_{0,i}\,\eta_i + a_{-1,i}\,\eta_{i-1} + a_{-2,i}\,\eta_{i-2}, \tag{3.43}$$

where

$$\begin{aligned}
a_{2,i} &= \left(\frac{f_3}{2\delta_s^3} + \frac{f_4}{\delta_s^4}\right),\\
a_{1,i} &= \left(\frac{f_1}{2\delta_s} + \frac{f_2}{2\delta_s^2} - \frac{f_3}{\delta_s^3} - \frac{4f_4}{\delta_s^4}\right),\\
a_{0,i} &= \left(f_0 - \frac{f_2}{\delta_s^2} + \frac{6f_4}{\delta_s^4}\right),\\
a_{-1,i} &= \left(-\frac{f_1}{2\delta_s} + \frac{f_2}{2\delta_s^2} + \frac{f_3}{\delta_s^3} - \frac{4f_4}{\delta_s^4}\right),\\
a_{-2,i} &= \left(-\frac{f_3}{2\delta_s^3} + \frac{f_4}{\delta_s^4}\right).
\end{aligned}$$

Then we obtain a linear matrix equation

$$\sigma\vec{\eta} = B\vec{\eta},$$

where

$$B = \begin{pmatrix}
a_{0,1} & a_{1,1} & a_{2,1} & & & & & a_{-2,1} & a_{-1,1}\\
a_{-1,2} & a_{0,2} & a_{1,2} & \ddots & & & & & a_{-2,2}\\
a_{-2,3} & a_{-1,3} & a_{0,3} & \ddots & & 0 & & & \\
 & \ddots & \ddots & \ddots & & & & & \\
 & & a_{-2,i} & a_{-1,i} & a_{0,i} & a_{1,i} & a_{2,i} & & \\
 & & & & & \ddots & \ddots & \ddots & \\
 & & 0 & & & \ddots & a_{0,S-2} & a_{1,S-2} & a_{2,S-2}\\
a_{2,S-1} & & & & & \ddots & a_{-1,S-1} & a_{0,S-1} & a_{1,S-1}\\
a_{1,S} & a_{2,S} & & & & & a_{-2,S} & a_{-1,S} & a_{0,S}
\end{pmatrix} \tag{3.44}$$

where the $-2\ldots2$ diagonals of B are given by the coefficients for $\eta_{i-2}\ldots\eta_{i+2}$, with appropriate correction for periodicity at the corners.

This is implemented in Matlab using the function `spdiags` for the diagonals, and the corner elements added individually. $f_0\ldots f_4$ are calculated from h_s using a method given by Fornberg [19].

b) Spectral method

An alternative approach to determining the eigenvalues of (3.37) is to use a spectral method, as described in detail in Trefethen [48]. This effectively extends the finite difference approximation to Nth order, and is correspondingly more accurate.

The perturbation $\eta(\theta)$, which is 2π-periodic in θ, is evaluated at N evenly spaced collocation points θ_j, and interpolated by a linear combination of S_N, the band-limited interpolant of the periodic delta-function.

$$S_N(\theta) = \frac{\sin(\pi\theta/\delta)}{(2\pi/\delta)\tan(\theta/2)}, \quad \text{where} \quad N = 2\pi/\delta.$$

D_N, the differentiation matrix, is Toeplitz and circulant[5], its columns being given by S_N. Thus $S_N(\theta_j)$ is the $(j+k) \mod N$th entry in the kth column of D_N. The columns of the higher order differentiation matrices $D_N^{(m)}$ are found using the derivative of S_N at the grid points θ_j, so $S_N^{(m)}(\theta_j)$ is the $(j+k) \mod N$th entry in the kth column of $D_N^{(m)}$. The derivatives of S_N are given by:

$$S_N'(\theta_j) = \begin{cases} 0 & j = 0 \mod N, \\ 1/2(-1)^j \cot(j\delta/2) & j \neq 0 \mod N, \end{cases} \tag{3.45}$$

$$S_N''(\theta_j) = \begin{cases} -\pi^2/3\delta^2 - 1/6 & j = 0 \mod N, \\ -(-1)^j/2\,\sin^2(j\delta/2) & j \neq 0 \mod N, \end{cases} \tag{3.46}$$

$$S_N^{(3)}(\theta_j) = \begin{cases} 0 & j = 0 \mod N, \\ (-1)^j \cot(j\delta/2)(-2\pi^2 + 3\delta^2/\sin^2(j\delta/2))/(4\delta^2) & j \neq 0 \mod N, \end{cases} \tag{3.47}$$

$$S_N^{(4)}(\theta_j) = \begin{cases} \frac{1}{30}\left(-1 + 10\pi^2/\delta^2 + 6\pi^4/\delta^4\right) & j = 0 \mod N, \\ -(-1)^j(2\delta^2 - \pi^2 + (\delta^2+\pi^2)\cos(\delta j))/(2\delta^2\sin(j\delta/2)^4) & j \neq 0 \mod N. \end{cases} \tag{3.48}$$

Each derivative $\frac{\mathrm{d}^m h}{\mathrm{d}\theta^m}$ in (3.37) is replaced by $D_N^{(m)}\vec{h}$ *etc.* as appropriate, leading to

$$\sigma\vec{\eta} = B\vec{\eta},$$

[5]Each column is a cyclic permutation of the previous one.

where B is the operator matrix

$$\begin{aligned} B = &- \left(\zeta 2\vec{h} \cdot D_N\vec{h} \cdot \left(D_N^{(3)}\vec{h} + D_N\vec{h} \right) + \zeta\vec{h}^2 \cdot \left(D_N^{(4)}\vec{h} + D_N^{(2)}\vec{h} \right) - 2\vec{h} \cdot D_N\vec{h} \cdot \sin\vec{\theta} - \vec{h}^2 \cdot \cos\vec{\theta} \right. \\ &\quad \left. + \left(1 + \alpha_u D_N\vec{h} \right) \cdot D_N\vec{h} + \left(\alpha_u D_N^{(2)}\vec{h} \right) \cdot \vec{h} \right) \\ &- \left(\zeta\vec{h}^2 \cdot \left(D_N^{(3)}\vec{h} + 2D_N\vec{h} \right) - \vec{h}^2 \cdot \sin\theta + \left(1 + 2\alpha_u D_N\vec{h} \right) \cdot \vec{h} \right) \cdot D_N \\ &- \left(\alpha_u \frac{\vec{h}^2}{2} + \zeta \frac{\vec{h}^3}{3} \right) \cdot D_N^{(2)} - \zeta\vec{h}^2 \cdot D_N\vec{h} \cdot D_N^{(3)} - \zeta \frac{\vec{h}^3}{3} \cdot D_N^{(4)} \end{aligned} \tag{3.49}$$

In (3.49), $\vec{\theta}$ is the vector of θ_j collocation points, $\vec{h} = h_s(\vec{\theta})$, $\vec{\eta} = \eta(\vec{\theta})$ and $\cdot$ indicates element-wise multiplication of vectors.

One of these two methods is used to obtain the matrix B, given in (3.44, 3.49). Then either all the eigenvalues of B are found, using Matlab function `eig.m` or else just a few, using Matlab function `eigs.m`. The latter code takes advantage of sparse matrices, and so can be run in a few minutes when the number of grid points is as large as 100,000 (for 1 eigenvalue), 10,000 (for 10 eigenvalues) or 1000 (for up to 400 eigenvalues). The eigenvalues found are those with the largest real part - in practice those closest to +100. `eigs.m` returns only the real part of the eigenvalues, but is nevertheless useful for checking results to a high number of grid points. `eig.m` requires a great deal more memory and time, and is therefore only usually used with up to 500 grid points. Both codes can return eigenvectors as well as eigenvalues.

If the eigenvalues σ have positive real part, then the perturbations grow in time. The corresponding eigenvectors are the perturbation modes.

If there are no eigenvalues with positive real part, then the solution h_s is stable. Also, if there is only one eigenvalue with positive real part, and the integral of the corresponding eigenvector is non-zero, then it can also be said that the solution is linearly stable to perturbations which conserve the mass of the film, for there are no mass-conserving linear combinations of the growing eigenvalue. This is the case for most solutions that we have found.

3.5.6 Numerical results of stability assessment

Both the finite difference and spectral stability methods have been applied to a range of film profiles. A selection of profiles is shown in figure 3.23, which have the parameters as shown in figure 3.24 and table 3.1.

Eigenvalue plots for these five film profiles are given in figure 3.25. The three columns

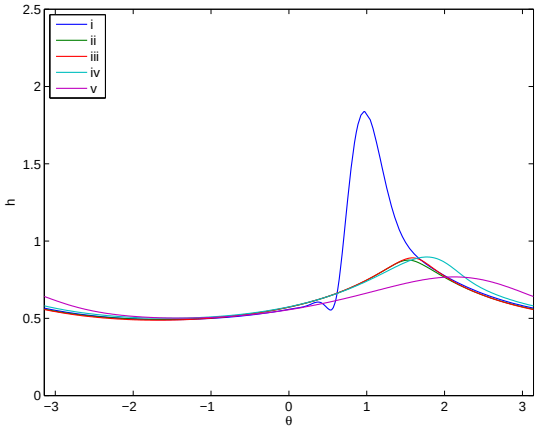

Figure 3.23: Steady solutions selected for stability analysis.

$\zeta \setminus \alpha_u$	10^{-5}	10^{-4}	10^{-3}	10^{-2}	10^{-1}	1
1						
10^{-1}						
10^{-2}						
10^{-3}			I			
10^{-4}						
10^{-5}						V
10^{-6}	II			III	IV	

Figure 3.24: Parameter map indicating the ζ and α_u parameters of the steady solutions selected for stability analysis

No.	A	α_u	ζ	F.D. (2)	F.D. (4)	S.M.
I	4.382	10^{-3}	10^{-3}	Stable[a]	Stable [a]	Stable
II	3.829	10^{-5}	10^{-6}	Stable	Stable [a]	Stable
III	3.829	10^{-2}	10^{-6}	Unstable[b]	Unstable[b]	Stable
IV	3.829	10^{-1}	10^{-6}	Unstable	Unstable	Stable
V	3.951	1	10^{-5}	Unstable	Unstable	Stable

[a]Single unstable eigenvalue, very small
[b]Some stable eigenvalues

Table 3.1: Parameters of the steady solutions selected for stability analysis

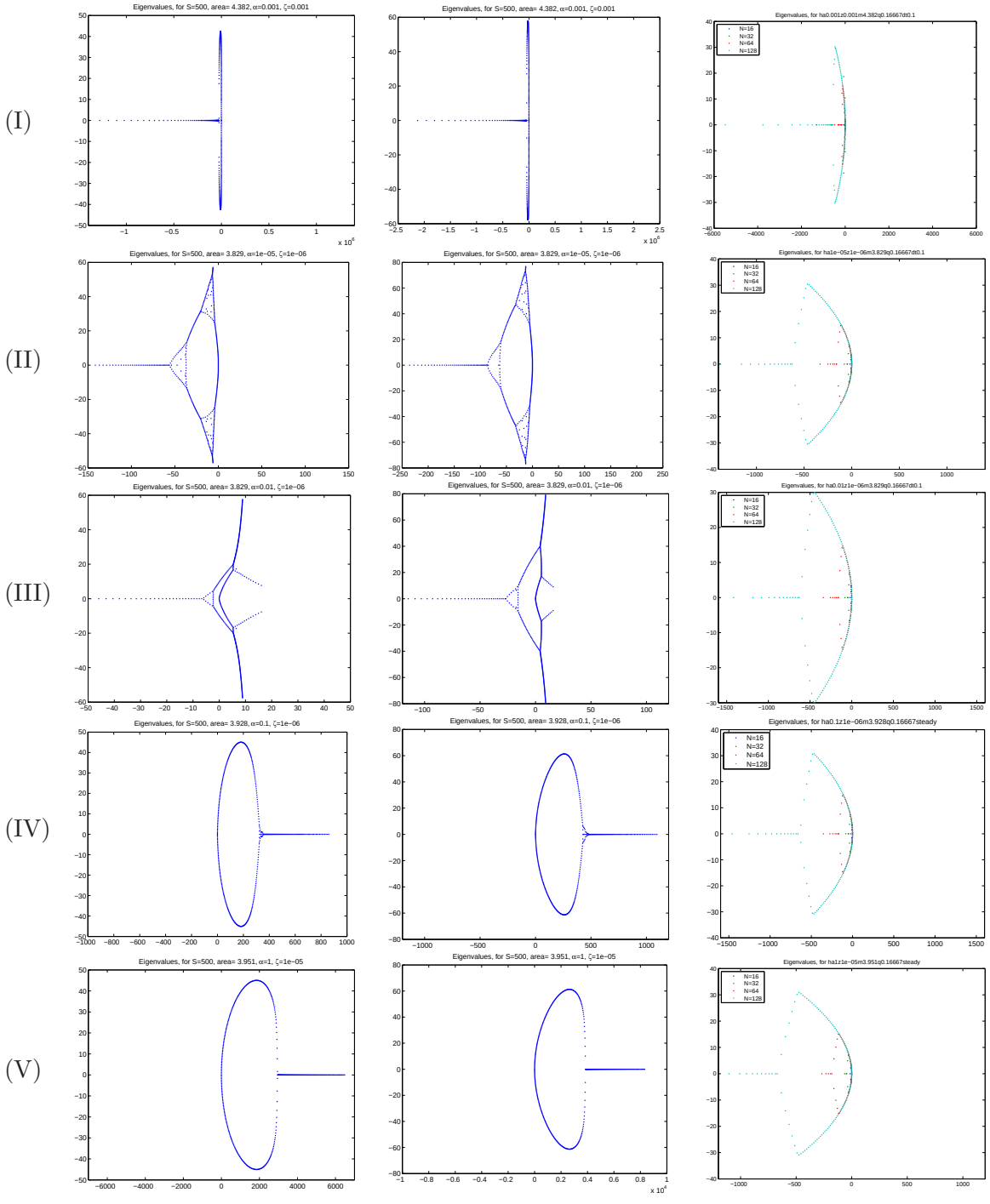

Figure 3.25: Eigenvalue plots (real vs imaginary part) showing the transition to instability (I) $A = 4.382$, $\alpha_u = 10^{-3}$, $\zeta = 10^{-3}$, (II) $A = 3.829$, $\alpha_u = 10^{-5}$, $\zeta = 10^{-6}$, (III) $A = 3.829$, $\alpha_u = 10^{-2}$, $\zeta = 10^{-6}$, (IV) $A = 3.829$, $\alpha_u = 10^{-1}$, $\zeta = 10^{-6}$, (V) $A = 3.951$, $\alpha_u = 1$, $\zeta = 10^{-5}$.

are the results for the finite difference method at order 2, finite difference and order 4, and spectral method respectively. The real vs imaginary parts of eigenvalues are plotted. Note that the axes scales changes between plots, but the origin is always at the centre. Different colours on the spectral method plots represent different resolutions. These results will be discussed in more detail in the following sections.

a) Specific case: a film profile expected to be stable

Test case (I) in figure 3.25 has $\alpha_u = 10^{-3}$, $\zeta = 10^{-3}$ and $A = 4.382$. The eigenvalue results are typical for the stable solutions from the parameter range $\alpha_u^3 < \zeta$ with $A > A_{crit}$. The area is large enough to permit a shock to the upper solution branch, and as $\alpha_u^3 < \zeta$ this is in the parameter range to have a surface-tension smoothed shock-solution by the matching argument. Such a solution was found by both the steady-state and transient codes.

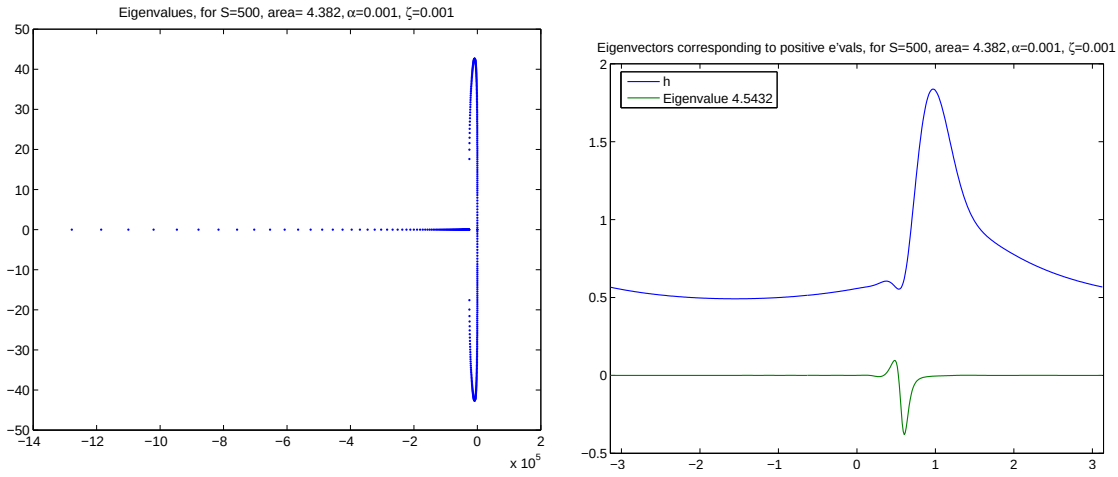

(i) (ii)

Figure 3.26: (i) Eigenvalues and (ii) film profile and growing mode eigenvector for $A = 4.382$, $\alpha_u = 10^{-3}$, $\zeta = 10^{-3}$, $S = 500$.

The scale of the real eigenvalue axis is very large however, and if we zoom in by several orders of magnitude, we find that there is an eigenvalue with small but positive real part, with value $4.54 + 0\mathrm{i}$. The corresponding eigenvector is a narrow peak at the same angular position as the jump in the film profile and is shown together with the profile in figure 3.26 (ii). A series of tests were conducted to confirm that this eigenvector was not just a numerical artefact. These included increasing the number of grid points, comparing results form transient and steady-state numerical solvers, and comparing results across a range of α_u and ζ values.

$\zeta \setminus \alpha_u$	10^{-5}	10^{-4}	10^{-3}	10^{-2}	10^{-1}	1
1	1	1	1	1	1	×
10^{-1}	1	1	1	1	1	×
10^{-2}	1	1	1	1	×	×
10^{-3}	1	1	1	1	×	×
10^{-4}	1	1	1	1	×	×
10^{-5}	1	1	1	×	×	×
10^{-6}	1	1	1	×	×	×

Figure 3.27: Parameter map of ζ and α_u indicating number of eigenvalues with positive real part, for $A = 4.382$

Because the eigenvector represents a perturbation that removes mass from the profile, a system that preserves mass cannot excite such an eigenvector and remains stable.

The range of ζ, α_u parameter space for which stable solutions are found is shown in the stability map for $A = 4.382$, in figure 3.27. The symbol × indicates that no steady solution was found, 1 indicates that a single eigenvalue with positive real part was found. These single eigenvalues all corresponded to perturbations that added mass to the profile, so the solutions are stable to zero-mass perturbations. There is an exact correspondence with figure 3.13, all transient solutions found were stable.

b) Specific case: a film profile expected to be unstable

Unstable steady solutions are by their nature unlikely to be found using the transient method, and numerically difficult to find even with the steady-state method. One example is given by test case (V) in figure 3.25, with parameters $\alpha_u = 1$, $\zeta = 10^{-5}$ and cross-sectional area $A = A_{crit} = 3.951$. Since $\zeta < \alpha_u^3$, the matching argument of §3.2 indicates an upper quadrant shock for this range of α_u, ζ, which kinematic wave theory suggests will be unstable. With this area there is only a tiny bulge in the $\pi/2 < \theta < \pi$ quadrant, but with $A > A_{crit}$, no solution could be found, even with the steady-state solver.

c) Stability of low-area profiles

Steady solutions were only found for $\zeta < \alpha_u^3$ when the area of the solution was less than that of the critical film profile, $A < 3.951$. Figure 3.28 shows a stability map for $A = 3.829$, using the steady-state solutions for $\zeta < \alpha_u^3$, and the transient solver for

$\zeta \setminus \alpha_u$	10^{-5}	10^{-4}	10^{-3}	10^{-2}	10^{-1}	1
1	1	1	1	1	1	×
10^{-1}	1	1	1	1	1	$6^{\dagger}$
10^{-2}	3	3	3	3	×	$22^{\dagger}$
10^{-3}	3	3	3	2	×	$70^{\dagger}$
10^{-4}	3	3	3	6	$58^{\dagger}$	$248^{\dagger}$
10^{-5}	3	5	6	20	$242^{\dagger}$	$499^{\dagger}$
10^{-6}	3	6	20	170	$499^{\dagger}$	×

Figure 3.28: Parameter map of ζ and α_u indicating number of eigenvalues with positive real part, for A=3.829. † Results obtained from steady-state solver

$\zeta > \alpha_u^3$. Again × indicates that no steady solution was found either by transient or steady-state code, and the number of eigenvalues (out of 500) with positive real part is given. In $\zeta < \alpha_u^3$, many positive eigenvalues were found, as illustrated in (III), (IV) of figure 3.25, suggesting that these profiles were not stable. In $\zeta > \alpha_u^3$ a few positive eigenvalues were also found, even though the results were obtained from the transient solver and appear stable. Once again, where a single positive eigenvalue was found, it corresponded to an eigenvector which added mass, so does not indicate instability to zero-mass perturbations. Also in the cases where three eigenvalues with positive real part were found, two were a complex conjugate pair and all three were mass-adding, so there is no linear combination which adds zero mass, and the solution was stable.

3.5.7 A comparison of finite difference and spectral methods

The two numerical methods described both lead to an algebraic eigenvalue problem $B\vec{\eta} = \sigma\vec{\eta}$, where in the finite difference method B is a banded matrix, and in the spectral method it is full. The eigenvalue command `eig` is called in Matlab to solve for eigenvalues σ in both cases. The spectral method returns all eigenvalues as having negative real part in all cases, but as illustrated in figure 3.25 the finite difference method returns eigenvalues which have positive real part when $\alpha_u < \zeta^3$. The order of the finite difference scheme does not seem to significantly affect the results, as results from second and fourth order are qualitatively similar.

For example in test case (IV) in figure 3.25, with parameters A=3.829, $\zeta = 10^{-6}$, $\alpha_u = 10^{-1}$, the finite difference method returns eigenvalues that all have positive real part. It was hypothesised that the finite difference method allows perturbations that add mass to the system, and therefore would not be stable, but in test case (IV), with

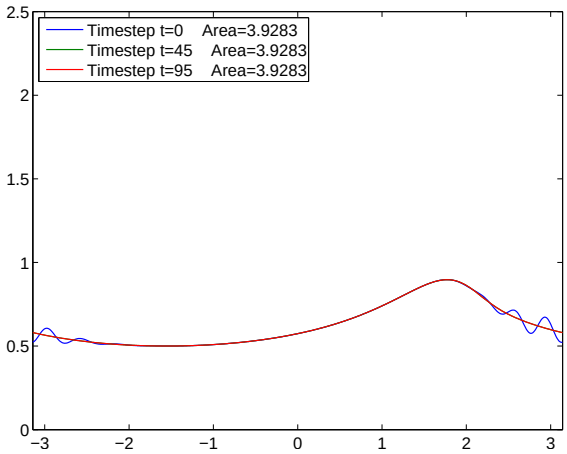

Figure 3.29: $A = 3.928$, $\alpha_u = 0.1$, $\zeta = 10^{-6}$, decay of a perturbation.

one exception, all eigenvectors when normalised to 1 have an integral of less than 10^{-5}. Hence they do not represent perturbations which add or subtract significant mass to the system.

When perturbations from this set are added to the original steady solution, some of them decay and some grow. As an example, we add the perturbation from the eigenvector that corresponds to $\sigma = 5.0243 + 8.5926i$. The amplitude of the perturbation is scaled by 0.5 to ensure the height of the film is not immediately swamped. As shown in figure 3.29, the perturbation quickly dissipates, and the steady solution is restored. Other, higher frequency perturbations from this set also quickly decay, even though their eigenvalues have positive real part. But for example if we add the eigenvector corresponding to $\sigma = 515.1 + 0i$ the perturbations decay to almost nothing, then the solution suddenly becomes unstable and another wave develops, as illustrated in figure 3.30, which causes the solution to fail.

Perturbations corresponding to eigenvectors found using the spectral method decay quickly, as illustrated in the example in figure 3.31. In this example the perturbation vanishes by four timesteps, and the solution remains stable.

Significant checking for any error in the code was undertaken. One possible explanation for the apparent discrepancy is that the spectral method restricts the possible eigenvectors, so that the these modes are indeed stable, and that some of the modes revealed by the finite difference method are not stable. It could also be that the system is close to being numerically unstable, and the eigenvalue routine is unreliable.

There is another possibility, that this is a case such as is discussed by Trefethen [49], in which non-normal effects play a part. Trefethen observed that in some problems small

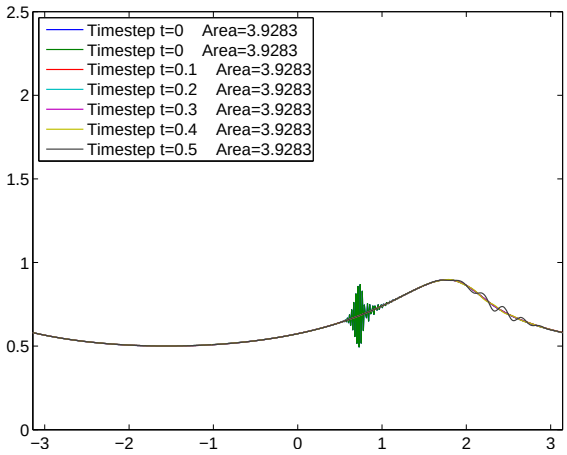

Figure 3.30: $A = 3.928$, $\alpha_u = 0.1$, $\zeta = 10^{-6}$, initial decay of a perturbation near 0.7 (green), then growth of a new wave in $\pi/2 < \theta < \pi$ (black).

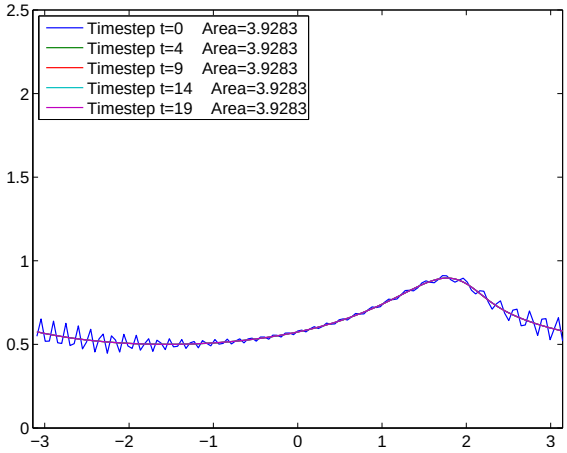

Figure 3.31: $A = 3.928$, $\alpha_u = 0.1$, $\zeta = 10^{-6}$, decay of a perturbation derived from the spectral method stability.

perturbations of the steady flow grow unstably in the short term but then non-linear effects — unseen by the linear analysis — take hold that dampen further growth. The linear eigenvalue analysis term behaviour will continue in the long term, so misses this and may be incomplete or even misleading.

Since a criterion of 'what can be found by the transient solver' represents results that are 'usefully' stable, this curiosity is not pursued further and is left unresolved.

3.6 Summary of this chapter

To focus on the key terms of surface tension and azimuthal droplet momentum, we set $c_1 = \zeta$, $c_2 = -1$, $c_3 = \alpha_u$, $c_4 = 1$, $c_5 = 0$, $c_6 = 0$ in the equation for film height when droplet mass is negligible, (2.71), to get the simplified form (3.2). When $\zeta, \alpha_u = 0$, (3.2) reduces to a cubic, which has a maximum of two positive real solutions, depending on the area of the film A. When $A \leq A_{crit} = 3.951$, there is a single completely-wetting solution for the film, When $A > A_{crit}$, shock solutions may occur, with fluid exceeding $A = A_{crit}$ building up into a shock somewhere in $0 < \theta < \pi$.

A matching argument suggested that for $\zeta, \alpha_u > 0$, only limited combinations of shocks are possible. If $\zeta \geq \alpha_u^3$, steady-state solutions can exist with a smoothed shock in $0 < \theta < \pi/2$. If $\zeta < \alpha_u^3$, the steady-state solutions can exist with a smoothed shock in $\pi/2 < \theta < \pi$. Kinematic wave theory suggests that only former are stable.

These results are confirmed by the transient numerical solver. The steady-state numerical solver is of limited use as A is not conserved and cannot be specified. Numerical results also showed the effect of ζ is to smooth shocks, tending to dampen peaks and be a stabilising influence. α_u slightly increases the size of peaks until it approaches $\alpha_u = \zeta$, when steady-state solutions cannot be found.

Eigenvalue analysis of the stability of these results is inconclusive, with contradictory results from spectral and finite difference methods. However tests on evolution of individual perturbations confirm that shock solutions in the parameter range $\zeta \geq \alpha_u^3$ are stable.

Chapter 4

Formulation of film profile and underlying flows, with significant variable droplet mass and momentum transfer at the surface

In this chapter we will reconsider the boundary conditions of the film. The droplet impact may not be uniform around the cylinder, so we will allow variation of the surface boundary conditions with azimuthal angle θ. We will also reconsider the conditions on the chamber wall, to include a rotating cylinder and outflow through a sink in the wall. The latter will permit steady-state flows in the case where the droplets contribute significant mass as well as momentum to the film.

This chapter is reserved for the derivation and other preparatory work, the results will follow in chapters 5–6.

4.1 Updates to derivation and solution method of film profile equation

4.1.1 Boundary conditions to allow flow out of a sink ($v_{cyl} \neq 0$), wall rotation ($u_{cyl} \neq 0$), and variable droplet input.

In the derivation of the film profile equations in Chapter 2, it was assumed that the droplets impact uniformly around the cylinder, i.e. u_E, v_E and α are constant in θ. However in the physical system this may not be the case, and it is interesting to allow them to vary with θ. When the inflow varies with θ, $\frac{\partial u_E}{\partial \theta}$, $\frac{\partial v_E}{\partial \theta}$ and $\frac{\partial \alpha}{\partial \theta}$ terms may appear at $O(\epsilon)$, but at leading order the derivation proceeds as before, to give:

$$\frac{\partial h}{\partial t} + \mathrm{Re_f}\frac{\partial}{\partial \theta}\left(\mathrm{We_f}\left(\frac{\partial h}{\partial \theta} + \frac{\partial^3 h}{\partial \theta^3}\right)\frac{h^3}{3} - \frac{\sin\theta}{\mathrm{Fr}}\frac{h^3}{3} + a(\theta)u_E(\theta)\left(u_E(\theta)\frac{\partial h}{\partial \theta} - v_E(\theta)\right)\frac{h^2}{2}\right) - a(\theta)\left(u_E(\theta)\frac{\partial h}{\partial \theta} - v_E(\theta)\right) = 0. \quad (4.1)$$

If the droplets impacting on the surface on the film are contributing significant mass as well as momentum, then in order to study the important steady-state case we must allow mass to also leave the system. This is physically achieved in a bearing chamber with one or more outlets (known as sinks or sumps), introducing a complex three-dimensional geometry. In two dimensions, an outlet for mass can be in the form of a porous wall, or one or more discrete sinks. In this work, we consider the latter model, with sinks defined across sections of the chamber wall.

Mathematically, the sink is included by changing the no-flow boundary condition at the wall, $y = 0$. For the sake of brevity we omit the dimensional formulation. The scaled no-flow condition (2.28) is replaced by

$$v = v_{cyl}(\theta) \quad \text{on} \quad y = 0, \quad (4.2)$$

where the outflow function v_{cyl} will be prescribed below.

We will also now be considering rotation of the chamber. This is also introduced by a change to the cylinder wall boundary conditions, replacing the scaled no-slip condition (2.29) by

$$u = u_{cyl}(\theta) \quad \text{on} \quad y = 0. \quad (4.3)$$

u_{cyl} will be given below, and is defined such that $u_{cyl} = 0$ for a stationary cylinder and $u_{cyl} > 0$ for a cylinder rotating anticlockwise.

Derivation of the modified film equations proceeds in similar manner to Chapter 2, with the film height equation at leading order (2.64) being replaced by

$$\frac{\partial h_0}{\partial t} - \frac{\partial}{\partial \theta}\left(\mathrm{Re_f}\left(\frac{\partial N_{l0}}{\partial \theta} + \frac{1}{\mathrm{Fr}}\sin\theta\right)\frac{h_0^3}{3}\right) + \frac{\partial}{\partial \theta}\left(T_0\frac{h^2}{2}\right) - M_0 + \frac{\partial}{\partial \theta}\left(u_{cyl}h_0\right) - v_{cyl} = 0. \quad (4.4)$$

Once again, N_{l0}, T_0 and M_0 are dependent on droplet properties, as discussed in §2.8.

Similarly (2.70) is replaced by

$$\frac{\partial h_0}{\partial t}+\mathrm{Re_f}\frac{\partial}{\partial\theta}\left(\overbrace{\mathrm{We_f}\left(\frac{\partial h_0}{\partial\theta}+\frac{\partial^3 h_0}{\partial\theta^3}\right)\frac{h_0^3}{3}}^{Surface\ Tension}-\overbrace{\frac{\sin\theta}{\mathrm{Fr}}\frac{h_0^3}{3}}^{Gravity}+\overbrace{a(\theta)u_E(\theta)\left(u_E(\theta)\frac{\partial h_0}{\partial\theta}-v_E(\theta)\right)\frac{h_0^2}{2}}^{Droplet\ Momentum}\right)$$
$$-\underbrace{a(\theta)\left(u_E(\theta)\frac{\partial h_0}{\partial\theta}-v_E(\theta)\right)}_{Droplet\ Mass}+\underbrace{\frac{\partial}{\partial\theta}\left(u_{cyl}h_0\right)}_{Wall\ Rotation}-\underbrace{v_{cyl}}_{Sink}=0. \quad (4.5)$$

Terms in the above are grouped for clarity and to identify the physical basis for each.

As noted in the derivation, there is nothing in this model to prevent mass from leaving the film as well as entering it. The term $au_E\frac{\partial h_0}{\partial\theta}$ can apparently cause mass to leave the surface of the film, on the downwards side of a hump. However it should be considered in conjunction with the term $-av_E$, which always adds mass to the film. Even when the gradient of h is negative, mass will not leave unless $|\frac{\partial h_0}{\partial\theta}| > |v_E|/|u_E|$, although the net flux into the film will be lower than when the gradient of h is positive. For all of the cases examined in Chapter 5 this restriction holds and the net flux into the film is positive everywhere. The only exceptions are those highlighted in §5.1.1 which are a mathematical diversion and correspond to non-physical combinations of parameters.

Once again, it is convenient to label the coefficients c_1 to $c_6(\theta)$. We choose not to absorb u_{cyl} into c_5, although it has a similar form, as a separation of the c_5 term into surface and wall components will be required for calculating the streamlines, in order to correctly select the base velocity. Similarly v_{cyl} is not absorbed into c_6. The modified version of (2.71) is

$$\frac{\partial h}{\partial t}+\frac{\partial}{\partial\theta}\left(c_1\left(\frac{\partial h}{\partial\theta}+\frac{\partial^3 h}{\partial\theta^3}\right)\frac{h^3}{3}+c_2\sin\theta\frac{h^3}{3}+\left(c_3(\theta)\frac{\partial h}{\partial\theta}+c_4(\theta)\right)\frac{h^2}{2}\right)$$
$$+\left(c_5(\theta)\frac{\partial h}{\partial\theta}+c_6(\theta)\right)+\frac{\partial}{\partial\theta}\left(u_{cyl}h\right)-v_{cyl}=0. \quad (4.6)$$

We will frequently refer to this equation in subsequent chapters.

4.1.2 Numerical solution methods

As in the simpler case described in section 3.4, the transient solver uses the Matlab function `bvp4c`. Discretising in time using a fully implicit backward time difference scheme, (4.6) becomes:

$$\frac{h_j - h_{j-1}}{\delta t} + c_1 \left(\frac{\partial^2 h_j}{\partial \theta^2} + \frac{\partial^4 h_j}{\partial \theta^4} \right) \frac{h_j^3}{3} + c_1 \left(\frac{\partial h_j}{\partial \theta} + \frac{\partial^3 h_j}{\partial \theta^3} \right) \frac{\partial h_j}{\partial \theta} h_j^2$$
$$+ c_2 \cos\theta \frac{h_j^3}{3} + c_2 \sin\theta \frac{\partial h_j}{\partial \theta} h_j^2 + \left(\frac{\partial c_3}{\partial \theta} \frac{\partial h_j}{\partial \theta} + c_3(\theta) \frac{\partial^2 h_j}{\partial \theta^2} \right) + \frac{\partial c_4}{\partial \theta} \frac{h_j^2}{2} + \left(c_3(\theta) \frac{\partial h_j}{\partial \theta} + c_4(\theta) \right) \frac{\partial h_j}{\partial \theta} h_j$$
$$+ \left((c_5(\theta) + u_{cyl}) \frac{\partial h_j}{\partial \theta} + (c_6(\theta) - v_{cyl}) \right) = 0. \quad (4.7)$$

Writing $H_1(\theta) = h_j$, $H_n = H'_{n-1}$, the 4th order ODE (4.7) can be expressed in terms of an equivalent set of four first-order equations:

$$\begin{aligned}
H'_1 &= H_2, \\
H'_2 &= H_1^{(2)} = H_3, \\
H'_3 &= H_1^{(3)} = H_4, \\
H'_4 &= H_1^{(4)} = -H_3 + \frac{3}{c_1 H_1^3} \Bigg(- \frac{H_1 - H_{1j-1}}{\delta t} - c_1 H_1^2 H_2 (H_4 + H_2) \\
&\qquad - c_2 \left(\frac{H_1^3}{3} \cos(\theta) + H_1^2 H_2 \sin(\theta) \right) \\
&\qquad - \left(\frac{\partial c_3}{\partial \theta} H_2 + c_3 H_3 + \frac{\partial c_4}{\partial \theta} \right) \frac{H_1^2}{2} - (c_3 H_2 + c_4) H_1 H_2 \\
&\qquad - ((c_5 + u_{cyl}) H_2 + (c_6 - v_{cyl})) \Bigg).
\end{aligned} \quad (4.8)$$

In the implementation, a file `initparam.m` is used to define all the necessary parameters. The functions $c_3(\theta)$ to $c_6(\theta)$ are defined within it, and function handles passed to a file`odesolver.m`, which implements the main solver. It has been found that problems with numerical errors may arise if the functions $c_i(\theta)$ (or their first derivatives) contain discontinuities. The single injector model of variable droplet input was an example of this. Such difficulties can be avoided by smoothing the discontinuity with a cubic polynomial in a narrow region matching on the discontinuity either side.

4.1.3 Numerical implementation of sinks

The code is developed to allow a sink to be located in an arbitrary position on the cylinder wall. A sink is implemented as a small finite section of the boundary, across which there is a constant outflow of fluid.

The outflow function used is

$$v_{cyl} = \begin{cases} 0 & \theta < \theta_s, \\ v_{out} & \theta_s < \theta < \theta_e, \\ 0 & \theta_e < \theta. \end{cases} \tag{4.9}$$

Since `bvp4c` adapts the mesh from one iteration to the next, then in order to keep the outflow constant it is necessary to ensure that there are always mesh points at θ_s and θ_e. This is done using the 'multipoint' capability of `bvp4c`, dividing the domain into three regions: $[-\pi, \theta_s]$, $[\theta_s, \theta_e]$, and $[\theta_e, \pi]$. The boundaries of the step change, θ_s and θ_e, are included exactly twice in the list of mesh points and the ODE for H_4' defined appropriately in each sub-domain. A sink located across the top of the cylinder or multiple sinks would require a slight amendment to the code.

A fixed outflow can be prescribed for v_{out}. If this is greater than the inflow then the film will become thicker; if it is less then the film will thin. In order to study steady solutions, most simulations have the total mass outflow set to match the total mass inflow. Thus if the definition of the film height contains a term of the form

$$c_5(\theta)\frac{\partial h}{\partial \theta} + c_6(\theta),$$

then the total mass entering the system is given by

$$TotalMassIn = \int_0^{2\pi} c_5(\theta)\frac{\partial h}{\partial \theta} + c_6(\theta)\,\mathrm{d}\theta.$$

The mass leaving the system is then set by defining the outflow velocity as

$$v_{cyl} = \begin{cases} 0 & -\pi < \theta < \theta_s, \\ \frac{1}{\theta_e - \theta_s}\int_0^{2\pi} c_5(\theta)\frac{\partial h}{\partial \theta} + c_6(\theta)\,\mathrm{d}\theta & \theta_s < \theta < \theta_e, \\ 0 & \theta_e < \theta < \pi. \end{cases} \tag{4.10}$$

The integration is carried out using the Matlab function `quadl`. If the droplet impact is uniform around the cylinder, $c_5(\theta)$ and $c_6(\theta)$ are constant. Then, since h is 2π-periodic, $TotalMassIn = c_6$. However if the droplet impact varies around the cylinder, the total mass input, and hence the total mass output, is dependent on h. It is possible in most cases to use h_{j-1} from the previous timestep, rather than having to solve the full integro-differential equation. The success of this is monitored by checking for changes in the total mass in the film.

4.1.4 Parameter continuation

In some cases parameter continuation is necessary to find a solution of (4.6) with the transient solver. For example, with A=4.382, $c_1 = 10^{-4}$, $c_2 = -1$, $c_3 = 10^{-3}$, $c_4 = 1$ and

$c_6 = 0$, the solution for $c_5 = -0.05$ cannot be found directly from the uniform film with the same area, or by continuation from $c_5 = -0.01$, as the film becomes suddenly too thin and ruptures. However by gradually increasing c_5 through $-0.02, -0.03, -0.04$ to -0.05, a solution is found. In other cases, a small timestep is needed to get away from the continuation solution without overshooting and failing, but then the convergence is very slow. This can be helped by continuing with a larger timestep. This was used for example for $c_5 = -0.01$ and $c_6 = -1$.

4.2 Modelling variable droplet input

In Chapter 3 we restricted our attention to uniform impact of droplets on the film. Now we consider the effect of the droplet impact varying azimuthally. In order to study a realistic model, we require three pieces of information: the droplet volume fraction (α), and velocity components (u_E and v_E) as functions of azimuthal coordinate θ.

There exists no reliable data on droplet impact that can be used directly for simulations. An informative approach, and one that is consistent with the modelling approach taken so far, is to apply simple functions which capture the key behaviours seen in these previous works. Then we can see the physical effects clearly. These functions will be explained in sections §4.2.1 and §4.2.2.

We will take two different models of the droplet distribution in the chamber. The first will be based on the droplets being sprayed into the chamber from a single injector block, and the second will assume the droplets are sprayed or scattered from evenly distributed points around the central shaft. The transient solver allows any of a, u_E or v_E, and therefore c_3 to c_6 to vary with θ. But since we don't have reliable data for velocities, in the examples that follow u_E, v_E are kept constant, and only a varied.

4.2.1 Input function to model a single injector

To model a single injector block, we will use an model based on the half-normal distribution of mass deposition used by Noakes [34], and apply this distribution to the droplet fraction a.

Noakes' work will be discussed again in Chapter 6, and her equation for film profile is given by (6.1). She used:

$$c_6 = \lambda I(\theta) = \begin{cases} \frac{\lambda}{\sqrt{2\pi}} e^{-\frac{(\theta+\pi-1)^2}{2}}, & -\pi + 1 \leq \theta \leq -\pi + 4 \\ 0 & \text{elsewhere} \end{cases} \tag{4.11}$$

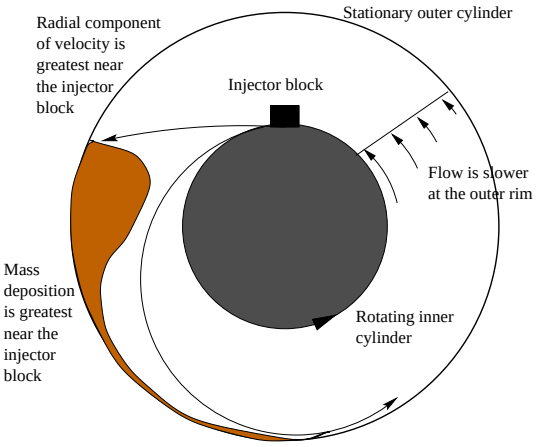

Figure 4.1: Illustration of variable mass input - single injection point

for constant λ, which has a peak mass input of $\lambda/\sqrt{2\pi}$ and total mass input of $\lambda/2$.

We modify this function, to

$$a(\theta) = (1-\phi_a)2\sqrt{2\pi}\bar{a}\mathrm{e}^{-\frac{((\theta-\theta_b) \mod 2\pi)^2}{2}} + \phi_a\bar{a}. \tag{4.12}$$

Thus the peak droplet fraction is $(1-\phi_a)2\sqrt{2\pi}\bar{a} + \phi_a\bar{a}$ and total droplet fraction is

$$\begin{aligned}
\int_{-\pi}^{\pi} a(\theta)\mathrm{d}\theta &= (1-\phi_a)\,2\pi\bar{a}\,2\int_{\theta_b}^{\theta_b+2\pi}\frac{1}{\sqrt{2\pi}}\mathrm{e}^{-\frac{(\theta-\theta_b)^2}{2}}\mathrm{d}\theta + \phi_a\bar{a}\int_{\theta_b}^{\theta_b+2\pi}\mathrm{d}\theta \\
&= (1-\phi_a)\,2\pi\bar{a}\,2\int_{0}^{2\pi}\frac{1}{\sqrt{2\pi}}\mathrm{e}^{-\theta^2/2}\mathrm{d}\theta + \phi_a\,2\pi\bar{a} \\
&= (1-\phi_a)\,2\pi\bar{a}\,(\mathrm{erf}(2\pi)) + \phi_a\,2\pi\bar{a} \\
&\approx 2\pi\bar{a}.
\end{aligned}$$

With $\theta_b = -\pi + 1$ and $\phi_a = 0$, (4.12) approximates Noakes' function. The scale factor of 4π is chosen so that the total mass input is consistent with the total mass input of a uniform distribution $a(\theta) = \bar{a}$. Moving the truncation from $\theta = -\pi + 4$ to $\pi + 1$, gives a change in total mass of only $\mathrm{erfc}(4) - \mathrm{erfc}(\pi) < 10^{-7}$, and it makes handling easier. The parameter ϕ_a allows us to mix the single injector with a uniform distribution, to investigate intermediate cases. $\phi_a = 1$ corresponds to a uniform distribution.

The function (4.12) is discontinuous across $\theta = \theta_b$. The code produced numerical errors and had difficulty with adaptive meshing due to this discontinuity. Since a discontinuity in the input is in any case unphysical, it is reasonable to smooth the corner with a narrow matching region, as illustrated in figure 4.2. A polynomial was chosen to match up to the first derivative of the normal distribution function. The region can be chosen to be very thin, yet still solve the numerical difficulties.

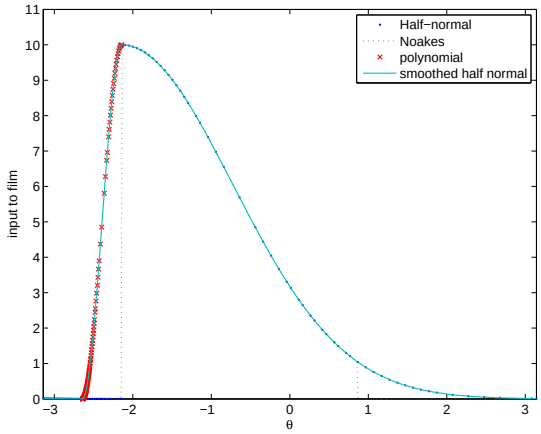

Figure 4.2: Illustration of the smoothed single injector function (width of smoothing region exaggerated)

The polynomial, a cubic, matched value and first derivative at end points. The coefficients p_n are given by the solution to

$$\sum_{n=0}^{3} p_n c^n = f(c) \qquad \sum_{n=0}^{3} p_n n c^{n-1} = f'(c) \tag{4.13}$$

$$\sum_{n=0}^{3} p_n b^n = f(b) \qquad \sum_{n=0}^{3} p_n n b^{n-1} = f'(b) \tag{4.14}$$

where

$$c = \theta_b$$

$$b = \theta_b - 0.1$$

f is the function before smoothing.

4.2.2 Input function to model distributed injector points

The second model of distributed injector points, as illustrated in figure 4.3, is based on work by Farrall [16–18]. Figure 4.4(i), showing momentum input variation in θ and z, is typical of the droplet input to the film model that results from his CFD and droplet tracking model of the core, when the droplets come from 10 discrete locations around the cylinder. The data appears chaotic, both axially and azimuthally. The effect of this highly erratic input on the film profiles shown in figure 4.4(ii) is not clear, although there are 10 oscillations which correspond roughly to the original 10 droplet sources of the input data.

In order that the relationship between input and output is clear, for our purposes the p distributed sources may be better modelled by a simple sin wave with period $2\pi/p$, as

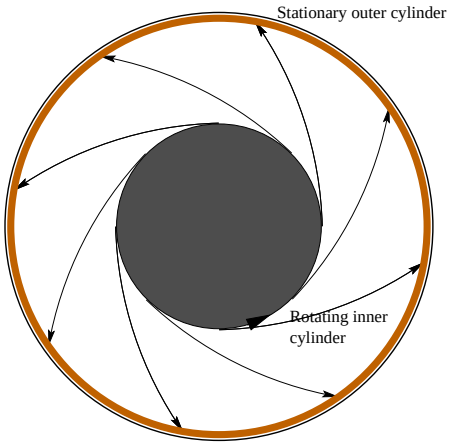

Figure 4.3: Illustration of variable mass input - distributed sources

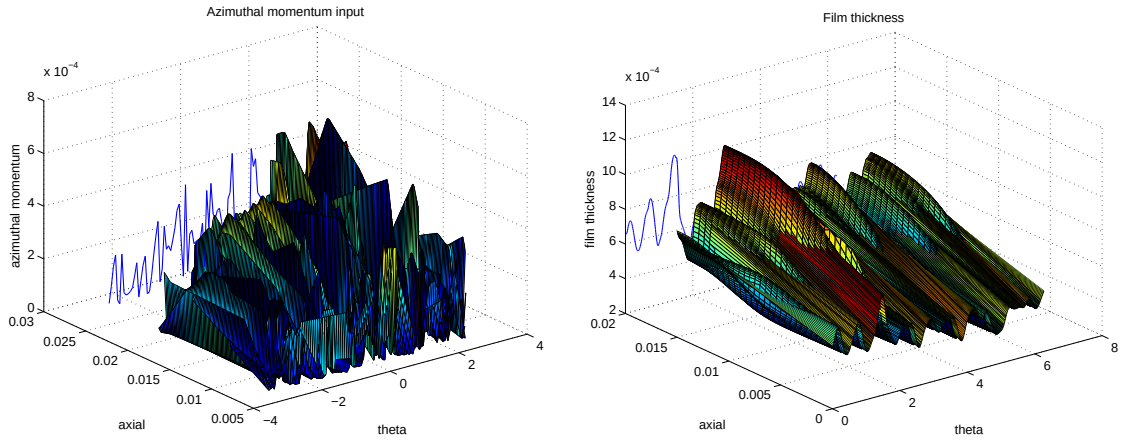

(i) (ii)

Figure 4.4: An example of (i) azimuthal momentum input and (ii) resulting film profile from droplet tracking model (data from Bearing Chamber tutorial [16]).

illustrated in figure 4.5. The droplet mass input function is defined by

$$a(\theta) = \bar{a}\left((1-\phi_a)\sin(p\,\theta)+1\right), \tag{4.15}$$

and the total droplet fraction is

$$\begin{aligned}\int_{-\pi}^{\pi} a(\theta)\mathrm{d}\theta &= \bar{a}\int_{-\pi}^{\pi}\left((1-\phi_a)\sin(p\,\theta)+1\right)\,\mathrm{d}\theta \\ &= 2\pi\bar{a}. \quad \text{for } p \text{ even}\end{aligned}$$

A similar model, using 18 release locations around the cylinder, is given in Chapter 7 of Farrall's thesis, [15].

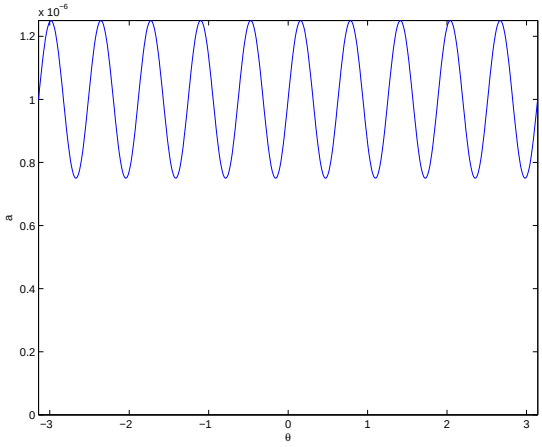

Figure 4.5: Illustration of variable mass input - distributed sources

4.3 Underlying flow

4.3.1 Derivation of streamfunction

The film profile shows the thickness of the flow, but in order to visualise the flow field, to see for example whether there is any recirculation, we need information on the streamlines. To find the velocity components u and v, we return to the derivation of the film-height governing equation in §2.7, bearing in mind the modifications made to the derivation in this chapter.

The leading order component of u is given by

$$u_0 = F_0 \left(\frac{y^2}{2} - h_0 y \right) + T_0 y + u_{cyl}, \tag{4.16}$$

where

$$F_0(\theta, t) = \mathrm{Re_f} \left(\frac{\partial N_{l0}}{\partial \theta} + \frac{1}{\mathrm{Fr}} \sin\theta \right), \tag{4.17}$$

and the leading order component of v is found by integrating the continuity equation:

$$v_0 = -\left(\frac{\partial F_0}{\partial \theta} \frac{y^3}{6} + \frac{\partial}{\partial \theta} \left(-F_0 h + T_0 \right) \frac{y^2}{2} \right) + v_{cyl}(\theta) - \frac{\partial u_{cyl}}{\partial \theta} y. \tag{4.18}$$

The choice of limit at the interface dictates N_{l0} and T_0, as described in §2.8. In the case we are considering in this chapter, where the film is driven by both momentum and mass, we have $\alpha = \epsilon a$, $U_E/U = \epsilon^{-1}$, and $V_E/U = 1$, and therefore

$$N_{l0} = -\mathrm{We_f} \left(h_0 + \frac{\partial^2 h_0}{\partial \theta^2} \right),$$
$$T_0 = -\mathrm{Re_f} a u_E \left(-u_E \frac{\partial h_0}{\partial \theta} + v_E \right),$$

i.e.

$$\frac{\partial N_{l0}}{\partial \theta} = -\mathrm{We_f}\left(\frac{\partial h_0}{\partial \theta} + \frac{\partial^3 h_0}{\partial \theta^3}\right),$$

$$\frac{\partial T_0}{\partial \theta} = -\mathrm{Re_f}\left(a u_E\left(-u_E\frac{\partial^2 h_0}{\partial \theta^2} - \frac{\partial u_E}{\partial \theta}\frac{\partial h_0}{\partial \theta} + \frac{\partial v_E}{\partial \theta}\right) + \left(a\frac{\partial u_E}{\partial \theta} + \frac{\partial a}{\partial \theta}u_E\right)\left(-u_E\frac{\partial h_0}{\partial \theta} + v_E\right)\right).$$

So from (4.17)

$$F_0 = \mathrm{Re_f}\left(-\mathrm{We_f}\left(\frac{\partial h_0}{\partial \theta} + \frac{\partial^3 h_0}{\partial \theta^3}\right) + \frac{1}{\mathrm{Fr}}\sin\theta\right), \tag{4.19}$$

$$\frac{\partial F_0}{\partial \theta} = \mathrm{Re_f}\left(-\mathrm{We_f}\left(\frac{\partial^2 h_0}{\partial \theta^2} + \frac{\partial^4 h_0}{\partial \theta^4}\right) + \frac{1}{\mathrm{Fr}}\cos\theta\right). \tag{4.20}$$

Then substituting into (4.16), the leading order component of u is given by

$$u_0 = \mathrm{Re_f}\left(-\mathrm{We_f}\left(\frac{\partial h_0}{\partial \theta} + \frac{\partial^3 h_0}{\partial \theta^3}\right) + \frac{1}{\mathrm{Fr}}\sin\theta\right)\left(\frac{y^2}{2} - h_0 y\right) - \mathrm{Re_f} a u_E\left(-u_E\frac{\partial h_0}{\partial \theta} + v_E\right)y + u_{cyl}, \tag{4.21}$$

and the leading order component of v by

$$\begin{aligned} v_0 = -\Bigg(&\mathrm{Re_f}\left(-\mathrm{We_f}\left(\frac{\partial^2 h_0}{\partial \theta^2} + \frac{\partial^4 h_0}{\partial \theta^4}\right) + \frac{1}{\mathrm{Fr}}\cos\theta\right)\left(\frac{y^3}{6} - \frac{h_0 y^2}{2}\right) \\ &- \mathrm{Re_f}\left(a u_E\left(-u_E\frac{\partial^2 h_0}{\partial \theta^2} - \frac{\partial u_E}{\partial \theta}\frac{\partial h_0}{\partial \theta} + \frac{\partial v_E}{\partial \theta}\right) + \left(a\frac{\partial u_E}{\partial \theta} + \frac{\partial a}{\partial \theta}u_E\right)\left(-u_E\frac{\partial h_0}{\partial \theta} + v_E\right)\right)\frac{y^2}{2} \\ &+ \mathrm{Re_f}\left(-\mathrm{We_f}\left(\frac{\partial h_0}{\partial \theta} + \frac{\partial^3 h_0}{\partial \theta^3}\right) + \frac{1}{\mathrm{Fr}}\sin\theta\right)\left(-\frac{\partial h_0}{\partial \theta}\frac{y^2}{2}\right)\Bigg) \\ &+ v_{cyl}(\theta) - \frac{\partial u_{cyl}}{\partial \theta}y. \end{aligned} \tag{4.22}$$

We can use these expressions to plot the streamfunction, or we can also calculate the streamfunction ψ directly. At leading order in ϵ, the streamfunction ψ is defined as

$$u_0 = \frac{\partial \psi}{\partial y}, \tag{4.23}$$

$$v_0 = -\frac{\partial \psi}{\partial \theta}. \tag{4.24}$$

(The $1/r$ term that arises in cylindrical coordinates does not occur at leading order in the thin film.)

Integrating (4.23) gives

$$\psi = F_0\frac{y^3}{6} + (-F_0 h + T_0)\frac{y^2}{2} + u_{cyl}y + f(\theta), \quad \text{for some function } f.$$

Differentiating w.r.t. θ and substituting into (4.24),

$$\frac{\partial F_0}{\partial\theta}\frac{y^3}{6}+\frac{\partial}{\partial\theta}\left(-F_0h_0+T_0\right)\frac{y^2}{2}+\frac{\partial u_{cyl}}{\partial\theta}y+f'(\theta)=\frac{\partial F_0}{\partial\theta}\frac{y^3}{6}+\frac{\partial}{\partial\theta}\left(-F_0h_0+T_0\right)\frac{y^2}{2}-v_{cyl}(\theta)+\frac{\partial u_{cyl}}{\partial\theta}y.$$

Thus f is given by

$$f(\theta)=\int -v_{cyl}(\theta)\mathrm{d}\theta,$$

and the streamfunction is determined up to an arbitrary constant

$$\psi=F_0\frac{y^3}{6}+\left(-F_0h_0+T_0\right)\frac{y^2}{2}+u_{cyl}y-\int v_{cyl}(\theta)\mathrm{d}\theta.$$

Substituting in (4.19) and (4.20),

$$\begin{aligned}\psi=&-\mathrm{Re_f}\left(\mathrm{We_f}\left(\frac{\partial h_0}{\partial\theta}+\frac{\partial^3h_0}{\partial\theta^3}\right)-\frac{1}{\mathrm{Fr}}\sin\theta\right)\frac{y^3}{6}\\&+\left(\mathrm{Re_f}\left(\mathrm{We_f}\left(\frac{\partial h_0}{\partial\theta}+\frac{\partial^3h_0}{\partial\theta^3}\right)-\frac{1}{\mathrm{Fr}}\sin\theta\right)h+\mathrm{Re_f}au_E\left(u_E\frac{\partial h_0}{\partial\theta}-v_E\right)\right)\frac{y^2}{2}\\&+u_{cyl}(\theta)y-\int v_{cyl}(\theta)\mathrm{d}\theta. \quad (4.25)\end{aligned}$$

4.3.2 Method of plotting streamlines

In terms of the variables c_1 to c_6, used by the numerical solver,

$$u_0=-\left(c_1\left(\frac{\partial h_0}{\partial\theta}+\frac{\partial^3h_0}{\partial\theta^3}\right)+c_2\sin\theta\right)\left(\frac{y^2}{2}-h_0y\right)+\left(c_3(\theta)\frac{\partial h_0}{\partial\theta}+c_4(\theta)\right)y,$$

$$\begin{aligned}v_0=&\left(c_1\left(\frac{\partial^2h_0}{\partial\theta^2}+\frac{\partial^4h_0}{\partial\theta^4}\right)+c_2\cos\theta\right)\left(\frac{y^3}{6}-\frac{h_0y^2}{2}\right)-\left(\frac{\partial c_3}{\partial\theta}\frac{\partial h_0}{\partial\theta}+c_3\frac{\partial^2h_0}{\partial\theta^2}+\frac{\partial c_4}{\partial\theta}\right)\frac{y^2}{2}\\&+\left(c_1\left(\frac{\partial h_0}{\partial\theta}+\frac{\partial^3h_0}{\partial\theta^3}\right)+c_2\sin\theta\right)\left(-\frac{\partial h_0}{\partial\theta}\frac{y^2}{2}\right)+v_{cyl},\end{aligned}$$

and

$$\begin{aligned}\psi=&-\left(c_1\left(\frac{\partial h_0}{\partial\theta}+\frac{\partial^3h_0}{\partial\theta^3}\right)+c_2\sin\theta\right)\frac{y^3}{6}\\&+\left(\left(c_1\left(\frac{\partial h_0}{\partial\theta}+\frac{\partial^3h_0}{\partial\theta^3}\right)+c_2\sin\theta\right)h_0+c_3(\theta)\frac{\partial h_0}{\partial\theta}+c_4(\theta)\right)\frac{y^2}{2}-\int v_{cyl}(\theta)\mathrm{d}\theta.\end{aligned}$$

With the outflow through a narrow sink between θ_s and θ_e, defined by (4.9), then

$$\int v_{cyl}(\theta)=\begin{cases}0 & -\pi<\theta<\theta_s\\ v_{out}\frac{\theta-\theta_s}{\theta_e-\theta_s} & \theta_s<\theta<\theta_e\\ v_{out} & \theta_e<\theta<\pi.\end{cases}$$

A contour plot of ψ gives a smooth streamline plot with few numerical errors, and the Matlab function `streamslice` on u and v provides arrows to show the direction of the flow.

4.3.3 Streamlines used to calculate residence times

Figure 4.6 shows an example of streamlines, for the case where $a = 10^{-6}$, $u_E = 10^2$ and $v_E = 10^4$ are kept constant, and mass flows out through a sink at $\theta = 0$ at a rate chosen to match the mass into the film at each timestep. This example is chosen as it is equivalent to values in Chapter 3 of $\zeta = 10^{-3}$, $\alpha_u = 10^{-2}$, with a small additional mass flow.

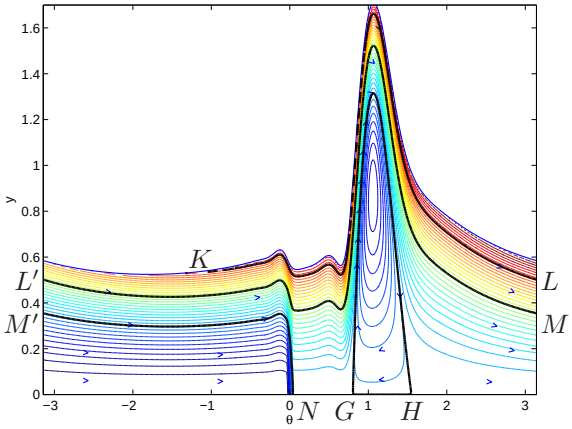

Figure 4.6: Residence cycles and recirculation based on a plot of streamlines

By following a streamline around, we can trace the path of a given fluid particle from its entrance into the film surface until it leaves at the sink. Starting for example at the point labelled $[K]$, fluid entering the surface at $\theta = -1$ follows the streamline with increasing θ, over the hump till at $\theta = \pi$, $[L]$, it is at approximately $y = 0.5$. At $\theta = -\pi$, $y = 0.5$ is on the streamline $[L']$. The particle goes round the cylinder again, past the sink, over the hump, till at $\theta = \pi$ it is at $y = 0.35$, $[M]$. At $\theta = -\pi$ this is on the streamline $[M']$, and this time the particle does not get past the sink at $\theta = 0$, and leaves the system at $[N]$. In this way we can see that fluid entering the surface goes around the cylinder between 2 and 3 times before leaving at the sink.

Calculating the residence *time*, rather than just the number of cycles, requires $\int u(\theta, y)\mathrm{d}\theta$. For each contour, u is interpolated at a number of θ positions, θ_i with y_i such as to remain on the contour. For that contour,

$$restime = \sum_i \frac{1}{2}\left(\frac{1}{u(\theta_{i+1}, y_{i+1})} + \frac{1}{u(\theta_i, y_i)}\right)(\theta_{i+1} - \theta_i)\,.$$

The total residence time is a sum over a set of contours which form a continuous path from the surface to the outflow. This data is of interest in analysing the larger system of oil flow through the bearing chamber and may be valuable in estimating heat transfer to the oil from the chamber wall.

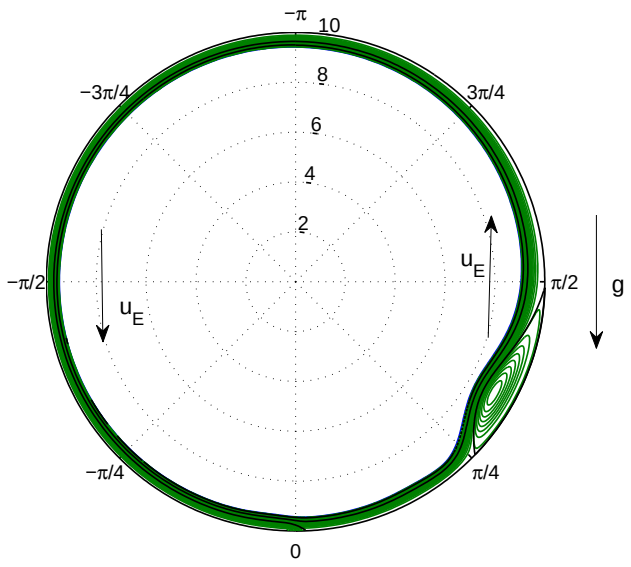

Figure 4.7: Film height profile and streamlines on a polar plot, with radius $R = 10$

4.3.4 Recirculation, stagnation and hotspots

In this example, there is recirculation, in a small region at the cylinder wall at around $\theta = 1$ (between $[G]$ and $[H]$ on figure 4.6) which never receives any fresh fluid from the surface. Temperature effects are not included in this model, but if advection of heat were to dominate conduction through the oil, this region could become a hot-spot, receiving cooling from the oil only by conductive transfer.

4.3.5 Polar plots

In order to visualise the physical behaviour of the system, it is instructive to plot the film profiles and streamlines on polar axes, as in figure 4.7. In the following chapters, the radius R used to scale the polar plot will vary for convenience. If R is too large, then variations in the film thickness cannot easily be seen. But if R is too small, then slight bulges in the film may be distorted to look like sharp peaks, with obtuse angles becoming acute. The value of R required for no distortion depends on the non-dimensionalisation used, and for those chosen in chapter 2, values of about $R = 100$ are typical, but in practice $R \approx 10$ is usually used.

4.4 Summary of this chapter

In this chapter we have extended the derivation of Chapter 2 to a more general set of boundary conditions, arriving at (4.6). We will model variable droplet input using one of the models given by (4.12) and (4.15). We have also shown how to plot streamlines which reveal underlying flow behaviour and can be used to determine residence times of fluid in the steady state. The results of this work will follow in Chapters 5–6.

Chapter 5

Film profiles for significant variable mass and momentum transfer at the surface

In Chapter 4 we derived (4.6), given on page 91, to describe the thickness of a rimming film driven by variable droplet impact, when droplets contribute significant mass as well as momentum, and when the cylinder wall may rotate and contain sinks to allow mass outflow. In this chapter, we will examine the effect of droplet mass (the parameters c_5 and c_6) on solutions of this equation. We will find that there are some parameters for which steady-state solutions cannot be found, and examine a simplified form of (4.6) to discover why. We will also consider the effect of changing the film area A on the solutions. We will re-dimensionalise in one example, to check on physical timescales. Finally we will consider the effect of non-uniform droplet impact on the film. Throughout this chapter we will examine the underlying flow as well as the film profiles.

5.1 Results with uniform droplet mass input

In the case where droplets contribute mass as well as momentum, the c_5 and c_6 terms of (4.6) are non-zero. In this section we focus on this mass contribution, to determine how important a role it plays, and in what manner it may change the film profile. For now, we take the cylinder wall to be stationary, $u_{cyl} = 0$. v_{cyl} is defined according to (4.10), with $\theta_s = -\pi/100$, $\theta_e = \pi/100$, so there is no flow out of the wall except through a sink about $\theta = 0$. At the sink sufficient flow leaves the cylinder at any timestep that the total mass of the film is conserved.

We fix the parameter values c_1 to c_4, and the cross-sectional area A, at values (given in table 5.1) which have been shown in Chapter 3 to produce a stable steady solution for $c_5, c_6 = 0$. We will explore a range of c_5 and c_6, investigating the effect of these parameters independently. $c_5 \leq 0$ and $c_6 \leq 0$, corresponding to mass addition to the

c_1	10^{-4}		
c_2	-1	A	4.382 (unless otherwise stated)
c_3	10^{-3}		
c_4	1		
c_5	≤ 0, varies	u_{cyl}	0
c_6	≤ 0, varies	v_{cyl}	as defined (4.10)

Table 5.1: Parameter values for this section

film from droplets travelling in the azimuthal and radial directions respectively. The results are summarised in figure 5.1. A great deal of complex behaviour can be seen, so several of the plots are also shown enlarged, in figures 5.2 to 5.5.

For comparison, figure 5.2 (and the top-left of figure 5.1) shows the base case when $c_5 = 0$ and $c_6 = 0$. Since $A > A_{crit}$, there is a shock, which is at about $\theta = \pi/4$.

5.1.1 Non-physical cases

Some of these parameter combinations are not physically feasible, but are still included to aid understanding of the importance of each component of the equation. Consider for example, the combination $c_5 = -1$, $c_6 = 0$, illustrated in figures 5.1 and 5.7. This film profile could arise if a clockwise rotation were included, $u_{cyl} = -1$, but in this section $u_{cyl} = 0$. For this to arise from the droplet terms alone would require droplets to have a momentum component that is primarily in the radial direction ($v_E > u_E$), but droplet mass moving in only in the azimuthal direction ($u_E > v_E$). This explains the streamlines in figure 5.7, which appear to indicate that droplets enter the surface on the left hand side of the shock, and leave on the right hand side of the shock, adding and subtracting mass according to the sign of $\frac{\partial h}{\partial \theta}$, but failing to impart any azimuthal momentum.

5.1.2 Varying c_6, when $c_5 = 0$

There are interesting solutions when non-zero c_6 is introduced. At $c_5 = 0$, as c_6 decreases from 0, we see a descending shock develop over the sink (see the first column of figure 5.1 and figure 5.3). The film thickens to the left hand side of the sink, because the mass building up there is about to fall down the sink. In each case here the total mass in the film is maintained constant at $A = 4.382$ by adjusting the outflow at the sink. When $c_6 = 0$, a shock at $\pi/4$ is required to accommodate all the fluid in a stable steady-state profile, since $A > A_{crit}$, but when $c_6 = -0.05$, so much fluid is built up on the left-hand side of the sink that the ascending shock and associated recirculation does not occur. If

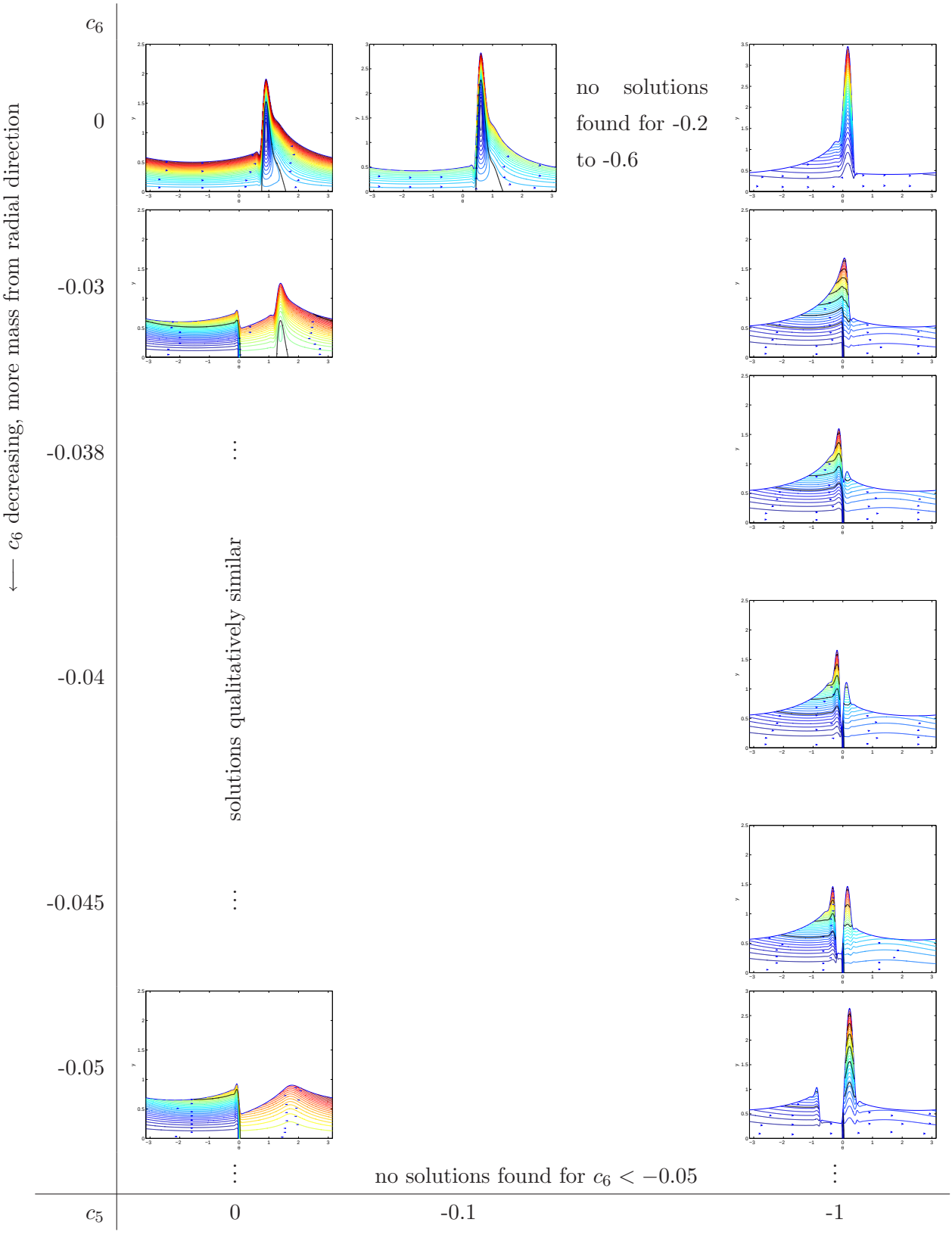

Figure 5.1: Summary of film profiles and streamlines when c_5 and c_6 are varied. Other parameters are $A = 4.382$, $c_1 = 10^{-4}$, $c_2 = -1$, $c_3 = 10^{-3}$, $c_4 = 1$, $u_{cyl} = 0$.

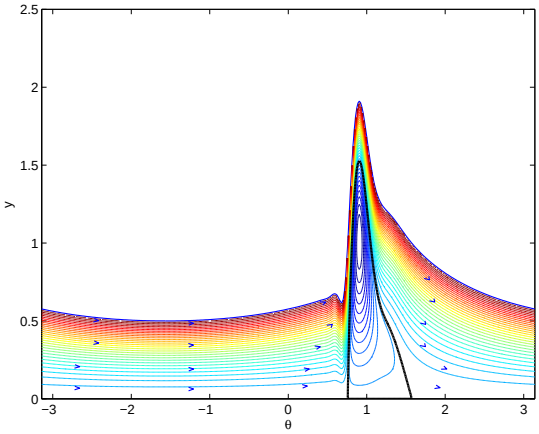

Figure 5.2: Streamlines when $c_5 = 0$, $c_6 = 0$. Other parameters are $A = 4.382$, $c_1 = 10^{-4}$, $c_2 = -1$, $c_3 = 10^{-3}$, $c_4 = 1$, $u_{cyl} = 0$.

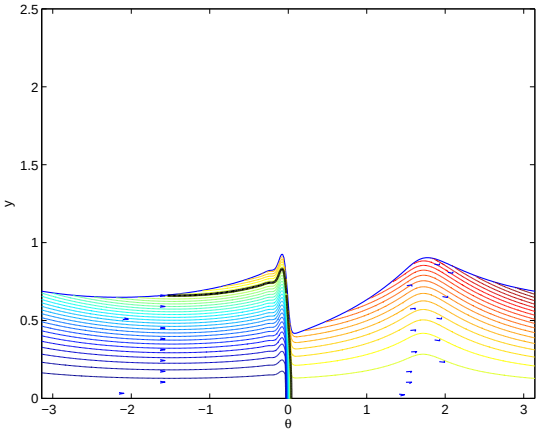

Figure 5.3: Streamlines when $c_5 = 0$, $c_6 = -0.05$. Other parameters are $A = 4.382$, $c_1 = 10^{-4}$, $c_2 = -1$, $c_3 = 10^{-3}$, $c_4 = 1$, $u_{cyl} = 0$.

c_6 is decreased beyond -0.05, even using the continuation method, we cannot find any stable steady-state solutions, it appears that too great a fraction of the total fluid A is entering and leaving at the sink to form a continuous film. A film may be formed with larger total mass A in the system.

5.1.3 Varying c_6, when $c_5 = -1$

The right-hand column of figure 5.1 shows the effect of fixing $c_5 = -1$ and varying $|c_6|$. At $c_5 = -1$ and $c_6 = 0$, the peak lies across the sink position $\theta = 0$, so as c_6 decreases from 0 the sink draws fluid directly out of the peak. For $c_6 = -0.03$, as shown in figure 5.4, a sharp dip starts to develop which for $c_6 = -0.05$ has broadened between two distinct peaks (figure 5.5). For all these cases, there are streamlines that go straight through the peak, so fluid is apparently leaving the film on the right-hand side of the peak. However, this is not a physically feasible set of parameters. The value of c_3 is small compared to c_4, but c_5 is large compared to c_6, and the substantial azimuthal component of mass flux is not matched by momentum in the same direction.

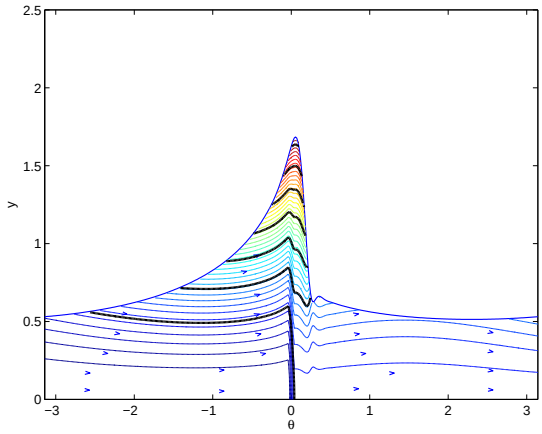

Figure 5.4: Streamlines when $c_5 = -1$, $c_6 = -0.03$. Other parameters are $A = 4.382$, $c_1 = 10^{-4}$, $c_2 = -1$, $c_3 = 10^{-3}$, $c_4 = 1$, $u_{cyl} = 0$. This is not a physically feasible parameter set (see text).

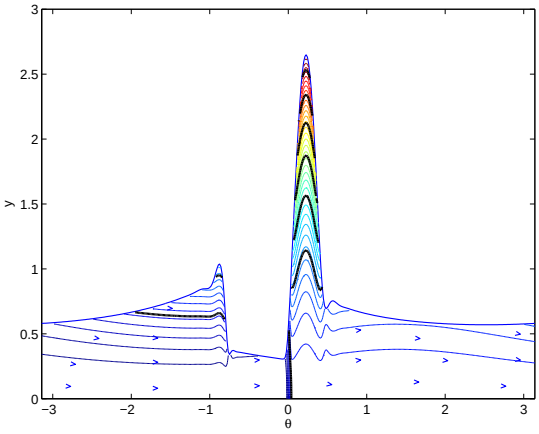

Figure 5.5: Streamlines when $c_5 = -1$, $c_6 = -0.05$. Other parameters are $A = 4.382$, $c_1 = 10^{-4}$, $c_2 = -1$, $c_3 = 10^{-3}$, $c_4 = 1$, $u_{cyl} = 0$.

5.1.4 Varying c_5 when $c_6 = 0$

Now consider the effect of changing the parameter c_5, the azimuthal component of the droplet mass flux contribution, for $c_6 = 0$ (the first row of figure 5.1). A distinct transition is seen between $c_5 = 0$ and $c_5 = -1$. Intermediate parameter ranges have been investigated, but stable steady solutions have not been found throughout the parameter regime between them. $c_5 = -0.15$ and $c_5 = -0.7$ both converged, but not $c_5 = -0.2$ or $c_5 = -0.6$ which were numerically unstable (the transient solver gradually lost mass from the system).

For $c_5 = -1$ the film profile h is identical to that with clockwise rotation, with $u_{cyl} = -1$. However the underlying streamlines are different. Figures 5.6 ($c_5 = -0.1$) and 5.7 ($c_5 = -1$) show the change between a rising shock in $\theta > 0$ and a descending shock near $\theta = 0$. It is worth noting that the descending shock is not in $\theta < 0$.

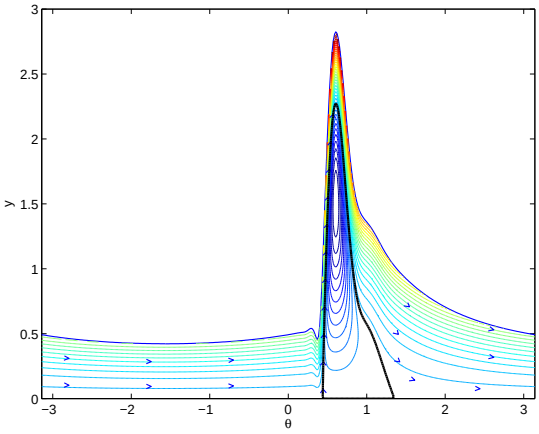

Figure 5.6: Streamlines when $c_5 = -0.1$, $c_6 = 0$. Other parameters are $A = 4.382$, $c_1 = 10^{-4}$, $c_2 = -1$, $c_3 = 10^{-3}$, $c_4 = 1$, $u_{cyl} = 0$. Qualitatively similar results were found for $c_5 = -0.15$

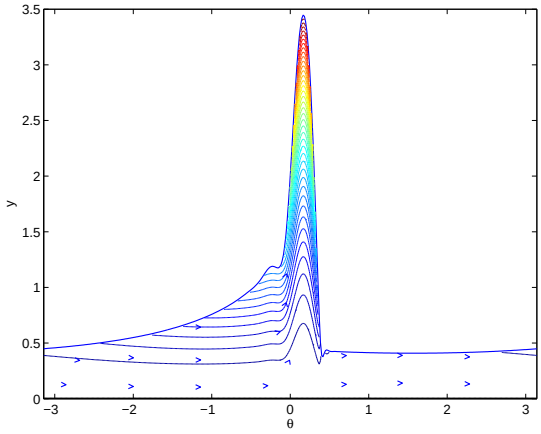

Figure 5.7: Streamlines when $c_5 = -1$, $c_6 = 0$. Other parameters are $A = 4.382$, $c_1 = 10^{-4}$, $c_2 = -1$, $c_3 = 10^{-3}$, $c_4 = 1$, $u_{cyl} = 0$. Qualitatively similar results were found for $c_5 = -0.7$

In the case $c_5 = 0$, the dominant forces are gravity and surface shear. With $c_5 = -1$, the film is also driven by mass addition from the azimuthal direction on the clockwise (left) side of any shock and, effectively, mass removal anticlockwise (right) of any shock. In the equation for film profile h this is equivalent to the case where a balance of wall rotation and gravity causes a build-up on $\theta < 0$, and the surface shear pulls it down to near $\theta = 0$.

5.1.5 Residence times

The residence time for fluid in the system is calculated as described in §4.3.3. With $A = 4.382$, $c_1 = 10^{-4}$, $c_2 = -1$, $c_3 = 10^{-3}$, $c_4 = 1$, then varying c_5 and c_6 the number of cycles for which a particle is resident are given in table 5.2. When $c_6 = 0$ there is no net mass input and the system is closed, so the residence time is given as ∞. The symbol $\times$ indicates that the transient solver failed to give a result. The residence time increases when there is little droplet mass contribution, being inversely proportional to c_6.

$c_6 \setminus c_5$	0	-10^{-3}	-10^{-2}	-10^{-1}	-1
0	∞	∞	∞	∞	∞
-0.001	26	26	27	55	483
-0.01	2	2	2	4	39
-0.02	1	1	1	2	14
-0.03	1	1	1	1	6
-0.04	0	0	0	0	4
-0.05	0	0	0	$\times$	5
-0.1	$\times$	$\times$	$\times$	$\times$	$\times$
-1	$\times$	$\times$	$\times$	$\times$	$\times$

Table 5.2: Residence times, c_5 vs c_6.

5.2 The leading order when the azimuthal droplet mass term dominates

In §5.1 we found that steady solutions of (4.6) with parameters as in table 5.1 existed for $c_5 = 0$ and $c_5 = -1$, but were very different in nature. Also for $-0.6 \leq c_5 \leq -0.2$ no steady solutions were found for $A = 4.382$. This leads us to look at (4.6) again. Steady solutions of (4.6) with $u_{cyl} = 0$, $c_6 = 0$ and c_5 constant are given by

$$c_1 \left(\frac{\partial h}{\partial \theta} + \frac{\partial^3 h}{\partial \theta^3} \right) \frac{h^3}{3} - \sin\theta \frac{h^3}{3} + \left(c_3 \frac{\partial h}{\partial \theta} + 1 \right) \frac{h^2}{2} + c_5 h = q. \tag{5.1}$$

Since c_1 and c_3 are small, we explore what happens when they are negligible, and see if this gives us insight into the full solutions. In this case, (5.1) reduces to the cubic

$$-\sin\theta \frac{h^3}{3} + \frac{h^2}{2} + c_5 h = q. \tag{5.2}$$

We will establish the range of c_5-q space for which shock solutions may exist. Then, given c_5, we will know which q to examine, and using a kinematic wave argument will narrow down the possible shock solutions. Finally, we will show that $A = 4.382$ is too large to find a steady solution for $c_5 = -0.5$.

5.2.1 Solutions of the cubic with the linear (c_5) term.

In this section we will categorise the roots of (5.2) analytically, and establish for which regions of the c_5-q parameter space it is possible to have continuous or shock solutions for the film profile.

Firstly, to find whether the roots of (5.2) are real or complex, we transform it into the form $x^3 + px + r = 0$, with discriminant $D = \left(\frac{p}{3}\right)^3 + \left(\frac{r}{2}\right)^2$. One real and two complex

conjugate roots of the cubic exist if $D > 0$, three real roots if $D \leq 0$ with two of the roots identical if $D = 0$. Note that real x corresponds to real h.

The transformation is given by

$$x = h - \frac{1}{2\sin\theta}$$

with

$$p = -\frac{3c_5}{\sin\theta} - \frac{3}{4\sin^2\theta}, \quad r = \frac{3q}{\sin\theta} - \frac{1}{4\sin^3\theta} - \frac{3c_5}{2\sin^2\theta}.$$

Therefore

$$D = \frac{1}{16\sin^4\theta}\left(6q\left(6q\sin^2\theta - 1 - 6c_5\sin\theta\right) - c_5^2\left(3 + 16c_5\sin\theta\right)\right). \tag{5.3}$$

The critical value $D = 0$ is at

$$12\sin^2\theta\, q = 1 + 6c_5 \pm \left(1 + 4c_5\sin\theta\right)^{3/2}. \tag{5.4}$$

At $\sin\theta = \pm 1$, (5.4) has up to four possible solutions, which are plotted in each of figures 5.8–5.11 using the following coloured lines.

$$12q = 1 + 6c_5 + \left(1 + 4c_5\right)^{3/2}, \qquad c_5 > -1/4, \qquad \text{blue}, \tag{5.5}$$

$$12q = 1 + 6c_5 - \left(1 + 4c_5\right)^{3/2}, \qquad c_5 > -1/4, \qquad \text{red}, \tag{5.6}$$

$$12q = 1 - 6c_5 + \left(1 - 4c_5\right)^{3/2}, \qquad c_5 < 1/4, \qquad \text{magenta}, \tag{5.7}$$

$$12q = 1 - 6c_5 - \left(1 - 4c_5\right)^{3/2}, \qquad c_5 < 1/4, \qquad \text{green}. \tag{5.8}$$

The four solutions meet at 6 critical points, given by $(c_5, q) = (\pm 1/4, -1/24)$, $(0, 1/6)$, $(0, 0)$ and $(\pm 0.2165, -1.48)$. The sign of D is dependent on the sign of θ. The regions of c_5-q space that result in positive or negative values of D for θ positive or negative are shown in figure 5.8. In this figure, the region marked for example $-+$ is where $D < 0$ for $\theta < 0$, $D > 0$ for $\theta > 0$, and there is at most one real root for $\theta < 0$, but three for $\theta > 0$.

Secondly, for a continuous physical film we are only interested in positive solutions of h, so we need to know which regions of c_5-q parameter space result in positive or negative roots. Note that we must look for positive solutions of h, not just the translated form x.

If the roots of (5.2) are given by h_1, h_2, h_3, then

$$\left(h - h_1\right)\left(h - h_2\right)\left(h - h_3\right) = h^3 - \frac{3}{2\sin\theta}h^2 - \frac{3c_5}{\sin\theta}h + \frac{3q}{\sin\theta}.$$

Hence

$$h_1 + h_2 + h_3 = \frac{3}{2\sin\theta}, \tag{5.9}$$

$$h_1h_2 + h_1h_3 + h_2h_3 = -\frac{3c_5}{\sin\theta}, \tag{5.10}$$

$$h_1h_2h_3 = -\frac{3q}{\sin\theta}. \tag{5.11}$$

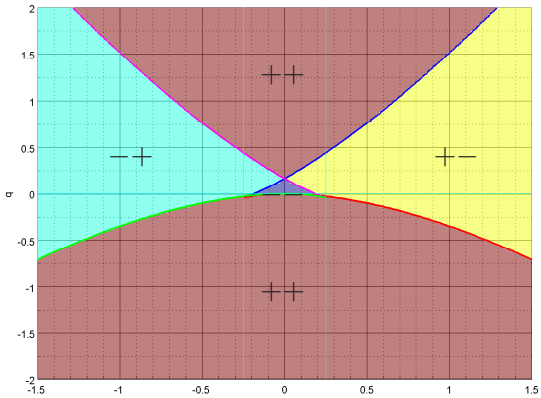

Figure 5.8: The sign of D in c_5-q space for $\theta < 0$ and $\theta > 0$ respectively. Regions are indicated ++ (red): $D > 0$, $D > 0$; +- (yellow): $D > 0$, $D < 0$; -+ (turquoise): $D < 0$, $D > 0$; – (lilac): $D < 0$, $D < 0$.

For $D > 0$, there is only one real root, h_1 say, and the two complex roots satisfy $h_3 = \bar{h}_2$ and $h_2 \times h_3 > 0$. So by (5.11)

$$1 \text{ positive real root, } h_1 > 0 \iff \frac{q}{\sin\theta} < 0. \tag{5.12}$$

For $D \leq 0$, there are 3 real roots, then by (5.11) there are

$$0 \text{ or } 2 \text{ positive real roots} \iff \frac{q}{\sin\theta} > 0. \tag{5.13}$$

$$1 \text{ or } 3 \text{ positive real roots} \iff \frac{q}{\sin\theta} < 0. \tag{5.14}$$

In (5.13) and (5.14), we still need to distinguish between the cases. This can be done by differentiating (5.2) with respect to h and considering whether turning points lie in $h > 0$ or $h < 0$. We find six cases:

θ	c_5	Number of positive real roots
−	−	1 or 2
−	0	1 (unless D=0, then 0 or 1 positive)
−	+	0 or 1
+	−	2 or 3
+	0	2 (unless D=0, then 1 or 2 positive)
+	+	1 or 2

By combining all this information we have sufficient information to predict the number of roots for any values of c_5 and q. This is given in table **??**.

Sample numerical solutions of the cubic in different regions of c_5-q space are illustrated in figures 5.9- 5.11, and they all agree with the results summarised in table 5.3.

Villegas-Díaz studied the equation

$$-\sin\theta\frac{h_*^3}{3} + \gamma\frac{h_*^2}{2} + h_* = q_*, \tag{5.15}$$

			$-\pi < \theta < 0$	$0 < \theta < \pi$
$q > 0$	$D > 0$	any c_5	1	0
	$D \leq 0$	$c_5 > 0$	1	2
		$c_5 = 0$	1	2
		$c_5 < 0$	1	2
$q < 0$	$D > 0$	any c_5	0	1
	$D \leq 0$	$c_5 > 0$	0	1
		$c_5 < 0$	2	3

Table 5.3: Number of positive roots of (5.2) in $\theta < 0$, $\theta > 0$, according to the sign of q, D, and c_5. sign$D$ is found from c_5 and q and θ according to figure 5.8.

and produced a similar chart of solutions in γ-q space [51]. Writing $h_* = h\gamma$, (5.15) becomes

$$-\sin\theta\frac{h^3}{3} + \frac{h^2}{2} + \frac{h}{\gamma^2} = \frac{q}{\gamma^3},$$

and we recover (5.2) with

$$c_5 = \frac{1}{\gamma} \text{ and } q = \frac{q_*}{\gamma^3}. \tag{5.16}$$

Villegas-Díaz found the critical lines

$$q_*^0 = \frac{1}{12}\left(\gamma(\gamma^2+6) + (\gamma^2+4)^{3/2}\right), q_*^\pi = \frac{1}{12}\left(\gamma(\gamma^2-6) - (\gamma^2-4)^{3/2}\right),$$

which with the substitution (5.16) become (5.5) and (5.8) respectively. However, Villegas-Díaz' results are only for real γ, so cannot tell us about $c_5 < 0$. Figure 5.9 is thus an extension to his figure 3.8, coinciding with it along the line $c_5 = 1$, $\gamma = 1$.

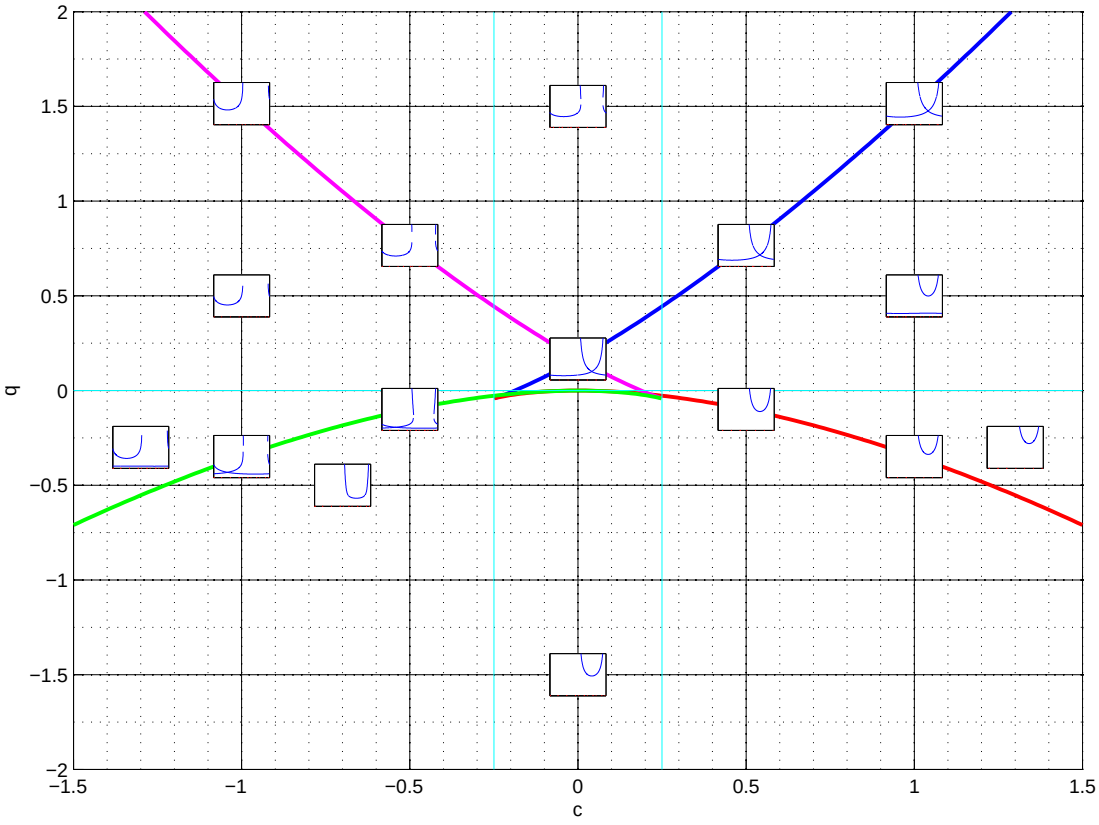

Figure 5.9: The possible solutions to the cubic (5.2) in c_5-q space. The lines represent $D = 0$, see (5.5-5.8) for colours.

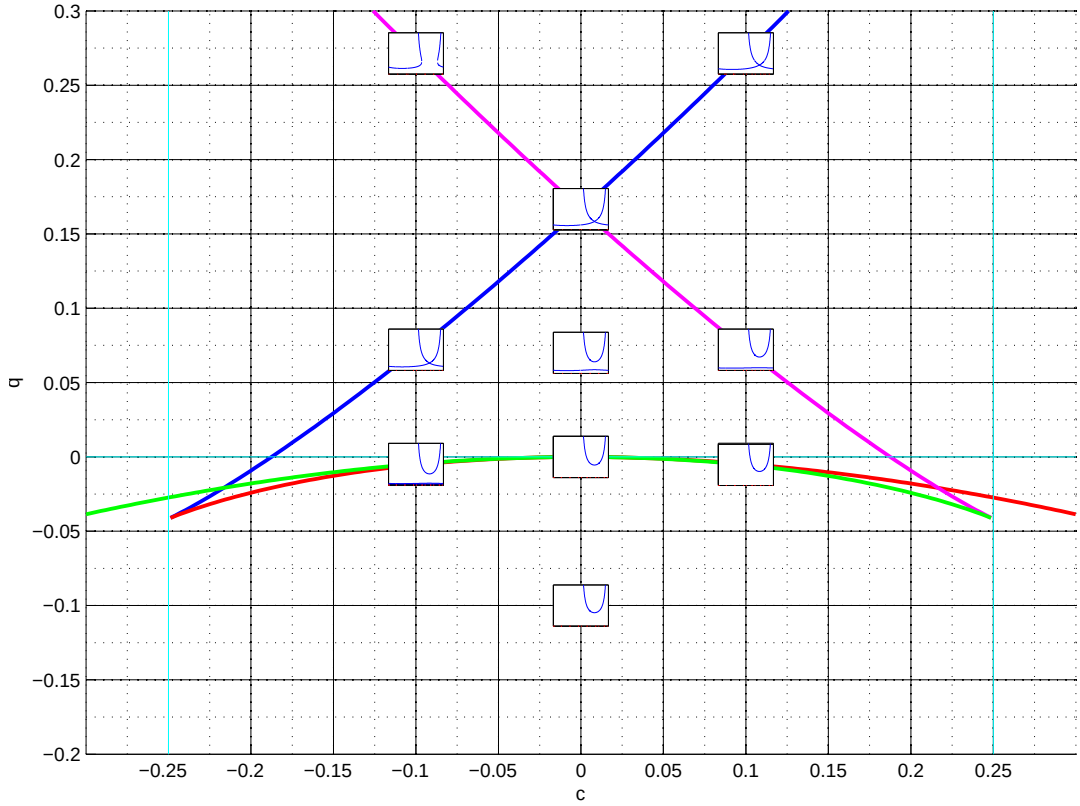

Figure 5.10: The possible solutions to the cubic (5.2) in c_5-q space, magnified about the origin. The lines represent $D = 0$, see (5.5-5.8) for colours.

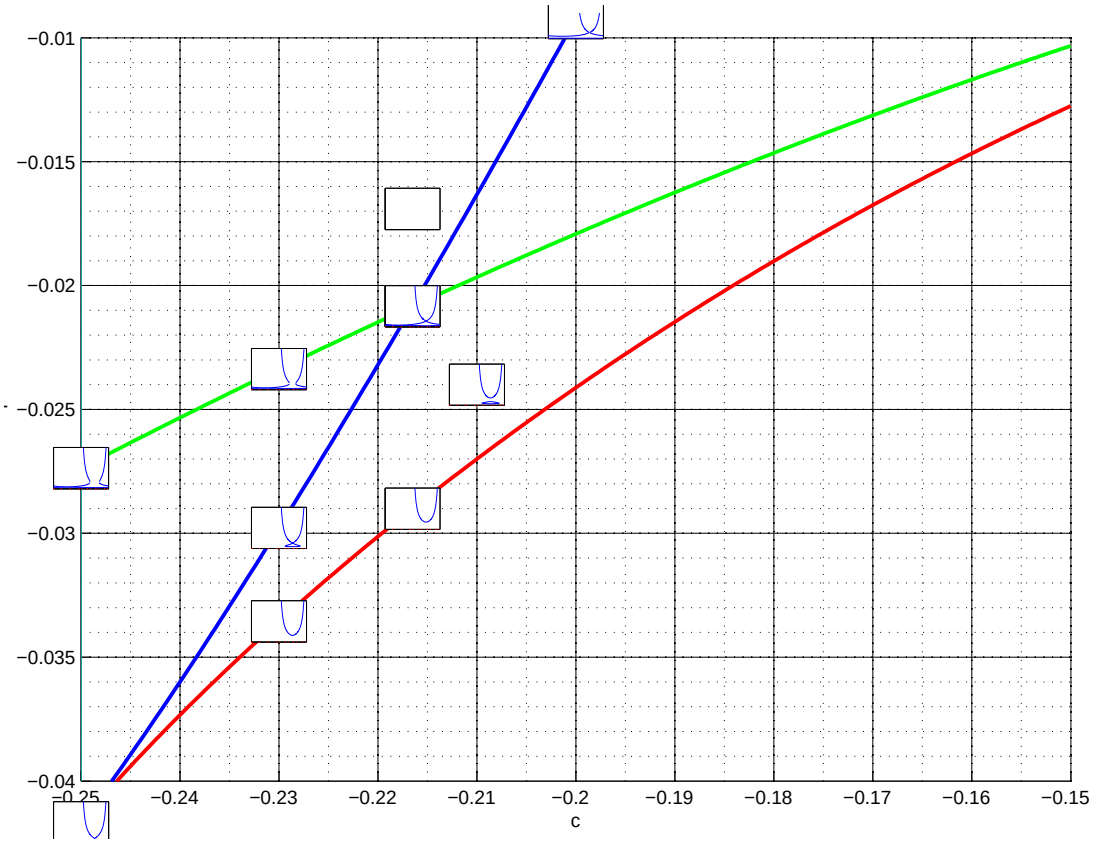

Figure 5.11: The possible solutions to the cubic (5.2) in c_5-q space, magnified about $-0.05 < q < 0$, where there is particularly complex behaviour. The lines represent $D = 0$, see (5.5-5.8) for colours.

Of the regions in these plots, the most important for our purposes is that where physical solutions can be found; that is where there exists a stable completely wetting film, possibly including shocks. In this region there is at least one piecewise-continuous positive real solution h for all θ. The region is given by the values of q and c_5 in table 5.3 for which there are 1, 2 or 3 roots, that is:

$$q > 0 \qquad \text{and} \begin{cases} \text{any } D \text{ when } \theta < 0 \\ D \leq 0 \text{ when } \theta > 0 \end{cases}$$

or

$$q < 0, c_5 < 0 \qquad \text{and} \begin{cases} D \leq 0 \text{ when } \theta < 0, \\ \text{any } D \text{ when } \theta > 0 \end{cases}$$

and is illustrated in figures 5.12 and 5.13.

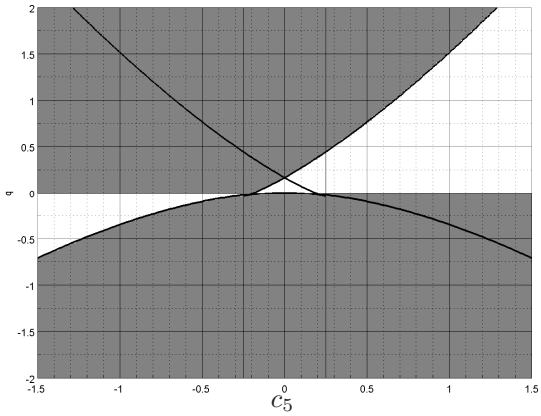

Figure 5.12: c_5-q space. White region: completely wetting films are possible. Grey region: no completely wetting solutions exist (even with shocks). The lines represent $D = 0$, see (5.5-5.8).

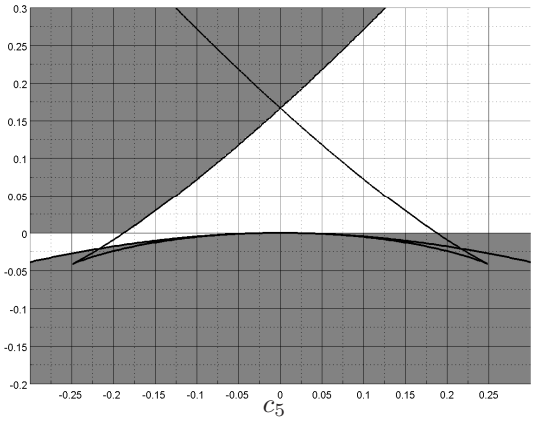

Figure 5.13: Magnified c_5-q space. White region: completely wetting films are possible. Grey region: no completely wetting solutions exist (even with shocks). The lines represent $D = 0$, see (5.5-5.8).

So, given the parameter c_5, we have found the range of flux q for which there is a completely wetting solution. For much of the region, there are also various larger branches, and there is the possibility of increasing the total area of the film by incorporating these using shocks. In the next sections, we will discover which of these shock solutions have the possibility of being stable, by applying a kinematic wave argument. Branches can be joined without shocks when they meet, when c_5 and q are on the lines given by (5.5-5.8). Particular values fulfilling these criteria that we will examine in the next section include

c_5	q
0	$1/6$
-0.5	-0.0997
-1.0	-0.3484

5.2.2 Possible stable shock solutions of the cubic

A similar matching argument to that in §3.2 could be employed to determine which shock solutions are plausible in the presence of smoothing from other terms. The argument would proceed as before, attempting to match an inner solution $H(\phi)$, where $\theta = \theta_K + \delta\phi$, to the outer solutions to the cubic h_j. We would linearize using $H(\phi) = h_j + f(\phi)$, and obtain f of the form

$$f = Ce^{\lambda\phi}, \quad \lambda^3 + a_j\,\lambda + b_j = 0.$$

where

$$a_j = \frac{3\,c_3}{2h_j\,c_1^{1/3}} > 0, \quad b_j = \frac{3}{h_j^2}\left(-h_j \sin\theta_K + 1 - c_5 h_j\right).$$

The sign of b_j would be critical in determining whether there is sufficient freedom in f to match as $\phi \to \pm\infty$. To proceed further we would have to consider individual regions of the c_5-q solution space; no general conclusions could be made.

Since the matching argument is not so straight-forward as in Chapter 3, we instead use kinematic wave theory to draw further conclusions about the cubic solutions produced in §5.2. This technique, discussed in some detail by Villegas-Díaz [51], does not allow us to consider the smoothing effects of the terms containing derivatives of h, but it does tell us something about which shocks may be stable.

For the kinematic equation $\frac{\partial h}{\partial t} + \frac{\partial q}{\partial \theta} = 0$, the kinematic wave speed is given by $w = \frac{\partial q}{\partial h}$. Small disturbances propagate in the direction of w and may be absorbed by shocks moving slightly to a new stable position, or build up at critical points where $w = 0$. As described in §3.5.4, disturbances moving towards a critical point are focussed there, their amplitudes increasing and the solution being unstable.

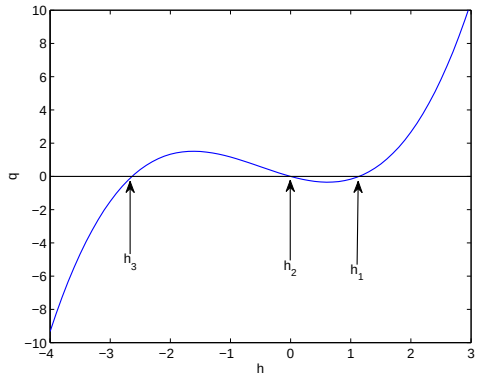

Figure 5.14: Sketch to illustrate why $w_1 > 0$ etc when $q \to \infty$ as $h \to \infty$. The gradients are reversed if $q \to -\infty$ as $h \to \infty$.

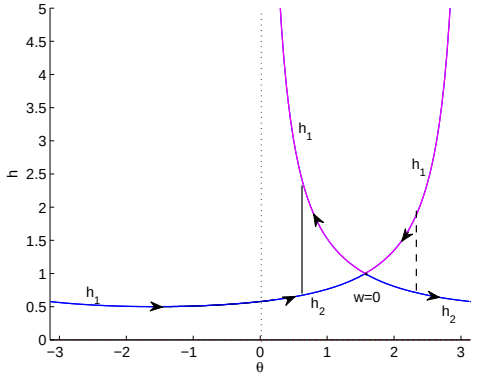

Figure 5.15: Possible shocks between positive branches of the cubic (5.2) when $c_5 = 0$, $q = 1/6$. Arrows indicate the direction of propagation of small disturbances. The solid line is a stable shock, the dashed line an unstable shock.

The cubic (5.2) has up to three real roots, $h_1 > h_2 > h_3$. For $i = 1, 2, 3$, the wave speed on that branch is

$$w_i = \left.\frac{\partial q}{\partial h}\right|_{h_i} = -h_i^2 \sin\theta + h_i + c_5.$$

As illustrated in figure 5.14, if $q \to \infty$ as $h \to \infty$ then the gradient and hence w is positive for the largest root, negative for the next etc. The sign of w_i is given by

$q \to \infty$ as $h \to \infty$ (i.e. $\theta < 0$)	$q \to -\infty$ as $h \to \infty$ (i.e. $\theta > 0$)
$w_1 > 0$	$w_1 < 0$
$w_2 < 0$	$w_2 > 0$
$w_3 > 0$	$w_3 < 0$

If there is only one real root, the wave speed w_1 has the same sign as above.

Shocks may occur between any of the branches h_1, h_2, h_3. But solutions with some

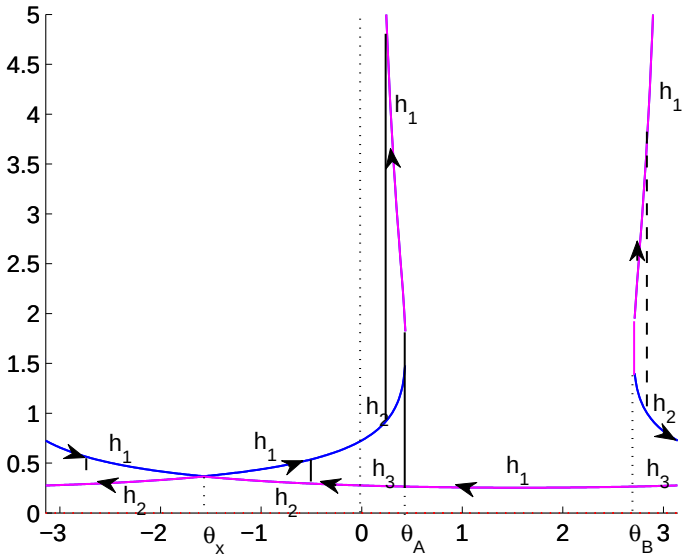

Figure 5.16: Possible shocks between positive branches of the cubic (5.2) when $c_5 = -0.5$, $q = -0.0997$. Arrows indicate the direction of propagation of small disturbances. θ_A, θ_B are the edge of the region with only one positive solution.

shock positions will be unstable. For example, in the case $c_5 = 0$, $q = 1/6$, illustrated in figure 5.15, then a shock at $0 < \theta < \pi/2$ is stable, and any disturbance will propagate in the direction of w towards the shock and be absorbed by it. However a shock at $\pi/2 < \theta < \pi$ is unstable. A disturbance will propagate away from it, and converge at the critical point $\theta = \pi/2$ at which $w = 0$.

Now if we apply this technique in the solution space where $c_5 = -0.5$, $q = -0.0997$ then we get a solution that has the solution branches illustrated in figure 5.16. The completely wetting positive solution having smallest area consists of branches

$$h = \begin{cases} h_2 & (-\pi < \theta < 0), \\ h_3 & (0 < \theta < \theta_A), \\ h_1 & (\theta_A < \theta < \theta_B), \\ h_3 & (\theta_B < \theta < \pi), \end{cases}$$

though this solution is unstable, as disturbances would build up at the critical point $\theta_x = -\pi/2$. There is no stable way to include the upper branch in $\theta < -\pi/2$, or the upper branch that occurs in $\theta_B < \theta < \pi$. But the other upper branches can be added to the smallest solution using shocks, in three ways:

- a descending shock from h_1 to h_2 in $\theta < 0$;
- a descending shock from h_2 to h_3 in $0 < \theta < \theta_A$;

- a rising shock from h_2 to h_1 in $0 < \theta < \theta_A$, then a descending shock from h_1 to h_3 in $0 < \theta < \theta_A$.

Kinematic wave theory suggests that the first two possibilities, illustrated in figure 5.17, are stable. The third option, in figure 5.18, may be unstable if the shocks are widely spaced, as the down shock is unstable if it is isolated. But if the two fronts are close enough together, then they can interact. The total double shock, considered as a whole, absorbs disturbances from either side, and may therefore be stable. The separation width beyond which they become unstable is alluded to by Shuaib *et al.* [43], and explained in more detail by Levy and Shearer [30].

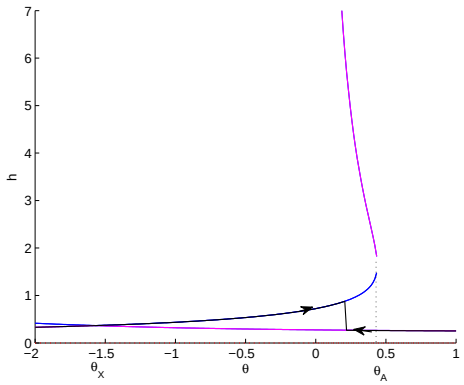

Figure 5.17: Close-up of the solution to the cubic (5.2), $c_5 = -0.5$, $q = -0.0997$ with a single descending shock. The shock is stable.

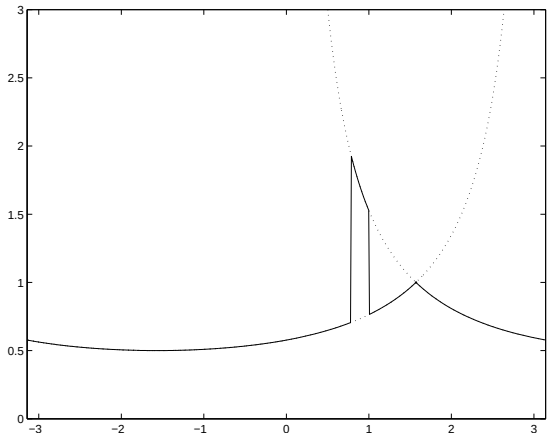

Figure 5.18: Close-up of the solution to the cubic (5.2), $c_5 = -0.5$, $q = -0.0997$, with a double shock. The second front is unstable alone, but if close enough interacts with the first, and the double shock is stable.

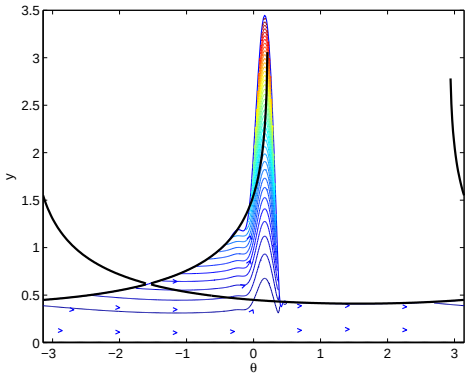

Figure 5.19: Overlay of cubic solution with A=4.382 and $c_5 = -1$ and full numerical solution with smoothing terms $c_1 = 10^{-4}$, $c_3 = 10^{-3}$.

5.2.3 Maximum supportable film area

Figure 5.19 shows that for $c_5 = -1$ the descending shock from h_2 to h_3 is close to the full numerical solution found in §5.1 for $c_5 = -1$. But why was no numerical solution obtained for $c_5 = -0.5$? In this region, for $q = -0.0997$ there is the cubic solution illustrated in figure 5.17 and the single shock is stable. But the branches are a little lower than for the $c_5 = -1$ case. We conjecture that the solution we have been seeking, with $A = 4.382$, contains too much mass for a single shock solution to be stable, and that if this mass necessitated a wide double shock up to h_1 in $\theta > 0$, then it may not be stable.

To analytically find the area under the branches of the cubic solutions for different shock positions is possible, but involves extremely unwieldy algebraic expressions, to little benefit. Instead we numerically seek the area for the particular case of interest to us.

To select the branches to include for the integration, we need to know the positions of the branch crossing points. For these we return to D, the discriminant of the cubic, given by (5.3). At the branch crossing points, two solutions h_i are identical and $D = 0$, leading to

$$\sin(\theta) = \frac{1}{18q^2}\left(9qc_5 + 4c_5^3 \pm 2^{1/2}\left(2c_5^2 + 3q\right)^{3/2}\right). \tag{5.17}$$

This yields four values of θ; in the case of $c_5 = -1$, $q = -0.3484$ they are $\theta_X = -\pi/2$ (repeated), $\theta_A = 0.2098$ and $\theta_B = 2.9318$.

The maximum area when there is only a single shock occurs when the shock is at θ_A, for a double shock the shocks are at 0 and θ_A. The single shocks are illustrated in

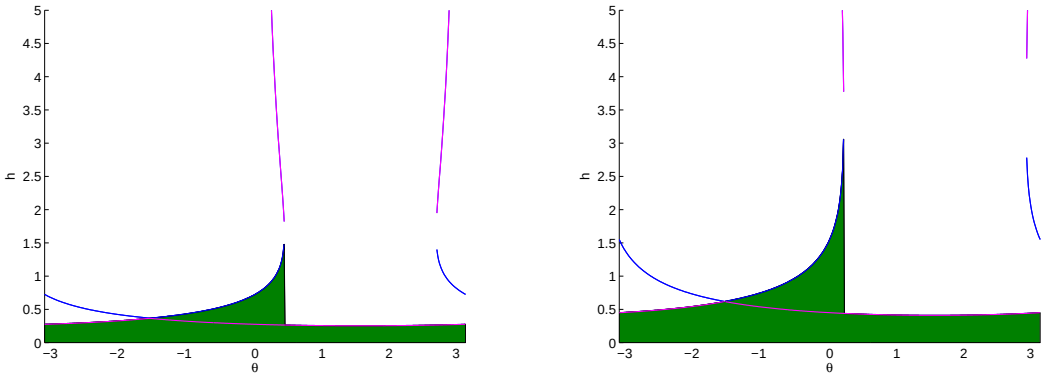

(i) (ii)

Figure 5.20: The cubic solution with maximum area using a single shock, for (i) $c_5 = -0.5$, (ii) $c_5 = -1$

figure 5.20. The areas are:

	A_{max} (single)	A_{max} (double)
$c_5 = -0.5$	2.38	*unbounded*
$c_5 = -1$	3.89	*unbounded*

For both values of c_5, the upper solution $h_1 \sim 3/(2\theta)$ as $\theta \to 0_+$. (This can be shown by series expansion of h_1). Hence the integral of the double shock increases as $3/2 \ln \theta$ as the position of the rising part of the shock tends to 0, and the area of the film is unbounded. As in (3.10), the limitation of the thin-film approximation prevents this from being physically inconsistent.

For $c_5 = -1$, the single shock maximum area is slightly less than the area $A = 4.382$ for which we managed to find a solution, illustrated in figure 5.19. The discrepancy may be due to the effect of the smoothing terms, or a slight double shock contribution from the upper solution branch.

For the case $c_5 = -0.5$, an area of $A = 4.382$ would require a wide double shock up to h_1 branch in $\theta > 0$, and indeed we do not find a stable numerical solution for $A = 4.0$ or above. If we run the full film calculation with $A = 2.381$, we find a stable film, which is illustrated in figure 5.21. As we increase the area as far as $A = 3.5$, the peak grows as shown in figure 5.22, although the smoothing terms prevent it from exactly matching the double shock.

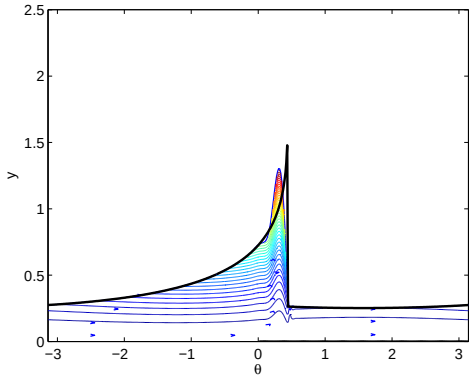

Figure 5.21: Overlay of cubic solution with A=2.381 and $c_5 = -0.5$ and full numerical solution with smoothing terms $c_1 = 10^{-4}$, $c_3 = 10^{-3}$.

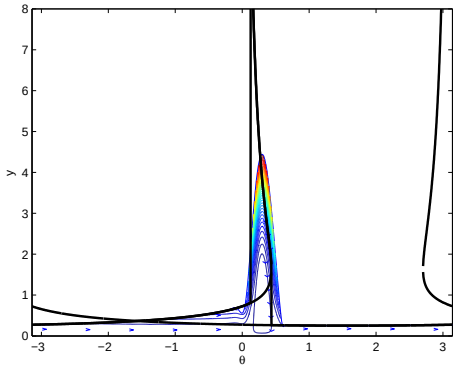

Figure 5.22: Overlay of cubic solution with A=3.5 and $c_5 = -0.5$ and full numerical solution with smoothing terms $c_1 = 10^{-4}$, $c_3 = 10^{-3}$.

5.3 Further results for uniform droplet input

We have seen in §5.1 some of the effects of changing the parameters associated with droplet mass, c_5 and c_6. However, much of the parameter range investigated in §5.1 is of mathematical interest only, as the direction of mass influx does not correspond to the direction of momentum influx. We now consider values of c_5 and c_6 for which the ratio $c_5 : c_6$ is the same as $c_3 : c_4$. We keep the values of c_1 to c_4 as in table 5.1 and take $c_5 = 10^{-3} \times c_6$, so the azimuthal contribution is small, but physically consistent. We vary A, and in order to achieve a steady state, fluid is withdrawn from the system at a sink at $\theta = 0$, at a rate to match the input. From the results in §5.1, with c_5 and c_6 both small we expect to see a base solution close to $q = 1/6$ with a shock in $0 < \theta < \pi/2$ if the area of the film exceeds $A = 3.951$. From figure 5.1, we also expect a descending shock over the sink as c_6 becomes more negative.

5.3.1 The effect of cross-sectional area A

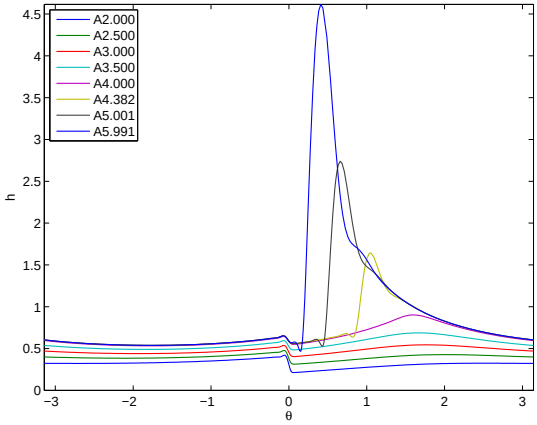

Figure 5.23: Film profile h when $c_5 = -10^{-5}$, $c_6 = -10^{-2}$, various A. Other parameters are $c_1 = 10^{-4}$, $c_2 = -1$, $c_3 = 10^{-3}$, $c_4 = 1$, $u_{cyl} = 0$.

Figure 5.23 shows the film profiles for a range of A, when droplet mass parameters are $c_5 = 10^{-5}$ and $c_6 = 10^{-2}$. Steady-state solutions were found for $A = 2.0$ to $A = 5.991$. In all cases, there is a small descending shock at the sink at $\theta = 0$. With $A = 2.0$, the profile is almost linear, growing steadily away from the sink. As A increases, the profile develops a hump around $\theta = \pi/2$, until around $A = 4.0$, where it is close to the critical profile. A further increase in area is incorporated with an ascending shock in $0 < \theta < \pi/2$. The loss of mass through the sink makes the film thin immediately after $\theta = 0$, and this makes it difficult to find solutions for very thin films. Continuation from nearby profiles was implemented, but no films were found with $A < 2.0$. For $A = 5.991$, the largest area which a steady profile with these parameters could be

obtained numerically, the shock is so close to the sink that the capillary wave at its foot is close to interacting with the down-shock.

The effect of varying area with greater droplet mass contribution is shown in figure 5.24, in which $c_5 = -6 \times 10^{-5}$, $c_6 = -6 \times 10^{-2}$. The build-up at $\theta < 0$, before the sink, is now sufficient to take away noticeable mass from the ascending shock, and even with $A = 4.383$ no ascending shock is required. Solutions with smaller area could not be obtained.

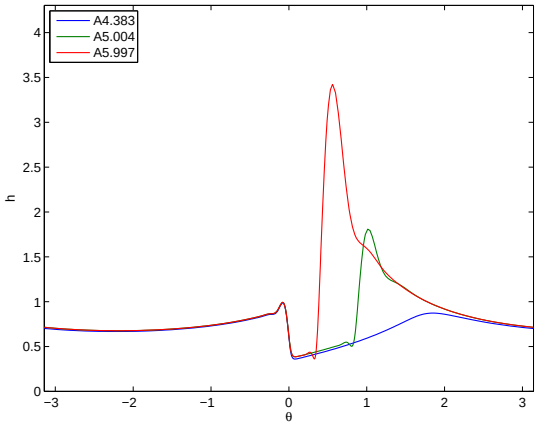

Figure 5.24: Film profile h when $c_5 = -6 \times 10^{-5}$, $c_6 = -6 \times 10^{-2}$, various A. Other parameters are $c_1 = 10^{-4}$, $c_2 = -1$, $c_3 = 10^{-3}$, $c_4 = 1$, $u_{cyl} = 0$

5.3.2 The effect of increasing droplet mass contribution

In this section we consider the effect of the droplet mass terms c_5 and c_6 on profiles of a fixed cross-sectional area. Again, the ratio is kept constant, $c_5 = 10^{-3} \times c_6$.

First consider a very thin film where there is less mass in the film than the critical value ($A < 3.951$). In figure 5.25 the area is only $A = 2.5$, and therefore no profiles include an ascending shock. The development of the down-shock at the sink can be seen as the droplet mass input increases and there is more mass extracted at the sink.

For this low area, with no ascending shock, the underlying flow is purely anticlockwise, with no recirculation. Figure 5.26 shows streamlines for a film with $A = 2.5$, and various droplet mass. In figure 5.26(i) the droplets contribute no mass. In (ii) they contribute a little, and fluid entering the surface have a residence time of two–three cycles before leaving at the sink. In (iii) the droplet mass term is as large as it can be for a stable steady film, and the fluid has a minimum residence time of less than one rotation. (This may be near to the ideal situation to achieve in a bearing chamber, as there is no recirculation or stagnation points, and the residence time is low, minimizing the risk of over-heating) If the droplet mass is increased any further, then a stable steady

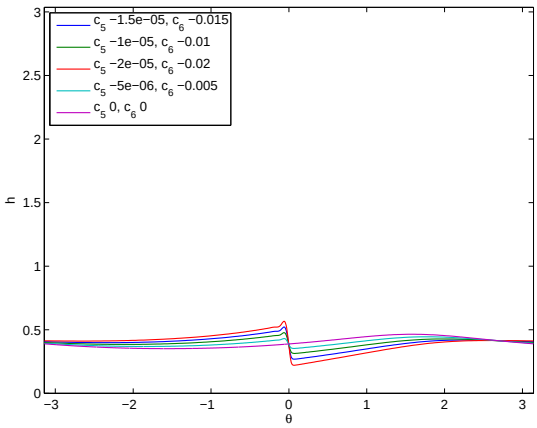

Figure 5.25: Film profiles h when $A = 2.5$, various c_5, $c_6 = 10^3 \times c_5$. Other parameters are $c_1 = 10^{-4}$, $c_2 = -1$, $c_3 = 10^{-3}$, $c_4 = 1$, $u_{cyl} = 0$.

continuous film cannot be found, as too much fluid leaves at the sink.

When the cross-sectional area of the fluid is increased beyond $A = 3.951$ then with no droplet mass contribution there is a shock at about $\theta = \pi/4$. In figure 5.27 the area is $A = 4.382$. As the mass builds up at $\theta < 0$ before the sink, this shock is no longer required to incorporate the super-critical mass, and moves to the right until from $c_6 = -4 \times 10^{-2}$ onwards there is no ascending shock at all.

Figure 5.28(i) shows the streamlines when $A = 4.382$ and droplets only contribute a little mass. As in the case where droplets contribute negligible mass, only momentum, there is a broad recirculation region, and stagnation points on the boundary. The residence time of fluid in this case is 3.5 to 4.5 cycles.

Figure 5.28(ii) shows streamlines for a film with the same area but much greater droplet mass input - the most for which a solution can be found, with maximum residence time of just over one rotation. In this case, so much fluid is built up on the upstream of the sink ($\theta < 0$) that there is not enough fluid to require a shock solution in $\theta > 0$. Therefore there is no recirculation, the flow is unidirectional

When the area is further increased, then the ascending shock and associated recirculation occurs even with very large droplet mass contribution. In figure 5.29 the area is to $A = 5.0$. A similar pattern is followed as in the previous example, with the shock moving to the right, but the case of the shock not existing no longer occurs. There is enough mass in the system that the ascending shock always occurs for the stable steady solutions that we are able to find numerically. Increasing the droplet mass contribution further might move the shock slightly further to the right, but such solutions are difficult to find numerically. Figure 5.30 shows the streamlines when $A = 5.0$ for two cases of droplet mass contribution, and figure 5.30(ii) reveals that the maximum residence time

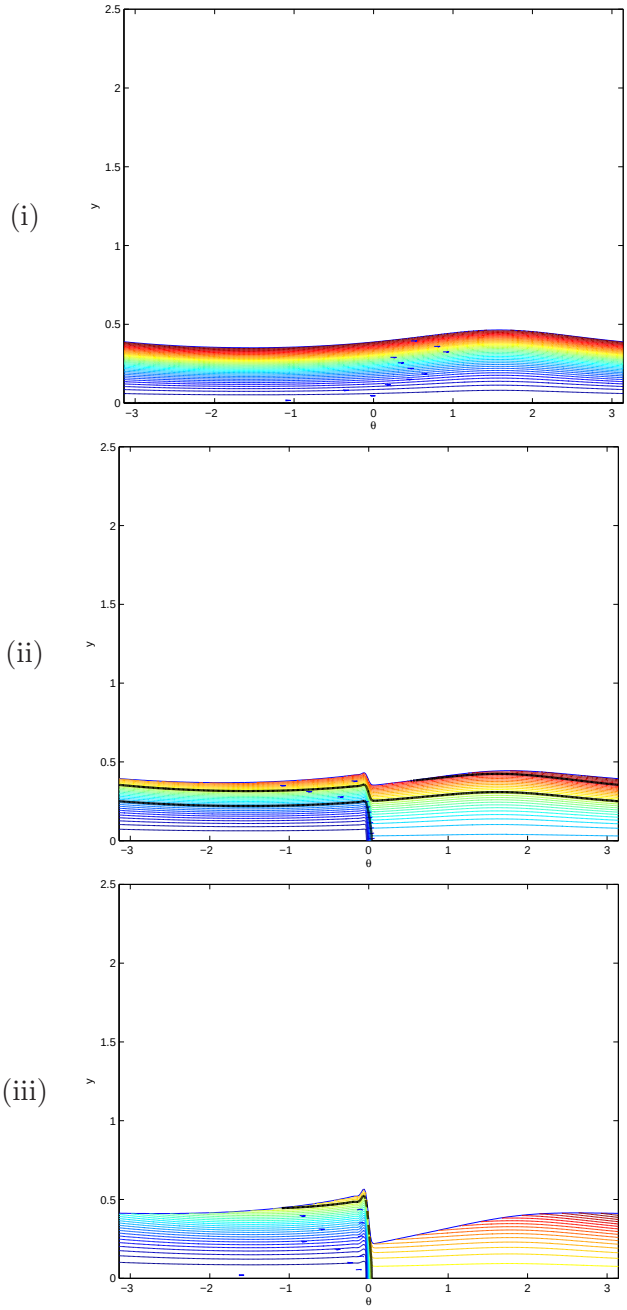

Figure 5.26: Streamlines for a thin film with droplet mass, (i) $c_5 = 0$, $c_6 = 0$, (ii) $c_5 = -5 \times 10^{-6}$, $c_6 = -5 \times 10^{-3}$, (iii) $c_5 = -2 \times 10^{-5}$, $c_6 = -2 \times 10^{-2}$, and $A = 2.5$. Other parameters are $c_1 = 10^{-4}$, $c_2 = -1$, $c_3 = 10^{-3}$, $c_4 = 1$, $u_{cyl} = 0$.

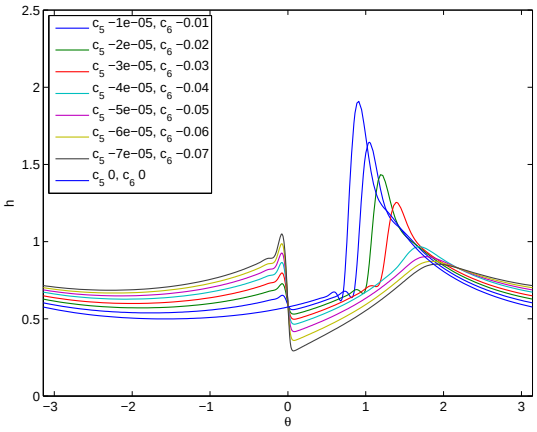

Figure 5.27: Film profiles h when $A = 4.382$, various c_5, $c_6 = 10^3 \times c_5$. Other parameters are $c_1 = 10^{-4}$, $c_2 = -1$, $c_3 = 10^{-3}$, $c_4 = 1$, $u_{cyl} = 0$. Corresponding streamlines for these profiles are plotted in figure 5.28.

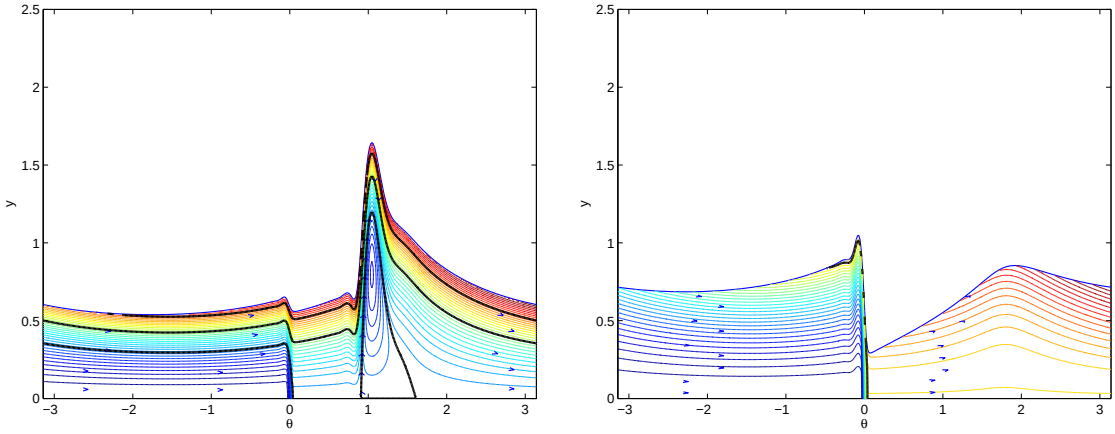

(i) (ii)

Figure 5.28: Streamlines when (i) $c_5 = -10^{-5}$, $c_6 = -10^{-2}$, (ii) $c_5 = -7 \times 10^{-5}$, $c_6 = -7 \times 10^{-2}$, and $A = 4.382$. Other parameters are $c_1 = 10^{-4}$, $c_2 = -1$, $c_3 = 10^{-3}$, $c_4 = 1$, $u_{cyl} = 0$.

for $c_5 = -7\times10^{-5}$, $c_6 = -7\times10^{-2}$ is only just above one cycle. This suggests that further increase in droplet mass flux would mean that no particles would spend a complete cycle in the system, and so a completely wetting film would not be sustained.

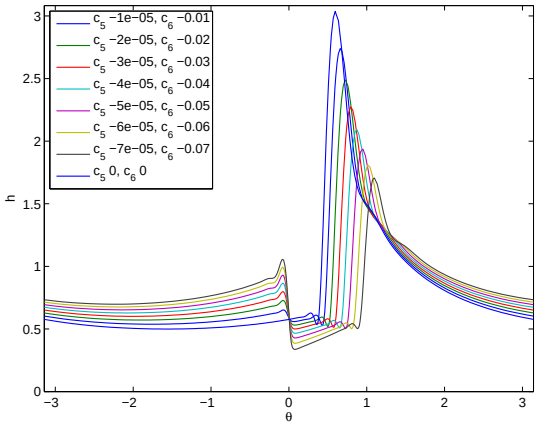

Figure 5.29: Film profile h when $A = 5.0$, various c_5, $c_6 = 10^3 c_5$. Other parameters are $c_1 = 10^{-4}$, $c_2 = -1$, $c_3 = 10^{-3}$, $c_4 = 1$, $u_{cyl} = 0$.

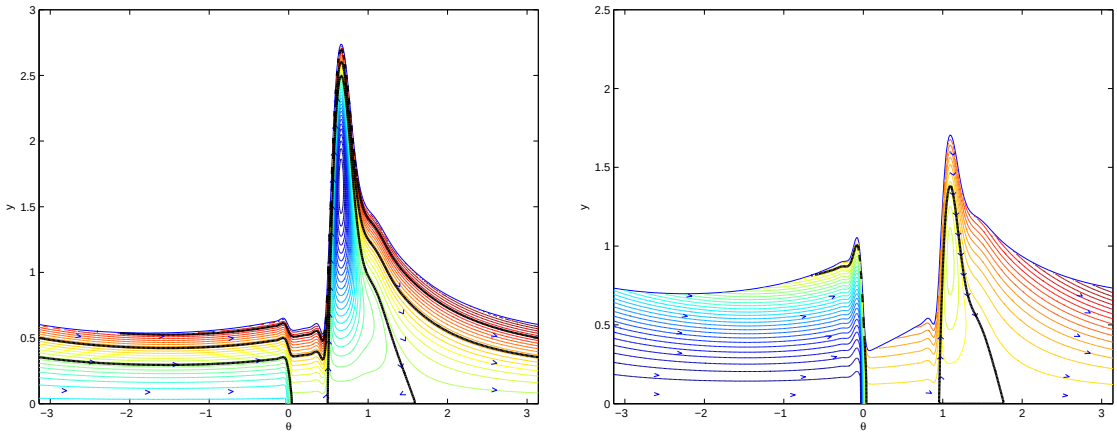

(i) (ii)

Figure 5.30: Streamlines when (i) $c_5 = -10^{-5}$, $c_6 = -10^{-2}$, (ii) $c_5 = -7 \times 10^{-5}$, $c_6 = -7\times10^{-2}$, and $A = 5.0$. Other parameters are $c_1 = 10^{-4}$, $c_2 = -1$, $c_3 = 10^{-3}$, $c_4 = 1$, $u_{cyl} = 0$.

5.4 The effect of sink position

In designing an engine bearing chamber, it may be possible to vary the position of the sink through which oil leaves the chamber. Thus far we have assumed that the sink is at the bottom of the cylinder, at $\theta = 0$, but now various sink positions are examined, to establish how varying the sink position alters the film. In particular, if there is sufficient fluid in the cylinder that a bulge and recirculation region is found, then what happens

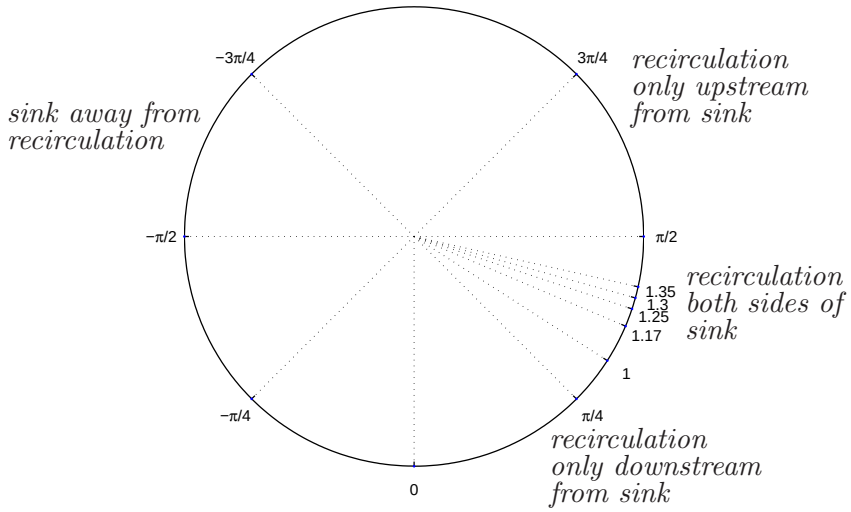

Figure 5.31: Sink positions for which streamlines are plotted in figure 5.32

when the sink is at that part of the cylinder? Could the recirculation be prevented by careful positioning of the sink?

For all the simulations in this section, the parameters are:

c_1	10^{-3}		
c_2	-1	A	4.382 (unless otherwise stated)
c_3	10^{-2}		
c_4	1		
c_5	-10^{-4}	u_{cyl}	0
c_6	-10^{-2}	v_{cyl}	as defined (4.10)

Figure 5.32 shows the film profiles and streamlines for sink positions ranging from $-3\pi/4$ to $3\pi/4$; the positions are illustrated in figure 5.31. For sink positions $-\pi < \theta < 0$, the sink is well away from the ascending shock and the solution behaves in a very similar way to that already discussed, there is no qualitative effect on the film profile in moving the sink. When the sink is in the quadrant $0 < \theta < \pi/2$ then it affects the shock. For shock position $\pi/4 < \theta < 1.25$ it causes the height of the shock to diminish, but there is still recirculation downstream of the sink position. For $\theta = 1.3$, the peak begins to emerge upstream of the sink, and there is recirculation on both sides of the sink. For $\theta \geq 1.35$, all the recirculation is upstream of the sink. So for these parameters there is are no sink positions which completely remove recirculation, although it diminished greatly when the sink was under the shock. Since results in §5.3.2 show that the size of recirculation regions diminish with reduced cross-sectional area A, then it seems likely that with slightly lower A then the existence of recirculation would depend upon sink position.

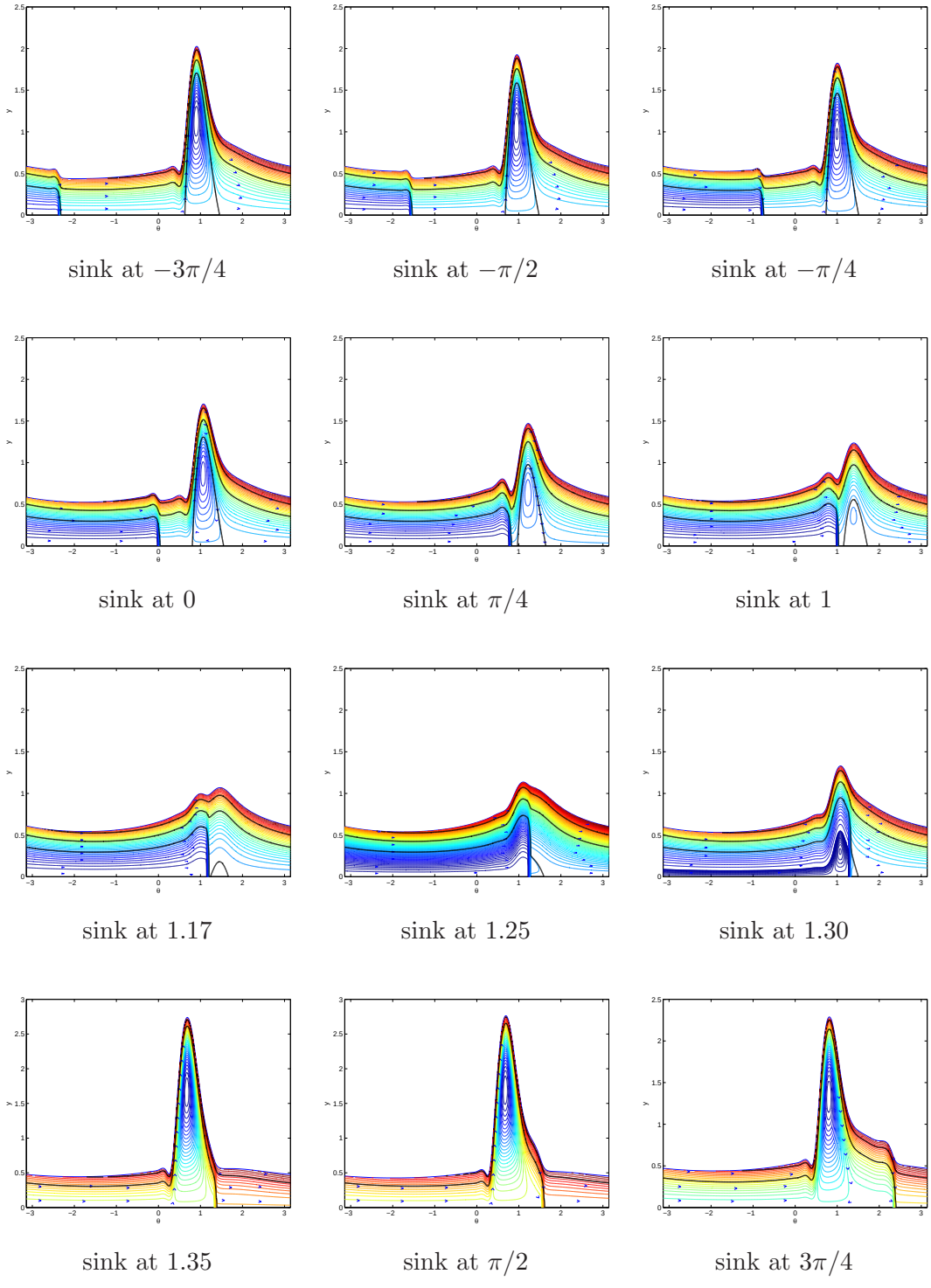

Figure 5.32: Streamlines for various sink positions. Parameters are $c_1 = 10^{-3}$, $c_2 = -1$, $c_3 = 10^{-2}$, $c_4 = 1$, $c_5 = -10^{-4}$, $c_6 - 10^{-2}$, $A = 4.382$.

5.5 An example with dimensional parameters

It is instructive to follow an illustrative physical example of a film in a bearing chamber through the derivation and results, to see what dimensional times and length emerge for evolution of the film. In chapter 2 we defined the relationship between dimensional variables (denoted $\hat{u}$ *etc*) and non-dimensional variables as:

$$\begin{array}{lll} \text{Time} & \hat{t} = (r_0/U)\, t, \\ \text{Film thickness} & \hat{h} = h_0 \quad h, \\ \text{Film Velocity (Az.)} & \hat{u} = U \quad u, \\ \text{Film Velocity (Rad.)} & \hat{v} = \epsilon U \quad v, \\ \text{Droplet Velocity (Az.)} & \hat{u}_E = U_E \quad u_E, \\ \text{Droplet Velocity (Rad.)} & \hat{v}_E = V_E \quad v_E. \end{array}$$

Table 5.4 shows typical values of physical parameters for a bearing chamber geometry, including estimates of film thickness and azimuthal velocity. The values for surface tension has been increased for this example in order to consider a film which presents no numerical difficulties in solution, and film velocity has been increased to the upper end of the range, but others remain as in table 2.1. Cylinder rotation is taken to be zero.

Property		Value
Gravity	g	$10\,\mathrm{m\,s^{-2}}$
Density	ρ	$10^3\,\mathrm{kg\,m^{-3}}$
Viscosity	μ	$10^{-2}\,\mathrm{kg\,m^{-1}s^{-1}}$
Cylinder radius	r_0	$10^{-1}\,\mathrm{m}$
Surface Tension	σ	$10\,\mathrm{kg\,s^{-2}}$
Film Thickness	h_0	$10^{-3}\,\mathrm{m}$
Film Velocity	U	$1\,\mathrm{m\,s^{-1}}$

Table 5.4: Estimates of physical parameters used as scalings (II).

From these physical parameters, relevant dimensionless groups are calculated, which are shown in table 5.5.

Now in the case when the droplets contribute both significant mass and momentum, the distinguished limit in §2.8.3, the scalings used are $U_E = U/\epsilon$, $V_E = U$, and $\alpha = \epsilon a$. Table 5.6 gives the dimensional droplet velocity components, and hence the non-dimensional values.

The values of $v_E = -10^2$ and $\mathrm{Re_f} = 10^2$ are of the size $1/\epsilon$, so are on the limit of validity of the distinguished limit, which has discarded terms of $O(\epsilon)$, since there might be terms

Aspect ratio	ϵ	$\frac{h_0}{r_0}$	10^{-2}
Reduced Reynolds Number	$\mathrm{Re_f}$	$\frac{\rho U h_0}{\mu}$	10^{2}
Reduced inverse Weber Number	$\mathrm{We_f}$	$\frac{\sigma h_0^2}{U^2 \rho r_0^3}$	10^{-5}
Froude Number	Fr	$\frac{U^2}{g h_0}$	10^{2}
Reynolds x Weber	$\mathrm{Re_f We_f}$	$\frac{\epsilon^3 \sigma}{\mu U}$	10^{-3}
Reynolds / Froude	$\frac{\mathrm{Re_f}}{\mathrm{Fr}}$	$\frac{\rho g h_0^2}{\mu U}$	1

Table 5.5: Estimates of size of non-dimensional groups

discarded that should be retained if coefficients become this large.

Dimensional Quantity			Scaling	Non-dimensional quantity	
Core air velocity	$\hat{u_E}$	$10^2 \mathrm{m\,s^{-1}}$	$U_E = U/\epsilon$	u_E	1
Core air rad vel	$\hat{v_E}$	$-10^2 \mathrm{m\,s^{-1}}$	$V_E = U$	v_E	-10^2
Drop vol fraction	α	10^{-6}	ϵ	a	10^{-4}

Table 5.6: Estimates of droplet parameters

From the values in tables 5.4–5.6, the coefficients of the film profile equation (4.6) are given as in table 5.7.

Coefficient		Quantity
c_1	$\mathrm{Re_f We_f}$	10^{-3}
c_2	$-\mathrm{Re_f/Fr}$	-1
c_3	$\mathrm{Re_f} a u_E^2$	10^{-2}
c_4	$-\mathrm{Re_f} a u_E v_E$	1
c_5	$-a u_E$	-10^{-4}
c_6	$a v_E$	-10^{-2}

Table 5.7: Coefficients of the equation (4.6).

The solution to the steady-state film profile and streamlines of the underlying flow are shown in figure 5.33. In this figure, non-dimensional values are plotted, so visually the peak is deceptively large. The polar plot in figure 5.34 has been scaled to show the actual aspect ratio of the film.

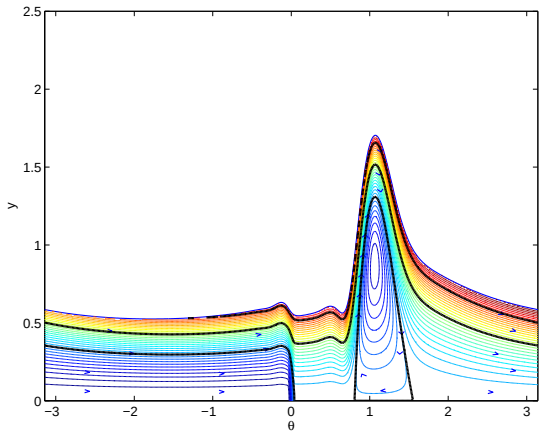

Figure 5.33: Streamlines for uniform input of mass and output at $\theta = 0$, when Area = 4.382, coefficients as table 5.7.

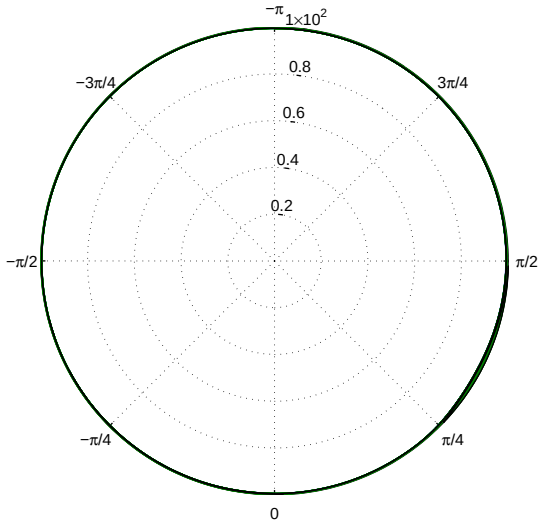

Figure 5.34: Polar plot to scale, for uniform input of mass and output at $\theta = 0$, when Area = 4.382, coefficients as table 5.7.

The solution took 22 timesteps with $\delta t = 1$ to evolve to this steady state, from a uniform film of thickness $\bar{h} = 0.70$. Of physical interest for oil degradation analysis, fluid particles entering at the surface have a residence of between 2 and 3 rotations before leaving at the sink. This corresponds to $t = 30$ (non-dimensional), or with the scaling above, $\hat{t} = 3$s.

Figure 5.35 shows the non-dimensional velocity profile at several cuts across the film, confirming that the surface of the film is moving whilst the wall is stationary.

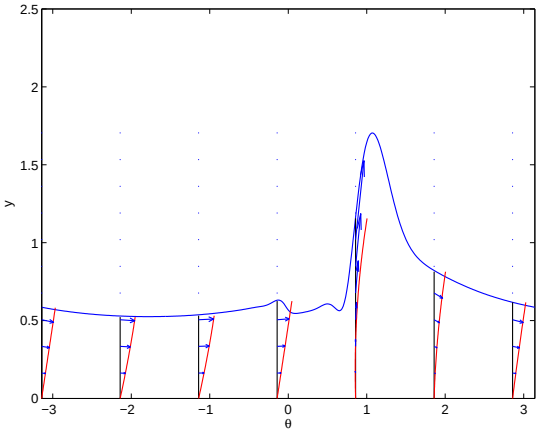

Figure 5.35: Velocity profile for uniform input of mass and output at $\theta = 0$, when Area = 4.382, coefficients as table 5.7.

Figures 5.36 and 5.37 show the u and v components of the non-dimensional velocity field. From the same data, in most of the film, $v \approx 0.01$, with a maximum around the face of the shock of $v \approx 2$. u is zero at the wall, and increases almost linearly towards the surface, to a maximum of $u \approx 0.7$. Converting back into dimensional variables, in most of the film $\hat{v} = 0.1\text{mm}\,\text{s}^{-1}$, up to a maximum of $\hat{v} = 0.02\text{m}\,\text{s}^{-1}$, and $\hat{u} \leq 0.7\text{m}\,\text{s}^{-1}$.

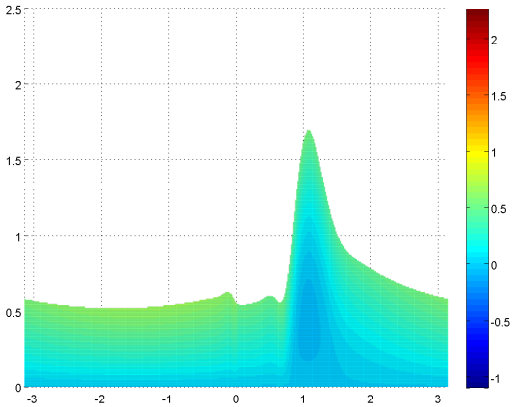

Figure 5.36: u component of velocity for uniform input of mass and output at $\theta = 0$, when Area = 4.382, coefficients as table 5.7.

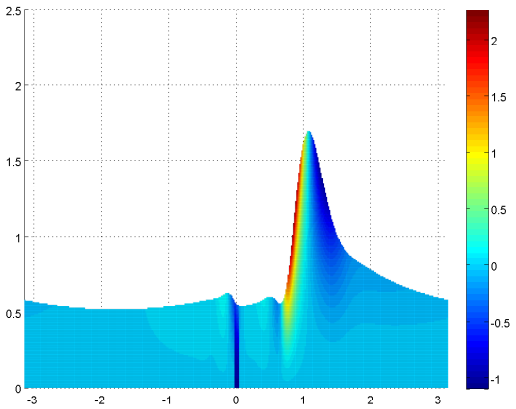

Figure 5.37: v component of velocity for uniform input of mass and output at $\theta = 0$, when Area = 4.382, coefficients as table 5.7.

The solution illustrated in figure 5.33, arises from the coefficients in table 5.7, which could be generated by other combinations of droplet input and underlying Reynolds number.

Users of this thesis should note that these are all *estimates* of physical parameters, for illustrative purposes only, and more careful calculations must be carried out for design purposes. In particular, in this example surface tension is too high for a physical fluid. As we reduce the c_1 coefficient to $c_1 = \mathrm{Re_f We_f} = 10^{-5}$, the peak becomes increasingly sharp. At $c_1 = \mathrm{Re_f We_f} = 10^{-6}$, which occurs at the physical value of surface tension $\sigma = 10^{-2}\mathrm{kg\,s^{-1}}$, the solution breaks down. As in the cases in Chapter 3, where the cut-off was $\zeta = \alpha_u^3$, here the cut-off is $c_1 = c_4^3$.

5.6 Results with variable droplet input

As discussed in §4.2, the incoming droplets that drive the film flow may not be evenly distributed about the cylinder. In this section we will consider what effect this non-uniform droplet distribution has on the film profiles and underlying flow.

The base case of uniform distribution is illustrated in figure 5.38 and has parameters $a = \bar{a} = 10^6$, $u_E = 10^2$ $v_E = 10^4$, equivalent to the coefficients given in table 5.8

This choice of a, u_E and v_E is such that varying a and u_E has very similar effect, whilst varying v_E has little effect.

c_1	10^{-3}		
c_2	-1	A	4.382 (unless otherwise stated)
c_3	10^{-2}		
c_4	1		
c_5	-10^{-4}	u_{cyl}	0
c_6	-10^{-2}	v_{cyl}	as defined (4.10)

Table 5.8: Parameters for uniform distribution example

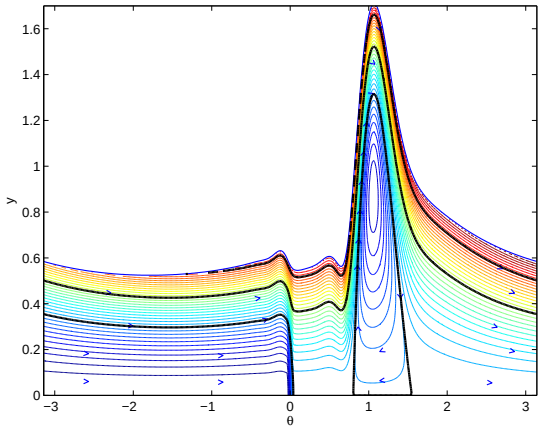

Figure 5.38: Streamlines for the base case of uniform input of droplets, parameters as table 5.8

5.6.1 Single injector point for droplets

Figure 5.40 shows an example of the film height profile and streamlines when a single injector type distribution of droplets is imposed. The droplet volume velocity is kept constant but droplet fraction varies around the cylinder as illustrated in figure 5.39, with a smoothed half-normal distribution given by (4.12):

$$a(\theta) = (1-\phi_a)2\sqrt{2\pi}\bar{a}\mathrm{e}^{-\frac{((\theta-\theta_b) \mod 2\pi)^2}{2}} + \phi_a\bar{a}.$$

$\bar{a} = 10^6$ and $\phi_a = 0$. The greatest droplet fraction is at $\theta_s = -\pi + 1$, which gradually tails off with increasing θ, as proposed in §4.2. Since a occurs in both droplet mass and momentum terms, both are affected.

The effect on the film height profile is to increase the height of the peak compared to the uniform case in figure 5.38. The peak is moved towards $\theta = 0$, and the film thins at about $-\pi + 1 < \theta < 0$. Studying the streamlines we can see that the underlying flow is drastically altered from the uniform case. The recirculation is now closer to $\theta = 0$ and does not meet the wall, and the flow at $\theta > 0$ (on the right hand side of the cylinder) is clockwise, falling towards the sink.

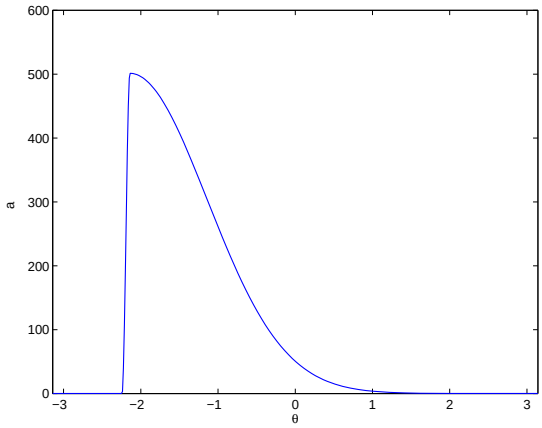

Figure 5.39: Droplet input function for single injector point, $\phi_a = 0$

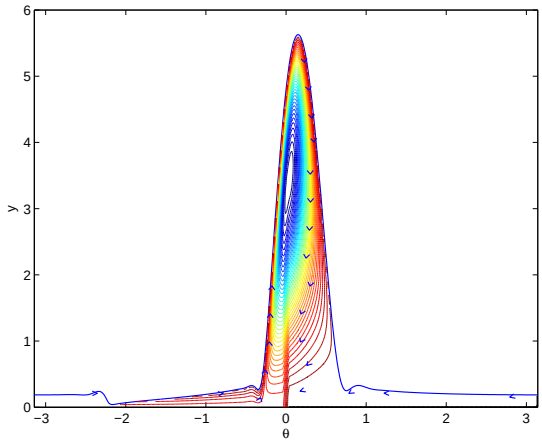

Figure 5.40: Streamlines for film with single injector droplet input function, a varying, $\phi_a = 0$, mean parameters as table 5.8

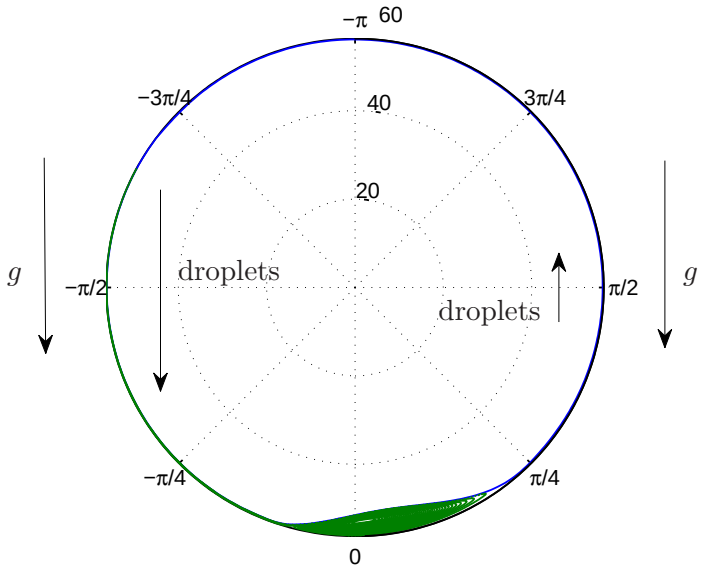

Figure 5.41: Polar plot of the film thickness with a single injector droplet input function, a varying, $\phi_a = 0$, mean parameters as table 5.8.

The polar plot in figure 5.41, illustrates the force balance of this steady-state solution more clearly. Caution should be taken interpreting the polar plot as the scaling exaggerates variations in film thickness. The droplet impact is small for $\theta > 0$, so is insufficient to overcome gravity. Therefore the fluid, fed with greater momentum on the left hand side, is pulled down left and right to pool at the bottom and fall out of the sink.

5.6.2 Intermediate Single Injector cases

The flow in the single injector case is qualitatively different from that in the uniform case, so intermediate cases with $0 < \phi_a < 1$ were investigated, to observe the transitional behaviour. Such a case may arise in the bearing chamber if the majority of droplets contact the wall directly after leaving the injector, but some are thrown off other parts of the chamber.

An intermediate situation input function with a mixture of uniform and single injector point droplet feeding, is illustrated by figure 5.42(i), and the corresponding film profile and streamlines shown in figure 5.42(ii). In this case gravity still dominates sufficiently that the recirculation bubble extends down to the sink, but on the surface there is sufficient momentum from the droplets to maintain the anticlockwise rotation. Although the recirculation bubble is very wide, it does not come into contact with the cylinder wall, the full length of which receives fresh fluid from the surface. Flow near the stagnation point near $\theta = 2$ may however be very slow.

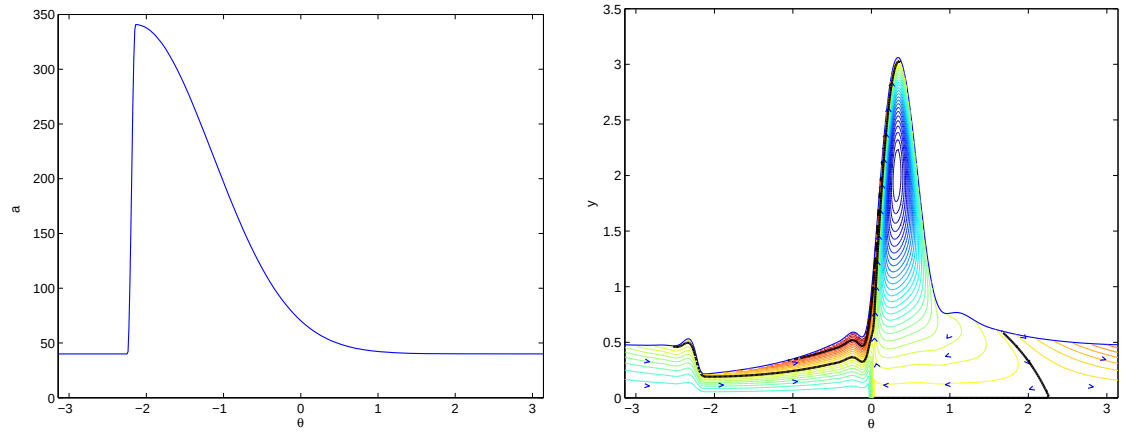

(i) (ii)

Figure 5.42: Single injector point combined with uniform input, $\phi_a = 0.4$. (i) Droplet input function, (ii) streamlines for film with mean parameters as table 5.8.

Figure 5.43(ii) shows another intermediate case, with a further increase in the uniform component of droplet distribution, corresponding to the distribution shown in

figure 5.43(i). The recirculation bubble has narrowed, the peak moved further away from the sink, and the minimum residence time has increased to be more than one rotation.

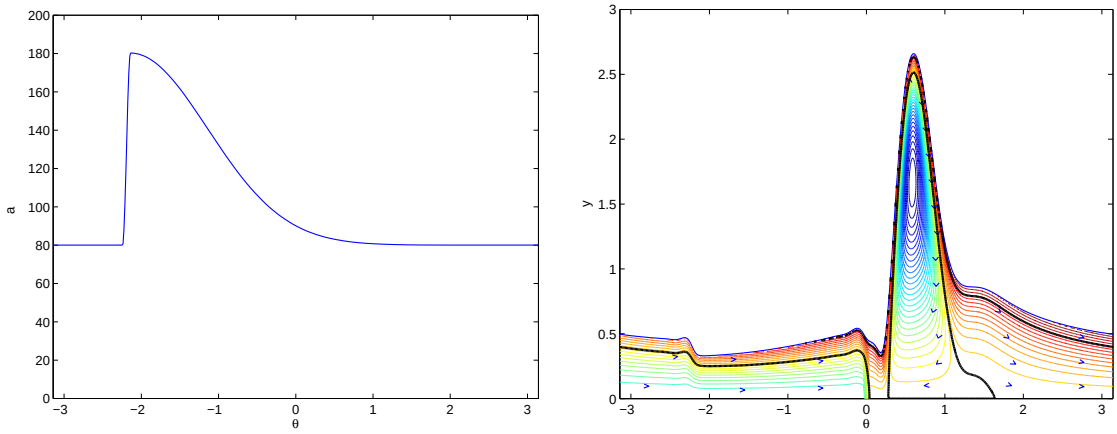

(i) (ii)

Figure 5.43: Single injector point combined with uniform input, $\phi_a = 0.8$. (i) Droplet input function, (ii) streamlines for film with mean parameters as table 5.8.

5.6.3 Distributed sources

A model of the droplet input function if there are 10 sources evenly distributed around the central shaft of the cylinder is given by (4.15),

$$a(\theta) = \bar{a}\left((1-\phi_a)\sin(p\,\theta)+1\right),$$

with $\bar{a} = 10^6$, $p = 10$ and $\phi_a = 0.75$. The distribution is illustrated by figure 5.44, and typical behaviour is illustrated by figure 5.45. The oscillations of the input are apparent in the output. The droplet residence time is shorter, only 1–2 cycles, but there are otherwise no major changes from the uniform input case.

5.7 Summary of this chapter

We have examined the effects of c_5 and c_6, the azimuthal and radial components of droplet mass flux in (4.6), the modified equation for film height profile. Initially, we varied these independently, having chosen a set of coefficients c_1 to c_4 and A which (from Chapter 3) we knew to produce a stable steady state film profile. The total fluid in the film, A, is kept constant by use of a sink. c_6 has the effect of a build-up on the

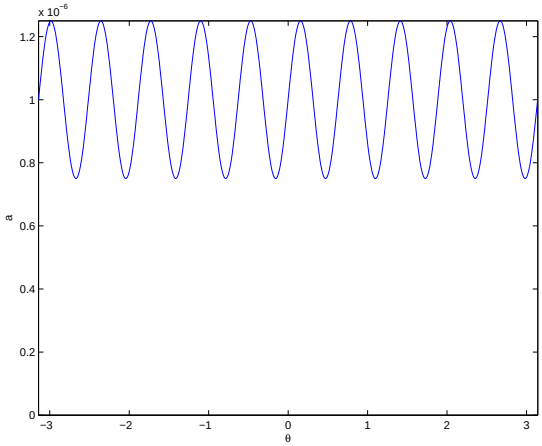

Figure 5.44: Droplet input function for distributed sources, $\phi_a = 0.75$, $p = 10$

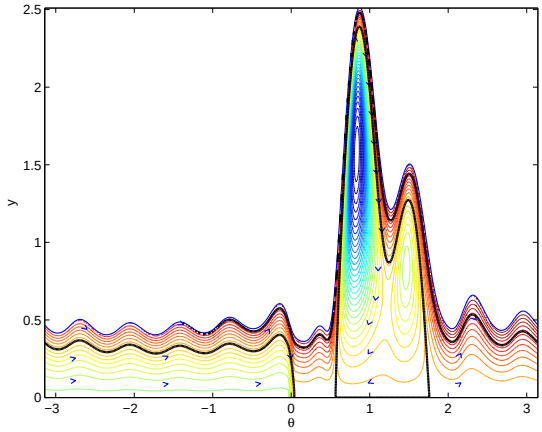

Figure 5.45: Streamlines for film with distributed sources, a varying, $\phi_a = 0.75$, $p = 10$ mean parameters as table 5.8

left-hand side of the sink, and since this parameter largely controls the outflow rate, causes a sharp drop in film height over the sink.

The effect of c_5 is initially more subtle, but if this parameter, equivalent to cylinder wall rotation u_{cyl} is substantially increases then the steady-state solution may cease to exist. If c_1, c_3 and c_6 are negligible, (4.6) reduces to a cubic of which c_5 is one of the coefficients, and we could plot the possible positive real solutions. Kinematic wave theory enabled us to narrow down the possible stable shock solutions. Thus we saw that A_{crit}, the area at which a shock solution is required, and A_{max}, the maximum area sustained by a stable steady shock solution, are dependent on c_5. Thus, for the parameters we had examined, $A > A_{max}$ which is why a stable solution was not observed.

The analogy between c_5 and u_{cyl}, the wall rotation, is useful for describing the film profile, but streamlines reveal that the flow beneath the surface is not the same for both.

In the section where c_5 and c_6 were chosen to be physically consistent with c_3 and c_4, we saw that increases in droplet mass input reduce the area required for ascending shocks and recirculation.

Non-uniform droplet impact can have surprising effects on the film. When a single injector is used, with the parameters chosen, the extra momentum imparted to the film at the injector site can cause such severe thinning that together with the lack of momentum on the rising side, the flow field is completely changed. No longer is a rimming flow seen, but the flow descends on both sides of the cylinder. Distributed injectors do not have this effect, but the variation from the input can be clearly seen in the film profile.

The streamlines show that the underlying flow has a recirculation region near the cylinder wall. This recirculation can be diminished but not eliminated by adjustment of the sink positions to be underneath the shock.

In an illustrative example, we showed how this method may be applied for physical data, and that the timescales for fluid residence in the cylinder may be in the order of seconds.

Chapter 6

Films with the additional features of rotation and thermal effects

In Chapters 2–5 we have considered the development of thin rimming films driven by the impact of droplets. The flow has been isothermal, and the cylinder wall stationary, $u_{cyl} = 0$. In this chapter, consideration is given to the additional effects of cylinder wall rotation and thermally-driven surface shear. Introducing rotation into the model gives us the opportunity to study a slightly wider parameter range, especially the case with interesting physical features where the surface shear drives against the rotation of the wall. A full examination of thermal effects on the film goes beyond the scope of this project, but in certain limits of the fluid's thermal properties, heating of the cylinder wall can cause surface shear. We will examine this effect, known as Marangoni shear, in the latter part of this chapter.

Both of these effects can be included in the model by an equation of the same form as (4.6), the film-height equation we have already derived, and the numerical techniques already developed can be directly applied. This therefore provides a convenient method of verifying the numerical code, as previous work in this field has concentrated on the case of rotating rather than stationary cylinders.

6.1 Rotating wall and droplet mass contribution

The case of a rotating cylinder with impacting droplets contributing radial mass but negligible azimuthal mass and negligible momentum was studied by Noakes [34]. She looked at both uniform and non-uniform droplet inputs, with and without an outflow. We begin by reviewing and reproducing some of her results, which were generated with a different numerical method without adaptive meshing, then look at the streamlines beneath the surface profiles.

6.1.1 Surface profiles for uniform injection of mass as verification of code

Noakes' key equation for film profiles is given by equation 3.2.1, in [34],

$$\frac{\partial h}{\partial t} + \frac{\partial}{\partial \theta}\left(\underbrace{\epsilon \frac{h^3}{3}\left(\frac{\partial h}{\partial \theta} + \frac{\partial^3 h}{\partial \theta^3}\right)}_{\text{surface tension}} - \underbrace{\frac{h^3}{3}\sin\theta}_{\text{gravity}} + \underbrace{h}_{\text{rotation}} \right) = \underbrace{\lambda I(\theta, t)}_{\text{net mass input}} , \tag{6.1}$$

where ϵ is a surface tension parameter. λI is the mass injection and extraction function, and for uniform injection and extraction is given by

$$I = \begin{cases} -99 & \text{for } \theta_s < \theta < \theta_e \\ 1 & \text{elsewhere} \end{cases}$$

where $\theta_s = -\pi/100$, $\theta_e = \pi/100$ for extraction through 1% of the surface. The droplet contribution is thus simplified, as if the droplet mass were raining lightly onto the surface, with no azimuthal component, and no momentum or shear.

This model is equivalent to (4.6), with parameter values:

c_1	ϵ		
c_2	-1	A	various
c_3	0		
c_4	0		
c_5	0	u_{cyl}	1
c_6	$-\lambda$	v_{cyl}	99λ at sink, 0 elsewhere.

We solve this equation by applying the method described in Chapter 4. Figure 6.1(i) shows the steady-state film profiles when $\epsilon = 10^{-5}$ and λ ranges from 0 to 0.1, and $A = 5.026$, equivalent to $\bar{h} = 0.8$. The results show good agreement with the equivalent figure 3.28 in [34]. There is an ascending shock in $0 < \theta < \pi/2$ and, as λ increases, mass accumulates in $\theta < 0$ and a descending shock develops over the sink at $\theta = 0$. The only discernible difference from Noakes' result is in the peak for $\lambda = 0$, which in our simulation is about 10% higher and correspondingly narrower. This is due to the the simulation tolerances being slightly less precise, which can be corrected by adjusting the relative and absolute tolerance parameters used by the `bvp4c` code, from the defaults of 10^{-3} and 10^{-6} to 10^{-4} and 10^{-7} respectively. The refined results are shown in figure 6.1(ii) and are indiscernible from Noakes' figure 3.28. Figure 6.1(ii) is also formatted to facilitate comparison with [34].

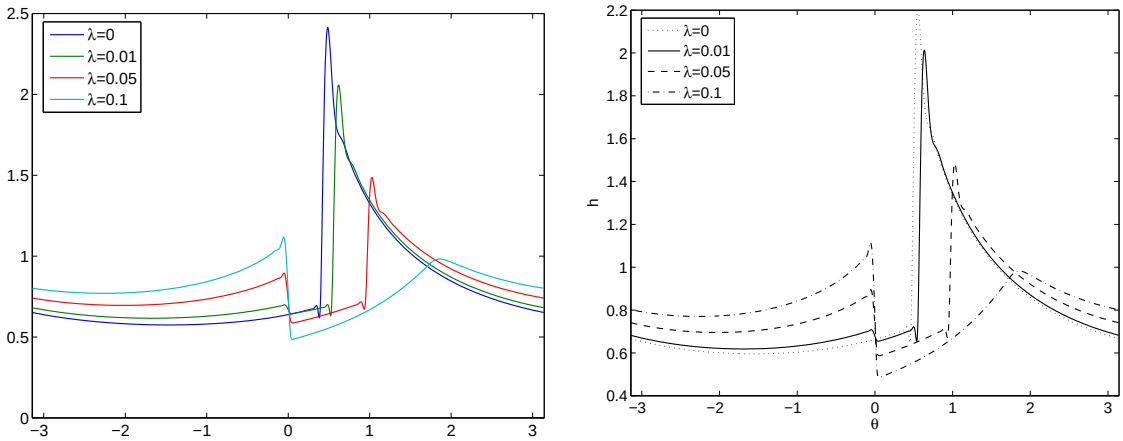

(i) (ii)

Figure 6.1: Film profiles with mass input $c_6 = -\lambda = 0, -0.01, -0.05$ and -0.1. Other parameters are $c_1 = 10^{-5}$, $c_2 = -1$, $u_{cyl} = 1$, $A = 5.026$. (i) Standard tolerances (ii) Reduced tolerances.

6.1.2 Underlying flow for uniform injection of mass

As well as reproducing the film profiles, we can investigate the flow beneath the surface. Figure 6.2 shows the streamlines for $c_6 = -0.01$ and -0.1. Unlike in the shock solutions generated by surface boundary condition of droplet impact, such as illustrated in figure 5.2, there is no recirculation under the peak. When mass input is small, there is very little radial motion through the steady-state film, and the fluid goes around the cylinder several times before leaving at the sink. However when mass input is large most of the fluid leaves after one rotation. This case illustrates the restriction on existence of a steady-state solution with large mass input, as with mass input increased further so much fluid would leave at the sink that insufficient remains to maintain a continuous film.

Figure 6.3 shows the polar plot for the same case, small mass input and $u_{cyl} = 1$, and illustrates the force balance. Rotation opposing gravity causes a thickening of the film to occur in the $0 < \theta < \pi/2$ quadrant. Equation (6.1) is symmetric in θ and therefore reversing the cylinder rotation causes the film thickening to appear in the $-\pi/2 < \theta < 0$ quadrant.

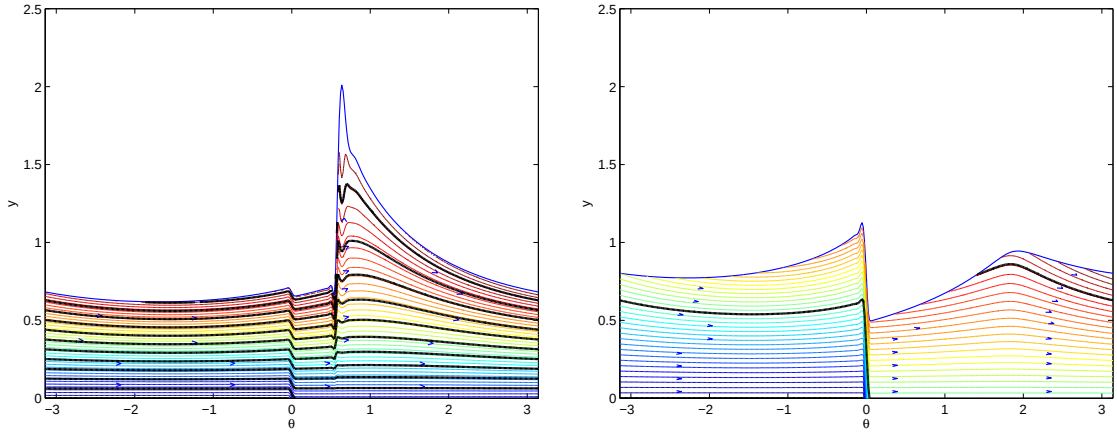

(i) (ii)

Figure 6.2: Streamlines for uniform mass input (i) $c_6 = -\lambda = -0.01$ (ii) $c_6 = -\lambda = -0.1$. Other parameters are $c_1 = 10^{-5}$, $c_2 = -1$, $u_{cyl} = 1$, $A = 5.026$

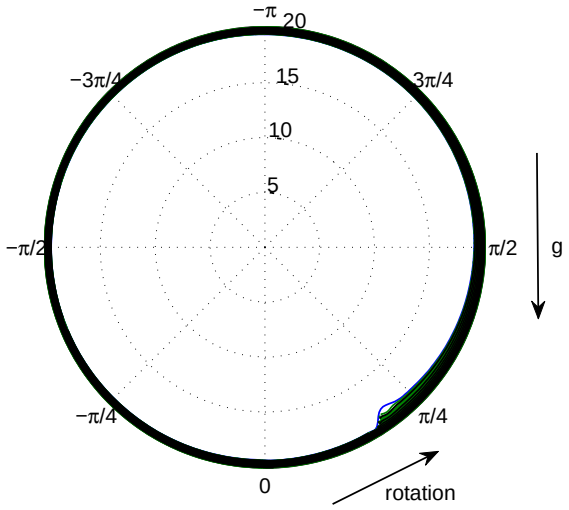

Figure 6.3: Polar plot of film profile for uniform input of mass and output at $\theta = 0$, when $c_1 = 10^{-5}$, $A = 5.027$, $c_6 = -0.01$, $c_5 = 0$ and cylinder rotating anticlockwise.

6.1.3 A rotating cylinder with non-uniform injection of mass

It is also of interest to examine results for (6.1) with non-uniform input of droplet mass into the film surface, as given by Noakes [34] figure 3.38. This is a model for droplets coming from a single injector point, and the mass-input profile is defined in (4.11) and illustrated in figure 4.2. Noakes' definition is such that a scaling factor of 4π is required to implement this function with our transient code, and to make meaningful comparisons with the uniform input case. To implement numerically we define $c_6(\theta)$ similarly to (4.12), with $\bar{c}_6 = \lambda/(4\pi)$, $\phi_a = 0$ and $\theta_b = -\pi + 1$.

Figure 6.4 shows the resulting film profiles, which are indistinguishable from figure 3.38 in [34].

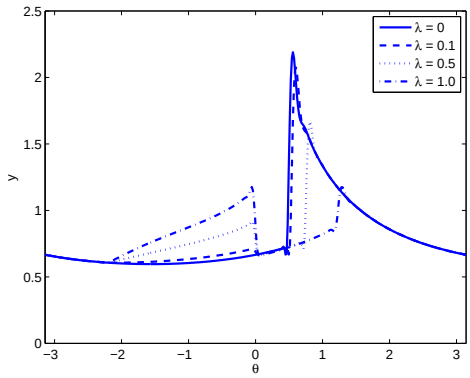

Figure 6.4: Film profiles for non-uniform radial injection of mass with a rotating cylinder, reproduction of Noakes' fig 3.38. $c_1 = \epsilon = 10^{-5}$, $A = 5.027$, $\lambda = 0, 0.1, 0.5, 1.0$, so $\bar{c}_6 = -\lambda/(4\pi) = 0, -0.008, -0.04, -0.08$, $u_{cyl} = 1$.

In order to compare with the uniform results we set $\bar{c}_6$ to the same values as in figure 6.1, resulting in the film profiles shown in figure 6.5. The most prominent feature is the sudden increase in gradient of h at $\theta = -\pi + 1$, where the injection of mass starts. Most of this extra mass is lost from the system at the sink, and the profiles between $\theta = 0$ and $\theta = -\pi + 1$ are close to steady solutions with no incoming mass.

Figures 6.6 shows the streamlines for two of these cases, $\bar{c}_6 = -0.01$ and $\bar{c}_6 = -0.1$. The first is little different from the uniform mass input shown in figure 6.2, but in the second we can see that most streamlines start in $-\pi + 1 < \theta < 0$, where most mass is taken into the system. There is a gradual thickening of the film in this region, which is physically intuitive when seen on the polar plot (figure 6.7). These solutions are very different from the non-uniform input solutions seen in Chapter 5, for here the azimuthal film motion is maintained by the cylinder wall rotation with or without mass input, whereas in the previous results $u_{cyl} = 0$, and the driving droplet momentum was significantly affected

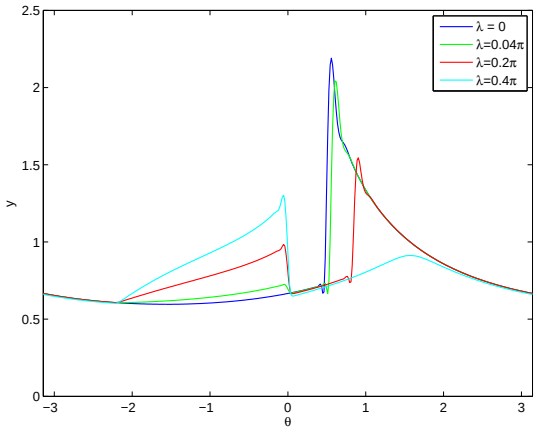

Figure 6.5: Film profiles for non-uniform radial injection of mass with a rotating cylinder. $c_1 = \epsilon = 10^{-5}$, $A = 5.027$, $\bar{c}_6 = -\lambda/(4\pi) = 0, -0.01, -0.05, -0.1$, $u_{cyl} = 1$.

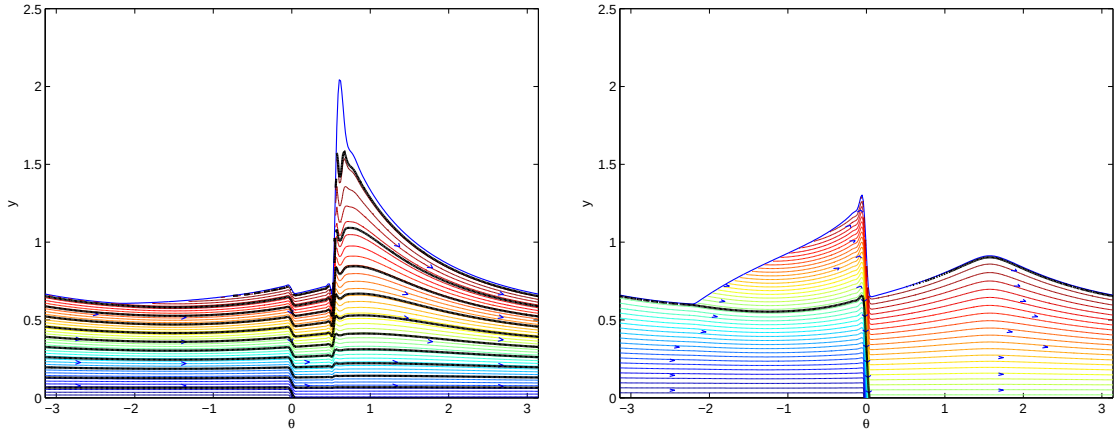

(i) (ii)

Figure 6.6: Streamlines for non-uniform input of mass, with (i) $\bar{c}_6 = -\lambda/(4\pi) = -0.01$, (ii) $\bar{c}_6 = -\lambda/(4\pi) = -0.1$. Other parameters are $\epsilon = 10^{-5}$, $A = 5.027$

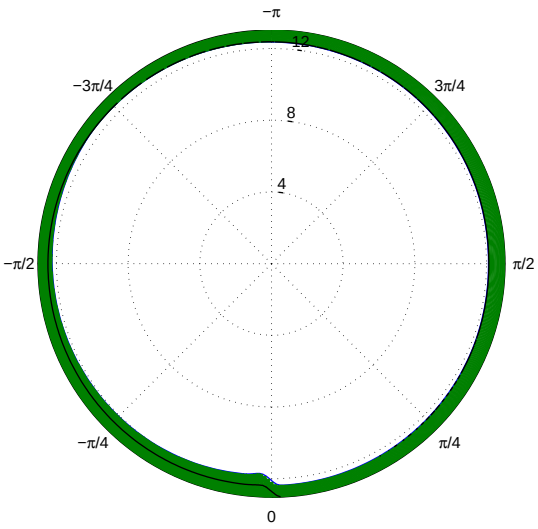

Figure 6.7: Polar plot of film for non-uniform input of mass and output at $\theta = 0$, when $\epsilon = 10^{-5}$, $\bar{h} = 0.8$ (Area = 5.027), $\lambda = 0.4\pi$.

by reducing $a(\theta)$ in part of the cylinder.

Residence times for both the uniform and non-uniform cases are given in table 6.1. There is little change in residence time between the uniform and non-uniform inputs.

	uniform			non-uniform		
c_6	Residence cycles	Residence time		Residence cycles	Residence time	
0	n/a	n/a	*	n/a	n/a	*
$0.1/(4\pi)$	–	–		12.3	91.0	*
0.01	10.3	75.6	*	10.1	78.6	
$0.5/(4\pi)$	–	–		2.3	15.7	*
0.05	1.9	13.9	*	2.0	15.0	
$1.0/(4/\pi)$	–	–		1.2	7.9	*
0.1	0.8	5.1	*	0.9	3.6	

Table 6.1: Minimum Residence times. * Results corresponding to parameters used by Noakes [34]

6.2 The distinction between the wall rotation (u_{cyl}) and azimuthal mass (c_5) terms

In the film-height equation (4.5) the terms $a\frac{\partial}{\partial\theta}(u_E h)$ and $\frac{\partial}{\partial\theta}(u_{cyl} h)$ have the same form in h. They are therefore interchangeable if we are just considering the film height profile h. However the first arises from the azimuthal mass contribution at the surface,

and the second from the rotating wall boundary condition. Therefore they are distinct in the calculation of the underlying film velocities u and v, and the two flows with $au_E = 1, u_{cyl} = 0$ and $au_E = 0, u_{cyl} = 1$ have distinct underlying behaviours.

As an example, consider the flow illustrated in figures 6.2(i) and 6.3, with $c_5 = -au_E = 0, u_{cyl} = 1$, and other parameters as given in table 6.2. The same film profile is produced when $c_5 = -au_E = 1, u_{cyl} = 0$, but as illustrated by the streamlines in figure 6.8, the underlying flow is completely different, with flow towards the sink on both sides of the cylinder. Since droplet momentum is negligible, $c_3, c_4 = 0$, although $v_E < u_E$, this is not a physically consistent set of parameters, but demonstrates the difference between the u_{cyl} and c_5 terms.

		Figure 6.2(i)	Figure 6.8
c_1	$\mathrm{Re_f We_f}$	10^{-5}	10^{-5}
c_2	$-\frac{\mathrm{Re_f}}{\mathrm{Fr}}$	-1	-1
c_3	$\mathrm{Re_f} au_E^2$	0	0
c_4	$-\mathrm{Re_f} au_E v_E$	0	0
c_5	$-au_E$	0	1
c_6	av_E	-0.1	-0.1
u_{cyl}		1	0
v_{cyl}		$as defined (4.10)$	
A		5.026	5.027

Table 6.2: Parameters for the two flows illustrated in figures 6.2(i) and 6.8

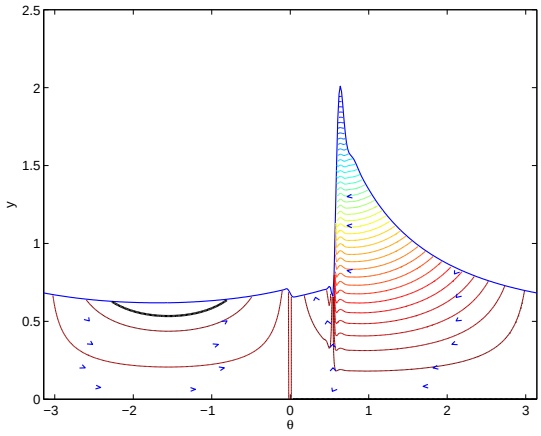

Figure 6.8: Streamlines for uniform input of mass and output at $\theta = 0$, when $c_5 = 1$ and cylinder stationary, $u_{cyl} = 0$. Other parameters are $c_1 = 10^{-5}$, $c_2 = -1$, $c_3 = 0$, $c_4 = 0$, $c_6 = -0.01$, $A = 5.027$

The velocity profiles in figures 6.9 and 6.10 illustrate why this difference arises. In figure 6.9 there is a large wall velocity. The profile is almost uniform in y, slowing

slightly at the top of the peak. In figure 6.10 there is no flow on the cylinder wall. With no driving shear, the fluid moves towards $\theta = 0$ on both sides of the cylinder, driven by gravity and a continuous top-up of mass from the c_5 and c_6 terms. The flow is fastest at the peak, driven by the large value of the c_5 term.

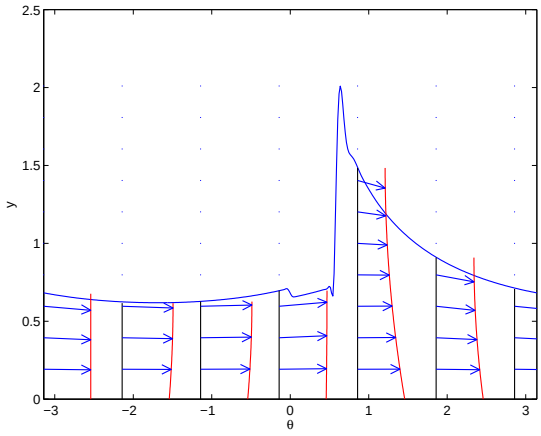

Figure 6.9: Velocity profiles for uniform input of mass and output at $\theta = 0$, when $c_5 = 0$ and cylinder rotating, $u_{cyl} = 1$. Other parameters are $c_1 = 10^{-5}$, $c_2 = -1$, $c_3 = 0$, $c_4 = 0$, $c_6 = -0.01$, $A = 5.027$

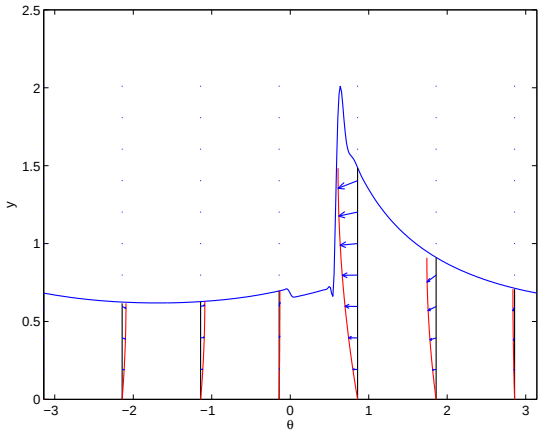

Figure 6.10: Velocity profiles for uniform input of mass and output at $\theta = 0$, when $c_5 = 1$ and cylinder stationary, $u_{cyl} = 0$. Other parameters are $c_1 = 10^{-5}$, $c_2 = -1$, $c_3 = 0$, $c_4 = 0$, $c_6 = -0.01$, $A = 5.027$

6.3 Rotation with opposing surface shear.

The case where the rotation opposes the direction of the core flow gives rise to some interesting flows, as discussed by Villegas-Díaz [51]. In that work, the effect of the droplets input was simplified to a surface shear term, equivalent to the c_4 term in (4.6) and azimuthal droplet momentum (c_3) and droplet mass (c_5, c_6) contributions were neglected. In this section we re-examine the corresponding results using the methods

developed in this thesis, including an analysis of the film-flow streamlines. We will then go on to look at the effect on these film profiles of the c_3 term.

6.3.1 Re-examination of Villegas-Díaz' results

One of the most interesting flows Villegas-Díaz found was in figure 4.9 of [51], for anticlockwise (positive) rotation with clockwise (negative) shear, and various surface tensions. The parameters (in his notation) are $B^{-1} = 10^{-5}$ to $B^{-1} = 10^{-1}$, $\Gamma = 1$, $\gamma = -2.1491$, with $\bar{h} = 0.5944$. Equivalent parameters in (4.6) are given by:

c_1, (B^{-1})	10^{-5} to 10^{-1}		
c_2, $(-\Gamma)$	-1	A	3.739
c_3	0		
c_4, (γ)	-2.1491		
c_5	0	u_{cyl}	1
c_6	0	v_{cyl}	0

Table 6.3: Parameter values for rotation opposing surface shear

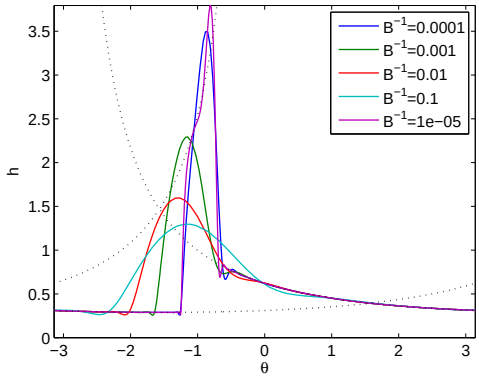

Figure 6.11: Film profiles for opposing shear $c_4 = -2.1491$ and cylinder rotation $u_{cyl} = 1$, with various c_1 (equivalent to B^{-1}). Other parameters are $c_2 = -1$ and $A = 3.739$. Dashed line is the cubic, $c_1 = 0$.

Figure 6.11 shows the corresponding film profiles, which are indistinguishable from Villegas-Díaz' figure 4.9. As we found in Chapter 3, the c_1 surface tension parameter has a stabilising effect, damping the profile peaks. The solution with $c_1 = 10^{-5}$ has little damping, and is an example of a double shock solution, reminiscent of the solutions reported by Bertozzi *et al.* [11] to occur in the case of flow down an inclined plane opposed by Marangoni stresses due to a temperature gradient on the plane. When

$c_1 = 0$ with these parameters, (4.6) reduces to the cubic

$$-\frac{h^3}{3}\sin\theta + \gamma\frac{h^2}{2} + u_{cyl}h = q,$$

the solution of which is included in the figure. The cubic has three branches which can be connected by shock solutions, and the film profile with $A = 3.739$ connects all three.

Figure 6.12 shows the film profile from figure 6.11 with the least surface tension, $c_1 = 10^{-5}$, on a polar plot. We can see that the bulge in the film primarily arises from the opposing effects of the shear and combined gravity and rotation terms, as it occurs in the $-\pi/2 < \theta < 0$ quadrant. On the polar plot the double shock appears as an extended recirculation region, thickening in the direction of rotation.

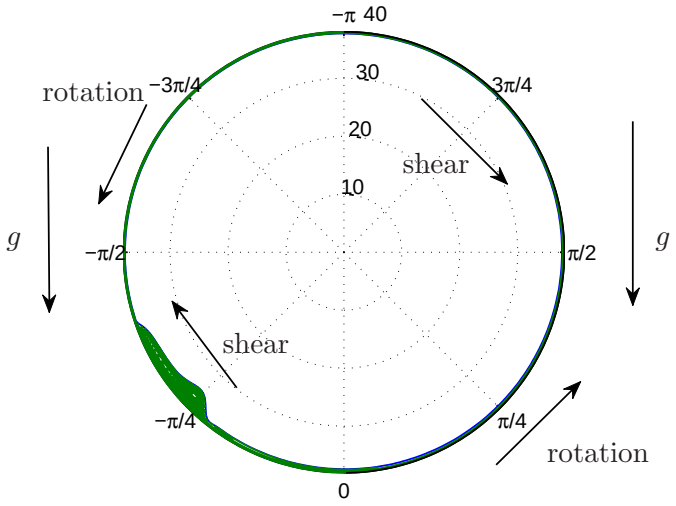

Figure 6.12: Polar plot of film profile for opposing shear, $c_4 = -2.1491$, and rotation, $u_{cyl} = 1$. Other parameters are $c_1 = 10^{-5}$, $c_2 = -1$ and $A = 3.739$.

With the streamline code, we are also able to look at the flow beneath the surface, shown in figure 6.13. There is a strong recirculation region under the main spike. There is a weak recirculation by the second shock, which is strongest for intermediate surface tension values, and absorbed by the main peak for very high surface tension.

6.3.2 Effect of azimuthal droplet momentum c_3 on shear and rotation cases

The work by Villegas-Díaz derives the film profiles in the case of rotation and an imposed surface shear. However our derivation in Chapter 2 shows that only for very low droplet volume fraction ($\alpha = O(\epsilon^3)$) and moderate impact angle can droplets impart this shear term — equivalent to c_4 — alone. Otherwise, they also contribute c_6 or the c_3 term, the azimuthal component of droplet momentum, which has a $\frac{\partial h}{\partial \theta}$ dependence. In Chapter 3,

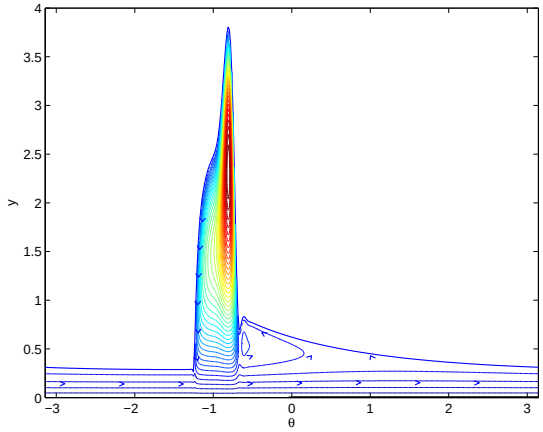

(i) $c_1 = 10^{-5}$

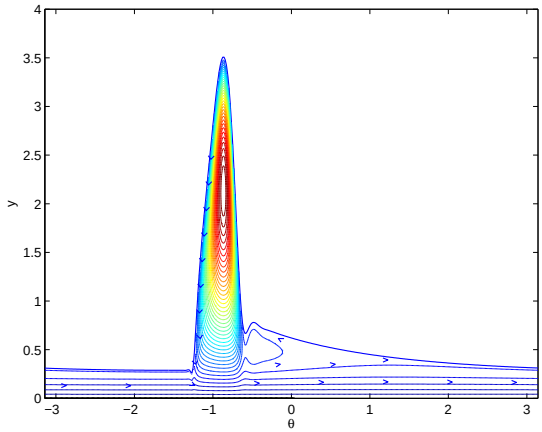

(ii) $c_1 = 10^{-4}$

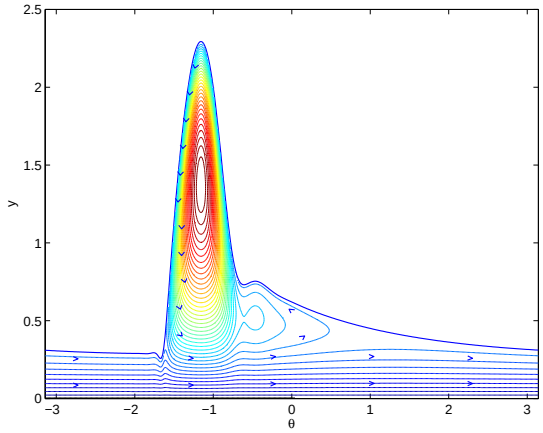

(iii) $c_1 = 10^{-3}$

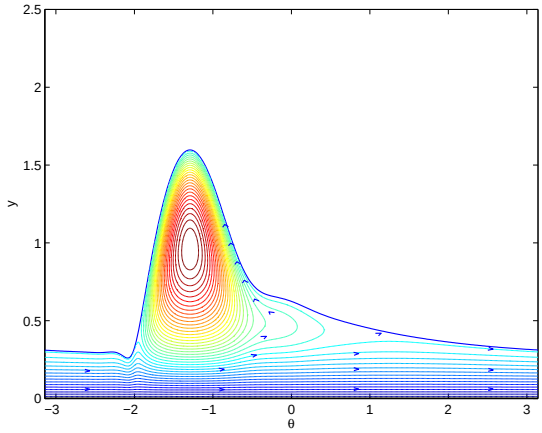

(iv) $c_1 = 10^{-2}$

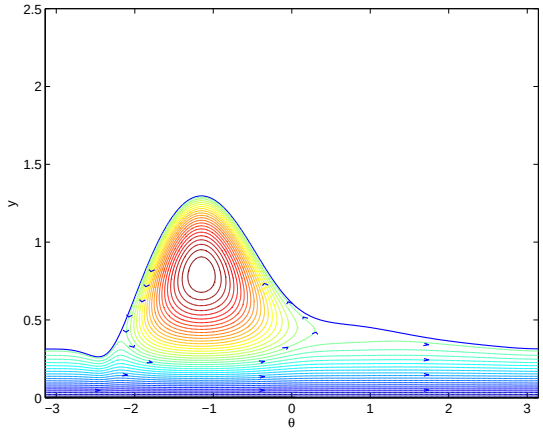

(v) $c_1 = 10^{-1}$

Figure 6.13: Streamlines for opposing shear and rotation, with increasing surface tension (c_1). Other parameters are $c_2 = -1$ $c_4 = -2.1491$ and $A = 3.739$.

the latter was shown to be significant, especially as a destabilising factor if it is large. The c_3 coefficient, because it arises from u_E^2, is always positive, regardless of the sign of c_4. Thus c_3 has a destabilising effect whichever the direction of the external flow or shear.

We now consider the effect of c_3 on the Villegas-Díaz solutions. The base case has been chosen as (iii) in figure 6.13, with $c_1 = 10^{-3}$, $c_4 = -2.1491$ and $A = 3.739$. To this we add c_3, from $c_3 = -10^{-5} \times c_4$ to $c_3 = -c_4$. The results are shown in figure 6.14. Results for $c_3 = 0$ to $c_3 = 2.1491 \times 10^{-4}$ are indistinguishable on this scale. There is little change between $c_3 = 0$ and $c_3 = 0.00215 = 10^{-3}|c_4|$, but when c_3 is increased to $c_3 = 0.215 = 10^{-2}|c_4|$ the peak sharpens, and for greater c_3 a steady-state film profile cannot be found.

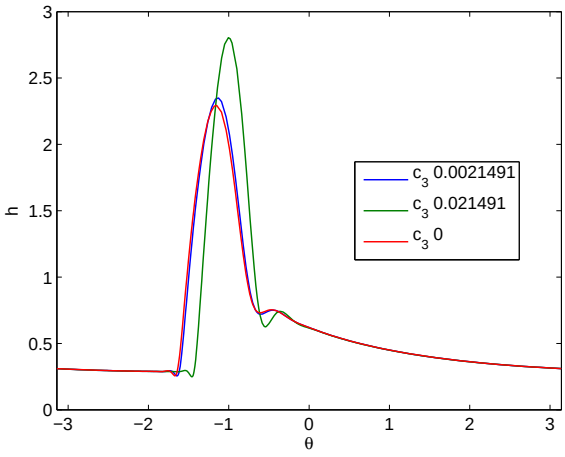

Figure 6.14: Film profiles for azimuthal droplet momentum $c_3 = 0, -0.0021, -0.0214$. Other parameters are $c_1 = 10^{-3}$, $c_2 = -1$, $c_4 = -2.1491$ and $A = 3.739$.

In another example, from Villegas-Díaz [51] figure 4.6, the parameters $c_1 = 10^{-5}$, $c_4 = -3.5$, $u_{cyl} = 1$ and $A = 13.12$ permit a single descending shock in the $-\pi/2 < \theta < 0$ quadrant. Figure 6.15 illustrates once again that adding a small c_3 term slightly increases the height of the peak. With these parameters, if $c_3 > 0.07$ then the shock solution is unstable, and a steady-state film profile cannot be found.

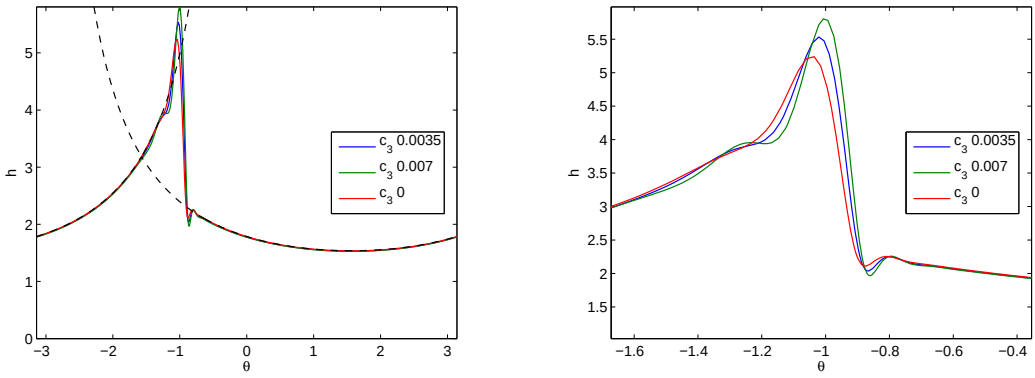

(i) (ii)

Figure 6.15: Film profiles for various c_3 azimuthal droplet momentum, with $c_1 = 10^{-5}$, $c_2 = -1$, $c_4 = -3.5$, $u_{cyl} = 1$, $A = 13.12$. (i) includes an overlay of the cubic $c_1 = 0$ (ii) is a close-up around the peak.

6.4 Derivation of heating effects

One of the purposes of the oil film on the chamber wall is to provide cooling of the hot surfaces. This raises questions of whether the fluid flow provides an effective cooling, and whether the heating of the oil influences the flow. This is a complex system, and we do not attempt to tackle it all here. But in certain limits, heating of the film contributes a term to the film profile equation that already occurs in (4.6), so work done on that equation can be applicable to the thermal case.

6.4.1 Heat equation

The temperature of the fluid is governed by the diffusion equation

$$\rho\, c_p \frac{\mathrm{D}\hat{T}}{\mathrm{D}\hat{t}} = k\nabla^2\hat{T} \tag{6.2}$$

where ρ is the density, c_p the constant pressure heat capacity, and k the thermal conductivity of the fluid. $\hat{T}$ is temperature, and $\hat{t}$ time. The properties of the fluid, in particular viscosity μ and density ρ are assumed to be constant with temperature.

In cylindrical polar coordinates with velocities as defined in chapter 2, the heat equation is:

$$\rho c_p \left(\frac{\partial \hat{T}}{\partial \hat{t}} + \hat{u}_r \frac{\partial \hat{T}}{\partial \hat{r}} + \frac{\hat{u}_\theta}{\hat{r}} \frac{\partial \hat{T}}{\partial \theta} \right) = k \left(\frac{1}{\hat{r}} \frac{\partial}{\partial \hat{r}} \left(\hat{r} \frac{\partial \hat{T}}{\partial \hat{r}} \right) + \frac{1}{\hat{r}^2} \frac{\partial^2 \hat{T}}{\partial \theta^2} \right). \tag{6.3}$$

We non-dimensionalise, using variables

$$y = \frac{r_0 - \hat{r}}{h_0}, \quad u = \frac{\hat{u}_\theta}{\Omega r_0}, \quad v = -\frac{\hat{u}_r}{\Omega h_0}, \quad t = \Omega \hat{t}, \quad T = \frac{\hat{T} - T_a}{T_w - T_a}, \quad h = \frac{\hat{h}}{h_0},$$

where T_a is the ambient temperature in the core of the cylinder, T_w is the temperature at the wall, and Ω is the rate of rotation of the cylinder. The scaling is chosen such that the non-dimensional temperature in the film is positive for $T_w > T_a$. As before, h_0 is the film thickness and r_0 the radius of the cylinder. Then (6.3) becomes

$$\mathrm{Pe} \left(\frac{\partial T}{\partial t} + v \frac{\partial T}{\partial y} + \frac{u}{1 - \epsilon y} \frac{\partial T}{\partial \theta} \right) = \frac{1}{1 - \epsilon y} \frac{\partial}{\partial y} \left((1 - \epsilon y) \frac{\partial T}{\partial y} \right) + \frac{\epsilon^2}{(1 - \epsilon y)} \frac{\partial^2 T}{\partial \theta^2} \tag{6.4}$$

where the Peclet number is given by

$$\mathrm{Pe} = \frac{\Omega h_0^2 \rho c_p}{k}, \quad \text{and} \quad \epsilon = \frac{h_0}{r_0}.$$

If the conductivity of the fluid is large compared to the heat capacity, or if the film is very thin, then diffusion of heat dominates its advection by the fluid, and $\mathrm{Pe} \ll 1$. Since the aspect ratio of the film is thin, $\epsilon \ll 1$. In this case (6.4) reduces to:

$$\frac{\partial^2 T}{\partial y^2} = 0 \text{ to leading order.} \tag{6.5}$$

6.4.2 Thermal Boundary Conditions

If the temperature at the cylinder wall is assumed to be constant, then

$$\hat{T} = T_w, \quad \text{so} \quad T = 1 \quad \text{at} \quad y = 0. \tag{6.6}$$

At the free surface, heat is transfered between the film fluid and the cylinder core. According to Newton's law of cooling, the rate of heat transfer from the surface is proportional to the temperature difference across the surface, so

$$k\nabla\hat{T} \cdot \mathbf{n} + \lambda\left(\hat{T} - T_a\right) = 0, \tag{6.7}$$

where λ is the heat transfer coefficient.

Non-dimensionalising, (6.7) becomes:

$$\left(1 + \left(\frac{\epsilon}{1-\epsilon y}\frac{\partial h}{\partial \theta}\right)^2\right)^{-1/2}\left(\frac{\partial T}{\partial y} - \left(\frac{\epsilon}{1-\epsilon y}\right)^2 \frac{\partial T}{\partial \theta}\frac{\partial h}{\partial \theta}\right) + \mathrm{Bi}\; T = 0, \quad \text{at} \quad y = h, \tag{6.8}$$

where the Biot number is given by

$$\mathrm{Bi} = \frac{\lambda h_0}{k}.$$

Note the sign of the $\frac{\partial h}{\partial \theta}$ term: if the film is hot, and $\frac{\partial h}{\partial \theta} < 0$, then $\frac{\partial T}{\partial \theta} > 0$, and this term *adds* a contribution to the main heat transfer in $\frac{\partial T}{\partial y}$. The ϵ^2 in this term arises from the $1/r$ in ∇T and $\mathbf{n}$.

For $\epsilon \ll 1$, (6.8) reduces to

$$\frac{\partial T}{\partial y} + \mathrm{Bi}\; T = 0, \quad \text{at} \quad y = h. \tag{6.9}$$

6.4.3 Temperature of the film to leading order

In summary, for $\epsilon \ll 1$ and $\mathrm{Pe} \ll 1$ the temperature of the fluid is given by (6.5)

$$\frac{\partial^2 T}{\partial y^2} = 0,$$

with boundary conditions (6.9) and (6.6)

$$\begin{aligned} T &= 1 \quad \text{at} \quad y = 0, \\ \frac{\partial T}{\partial y} + \mathrm{Bi}\; T &= 0 \quad \text{at} \quad y = h. \end{aligned}$$

This system the solution

$$T = 1 - \frac{\mathrm{Bi}}{1 + \mathrm{Bi}\, h}\, y. \tag{6.10}$$

Thus because the film is thin, and conduction dominates advection, the second order gradients of temperature can be neglected, and the temperature has a linear profile in y. At the surface, the temperature is

$$T|_{y=h} = \frac{1}{1+\mathrm{Bi}\,h}$$

so for a heated wall, the surface temperature decreases if the film thickness increases.

6.4.4 Surface Tension

Now surface tension is a function of temperature of the fluid and we follow Kalliadasis *et al.* [28, 50] in modelling it using a linear approximation (6.11) for surface tension, with σ_a the surface tension at T_a, and $\beta > 0$ for typical liquids. So surface tension reduces when the film is hotter than the ambient.

$$\sigma = \sigma_a - \beta\left(\hat{T} - T_a\right). \tag{6.11}$$

Unlike in previous chapters of this thesis, the surface tension is not uniform, since the surface temperature varies according to the thickness of the film. Substituting $y = h$ into (6.10) and (6.11), the surface tension is given by

$$\sigma = \sigma_0 - \frac{\beta\,(T_w - T_a)}{1+\mathrm{Bi}\,h}, \tag{6.12}$$

and for a hot wall increases as the film thickness increases. Variation in surface tension generates a surface shear, given by $\nabla\sigma\cdot\mathbf{t}$ on $y = h$ where $\mathbf{t}$ is the tangent to the surface. $\frac{\partial\sigma}{\partial y} = 0$, so this reduces to

$$\nabla\sigma\cdot\mathbf{t} = \frac{1}{r_0(1-\epsilon h)}\frac{\partial\sigma}{\partial\theta}t_\theta.$$

Substituting in (6.12) and $\mathbf{t}$ as in Chapter 2,

$$\nabla\sigma\cdot\mathbf{t} = \frac{1}{r_0(1-\epsilon h)}\frac{\beta\,(T_w-T_a)\,\mathrm{Bi}}{(1+\mathrm{Bi}\,h)^2}\frac{\partial h}{\partial\theta}\left(1+\left(\frac{\epsilon}{1-\epsilon h}\frac{\partial h}{\partial\theta}\right)^2\right)^{-1/2}.$$

So to leading order in ϵ, the surface shear is given by

$$\nabla\sigma\cdot\mathbf{t} = \frac{\beta\,(T_w-T_a)\,\mathrm{Bi}}{r_0\,(1+\mathrm{Bi}\,h)^2}\frac{\partial h}{\partial\theta}. \tag{6.13}$$

We can simplify this by introducing the Marangoni number, defined as

$$\mathrm{Ma} = \frac{\beta(T_w-T_a)}{\Omega\mu\,r_0},$$

so

$$\nabla\sigma\cdot\mathbf{t} = \Omega\mu\mathrm{Ma}\frac{\mathrm{Bi}}{(1+\mathrm{Bi}\,h)^2}\frac{\partial h}{\partial\theta}. \tag{6.14}$$

Now if $\epsilon < \mathrm{Bi} \ll 1$, as would occur for a thin film if $\lambda \sim k$, then (6.14) reduces to:

$$\nabla\sigma \cdot \mathbf{t} = \Omega\mu\mathrm{MaBi}\,\frac{\partial h}{\partial\theta}.$$

Modifying the argument of Chapter 4, this additional surface shear term contributes to the tangential stress $T(\theta, t)$ in (2.35), (2.64). Therefore if temperature effects are included, we get an additional term in (4.6) of the form

$$\frac{\partial}{\partial\theta}\left(\frac{1}{2}\mathrm{MaBi}\,\frac{\mathrm{d}h}{\mathrm{d}\theta}h^2\right). \tag{6.15}$$

Alternatively, we can write

$$\mathrm{MaBi}\,\frac{\partial h}{\partial\theta} = \gamma,$$

and γ is analogous to an imposed surface shear stress as investigated by Villegas-Díaz *et al.* [51, 53]. We can therefore follow their argument to derive the flux, and reach

$$\frac{\partial h}{\partial t} + \frac{\partial}{\partial\theta}\left(h + \frac{1}{2}\mathrm{MaBi}\,\frac{\mathrm{d}h}{\mathrm{d}\theta}h^2 - \frac{h^3}{3}\sin\theta\right) = 0, \tag{6.16}$$

for a leading-order balance between gravity, rotation and shear stress. (Adapting equation (3.13) of [53], with $B^{-1} = 0$.)

Equation (6.16) is equivalent to (4.6), with coefficients given by

c_1	0		
c_2	-1		
c_3	MaBi		
c_4	0		
c_5	0	u_{cyl}	1
c_6	0	v_{cyl}	0

In the film-height equation, the term (6.15) is equivalent to the c_3 term that we have already generated from azimuthal droplet momentum. So one effect of heating the cylinder wall relative to the ambient temperature would be to create a positive Marangoni number, and increase c_3. As discussed in Chapter 3 and §6.3.2 the c_3 (or α_u) term tends to sharpen any peaks (see figure 3.15) and create a destabilising effect. This is also observed in flow down a heated plane [27].

A side effect of heating is to change the surface tension contribution in other terms. Surface tension acts on the normal boundary condition on the surface (2.11), and occurs in the c_1 coefficient of (4.6). From (6.12), when $\epsilon < \mathrm{Bi} \ll 1$,

$$\sigma = \sigma_0 - \beta\left(T_w - T_a\right),$$

and surface tension is modified by the temperature effects, but only by a constant at leading order, there is no h dependence. The heated wall will thus reduce the surface tension along the whole film profile, tending to increase the size of any peaks and, from our findings in Chapter 3, further contribute to instability. At first order in Bi h, surface tension increases with film thickness and may slightly reduces this effect.

6.5 Summary of this chapter

In this chapter we have considered the additional effects of rotation and heating upon the film profile. Streamline plots of the underlying flow in the film show that although the wall rotation u_{cyl} and azimuthal droplet mass input c_5 are equivalent in the equation for h, the underlying flow is quite different.

There is good agreement with Noakes' results, both for uniform and non-uniform droplet mass input. In these cases, where there is no significant droplet momentum or surface shear and the flow is driven by rotation, there is no recirculation. Also in these cases, non-uniform input of droplets does not change the direction of the flow, as we have seen it might in Chapter 5 where droplet momentum was a significant driver. Here, non-uniform impact has no effect on residence times.

There is also good alignment with Villegas-Díaz' results, and plots of underlying flow show where recirculation occurs beneath the example with a double shock. The effect on the Villegas-Díaz solutions of including the c_3 term necessary to extend the range of droplet parameters for which his work is valid, is to increase the size of peaks and to be destabilising.

In some limits of thermal properties, a Marangoni shear term arises in the film profile equation. It is directly equivalent to the c_3 term arising from the azimuthal droplet momentum, and the same solution methods can be applied as we have already considered. Therefore, as we have shown in Chapter 3, heating the wall will tend to have a destabilising effect on the film, increasing the size of any peaks.

Chapter 7

Conclusions

The key contribution of this thesis is a more thorough development and analysis of equations governing the interaction between the core, droplet-laden flow and the rimming flow of an aero-engine bearing chamber than has previously been undertaken.

The interface between these flows is in reality a complex region, where droplets splash and rebound. In this thesis it has been modelled as a single interface through which droplet exchange occurs. Conservation of mass and momentum have been applied across the interface. The thin aspect ratio (ϵ) of the film has allowed simplification, and led to (4.6), the equation for film height h. The coefficients c_1 to c_6 in this equation arise from the droplet-driven boundary conditions, also from surface tension, gravity, and rotation of the cylinder. An equation of the same form as (4.6) arises when Marangoni forces due to heat transfer are included in the model.

As described at the end of Chapter 2, various combinations of the parameters c_1 to c_6 occur at leading order, according to the volume fraction (α) and the direction of motion of the droplets. With the assumption that the film is primarily driven by a balance between droplet shear and gravity, only certain combinations are valid. c_4, the term equivalent to an imposed surface shear, always occurs. If $\alpha = O(\epsilon^3)$, the shear-only mode — as studied by Villegas-Díaz [51] — can exist but to extend the model up to $\alpha = O(\epsilon^2)$ and beyond at least one of c_3 or c_6 must occur.

Much can be learnt from solutions to the cubic equation (5.2) when the derivative terms in (4.6) are negligible. Given c_2, c_4, c_5 and u_{cyl} we can find the flux q for which steady solutions exist, and by kinematic wave theory deduce which branches are stable. The cubic can have up to three possible real solutions. Villegas-Díaz drew up a chart in c_4-q space, with $u_{cyl} = 1$, to show the various possible solutions, and in Chapter 5 we showed the equivalent in u_{cyl}-q space with $c_4 = 1$.

For the case with $u_{cyl} = 0$, when the flow is governed by gravity c_2 and droplet input or

shear c_4 only, and droplet mass is negligible, the cubic is given by (3.3) and the critical mass is $A_{crit} = 3.951$. If $A > A_{crit}$, then there must be a shock between branches of the cubic solution. Including the derivative terms of (4.6) smooths the shock. The shock is associated with recirculation within the flow. When $c_6 > 0$, and droplet mass is significant, A_{crit} is increased. Unlike the case of the Moffatt problem, with $u_{cyl} = 1$ and $c_4 = 0$, the shock solution can support an arbitrarily large area A of fluid, up to the limit of validity of the thin-film approximation.

Solutions of the cubic (3.3) with $A < A_{crit}$ are neutrally stable. Kinematic wave theory is a useful tool, especially when there are three positive solutions of the cubic and hence a wide range of possible shocks. We used it to deduce which shock solutions can be stable. From this we found the maximum areas possible for various parameter ranges. For the case $u_{cyl}, c_5 = 0$, we found that the ascending shocks are stable, but descending shocks were not, which limited the possible shock solutions to those with the shock in the $0 < \theta < \pi/2$ quadrant.

A disadvantage of the steady-state solver is that it does not conserve A, equivalent to the mass in the system and thus any one of a family of solutions may be found, depending on the initial guess. This gives insight into possible solutions but it is difficult to make meaningful comparisons of the results for fixed areas. We also found that the solver often failed to converge in cases where ζ was small.

A more versatile approach was to develop a full transient solver, and seek steady solutions by looking for convergence through time. The agreement with the indication of the asymptotic matching is excellent, although solutions close to the $\zeta = \alpha_u^3$ cut-off area difficult to find and require continuation from nearby solutions.

The same code was used to reproduce results published by Noakes [34] and Villegas-Díaz [51].

Both the numerical solvers showed that surface tension tends to damp peaks and azimuthal droplet momentum, c_3, to increase them. A matching argument in Chapter 3, backed up by numerical results, showed that there is a balance of $c_1 = c_3^3$. When the cross-sectional area of the film is less than A_{crit}, steady-state solutions without shocks may exist for any range of c_1, c_3. When the cross-sectional area of the film exceeds A_{crit}, then for parameter values: $c_3 = 0$, $c_1 = 0$, steady-state solutions with shocks anywhere in $0 < \theta < \pi$ can exist; $c_1 \geq c_3^3$, steady-state solutions with smoothed shocks in lower quadrant $0 < \theta < \pi/2$ can exist; and $c_1 < c_3^3$, steady-state solutions with smoothed shocks in upper quadrant $\pi/2 < \theta < \pi$ can exist. However the latter are unstable.

Surface tension has a strong smoothing effect but increasing c_3 has little quantitative

effect on the film profile, only a slight steepening of the shock, until we reach the cut-off of $c_3^3 = c_1$ predicted by the matching argument. At this point the destabilising effect of c_3 is too large, and no solutions are sustained.

The term c_3 was omitted from the model of Villegas-Díaz, limiting the validity to $\alpha = O(\epsilon^3)$. When c_3 is included, the validity is extended, but c_3 has the same destabilising effect.

Equivalent to c_3 is the term arising from Marangoni forces when the film is heated. If the cylinder wall is heated relative to the ambient temperature, the Marangoni number is positive and c_3 increased. As discussed in Chapters 3 and 6, the c_3 term tends to sharpen any peaks and be destabilizing. This is also observed in flow down a heated plane.

That the steady-state solutions found by the transient solver are stable was confirmed by adding perturbations and allowing them to evolve in time. It was found that for solutions predicted to be stable according to the matching argument, perturbations decay quickly. However there were unstable steady solutions found using the steady-state solver for which perturbations could grow. Perturbations which add mass shift a stable steady solution to a nearby one with a slightly larger shock. The results of eigenvalue analysis of stability were inconclusive, with conflicting results from finite difference and spectral methods.

When droplets contribute significant mass as well as momentum to the film, a steady solution can be found when there is an outflow at the sink with the flux matched to the total inflow. c_5 and c_6 are the coefficients in (4.6) of droplet mass impacting on the film from the azimuthal and radial directions respectively. The mass mass outflow, primarily balancing the c_6 term, tends to generate a down-shock at the sink, and reduce the size of other peaks. Sufficient mass influx c_6 can prevent any steady solutions of this form existing.

If $c_5 = 0$, as c_6 increases in magnitude, we see a descending shock develop over the sink. The film thickens to the left-hand side of the sink. If $c_6 = 0$ and c_5 changed, then for the film area A that was studied, a distinct transition is seen between $c_5 = 0$ and $c_5 = -1$, and stable steady solutions are not found throughout the parameter range between them. We showed in Chapter 5 that this was because for $c_5 = -0.5$ for example, A_{crit} is reduced.

For $c_5 = -1$ the film profile h is identical to that with clockwise rotation, as if $u_{cyl} = -1$. However the underlying streamlines are different.

The droplets may not impact uniformly around the cylinder, that is the droplet fraction

α and velocities u_E, v_E may be function of θ. In the absence of data about the distribution of velocities, we have varied only the distribution of droplet fraction, but this affects both droplet mass and momentum input functions.

The effect of altering the droplet distribution is dependent on the average droplet parameters and whether the cylinder is rotating. In the Noakes case, changing the droplet distribution has little effect, but for the parameters examines in Chapter 5 it as dramatic effects. If oil is introduced with a single injector, the distribution function may be similar to a half-normal. If the flow is driven by shear, so that the droplet momentum is large, then a single injector input can cause a *thinning* of the film after the injector. This is in contrast to the thickening seen after a single injector point when the film is driven by rotation, and the droplets contribute purely mass with negligible momentum. In the latter case the non-uniform input barely affects the residence time of the film fluid, only changing behaviour near the surface. In the former case, the non-uniform input changes the direction as well as speed of the underlying flow.

Shear-driven flow contrasts with rotation-drive flow in that beneath a shock in the film profile is a recirculation region on the cylinder wall. This may be associated with hot-spots, although we have not undertaken the thermal modelling required to establish the severity of these. Such modelling is considered the most critical area for further development.

Reducing the total mass below A_{crit} and hence eliminating shock solutions may remove recirculation. Strategic placement of the sink has also been considered, and although for the parameters examined there are no sink positions which completely eliminate recirculation, it greatly diminished when the sink was under the shock. Since results in Chapter 5 show that the size of recirculation regions diminishes with reduced A, then it seems likely that with slightly reduced A then the recirculation could be eliminated completely by careful sink position.

Another important area for further work is to couple this model to a numerical model of the core flow, so that more precise droplet distribution parameters can be established.

Appendix A

Nomenclature

Other variables may appear, but if not included in this list they should be locally defined.

Greek:

α	volume fraction of droplets in upper fluid
α_u	droplet momentum parameter
β	characterises droplet impact angle, $V_E = \epsilon^\beta U_E$
β	coefficient relating surface tension to temperature (Chap. 6 only)
δ_{ij}	the Kronecker delta
$\epsilon = \frac{h_0}{r_0}$	the aspect ratio of the film
ζ	non-dimensional surface tension related parameter
$\eta(s)$	small perturbation
θ	annular/cylindrical polar coord, measured anticlockwise from downwards vertical
κ	surface curvature
λ	heat transfer coefficient (Chap. 6 only)
μ	coefficient of viscosity
$\xi(\theta, t) = 0$	surface function (in derivation of boundary conditions)
$\xi(\theta, t)$	small perturbation (in stability analysis)
ρ	density
σ	surface tension coefficient
τ_{ij}	viscous stress tensor
ϕ	angle of droplet impact
Ω	rotation rate

Latin lowercase:

a	scaled volume fraction of droplets
c_1 to c_6	coefficients of the film-height equation
c_p	constant pressure heat capacity (Chap. 6 only)
$\mathbf{e}_i$	coordinate base vector
$\mathbf{e}_{ij}$	tensor
g	acceleration due to gravity
$h(\theta,t), \hat{h}(\theta,t)$	function giving height of surface, non-dim/dimensional, annular
$\hat{h_r}(\theta,t)$	height of surface, dimensional, cylindrical coords
h_0	scaling on height $\hat{y} = h_0 y$
k	scaling on droplet fraction. $\alpha = \epsilon^k a$
k	thermal conductivity (Chap. 6 only)
$\mathbf{n}$	normal to free surface
$p, \hat{p}$	pressure, non-dim/dimensional $\hat{p} = \frac{\rho U^2}{\epsilon} p$
$q = \int_0^h u \mathrm{d}y$	azimuthal flux
$\hat{r}$	radial polar coordinate, dimensional
r_0	radius of cylinder
$t, \hat{t}$	time, non-dim/dimensional $\hat{t} = \frac{r_0}{U} t$
$\mathbf{t}$	tangent to free surface
$\mathbf{u}$	velocity vector
$\hat{u}_\theta, \hat{u}_r$	components of velocity in θ, r directions, dimensional
$u, v, \hat{u}, \hat{v}$	components of velocity in θ, y directions, non-dim/dim.
$w = \frac{\partial q}{\partial h}$	kinematic wave speed
$y, \hat{y}$	coordinate normal to cylinder in 2-d annular coords, non-dim/dim.

Latin uppercase:

A	dimensionless measure of cross-sectional area of the film
BC	abbreviation for boundary condition(s)
$\mathrm{Bi} = \frac{\lambda h_0}{k}$	Biot number
$\frac{\mathrm{D}}{\mathrm{D}t}$	convective derivative
$\mathrm{Fr} = \frac{U^2}{g h_0}$	Froude number
M, N_l, T	droplet dependent terms in boundary conditions
$\mathrm{Ma} = \frac{\beta(T_w - T_a)}{\Omega \mu r_0}$	Marangoni number
$N = \left(1 + \left(\frac{\epsilon}{1-\epsilon h} \frac{\partial h}{\partial \theta}\right)^2\right)^{-1/2}$	factor of surface normal (may be variously defined in derivations)
P, Q, R, S, V	general quantities used in the derivation of boundary conditions
$\mathrm{Pe} = \frac{\Omega h_0^2 \rho c_p}{k}$	reduced Peclet number

$\mathrm{Re_f} = \frac{\rho U h_0}{\mu}$	reduced Reynolds number of the film
T_{ij}	stress tensor
T	temperature (Chap. 6 only)
U, V	scaling on u, v. $\hat{u} = Uu$
$\mathrm{We_f} = \frac{\sigma h_0^2}{U^2 \rho r_0^3}$	reduced inverse Weber number of the film

Subscripts:

i, j	subscripts used in the summation convention
E	subscript used for fluid *external* to the film, in the core of the chamber
I	subscript used for fluid *internal* to the film (usually omitted).
θ, r	cylindrical polar subscripts
θ, y	annular subscripts
s	steady solution
K	shock position, solution at shock
cyl	conditions on the cylinder wall
a, w	ambient, wall (Chap. 6 only)

hat $\hat{}$ is used for dimensional variables.

The jump notation $[x]$ indicates $x_E - x_I$, the jump in a quantity across the interface.

Appendix B

Useful Identities

B.1 Grad and Div in cylindrical coordinates.

In cylindrical polars neglecting the axial (z) component, for general ϕ, $\mathbf{F}$ [1]:

$$\nabla\phi = \frac{\partial\phi}{\partial\hat{r}}\mathbf{e}_r + \frac{1}{\hat{r}}\frac{\partial\phi}{\partial\theta}\mathbf{e}_\theta, \quad \nabla\cdot\mathbf{F} = \frac{F_r}{\hat{r}} + \frac{\partial F_r}{\partial\hat{r}} + \frac{1}{\hat{r}}\frac{\partial F_\theta}{\partial\theta}.$$

In the annular coordinate system, dimensionless variables,

$$\nabla\phi = \frac{1}{h_0}\frac{\partial\phi}{\partial y}\mathbf{e}_y + \frac{1}{r_0 - h_0 y}\frac{\partial\phi}{\partial\theta}\mathbf{e}_\theta,$$

so the unit outward normal has components

$$n_\theta = -\frac{\epsilon}{1-\epsilon y}\frac{\partial h}{\partial\theta}\left(1+\left(\frac{\epsilon}{1-\epsilon y}\frac{\partial h}{\partial\theta}\right)^2\right)^{-1/2}, \quad n_y = \left(1+\left(\frac{\epsilon}{1-\epsilon y}\frac{\partial h}{\partial\theta}\right)^2\right)^{-1/2},$$

and the unit tangent in the θ direction has components

$$t_\theta = \left(1+\left(\frac{\epsilon}{1-\epsilon y}\frac{\partial h}{\partial\theta}\right)^2\right)^{-1/2}, \quad t_y = \frac{\epsilon}{1-\epsilon y}\frac{\partial h}{\partial\theta}\left(1+\left(\frac{\epsilon}{1-\epsilon y}\frac{\partial h}{\partial\theta}\right)^2\right)^{-1/2}.$$

B.2 Stress Tensor

The stress tensor is given by

$$T_{ij} = -p\delta_{ij} + 2\mu e_{ij}$$

where in cylindrical polar coordinates

$$e_{rr} = \frac{\partial\hat{u}_r}{\partial\hat{r}}, \quad e_{\theta\theta} = \frac{1}{\hat{r}}\frac{\partial\hat{u}_\theta}{\partial\theta} + \frac{\hat{u}_r}{\hat{r}}, \quad 2e_{r\theta} = \hat{r}\frac{\partial}{\partial\hat{r}}\left(\frac{\hat{u}_\theta}{\hat{r}}\right) + \frac{1}{\hat{r}}\frac{\partial\hat{u}_r}{\partial\theta}.$$

Appendix C

Film-height equation to $O(\epsilon)$

C.1 Film height equation for generic droplet conditions

The derivation of the film profile equations to $O(\epsilon)$ was carried out, and is provided here for reference. We use the information from the $O(\epsilon)$ term, (2.47-2.49) with boundary conditions (2.55-2.59) to find p_1, u_1, v_1 and h_1.

p_0, u_0, v_0 are determined in terms of $h_0(\theta, t)$ (2.60). Integrating (2.48) and applying the boundary condition (2.55),

$$p_1 = -\frac{1}{\mathrm{Fr}}\cos\theta(y - h_0) + 3h_0 N_{l0} + N_{l1}. \tag{C.1}$$

Differentiating wrt θ and substituting into (2.47) leads to

$$\frac{\partial^2 u_1}{\partial y^2} = \mathrm{Re_f}\left(\frac{\partial u_0}{\partial t} + u_0\frac{\partial u_0}{\partial \theta} + v_0\frac{\partial u_0}{\partial y} - y\frac{\partial p_0}{\partial \theta} + \frac{\partial p_1}{\partial \theta} + \frac{1}{\mathrm{Re_f}}\left(2y\frac{\partial^2 u_0}{\partial y^2} + \frac{\partial u_0}{\partial y}\right) - 2y\frac{1}{\mathrm{Fr}}\sin\theta\right). \tag{C.2}$$

Substituting in the known u_0, v_0 and p_0 gives a polynomial in y

$$\frac{\partial^2 u_1}{\partial y^2} = \sum_{n=0}^{4} G_n y^n, \tag{C.3}$$

where

$$\begin{aligned}
G_0 =& \mathrm{Re_f}\frac{\partial}{\partial \theta}\left(\frac{\cos\theta}{\mathrm{Fr}}h_0 + N_{l1} + 3hN_{l0}\right) - F_0 h_0 + T_0,\\
G_1 =& \mathrm{Re_f}\left(\frac{\partial}{\partial t}\left(-F_0 h_0 + T_0\right)\right) + 2F_0,\\
G_2 =& \mathrm{Re_f}\left(\frac{1}{2}\frac{\partial F_0}{\partial t} + \frac{1}{4}\frac{\partial}{\partial \theta}\left(\left(-F_0 h_0 + T_0\right)^2\right)\right),\\
G_3 =& \mathrm{Re_f}\left(F_0\frac{\partial}{\partial \theta}\left(-F_0 h_0 + T_0\right) + \frac{1}{3}\left(-F_0 h_0 + T_0\right)\frac{\partial F_0}{\partial \theta}\right),\\
G_4 =& \mathrm{Re_f}\left(\frac{1}{24}\frac{\partial}{\partial \theta}\left(F_0^2\right)\right).
\end{aligned}$$

Integrating twice, using boundary conditions (2.56) on $y = h_0$ and (2.58) on $y = 0$ gives

$$u_1 = \sum_{n=1}^{6} H_n y^n, \tag{C.4}$$

where

$$\begin{aligned}
H_1 =& \left(-\sum_{n=0}^{4} G_n \frac{(h_0^{n+1})}{n+1} + 3h_0T_0 + T_1 - \left(F_0 \frac{h_0^2}{2} + (-F_0h_0 + T_0)\, h_0 \right) - h_1F_0 \right), \\
H_2 =& G_0/2, \\
H_3 =& G_1/6, \\
H_4 =& G_2/12, \\
H_5 =& G_3/20, \\
H_6 =& G_4/30.
\end{aligned}$$

Now differentiating wrt θ and use the first-order terms of the continuity equation (2.49) and (2.63) gives $\frac{\partial v_1}{\partial y}$. Integrating with the boundary condition (2.59)on $y = 0$ gives:

$$v_1 = -\sum_{n=1}^{6} \frac{\partial H_n}{\partial \theta} \frac{y^{n+1}}{n+1} - \left(\frac{\partial F_0}{\partial \theta} \frac{y^4}{6} + \frac{\partial}{\partial \theta} (-F_0h_0 + T_0) \frac{y^3}{2} \right). \tag{C.5}$$

Evaluating at $y = h_0$ and substituting into the $O(\epsilon)$ terms of the kinematic boundary condition (2.57) gives:

$$\frac{\partial h_1}{\partial t} + \frac{\partial}{\partial \theta} \left(h_1 \left(-\frac{F_0h_0^2}{2} + T_0h_0 \right) \right) - h_0 \frac{\partial h_0}{\partial t} + \sum_{n=1}^{6} \frac{\partial}{\partial \theta} \left(\frac{H_n h_0^{n+1}}{n+1} \right) = M_1$$

Substituting back in for H_n and then G_n leads to a pde for h_1.

$$\begin{aligned}
&\frac{\partial h_1}{\partial t} + \frac{\partial}{\partial \theta} \left(h_1h_0 \left(-F_0h_0 + T_0 \right) \right) - h_0 \frac{\partial h_0}{\partial t} \\
&\quad + \frac{\partial}{\partial \theta} \left(\left(3h_0T_0 + T_1 - \left(F_0 \frac{h_0^2}{2} + (-F_0h_0 + T_0)\, h_0 \right) \right) \frac{h_0^2}{2} \right. \\
&\quad - \left(\mathrm{Re_f} \frac{\partial}{\partial \theta} \left(\frac{\cos\theta}{\mathrm{Fr}} h_0 + N_{l1} + 3h_0N_{l0} \right) - F_0h_0 + T_0 \right) \frac{h_0^3}{3} \\
&\quad - \left(\mathrm{Re_f} \left(\frac{\partial}{\partial t} \left(-F_0h_0 + T_0 \right) \right) + 2F_0 \right) \frac{h_0^4}{24} \\
&\quad - \left(\mathrm{Re_f} \left(\frac{1}{2} \frac{\partial F_0}{\partial t} + \frac{1}{4} \frac{\partial}{\partial \theta} \left((-F_0h_0 + T_0)^2 \right) \right) \right) \frac{h_0^5}{20} \\
&\quad - \left(\mathrm{Re_f} \left(\frac{1}{3} \left(-F_0h_0 + T_0 \right) \frac{\partial F_0}{\partial \theta} \right) \right) \frac{7h_0^6}{60} \\
&\quad - \left(\mathrm{Re_f} \left(\frac{1}{24} \frac{\partial}{\partial \theta} \left(F_0^2 \right) \right) \right) \frac{2h_0^7}{21} \Bigg) = M_1,
\end{aligned}$$

where $F_0 = \mathrm{Re_f} \left(\frac{\partial N_{l0}}{\partial \theta} + \frac{1}{\mathrm{Fr}} \sin\theta \right)$, and N_{l0}, N_{l1}, T_0, T_1 and M_0, M_1 are determined by the choice of droplet conditions.

C.2 Distinguished limits - Droplet cases

C.2.1 Very low droplet volume fraction, steep angle $k = 3$, $\beta = -1$

$$
\begin{aligned}
N_{l1} &= -\mathrm{We_f}\left(-2h_0^2 + \frac{1}{2}\left(\frac{\partial h_0}{\partial \theta}\right)^2 - h_0\frac{\partial^2 h_0}{\partial \theta^2} + h_1 + \frac{\partial^2 h_1}{\partial \theta^2}\right) + a(-3h_0)\left(v_E\right)^2, \\
T_1 &= \mathrm{Re_f} a v_E\left(3h_0 u_E + 2h_0 v_E\frac{\partial h_0}{\partial \theta} + u_0 - v_E\frac{\partial h_1}{\partial \theta}\right) \\
M_1 &= a\left(h_0 v_E\right).
\end{aligned}
$$

C.2.2 Very low droplet volume fraction, shallow angle $k = 3$, $\beta = 1$

$$
\begin{aligned}
N_{l1} &= -\mathrm{We_f}\left(-2h_0^2 + \frac{1}{2}\left(\frac{\partial h_0}{\partial \theta}\right)^2 - h_0\frac{\partial^2 h_0}{\partial \theta^2} + h_1 + \frac{\partial^2 h_1}{\partial \theta^2}\right), \\
T_1 &= -\mathrm{Re_f} a u_E\left(2h_0 u_E\frac{\partial h_0}{\partial \theta} - 3h_0 v_E - u_E\frac{\partial h_1}{\partial \theta}\right), \\
M_1 &= a\left(u_E\frac{\partial h_0}{\partial \theta} - v_E\right).
\end{aligned}
$$

C.2.3 Low droplet volume fraction $k = 2$, $\beta = 0$

$$
\begin{aligned}
N_{l1} &= -\mathrm{We_f}\left(-2h_0^2 + \frac{1}{2}\left(\frac{\partial h_0}{\partial \theta}\right)^2 - h_0\frac{\partial^2 h_0}{\partial \theta^2} + h_1 + \frac{\partial^2 h_1}{\partial \theta^2}\right) + \left(v_E\right)^2, \\
T_1 &= -\mathrm{Re_f} a\left(-h_0 u_E v_E + \left(-h_0 u_E + v_E\frac{\partial h_0}{\partial \theta} - u_0\right)v_E + u_E\left(-u_E\frac{\partial h_0}{\partial \theta} - h_0 v_E\right)\right), \\
M_1 &= a\left(u_E\frac{\partial h_0}{\partial \theta} + h_0 v_E\right).
\end{aligned}
$$

C.2.4 Moderate droplet volume fraction $k = 1$, $\beta = 1$

$$
\begin{aligned}
N_{l1} &= -\mathrm{We_f}\left(-2h_0^2 + \frac{1}{2}\left(\frac{\partial h_0}{\partial \theta}\right)^2 - h_0\frac{\partial^2 h_0}{\partial \theta^2} + h_1 + \frac{\partial^2 h_1}{\partial \theta^2}\right), \\
T_1 &= -\mathrm{Re_f} a\left(u_E\left(-h_0 v_E + u_0\frac{\partial h_0}{\partial \theta} - v_0\right) - \left(2h_0 u_E + u_0\right)\left(-u_E\frac{\partial h_0}{\partial \theta} + v_E\right)\right. \\
&\qquad \left. - u_E\left(u_E\frac{\partial h_1}{\partial \theta}\right)\right), \\
M_1 &= a\frac{\partial h_0}{\partial t} + a h_0 v_E + a u_E\frac{\partial h_1}{\partial \theta}.
\end{aligned}
$$

Appendix D

Extension of analysis to negative u_E

Equation (3.1) holds for both positive and negative u_E, that is droplets travelling in either a clockwise or anti-clockwise direction. It is worth checking that the symmetry holds in terms of where stable shocks may or may not be found.

If u_E (and hence α_u can be negative, (3.2) should be written

$$\frac{\partial h}{\partial t}+\frac{\partial q}{\partial \theta}=0, \qquad q=\zeta\frac{h^3}{3}\left(\frac{\partial h}{\partial \theta}+\frac{\partial^3 h}{\partial \theta^3}\right)-\sin\theta\frac{h^3}{3}+\left(\alpha_u\frac{\partial h}{\partial \theta}+\mathrm{sign}(\alpha_u)\right)\frac{h^2}{2}, \quad \text{(D.1)}$$

and (3.3) is replaced by

$$q=-\sin\theta\frac{h^3}{3}+\mathrm{sign}(\alpha_u)\frac{h^2}{2}. \quad \text{(D.2)}$$

When $\alpha_u<0$, the solutions of (D.2) are the same as for (3.3), but with q and θ negative. So the critical point is now at $\theta_c=-\pi/2$, for a flux of $q=-1/6$, and there are two branches of the solution in $-\pi<\theta<0$.

D.1 Smoothing of shocks by surface tension and droplets

The argument about matching shock solutions proceeds much as before, with (3.11) replaced by

$$q=\zeta\frac{H^3}{3}\left(\frac{1}{\delta^3}\frac{\mathrm{d}^3H}{\mathrm{d}\phi^3}+\frac{1}{\delta}\frac{\mathrm{d}H}{\mathrm{d}\phi}\right)-\frac{H^3}{3}\sin(\theta_K+\delta\phi)+\mathrm{sign}(\alpha_u)\frac{H^2}{2}\left(1+\frac{\alpha_u}{\delta}\frac{\mathrm{d}H}{\mathrm{d}\phi}\right). \quad \text{(D.3)}$$

D.1.1 Surface tension dominant

For general α_u, equation (3.13) is replaced by

$$q=\frac{H^3}{3}\left(\frac{\mathrm{d}^3H}{\mathrm{d}\phi'^3}\right)-\frac{H^3}{3}\sin(\theta_K)+\frac{H^2}{2}\left(\mathrm{sign}(\alpha_u)+\mathrm{sign}(\alpha_u)\frac{\alpha_u}{\zeta^{1/3}}\frac{\mathrm{d}H}{\mathrm{d}\phi'}\right), \quad \text{(D.4)}$$

and the equation for f_j becomes

$$\frac{\mathrm{d}^3 f_j}{\mathrm{d}\phi^3}+a_j\frac{\mathrm{d}f_j}{\mathrm{d}\phi}+b_j f_j=0, \quad \text{(D.5)}$$

$$\text{where} \quad a_j = \text{sign}(\alpha_u)\frac{3\alpha_u}{2\zeta^{1/3}}\frac{1}{h_j}, \quad b_j = -\frac{3}{2h_j^2}\left(h_j \sin\theta_K + \text{sign}(\alpha_u)\right).$$

So for $\alpha_u < 0$,

$$a_1 > 0, \quad a_2 > 0, \quad b_1 > 0, \quad \text{and} \quad b_2 < 0.$$

As $\phi' \to \infty$, f_j can only be bounded with two non-zero coefficients if $C_1 = 0, C_2, C_3 \neq= 0$ and $x_j > 0$, which is only satisfied by x_2. Therefore, as $\phi \to \infty$, the inner solution $H(\phi)$ can only be matched by the lower branch.

As $\phi' \to -\infty$, f_j can only be bounded with two non-zero coefficients if $C_1 = 0, C_2, C_3 \neq= 0$ and $x_j < 0$, which is only satisfied by x_1. Therefore, as $\phi \to -\infty$, the inner solution $H(\phi)$ can only be matched by the upper branch.

So for $\alpha_u < 0$, that is for $u_E < 0$, with surface tension dominant it is only possible to match the inner solution to the outer cubic for a shock falling from the upper branch to the lower branch. Since the flux q is reversed, this is symmetric to the $\alpha_u > 0$ case.

D.1.2 Droplet momentum dominant

For general α_u, (3.19) is replaced by

$$q = \frac{\zeta}{|\alpha_u|^3}\frac{H^3}{3}\frac{\mathrm{d}^3 H}{\mathrm{d}\phi'^3} + \frac{\zeta}{|\alpha_u|}\frac{H^3}{3}\frac{\mathrm{d}H}{\mathrm{d}\phi'} - \frac{H^3}{3}\sin(\theta_K) + O(|\alpha_u|) + \text{sign}(\alpha_u)\frac{H^2}{2}\left(1 + \text{sign}(\alpha_u)\frac{\mathrm{d}H}{\mathrm{d}\phi'}\right). \tag{D.6}$$

and (3.20) becomes

$$q = -\frac{H^3}{3}\sin\theta_K + \frac{H^2}{2}\left(\text{sign}(\alpha_u) + \frac{\mathrm{d}H}{\mathrm{d}\phi'}\right), \tag{D.7}$$

leading to

$$\frac{\mathrm{d}\phi'}{\mathrm{d}H} = \frac{H^2}{2\left(q + \frac{H^3}{3}\sin(\theta_K) - \text{sign}(\alpha_u)\frac{H^2}{2}\right)}. \tag{D.8}$$

Proceeding as before, but with the roots h_j of the more general cubic (D.2), leads again to (3.27).

For $\alpha_u < 0$, the only difference from before is that the shock must be in $-\pi < \theta_K < 0$, and therefore $\sin\theta_K < 0$, changing the sign of the left-hand side of (3.28) and (3.29). Therefore it is only possible to match a rising shock, from h_2 to h_1, which must be in the quadrant $-\pi < \theta_K < \pi/2$. Since the flux q is reversed, this is symmetric to the $\alpha_u > 0$ case.

Appendix E

Derivation of linear stability analysis

Consider perturbations to a steady solution of (3.2). Let h_s be a steady solution to the equation

$$\frac{\partial h}{\partial t}+\frac{\partial q}{\partial \theta}=0, \quad q=\left(\frac{\zeta h^3}{3}\left(\frac{\partial^3 h}{\partial \theta^3}+\frac{\partial h}{\partial \theta}\right)-\frac{h^3}{3}\sin(\theta)+\left(1+\alpha_u\frac{\partial h}{\partial \theta}\right)\frac{h^2}{2}\right).$$

Apply the perturbation $h=h_s(\theta)+\delta\xi(\theta,t)$, where $\delta \ll |\alpha_u|$, $\delta \ll \zeta$ and $\delta \ll 1$. Then

$$\begin{aligned} q=q_s+\delta\Bigg[&\left(\zeta h_s^2\left(\frac{\mathrm{d}^3 h_s}{\mathrm{d}\theta^3}+\frac{\mathrm{d}h_s}{\mathrm{d}\theta}\right)-h_s^2\sin\theta+\left(\mathrm{sign}(\alpha_u)+|\alpha_u|\frac{\mathrm{d}h_s}{\mathrm{d}\theta}\right)h_s\right)\xi \\ &+\left(|\alpha_u|\frac{h_s^2}{2}+\zeta\frac{h_s^3}{3}\right)\frac{\mathrm{d}\xi}{\mathrm{d}\theta}+\left(\zeta\frac{h_s^3}{3}\right)\frac{\mathrm{d}^3\xi}{\mathrm{d}\theta^3}\Bigg]+O(\delta^2), \end{aligned} \tag{E.1}$$

where the base flow is

$$q_s=\zeta\frac{h_s^3}{3}\left(\frac{\mathrm{d}^3 h_s}{\mathrm{d}\theta^3}+\frac{\mathrm{d}h_s}{\mathrm{d}\theta}\right)-\frac{h_s^3}{3}\sin\theta+\left(\mathrm{sign}(\alpha_u)+|\alpha_u|\frac{\mathrm{d}h_s}{\mathrm{d}\theta}\right)h_s=const.$$

Therefore neglecting quadratic terms, we have

$$\begin{aligned} \frac{\partial \xi}{\partial t}+\frac{\partial}{\partial \theta}\Bigg[&\left(\zeta h_s^2\left(\frac{\mathrm{d}^3 h_s}{\mathrm{d}\theta^3}+\frac{\mathrm{d}h_s}{\mathrm{d}\theta}\right)-h_s^2\sin\theta+\left(\mathrm{sign}(\alpha_u)+|\alpha_u|\frac{\mathrm{d}h_s}{\mathrm{d}\theta}\right)h_s\right)\xi \\ &+\left(|\alpha_u|\frac{h_s^2}{2}+\zeta\frac{h_s^3}{3}\right)\frac{\mathrm{d}\xi}{\mathrm{d}\theta}+\left(\zeta\frac{h_s^3}{3}\right)\frac{\mathrm{d}^3\xi}{\mathrm{d}\theta^3}\Bigg]=0. \end{aligned} \tag{E.2}$$

Expanding,

$$\begin{aligned} &\frac{\partial \xi}{\partial t}+\frac{\partial}{\partial \theta}\left(\zeta h_s^2\left(\frac{\mathrm{d}^3 h_s}{\mathrm{d}\theta^3}+\frac{\mathrm{d}h_s}{\mathrm{d}\theta}\right)-h_s^2\sin\theta+\left(1+\alpha_u\frac{\mathrm{d}h_s}{\mathrm{d}\theta}\right)h_s\right)\xi \\ &+\left(\left(\zeta h_s^2\left(\frac{\mathrm{d}^3 h_s}{\mathrm{d}\theta^3}+\frac{\mathrm{d}h_s}{\mathrm{d}\theta}\right)-h_s^2\sin\theta+\left(1+\alpha_u\frac{\mathrm{d}h_s}{\mathrm{d}\theta}\right)h_s\right)+\frac{\mathrm{d}}{\mathrm{d}\theta}\left(\alpha_u\frac{h_s^2}{2}+\zeta\frac{h_s^3}{3}\right)\right)\frac{\mathrm{d}\xi}{\mathrm{d}\theta} \\ &+\left(\alpha_u\frac{h_s^2}{2}+\zeta\frac{h_s^3}{3}\right)\frac{\mathrm{d}^2\xi}{\mathrm{d}\theta^2}+\frac{\mathrm{d}}{\mathrm{d}\theta}\left(\zeta\frac{h_s^3}{3}\right)\frac{\mathrm{d}^3\xi}{\mathrm{d}\theta^3}+\left(\zeta\frac{h_s^3}{3}\right)\frac{\mathrm{d}^4\xi}{\mathrm{d}\theta^4}=0, \end{aligned} \tag{E.3}$$

and further rearranging

$$\begin{aligned}
&\frac{\partial \xi}{\partial t} + \left(\zeta 2 h_s \frac{\mathrm{d}h_s}{\mathrm{d}\theta} \left(\frac{\mathrm{d}^3 h_s}{\mathrm{d}\theta^3} + \frac{\mathrm{d}h_s}{\mathrm{d}\theta} \right) + \zeta h_s^2 \left(\frac{\mathrm{d}^4 h_s}{\mathrm{d}\theta^4} + \frac{\mathrm{d}^2 h_s}{\mathrm{d}\theta^2} \right) - 2 h_s \frac{\mathrm{d}h_s}{\mathrm{d}\theta} \sin\theta - h_s^2 \cos\theta \right. \\
&\qquad \left. + \left(1 + \alpha_u \frac{\mathrm{d}h_s}{\mathrm{d}\theta} \right) \frac{\mathrm{d}h_s}{\mathrm{d}\theta} + \left(\alpha_u \frac{\mathrm{d}^2 h_s}{\mathrm{d}\theta^2} \right) h_s \right) \xi \\
&\quad + \left(\zeta h_s^2 \left(\frac{\mathrm{d}^3 h_s}{\mathrm{d}\theta^3} + 2 \frac{\mathrm{d}h_s}{\mathrm{d}\theta} \right) - h_s^2 \sin\theta + \left(1 + 2\alpha_u \frac{\mathrm{d}h_s}{\mathrm{d}\theta} \right) h_s \right) \frac{\mathrm{d}\xi}{\mathrm{d}\theta} \\
&\quad + \left(\alpha_u \frac{h_s^2}{2} + \zeta \frac{h_s^3}{3} \right) \frac{\mathrm{d}^2 \xi}{\mathrm{d}\theta^2} \\
&\quad + \zeta h_s^2 \frac{\mathrm{d}h_s}{\mathrm{d}\theta} \frac{\mathrm{d}^3 \xi}{\mathrm{d}\theta^3} \\
&\quad + \zeta \frac{h_s^3}{3} \frac{\mathrm{d}^4 \xi}{\mathrm{d}\theta^4} = 0.
\end{aligned} \tag{E.4}$$

Equation (E.4) is a 4th order ode for ξ.

Bibliography

[1] D. J. Acheson. *Elementary fluid dynamics*. Oxford applied mathematics and computing science series. Clarendon Press, Oxford, 1990.

[2] A. Acrivos and B. Jin. Rimming flows within a rotating horizontal cylinder: asymptotic analysis of the thin-film lubrication equations and stability of their solutions. *Journal of Engineering Mathematics*, 50(2-3):99–120, 2004.

[3] J. Ashmore, A. E. Hosoi, and H. A. Stone. The effect of surface tension on rimming flows in a partially filled rotating cylinder. *Journal of Fluid Mechanics*, 479:65–98, 2003.

[4] G. K. Batchelor. *An introduction to fluid dynamics*. Cambridge mathematical library. University Press, Cambridge, 2000.

[5] E. S. Benilov. Does surface tension stabilize liquid films inside a rotating horizontal cylinder? Part 2: Multidimensional disturbances. *Studies in Applied Mathematics*, 116(1):1–20, 2006.

[6] E. S. Benilov, N. Kopteva, and S. B. G. O'Brien. Does surface tension stabilize liquid films inside a rotating horizontal cylinder? *Quarterly Journal of Mechanics and Applied Mathematics*, 58:185–200, 2005.

[7] E. S. Benilov and S. B. G. O'Brien. Inertial instability of a liquid film inside a rotating horizontal cylinder. *Physics of Fluids*, 17(5):052106, 2005.

[8] E. S. Benilov, S. B. G. O'Brien, and I. A. Sazonov. A new type of instability: explosive disturbances in a liquid film inside a rotating horizontal cylinder. *Journal of Fluid Mechanics*, 497:201–224, 2003.

[9] T. B. Benjamin, W. G. Pritchard, and S. J. Tavener. Steady and unsteady flows of a highly viscous liquid in a rotating horizontal cylinder. *Preprint*, 1993.

[10] A. Bertozzi and M. Shearer. Existence of undercompressive traveling waves in thin film equations. *SIAM Journal on Mathematical Analysis*, 32(1):194–213, 2000.

[11] A. L. Bertozzi, A. Münch, and M. Shearer. Undercompressive shocks in thin film flows. *Physica D*, 134(4):431–464, 1999.

[12] B. R. Duffy and S. K. Wilson. Thin-film and curtain flows on the outside of a rotating horizontal cylinder. *Journal of Fluid Mechanics*, 394:29–49, 1999.

[13] P. Evans, L. Schwartz, and R. Roy. Three-dimensional solutions for coating flow on a rotating horizontal cylinder: Theory and experiment. *Physics of Fluids*, 17(7):–, 2005.

[14] P. L. Evans, L. W. Schwartz, and R. V. Roy. Steady and unsteady solutions for coating flow on a rotating horizontal cylinder: Two-dimensional theoretical and numerical modeling. *Physics of Fluids*, 16(8):2742–2756, 2004.

[15] M. Farrall. *Numerical modelling of two-phase flow in a simplified bearing chamber*. PhD thesis, University of Nottingham, 2000.

[16] M. Farrall. Film module documentation for FCM1.0. *Report to Rolls Royce and User Guide*, (UTC/TF/2004/36/MF), 2004.

[17] M. Farrall, S. Hibberd, K. Simmons, and D. Giddings. Prediction of air/oil exit flows in a commercial aero-engine bearing chamber. *Proceedings of the Institution of Mechanical Engineers Part G - Journal of Aerospace Engineering*, 220(G3):197–202, 2006.

[18] M. Farrall, K. Simmons, S. Hibberd, and P. Gorse. A numerical model for oil film flow in an aeroengine bearing chamber and comparison to experimental data. *Journal of Engineering for Gas Turbines and Power - Transactions of the ASME*, 128(1):111–117, 2006.

[19] B. Fornberg. Generation of finite-difference formulas on arbitrarily spaced grids. *Mathematics of Computation*, 51(184):699–706, 1988.

[20] E. J. Hinch and M. A. Kelmanson. On the decay and drift of free-surface perturbations in viscous thin-film flow exterior to a rotating cylinder. *Proceedings of the Royal Society of London Series A - Mathematical, Physical and Engineering Sciences*, 459(2033):1193–1213, 2003.

[21] E. J. Hinch, M. A. Kelmanson, and P. D. Metcalfe. Shock-like free-surface perturbations in low-surface-tension, viscous, thin-film flow exterior to a rotating cylinder. *Proceedings of the Royal Society of London Series A - Mathematical, Physical and Engineering Sciences*, 460(2050):2975–2991, 2004.

[22] A. E. Hosoi and L. Mahadevan. Axial instability of a free-surface front in a partially filled horizontal rotating cylinder. *Physics of Fluids*, 11(1):97–106, 1999.

[23] D.-Y. Hsieh and H. S.P. *Wave and Stability in Fluids*. World Scientific, 1994.

[24] T. P. Hynes. *Stability of thin films*. PhD thesis, Cambridge, 1978.

[25] R. E. Johnson. Steady-state coating flows inside a rotating horizontal cylinder. *Journal of Fluids Mechanics*, 190:321–342, 1988.

[26] R. E. Johnson. Coating flow stability in rotational molding. In G. Yates, editor, *Engineering Science, Fluid Dynamics: A symposium to honor T. Y. Wu*, pages 435–449. World Scientific, Singapore, 1990.

[27] S. Kalliadasis, E. A. Demekhin, C. Ruyer-Quil, and M. G. Velarde. Thermocapillary instability and wave formation on a film falling down a uniformly heated plane. *Journal of Fluid Mechanics*, 492:303–338, 2003.

[28] S. Kalliadasis, A. Kiyashko, and E. A. Demekhin. Marangoni instability of a thin liquid film heated from below by a local heat source. *Journal of Fluid Mechanics*, 475:377–408, 2003.

[29] C. Kleinstreuer. *Two-phase flow: theory and applications*. Taylor & Francis, New York, NY; London, 2003.

[30] R. Levy and M. Shearer. The motion of a thin liquid film driven by surfactant and gravity. *SIAM Journal on Applied Mathematics*, 66(5):1588–1609, 2006.

[31] A. M. M. Maqableh. *Computational study of multi-phase air/oil heat transfer in aero-engine bearing chambers*. PhD thesis, University of Nottingham, 2005.

[32] A. M. M. Maqableh, K. Simmons, S. Hibberd, H. Power, and C. Young. CFD modelling of three-component air/oil flow and heat transfer in a rotating annulus. In *11th International Conference on CFD*, 2003.

[33] H. K. Moffatt. Behaviour of a viscous film on the outer surface of a rotating cylinder. *Journal de Méchanique*, 16(5):651–673, 1977.

[34] C. J. Noakes. *The dynamics of liquid films on rotating surfaces*. PhD thesis, University of Nottingham, 2001.

[35] C. J. Noakes, J. R. King, and D. S. Riley. On three-dimensional stability of a uniform, rigidly rotating film on a rotating cylinder. *Quarterly Journal of Mechanics and Applied Mathematics*, 58:229–256, 2005.

[36] C. J. Noakes, J. R. King, and D. S. Riley. On the development of rational approximations incorporating inertial effects in coating and rimming flows: a multiple-scales approach. *Quarterly Journal of Mechanics and Applied Mathematics*, 59:163–190, 2006.

[37] S. B. G. O'Brien. Linear stability of rimming flow. *Quarterly of Applied Mathematics*, 60(2):201–211, 2002.

[38] S. B. G. O'Brien. A mechanism for linear instability in two-dimensional rimming flow. *Quarterly of Applied Mathematics*, 60(2):283–299, 2002.

[39] S. B. G. O'Brien and E. G. Gath. The location of a shock in rimming flow. *Physics of Fluids*, 10(4):1040–1042, 1998.

[40] F. M. Orr and L. E. Scriven. Rimming flow - numerical simulation of steady, viscous, free-surface flow with surface tension. *Journal of Fluid Mechanics*, 84(JAN):145–165, 1978.

[41] K. J. Ruschak and L. E. Scriven. Rimming flow of liquid in a rotating horizontal cylinder. *Journal of Fluid Mechanics*, 76(Jul 14):113–125, 1976.

[42] L. F. Shampine and J. Kierzenka. Solving boundary value problems for ordinary differential equations in Matlab with bvp4c. `http://www.mathworks.com/bvp_tutorial/`.

[43] N. H. Shuaib, H. Power, S. Hibberd, and K. Simmons. A numerical study of wave structures developed on the free surface of a film flowing on inclined planes and subjected to surface shear. *International Journal for Numerical Methods in Engineering*, 68(7):755–789, 2006.

[44] U. Thiele and E. Knobloch. Thin liquid films on a slightly inclined heated plate. *Physica D-Nonlinear Phenomena*, 190(3-4):213–248, 2004.

[45] S. T. Thoroddsen and L. Mahadevan. Shark-teeth pattern in coating flow inside a horizontally rotating cylinder. *Physics of Fluids*, 8(9):S10, 1996.

[46] S. T. Thoroddsen and L. Mahadevan. Experimental study of coating flows in a partially-filled horizontally rotating cylinder. *Experiments in Fluids*, 23(1):1–13, 1997.

[47] M. Tirumkudulu and A. Acrivos. Coating flows within a rotating horizontal cylinder: Lubrication analysis, numerical computations, and experimental measurements. *Physics of Fluids*, 13(1):14–19, 2001.

[48] L. N. Trefethen. *Spectral methods in Matlab*. Software, environments, tools. Society for Industrial and Applied Mathematics, Philadelphia, PA, 2000.

[49] L. N. Trefethen and M. Embree. *Spectra and pseudospectra: the behavior of nonnormal matrices and operators*. Princeton University Press, Princeton, N.J.; Oxford, 2005.

[50] P. M. J. Trevelyan and S. Kalliadasis. Wave dynamics on a thin-liquid film falling down a heated wall. *Journal of Engineering Mathematics*, 50(2-3):177–208, 2004.

[51] M. Villegas-Díaz. *Analytical and numerical studies of thin-film rimming flow subject to surface shear*. PhD thesis, University of Nottingham, 2005.

[52] M. Villegas-Díaz, H. Power, and D. S. Riley. On the stability of rimming flows to two-dimensional disturbances. *Fluid Dynamics Research*, 33(1-2):141–172, 2003.

[53] M. Villegas-Díaz, H. Power, and D. S. Riley. Analytical and numerical studies of the stability of thin-film rimming flow subject to surface shear. *Journal of Fluid Mechanics*, 541:317–344, 2005.

[54] Y. Wang, K. Simmons, and S. Hibberd. Numerical study of the effect of injected oil droplets on the core air flow with a HP-IP bearing chamber model. *Report to Rolls Royce*, (UTC/TF/2000/17/YW), 2000.

[55] Y. Wang, K. Simmons, and S. Hibberd. Numerical investigation of the turbulent flow field and oil droplet motion in an annulus with co-/contra- rotating shafts. *Report to Rolls Royce*, (UTC/TF/2001/29/YW), 2001.

[56] Y. Wang, K. Simmons, S. Hibberd, and C. Eastwick. CFD study of the single-phase air flow field and oil droplet motion in the Rolls-Royce HP-IP bearing chamber. *Report to Rolls Royce*, (UTC/TF/1999/13/YW), 1999.

[57] E. W. Washburn, C. J. West, and C. Hull. *International critical tables of numerical data, physics, chemistry and technology*. Published for the National Research Council by McGraw-Hill, New York, 1st edition, 1926.

[58] S. D. R. Wilson and J. Williams. [1] the flow of a liquid film on the inside of a rotating cylinder, and some related problems. *Physics of Fluids*, 9(8):2184–2190, 1997.

[59] S. K. Wilson, B. R. Duffy, and G. J. B. Black. Thin-film flow on a stationary or uniformly rotating horizontal cylinder subject to a prescribed uniform shear stress at the free surface of the film., Preprint, 2004.

[60] S. K. Wilson, R. Hunt, and B. R. Duffy. On the critical solutions in coating and rimming flow on a uniformly rotating horizontal cylinder. *Quarterly Journal of Mechanics and Applied Mathematics*, 55:357–383, 2002.

[1] Not to be confused with the current author